ABSTRACT

Title of dissertation: ULTRA-HIGH IMPEDANCE SUPERCONDUCTING CIRCUITS

Raymond Alonso Mencia, Doctor of Philosophy, 2023

Dissertation directed by: Professor Vladimir E. Manucharyan
University of Maryland Joint Quantum Institute

Chains of Josephson junctions are known to produce some of the largest kinetic per-unit-length inductance, which can exceed the conventional geometric one by about 10^4. However, the maximum total inductance is still limited by the stray capacitance of the chain, which results in parasitic self-resonances. This stray capacitance is unnecessarily large in most circuits due to the high dielectric constant of silicon or sapphire substrates used. Here, we explore a regime of ultra-high impedance superconducting circuits by introducing the technique of releasing the Josephson chain off the substrate. The ultra-high impedance regime ($Z > 4 \times R_Q \approx 25.8\text{k}\Omega$) is realized by combining a maximal per-unit-length inductance with a minimal stray capacitance and demonstrating the highest impedance electromagnetic structures available today. We begin with suspended "telegraph" transmission lines, composed of 30,000+ junctions and show that the wave impedance can exceed $5 \times R_Q$ (33 kΩ) while the line still maintains a negligible DC resistance. To quantify the effects of parasitic chain modes in ultra-high impedance circuits, we use high-inductance fluxonium qubits. We show that chain modes are ultra-strongly coupled to the qubit but can be moved to a higher frequency with the Josephson chain-releasing technique. Finally, we create a superconducting quasicharge qubit (blochnium),

dual of transmon, whose impedance reaches over 30 $\times$ R_Q (200 kΩ) with no evidence of parasitic modes below 10 GHz. This qubit completes the periodic table of superconducting atoms and demonstrates the dual nature of a small Josephson junction in ultra-high impedance circuits, which we probe in a DC experiment in the final chapter.

ULTRA-HIGH IMPEDANCE SUPERCONDUCTING CIRCUITS

by

Raymond Alonso Mencia

Dissertation submitted to the Faculty of the Graduate School of the
University of Maryland, College Park in partial fulfillment
of the requirements for the degree of
Doctor of Philosophy
2023

Advisory Committee:
Professor Vladimir E. Manucharyan, Chair/Advisor
Professor Mohammad Hafezi, Dean's representative
Professor Alicia Kollár
Professor Christopher Lobb
Professor Jay Deep Sau

Dedication

This thesis is dedicated to the memory of Josh Lowy and Zach Muir; two lifelong friends who tragically passed away in 2020 and 2021, respectively. I would also like to further dedicate this thesis to my family, friends, and supporters along the way.

Acknowledgments

This thesis is the product of many different people's contributions and it is nearly impossible to thank everyone that had a hand in the successful completion of this dissertation.

Firstly, I need to thank Bill Billingsley, Alan Edelstein, and John Timmerwilke who were my first mentors as an experimental physicist.

While working as a graduate student I had the great pleasure of being mentored by every post-doctoral researcher passing through our group at a certain point. First, I would like to thank Yen-Hsiang Lin who mentored me as an undergraduate while working on titanium nitride. I would like to thank Roman Kuzmin who mentored me in JJ transmission lines and Bloch oscillations and would like to thank him for meeting with me for weekly paper discussions. I need to thank Ivan Pechenezhskiy who mentored me in measuring superconducting qubits, python coding, and parasitic chain modes while working together on the blochnium project. I also need to thank him for basically tutoring me in any physics subject I asked for; his impact on this thesis and my development as an experimentalist is undeniable. Finally, I would like to thank Quentin Ficheux who mentored me in qubit measurements while studying fluxoniums. I thoroughly enjoyed sharing an office, especially during the COVID pandemic.

Next, I would like to thank Long Nguyen for introducing me to many new ideas with fluxonium and coherence; Nick Grabon for introducing me to fabrication and being a dinner/beer buddy on late work nights; Natalia Pankratova for also teaching me how to fabricate and for being personable by always celebrating my birthday; Nathanaël Cottet who introduced me to many new concepts and shared his enthusiasm for the field; Nitish Mehta for always being willing to answer my physics questions no matter the time or place; Hanho Lee for helping me with DC measurements and sharing his wide range of experimental knowledge. I would also like to thank Hanho for helping me take care of the wirebonder and

the Plassys. I would like to thank Aaron Somoroff for showing me his techniques for measuring low-frequency fluxoniums and would like to thank him for introducing me to chess and poker while also being my most frequent billiards opponent; and finally Haonon Xiong for always being willing to discuss cryogenics and different measurement techniques.

I would like to thank Vlad Manucharyan for providing the resources and many of the main ideas for this thesis. I would like to further thank Vlad for mentoring me during my undergraduate and graduate education and having my back throughout my graduate school career always presenting me with new research opportunities whether it is collaborations, conferences, or fellowships. Thank you for your guidance and support along the way.

Finally, I would like to thank David Ferguson for the discussions about parasitic chain modes. I would like to thank Michel Devoret, Benjamin Huard, and Ioan Pop for organizing the Les Houches 2019 Quantum Machines summer school. I recognize this event as a turning point in my graduate career. I would like to acknowledge a few close friends and colleagues I met at this summer school including Jeremey Stevens, Raphaël Lescanne, Martin Spiecker, and Michiel Burgelman. Truly, each and everyone at the conference had an impact through discussion which inspired a colloquial aspect of our field. Furthermore, I would like to acknowledge my ARO/LPS Quantum computing graduate research fellowship and thank them for their support.

On a personal note, I would like to thank my parents, Rick and Eileen, for always supporting me in the endeavors which I pursue. I would like to thank my grandmother, Cristina D'Erasmo, for always being an unwavering supporter. You guys are appreciated.

Table of Contents

List of Constants, Variables, and Abbreviations

List of Constants:

---

h - Planck's constant = $6.626 \cdot 10^{-34}$ J·s
$\hbar$ - Reduced Planck's constant = $1.055 \cdot 10^{-34}$ J·s
e - electron charge = $1.602 \cdot 10^{-19}$ C
k_B - Boltzmann factor = $1.381 \cdot 10^{-23}$ J/K
ε_0 - vacuum permittivity = $8.854 \cdot 10^{-12}$ F/m
μ_0 - vacuum permeability = $4\pi \cdot 10^{-7}$ H/m
Z_{vac} - impedance of free space = $\sqrt{\mu_0/\varepsilon_0}$ = 377 Ω
Φ_0 - magnetic flux quantum = $h/2e$= $2.068 \cdot 10^{-15}$ Wb
φ_0 - reduced flux quantum = $\Phi_0/2\pi = 3.291 \cdot 10^{-16}$ Wb
R_K - von Klitzing constant = h/e^2 = 25.81 kΩ
R_Q - Resistance quantum = $h/4e^2$ = 6.45 kΩ
K_J - Josephson constant = $1/\Phi_0 = 483,598$ GHz/V

List of Definitions

$E_J = \Delta R_Q/2R_N = \hbar I_0/2e$ – Josephson energy,
$E_C = e^2/2C_\Sigma$ – Charging energy,
$E_L = \varphi_0^2/L = \varphi_0^2/NL_J^A$ – Inductive energy,

$\omega_p/2\pi = \sqrt{8E_JE_C}$ – Plasma frequency
$Z_\infty = \sqrt{2L_J/C_g}$ – Characteristic impedance,
$v = a/\sqrt{2L_JC_g}$ – Velocity of light,
$k = \pi/2L + n\pi/L$ – Wavenumber,
$\omega(k) = vk/\sqrt{1+(vk/\omega_p)^2}$ – Wave dispersion

IFQ, $\Phi_{\text{ext}} = \mathbb{Z}\Phi_0$ – Integer flux quantum,
HFQ, $\Phi_{\text{ext}} = \mathbb{Z}\Phi_0/2$ – Half-integer flux quantum
$\varphi_{\text{zpf}} = 2\pi\Phi_{\text{zpf}}/\Phi_0 = \sqrt{\pi Z/R_Q} = \{2E_C/E_L\}^{1/4}$ – Phase-difference ZPF,
$\hat{\varphi} = 2\pi\hat{\Phi}/\Phi_0 = \varphi_{\text{zpf}}(\hat{a}+\hat{a}^\dagger)$,

$n_{\mathrm{zpf}} = Q_{\mathrm{zpf}}/2e = \sqrt{R_Q/4\pi Z} = \{E_L/32E_C\}^{1/4}$ – Cooper-pair number ZPF,
$\hat{n} = \hat{Q}/2e = in_{\mathrm{zpf}}(\hat{a}^\dagger - \hat{a})$,

$1/T_2 = 1/2T_1 + 1/T_\phi$ – Decoherence time

List of Variables:

I_0 - Critical current
L_J - Josephson inductance
L_{tot} - Total inductance
C_J - Josephson capacitance
C_g - Ground capacitance
C_B - Bloch capacitance
C_Σ - Total capacitance
R_N - Normal resistance
T_1 - Energy relaxation time
T_2^E - Hanh-echo decoherence time
T_2^* - Ramsey decoherence time
T_ϕ - Dephasing time
T_{eff} - Effective temperature

List of Abbreviations:

BB - Bloch band
CPB - Cooper-pair box
JJ - Josephson junction
SCQC - Superconducting Quantum Circuits
SQUID - Superconducting interference device
ZPF - Zero-point fluctuations

1 Introduction

"Science is what we understand well enough to explain to a computer. Art is everything else we do." — Donald Knuth

The genesis of quantum mechanics at the beginning of the 20th century ushered in a new description of the physical world inaccessible to human senses; physics on the atomic scale. The bizarre world of quantum mechanics replaces classical physics continual certainty of determinism with a probabilistic theory of randomness and interference. These two physical descriptions of the world are separated by a wide rift with various attempts by founders of the field to stitch the two pictures together through various thought experiments. Most notably demonstrated by Bohr's correspondence principle, Heisenberg's microscope, and Schrödinger's cat. Yet, the realization of coherent macroscopic quantum mechanics still eluded experiments.

Superconductivity in itself is a macroscopic quantum phenomenon that manifests in a material upon cooling below a critical temperature T_c [147] and has the properties that include zero resistance when biased with direct current (DC) and the expulsion of magnetic fields (Meissner effect). According to the macroscopic phenomenological quantum model of superconductivity, below the critical temperature, the charge carriers in a supercon-

ductor condense forming paired electrons called Cooper pairs. The superconducting condensate formed can be described by a single wave function within the material and takes the following form [175]:

$$\psi(r,t) = \sqrt{n(r,t)}e^{i\phi(r,t)} \ , \tag{1.1}$$

where n is the density of Cooper pairs and ϕ is known as the superconducting phase. The superconducting state represents a dramatic reduction of complexity within the system.

In 1961, Brian Josephson theorized charge carriers in superconducting leads separated by an insulating barrier should exhibit coherent tunneling through the barrier [89]. This quantum phenomenon was measured experimentally thereafter, confirming the existence of coherent tunneling through a macroscopic barrier. This collective phenomenon occurs in systems comprised of billions of atoms yet can be simply described with just a single wavefunction. The technology for engineering quantum electrical circuits is based upon this effect and the electrical component with this behavior is referenced to as a Josephson junction (JJ).

The field of superconducting quantum circuits came probably around the time when Anthony Legget proposed, in 1980 [107], that the observation of quantum *coherence* between macroscopically different flux states in a superconducting loop should be realistically observable. During the next few decades, the field of superconducting circuits progressed rather rapidly with the first forms of the charge qubit being suggested in 1987 [21] and experimentally realized by the Saclay group [15] experimentally in 1997. While in the year 1999, Nakumara et al [133] first demonstrated coherent control of a macroscopic quantum state in a superconducting circuit by observing the quantum state evolution in the time domain with ultra-fast electronics. By 2002, the full coherent manipulation of a superconducting circuit was realized [179] and later realized in other varieties of superconducting circuits [27]. Several years later, in 2004, the circuit analog to cavity QED [113] was experimentally realized [183] which coupled a photon in a resonator to a superconducting circuit. These initial highlighted works provided a strong foundation for exploring macroscopic quantum phenomena with superconducting electrical circuits which are the foundation for the field.

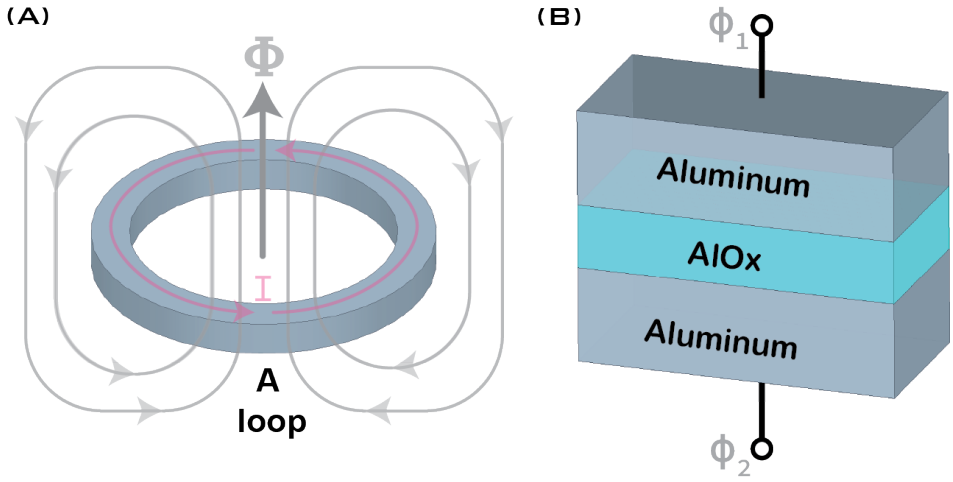

Figure 1.1: (A) A superconducting loop with circulating current has a fixed amount of total flux threading the loop given by integer values of $\Phi_{\text{tot}} = m\Phi_0$. (B) Two superconducting leads separated by a dielectric barrier forms the superconducting Josephson junction. Each lead has a superconducting phase $\phi_{1,2}$.

1.1 Macroscopic quantum nature of an electrical circuit

Superconducting circuits exploit the remarkable property that macroscopic degrees of freedom, such as the magnetic flux through a loop or the number of charges stored on an island, can behave coherently. This behavior is in part due to the quantum nature of superconductors but probably manifests itself experimentally due to the lack of electrical dissipation of the collective excitations present in these systems.

1.1.1 Flux-quantization

Consider a large superconducting ring that has externally applied magnetic flux (Φ_{ext}) penetrating the space occupied by the loop. The magnetic flux inside the superconductor volume will be expelled by the Messiner effect yet a finite amount of magnetic flux still penetrates the inner part of the loop. This residual flux is created not only by the externally applied flux but also by an induced supercurrent flowing on the surface. To find the total amount of magnetic field present inside the superconducting loop a path integral around a contour within the superconducting material itself is utilized

[130]:

$$\int_{\phi_1}^{\phi_2} \left(\nabla\phi - \frac{2e}{\hbar} A \right) \cdot dl = 0$$
$$\int_{\phi_1}^{\phi_2} \nabla\phi \cdot \mathrm{d}l = \frac{2e}{\hbar} \oiint_S B \cdot \mathrm{d}S \tag{1.2}$$

where A is the magnetic vector potential and the line integral of A around the closed loop from ϕ_1 to ϕ_2 is equal to the total magnetic flux enclosed through Stoke's theorem. Additionally, the problem has another constraint, that the wavefunction (equation 1.1) must be single-valued at the same point in space which implies $\phi_2 = \phi_1 - 2\pi m$; where m is defined as all real integers. Plugging this into the expression above creates the final solution:

$$\Phi_{\text{tot}} = \frac{h}{2\pi}\frac{1}{2e}(\phi_1 - \phi_2) = m \times \frac{h}{2e} = m \times \Phi_0 \tag{1.3}$$

where Φ_0 is a fundamental constant called a magnetic flux quantum with a value of:

$$\Phi_0 = \frac{h}{2e} = 2.068 \times 10^{-15} \text{ Wb} . \tag{1.4}$$

The magnetic flux is often represented in a normalized form and is expressed as: $\varphi_{\text{tot}}/2\pi = \Phi_{\text{tot}}/\Phi_0 = m$. This result demonstrates the magnetic flux threading the loop is quantized in integer values (m) of the magnetic flux quantum made possible by the induced supercurrent which adjusts value in order to maintain this quantization effect.

1.1.2 Josephson equations

A Josephson junction (JJ) [89] is formed when two superconducting wires are electrically separated by a thin insulating barrier and is the essential building block to SCQC. Typically, two aluminum wires are separated by a thin aluminum oxide barrier forming an S-I-S junction. When a junction is cooled to a sufficiently low temperature ($T < T_c$) the electrodes become superconducting and present zero resistance to direct current (DC) while the thin barrier remains in an insulating state.

Remarkably, a zero voltage supercurrent is able to flow across the insulating barrier between the two superconducting electrodes. The supercurrent is a non-linear sinusoidal function whose argument is the Cooper-pair condensate phase difference between the JJ electrodes. When the phase difference is constant the voltage difference between the electrodes is zero; conversely when the phase difference is changing with respect to time, a non-zero voltage appears implying the junction is now accompanied by a finite resistance. This phenomenon is described by the first (DC) and second (AC) Josephson equations [89, 175]:

$$\begin{aligned} I &= I_0 \sin(\varphi) \\ V &= \varphi_0 \frac{d\varphi}{dt} \end{aligned} \quad . \tag{1.5}$$

where $(\varphi = \frac{2\pi}{\Phi_0}\{\phi_2 - \phi_1\} = \{\varphi_2 - \varphi_1\})$ is the normalized phase difference between the Cooper pair wave functions for each of the two superconducting wires. While I_0 is defined as the critical current – that is the maximum amount of supercurrent the junction can support before turning normal and is more or less a constant value depending on the junction properties itself.

The second Josephson equation describes when a non-zero voltage is created between the two superconducting leads. When the voltage exceeds twice the value of the superconducting gap (Δ) V$> 2\Delta$, the JJ will radiate at a frequency proportional to the value of the voltage difference across the JJ [147]. This astounding effect is used as the fundamental quantum standard for the SI unit voltage. The frequency-voltage relation is $f = \frac{2e\langle V \rangle}{h}$.

The non-dissipative, non-linear properties of a Josephson junction will be used to convert ordinary macroscopic superconducting circuits into "artificial atoms" [28] and will be one of the main circuit elements discussed throughout this work.

1.2 Linear circuit elements

The three key elements in SCQC are the capacitor, the inductor, and the Josephson junction. Basic circuit analysis uses generalized magnetic flux and electric charge as the time integral of voltage and current, respectively

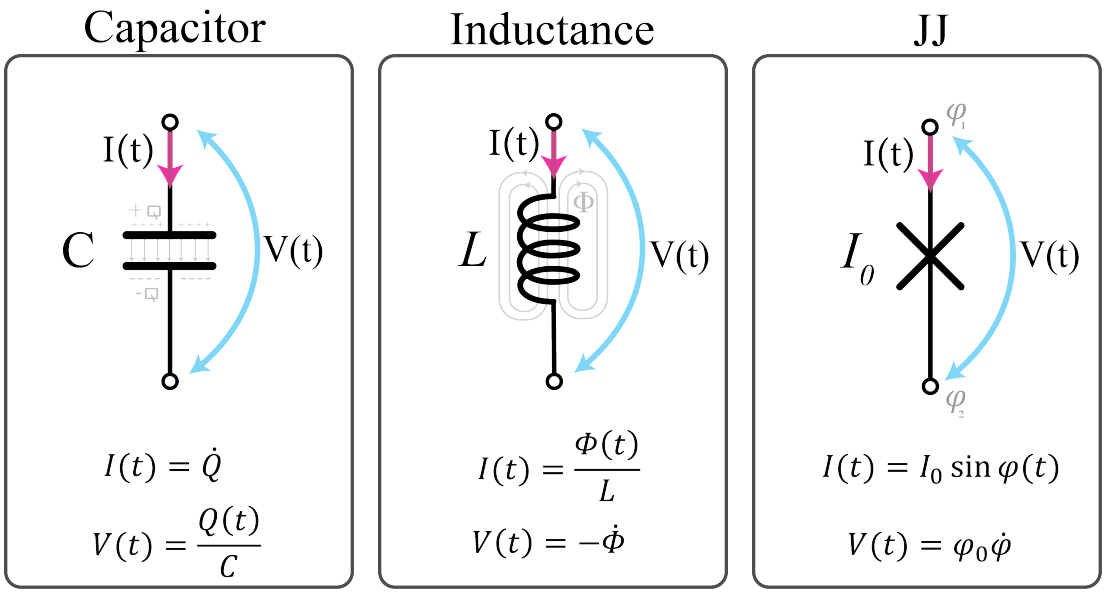

Figure 1.2: A capacitance C has total charge Q on each plate due to a voltage V. Energy is stored in the electric field between the two plates. A time-varying voltage causes the plates to charge and discharge. An inductance (L) has a current flowing along the wire which in turn produces a magnetic flux through the loop. A JJ has a non-linear current flowing across the barrier where the maximum amount of super current is denoted as I_0. When the phase difference between the two leads changes in time, a finite voltage appears.

[36]. Defining the generic circuit branch variables as:

$$\begin{aligned} \Phi_b(t) &= \int_{-\infty}^{t} V_b(t')\, dt' \\ Q_b(t) &= \int_{-\infty}^{t} I_b(t')\, dt' \,. \end{aligned} \tag{1.6}$$

The first linear circuit element is the capacitor which stores a total charge (Q) proportional to the voltage drop across separated leads. The capacitor stores energy in the electric field between the two plates where the amount of charge accumulated on each lead is dependent on the amount of voltage applied:

$$V(t) = \frac{Q(t)}{C}, \tag{1.7}$$

where C is the capacitance. Using the other generalized circuit equation for current the rather obvious relation: $I(t) = \dot{Q}(t)$ is recovered. The ca-

pacitor produces an imaginary reactive impedance to AC electrical signals that decreases with increasing signal frequency. The expression is given as: $Z_C(\omega) = 1/i\omega C$. An AC signal imposed on a capacitor produces a displacement current which can be understood as a time-varying electric field between the capacitor plates caused by the charging and discharging of capacitance.

The second linear circuit element is the inductor which stores energy in the form of a magnetic field that is proportional to the current traversing the wire. The flux is defined as the magnetic field per unit area and the inductance L is a proportionality constant that determines the ability to convert current into flux. The basic linear equation describing the relationship between current, flux, and inductance is:

$$I(t) = \dot{Q}(t) = \frac{\Phi(t)}{L} \, . \tag{1.8}$$

While the other generalized circuit branch equation is the relation:$V(t) = \dot{\Phi}(t)$. Noting this equation's similarity to the second Josephson equation. The inductor also produces an imaginary reactive impedance to AC electrical signals where now the impedance increases with increasing signal frequency. The expression for impedance is given as: $Z_L(\omega) = i\omega L$. An AC signal imposed on an inductor produces a fluctuating current causing a time-varying magnetic flux.

These basic variables each obey Kirchhoff's laws to simplify into node variables. For flux tunable devices, where the circuit forms a loop, the external biasing field must be included such that:

$$\Phi_{\text{ext}} = \sum_{\text{loop, } b} \Phi_b \, . \tag{1.9}$$

This exerts a physical constraint on the node variables which relates the external flux bias to the superconducting phase difference across a JJ embedded in a loop.

1.3 Energy scales

Each electrical component contributes an energy that governs the dynamics of an electrical circuit comprised of the three basic building blocks. Each energy scale can be engineered through careful design and fabrication. When properly executed the three building blocks are used to create macroscopic artificial atoms.

An important comment on the usual units convention is: normally, energy is discussed in units of eV or Joules, however, in SCQC the energy is usually divided by Plank's constant and is represented in units of Hertz (Hz).

1.3.1 Josephson energy

Based on the Josephson equations, the JJ energy is a highly non-linear function of the phase difference, φ, between the two superconducting electrodes separated by the thin insulating barrier. The energy scale for tunneling of Cooper-pairs is easily calculated as the work of an external circuit which increases the phase difference from zero to some value φ':

$$E_{\mathrm{JJ}} = \int I(t)V(t)\,dt = \frac{\hbar I_0}{2e}\int_0^{\varphi'} \sin(\varphi)\,d\varphi = \frac{\hbar I_0}{2e}(1-\cos(\varphi')) = E_{\mathrm{J}}(1-\cos(\varphi'))\,. \tag{1.10}$$

For a single JJ the total energy is E_{JJ} with the amplitude E_J a constant value. The usual range for E_J in SCQC is somewhere within the range of 1-100 GHz. A "small" or "weak" JJ is typically when $E_J < 10$ GHz. From a practical, experimental viewpoint, the Josephson energy can be written utilizing the Ambegaokar-Baratoff formula [130] which defines $I_0 = \frac{\pi\Delta}{2eR_N}$ where the superconducting gap of the Al leads is $\Delta \cong 40$ GHz and R_N is the room temperature normal resistance of the JJ. This allows for the expression of the Josephson energy as a function proportional to the ratio of the resistance quantum ($R_Q = h/2e^2 = 6.45$ kΩ) to the normal resistance. The value of the energy scale representing E_J is finally expressed as:

$$\boxed{E_{\mathrm{J}} = \frac{\Delta R_{\mathrm{Q}}}{2R_{\mathrm{N}}} = \frac{\hbar I_0}{2e}}\,. \tag{1.11}$$

This formula gives experimental intuition for how the Josephson energy scales with dimension; realizing $R_{\mathrm{N}} \propto \frac{1}{\text{area}}$ which means the smaller the area of a JJ the lower the value of E_{J} or simply stated: $E_{\mathrm{J}} \propto$ area.

Now using the AC Josephson equation and the generalized branch integral for flux, an illuminating integral showing the likeness of a JJ and an inductor is found:

$$\Phi(t) = \int_{-\infty}^{t} V(t')\, dt' = \int_{-\infty}^{t} \frac{\Phi_0}{2\pi} \frac{d\varphi}{dt'}\, dt' = \varphi_0 \varphi(t)\ . \tag{1.12}$$

This shows the equivalence between the branch flux and the superconducting phase difference across a JJ which is seen to be proportional to one another enabling the phase difference to be likewise defined as:

$$\varphi(t) = \frac{2\pi}{\Phi_0} \int_{-\infty}^{t} V(t')\, dt'\ . \tag{1.13}$$

This shows a clear similarity of the Josephson equations with Faraday's law of induction [54]; the change in the phase difference across the junction barrier is proportional to the voltage just like the change in the magnetic flux threading a loop is proportional to the voltage. Following this analogy, the Josephson inductance (L_{J}) is defined as:

$$L_{\mathrm{J}}(\varphi) = \frac{V}{dI/dt} = \frac{\Phi_0}{2\pi I_0 \cos(\varphi)} = \frac{\Phi_0}{2\pi I_0} \frac{1}{\sqrt{1 - \frac{I}{I_0}}}\ . \tag{1.14}$$

However, counter to the usual inductance, the Josephson inductance is nonlinear while also being able to take on positive and negative values alike. The relation for $L_{\mathrm{J}}(\varphi)$ allows for another form of $E_{\mathrm{JJ}}(\varphi)$ expressed as: $E_{\mathrm{JJ}}(\varphi) = \frac{\Phi_0}{2\pi L_{\mathrm{J}}(\varphi)}$.

1.3.2 Inductive energy

Traditionally, inductances are constructed of compactly turned wires which form a coil. The more turn density the stronger the electromagnet and so this usual form of producing an inductance is considered geometrical in nature. However, as was seen for JJs in equation 1.14, another form of inductive

energy exists in a superconductor. This inductive energy is associated with the amount of energy stored in the kinetic movement of the charge carriers. A superconductor possesses significant kinetic inductance due to the lack of scattering which normally thwarts this phenomenon in normal metals below optical frequency. Kinetic inductance can be solved by setting the total kinetic energy equal to the inductive energy and solving the inductance [2]:

$$L_{\text{kinetic}} = \frac{m_e}{2ne^2}\frac{l}{A} = \frac{\hbar R_\square}{1.76\pi k_B T_c} \,. \tag{1.15}$$

Where the second expression is found using the Mattis–Bardeen formula for the imaginary component of the complex conductivity [175] which is attributed to the kinetic inductance.

Experimentally, the first equation shows kinetic inductance can be increased by making a longer wire or by producing a thinner film. However, the kinetic inductance can further become enhanced depending on the material's Cooper pair density (n). In a superconductor that is "disordered", meaning superconducting grains are separated by some small region of non-superconducting material, the supercurrent can only exist in bulk if the charge carriers tunnel from one superconducting grain to another. This means the Cooper pair density is suppressed between the grains effectively increasing the kinetic inductance. The disorder of a superconductor is also reflected in the normal sheet resistance ($R_\square$) and the T_c as represented in the second equation.

An example of a disordered superconducting material is reactively evaporated titanium nitride (TiN) [127]. This material has large kinetic inductance sheet values ranging between $0.1 - 2$ nH/$\square$. This material's disorder is actually tunable with thickness and chemical composition which are both used as tuning knobs to push the disorder superconductor through the superconductor-insulator-transition (SIT) [110].

Likewise, an array of JJs can also act as a (synthetically) disordered wire. The insulating junction barrier suppresses Cooper pair density and therefore has a large kinetic inductance due to the reduced number of charge carriers tunneling through the junction interface. Furthermore, for sufficiently low currents compared to the critical current I_0, a small phase difference

enables a Taylor series approximation of the Josephson inductance represented in equation 1.14. The approximation leads to the JJ linear inductance $L_J = \frac{\Phi_0}{2\pi I_0}$. This inductance is inversely proportional to the critical current and becomes larger when the junction area is decreased. When a wire is comprised of many identical large JJs in series and $I \ll I_0$, the series of JJ can be linearized producing a total inductive energy:

$$\boxed{E_L = \frac{\Phi_0^2}{4\pi^2}\frac{1}{L_{\text{tot}}} = \frac{\Phi_0^2}{4\pi^2}\frac{1}{NL_J^A}} \tag{1.16}$$

where L_{tot} is the total sum of all of the Josephson inductances in the chain and is simply defined as the inductance per junction L_J^A times the number of junctions N. Typical values of inductive energy range between 1 GHz and 0.06 GHz in this thesis.

1.3.3 Charging energy

The final energy scale relevant to SCQC is the charging energy which is essentially the amount of energy required to place a charge onto a metallic island. To properly define the charging energy (E_C) consider an isolated superconducting island with a capacitance C to ground. The number of charges on the island will be defined as $Q = 2eN$ where N represents the integer number of excess Cooper pairs located on the island. The excess charge on the surface of the superconducting island will spread out and produce a static electric potential (U_Q) which requires the energy E_C for any new charge which is inclined to hop onto the island. If a voltage source is in the vicinity with capacitance C_{g} to the island then "external charge" can be induced: $Q_{\text{ext}} = 2e \times n_g = -C_g V_g$. The total charge on the island is then used to find the electrostatic potential:

$$Q = CU_Q + C_g(U_Q - V_g) \Rightarrow U_Q = \frac{Q}{C+C_g} + \frac{CV_g}{C+C_g} \tag{1.17}$$

and further defining the full self-capacitance of the island as $C_\Sigma = C + C_g$. So the total electrostatic charging energy of the island is given as:

$$\begin{aligned} E_{\text{cap}}(Q) =& \frac{Q^2}{2C_\Sigma} - \frac{QQ_{\text{ext}}}{C_\Sigma} = \frac{(Q-Q_{\text{ext}})^2}{2C_\Sigma} + \text{constant} \\ =& 4e^2 \frac{(N-n_g)^2}{2C_\Sigma} \, . \end{aligned} \tag{1.18}$$

The formal definition of the charging energy E_C can now be defined as:

$$\boxed{E_C = \frac{e^2}{2C_\Sigma}} \, . \tag{1.19}$$

Plugging this into equation 1.18 gives the full term expressed as $E_{\text{cap}} = 4E_C(N-n_g)^2$. The electrostatic charging energy of an island manifests charge quantization since if N was continuous then the minimum energy would always be $E_{\text{cap}} = 0$ at $N = n_g$. This is actually the case for any circuit element with a direct DC shortcut between itself and the source.

For a JJ there is always an innate capacitance associated with the parallel plate likeness of the S-I-S geometry. The usual JJ capacitance (C_J) is proportional to the area of the junction with a phenomenological value for Al/AlOx/Al which scales with area according to $C_J \approx 45$ fF/μm^2. It turns out, the separation this oxide creates between the superconducting leads (~ 1 nm) is enough to form the electrical disconnection which renders charge quantized on a superconducting island that is connected to ground through a single JJ.

1.3.4 A classical Josephson junction

The most basic model of a JJ is a current-biased junction in parallel with the innate junction capacitance C_J and a resistor. This model utilizes the Josephson equations and circuit analysis of Kirkohfs laws to find the equation of motion as:

$$I = \frac{\hbar C_J}{2e}\frac{d^2\varphi}{dt^2} + \frac{\hbar}{2e}\frac{1}{R}\frac{d\varphi}{dt} + I_0 \sin\varphi \, . \tag{1.20}$$

Where the resistance value (R) is of the junction in the normal state and is the resistance presented to normal electrons/quasiparticles [citation]. This

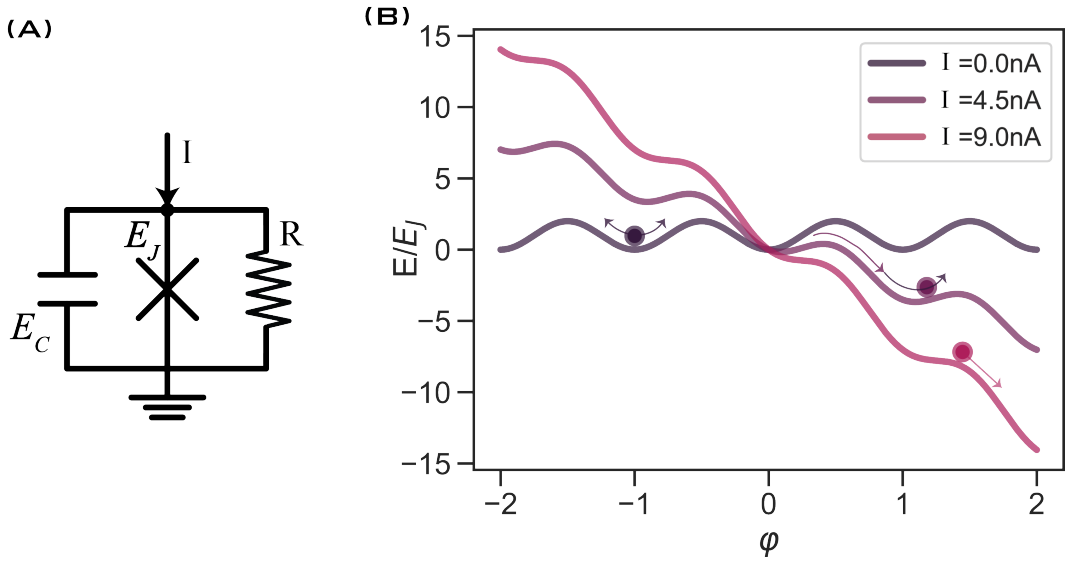

Figure 1.3: (A) The classical circuit for a current-biased JJ in parallel with a capacitor and a resistor. (B) The washboard potential for a JJ with $I_0 = 6$ nA. The current tilts the potential until the particles rolls down the Josephson potential at a rate $d\phi/dt$ given by the resulting voltage.

model is of the form similar to a forced damped oscillator, i.e. like a forced pendulum in gravity oscillating in a damping medium. More intuitively, we can think of this model as a particle moving in a viscous medium living in a sinusoidal potential. The position of the particle is represented by the phase difference φ, the amplitude of the potential is given by $A = \frac{\hbar I_0}{2e} = E_J$ creating the potential $U(\phi) = E_J(1-\cos\varphi)$, the particle's mass is given by $M = \frac{\hbar^2}{8E_C}$, and the viscosity given by $\eta = \frac{\hbar^2}{8E_C RC}$.

When the external current is non-zero the potential is modified: $E_J(1-\cos\varphi) - \frac{I}{I_0}\varphi$ resembling a "tilted-washboard". The external current creates a tilt to the cosinusodial Josephson potential. The simplified equation of motion using the mechanical analog is [90]:

$$M\frac{d^2\varphi}{dt^2} = -\eta\frac{d\varphi}{dt} - \frac{dU(\varphi)}{d\varphi}\,. \tag{1.21}$$

When the particle is confined to a single Josephson well it oscillates

about the minimum at the plasma frequency ($\omega_p/2\pi$) which is found by expanding the cosinusodial term for small phase difference and assuming $I \ll I_0$.

$$\omega_p/2\pi = \sqrt{8E_J E_C} \tag{1.22}$$

When the potential becomes tilted such that the particle can travel from well to well, $\frac{d\varphi}{dt} \neq 0$ meaning, by Josephson's second equation, a finite value of voltage appears and the value of voltage is directly proportional to $\frac{d\varphi}{dt}$ – meaning it is oscillating in time depending on the particle's velocity as it travels down the potential.

This basic equation of the JJ gives only one equation to find both I(t) and V(t); another equation to relate these two functions is to consider the impedance of the external "embedding" circuitry which surrounds the junction. In SCQC, the external system is usually made up of capacitors or inductances which are connected to the leads of the JJ. Therefore, the embedding circuitry's impedance can also determine the current and voltages of the JJ: $Z_e(\omega) = -V_J(\omega)/I_J(\omega)$. This means, in reality, fast variations in the current can be induced in the JJ by external microwave sources which are coupled to the external embedding circuitry surrounding the junction itself.

1.4 Quantum engineering of electrical circuits

In this section, the basic idea for describing voltages and currents in a superconducting circuit using a quantum mechanical description is formulated. The research presented in this work uses superconducting circuits to experimentally study macroscopic quantum systems where, ideally, the experiments are made out of dissipationless circuit elements. The ability to engineer the energy scales of each circuit element enables the quantum behavior of the circuit as a whole to either have a well-defined phase difference or a well-defined charge based on the relevant quantum zero-point fluctuations (zpf) of these two variables.

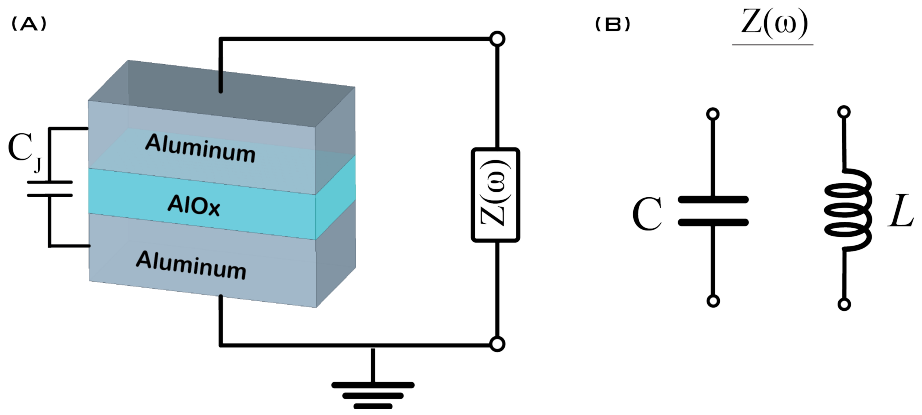

Figure 1.4: (A) A Josephson junction will always have intrinsic capacitance C_J formed by the two superconducting leads separated by an insulating layer. To measure the junction, it must be embedded into some circuitry represented by an arbitrary impedance $Z(\omega)$ which shunts the junction. (B) The shunting impedance can, in the simplest forms, either be a capacitance or inductance. The value of the shunting impedance depends on the value of C or L and the operating frequency.

1.4.1 Zero point fluctuations of an LC oscillator

The most basic dissipationless circuit is the LC oscillator where the parallel combination of capacitance and inductance is considered. The parallel LC oscillator can be described by the flux (Φ) threading through the inductor and the charge (Q) accumulated on the capacitor.

The Lagrangian is simply written as:

$$\mathscr{L} = T - U = \frac{C\dot{\Phi}^2}{2} - \frac{\Phi^2}{2L} \tag{1.23}$$

and applying the Legendre transformation to derive the equations of motion, we verify the LC circuit exhibits harmonic motion:

$$-\frac{d}{dt}\frac{\partial \mathscr{L}}{\partial \dot{\Phi}} = \frac{\partial \mathscr{L}}{\partial \Phi} \Rightarrow \ddot{\Phi} = -\frac{1}{LC}\Phi\,. \tag{1.24}$$

Finding the generalized momentum (charge)$Q = \frac{\partial \mathscr{L}}{\partial \dot{\Phi}} = C\dot{\Phi}$ produces a Lagrangian in the form: $\mathscr{L} = \frac{Q^2}{2C} - \frac{\Phi^2}{2L}$. The Hamiltonian ($\mathscr{H}$) is then defined

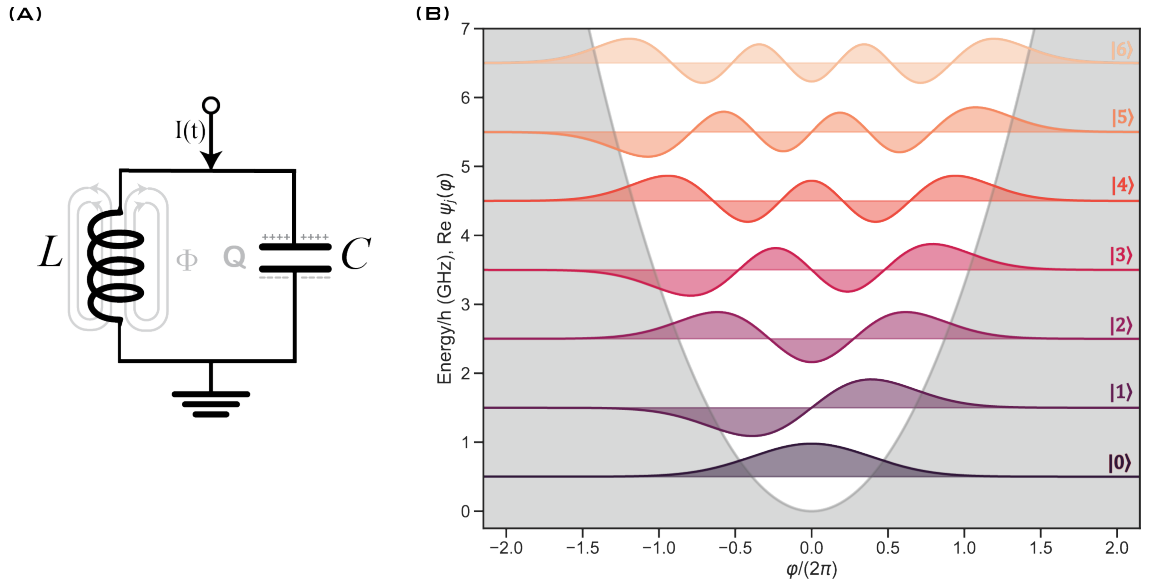

Figure 1.5: (A) An inductance, L, and capacitance, C, in parallel form a resonant circuit where the energy oscillates between being stored in the flux Φ which threads the inductor and the charge $\pm$Q which accumulates on the parallel plate capacitor. (B) The first few wavefunctions of the quantum harmonic oscillator (HO) which are offset by the eigenenergies of the system.

as:

$$\mathscr{H} = Q\dot{\Phi} - \mathscr{L} = \frac{Q^2}{2C} + \frac{\Phi^2}{2L} \tag{1.25}$$

To see further connections, Hamilton's equations show the current in the inductor is inversely related to the value of inductance, and the voltage across the capacitor is inversely related to the value of capacitance:

$$\begin{aligned} \dot{\Phi} &= \frac{\partial \mathscr{H}}{\partial Q} = \frac{Q}{C} = V \\ \dot{Q} &= \frac{\partial \mathscr{H}}{\partial \Phi} = \frac{-\Phi}{L} = I \end{aligned} \tag{1.26}$$

mirroring the solutions to the generalized branch variables.

Poisson brackets of the phase space coordinates $\{\Phi, Q\} = 1$ meaning the phase space variables can be promoted to quantum operators with a commutation relation $\frac{[\Phi,Q]}{\hbar} = \{\Phi, Q\} = 1$ such that $[\hat{\Phi}, \hat{Q}] = \hbar$. These now quantum variables will obey Heisenberg's uncertainty relation: $\delta\Phi\delta Q \geq \hbar/2$.

We can now think of this circuit as a quantum harmonic oscillator where the electrical circuit is oscillating between the current flowing through the inductor storing energy in the magnetic field or charge on the plates of the capacitance storing energy in the electric field. The dimensionless flux and charge are now defined as quantum operators written as a function of the raising and lowering operators used in the usual formalism of the quantum harmonic oscillator [61].

$$\hat{\varphi} = \frac{2\pi\hat{\Phi}}{\Phi_0} = \sqrt{\frac{\pi Z}{R_Q}}(\hat{a}+\hat{a}^\dagger) = \frac{1}{\sqrt{2}}\left\{\frac{8E_C}{E_L}\right\}^{1/4}(\hat{a}+\hat{a}^\dagger) \tag{1.27}$$

$$\hat{n} = \frac{\hat{Q}}{2e} = \sqrt{\frac{R_Q}{4\pi Z}}i(\hat{a}^\dagger-\hat{a}) = \frac{i}{\sqrt{2}}\left\{\frac{E_L}{8E_C}\right\}^{1/4}(\hat{a}^\dagger-\hat{a})\ . \tag{1.28}$$

Where the new constants of resistance quantum (R_Q) and impedance (Z) are defined as:

$$R_Q = \frac{h}{(2e)^2} = 6.45\ \text{k}\Omega, \quad Z = \sqrt{\frac{L}{C}}\ . \tag{1.29}$$

The dimensionless operators $\hat{n}$ and $\hat{\varphi}$ now obey the canonical dimensionless commutation relation $[\hat{\varphi},\hat{n}] = i$ and the dimensionless Heisenberg's uncertainty relation: $\delta\varphi\delta n \geq 1/2.$.

The coefficients in front of $\hat{\varphi}$ and $\hat{n}$ define the zero-point quantum fluctuations (zpf) of the respective operator and is a consequence of Heisenberg's uncertainty relation. The zpf of flux is smaller than the zpf of charge in circuits with impedance lower than R_Q while the converse is true when $Z > R_Q$. Using this idea, the oscillator is considered low-impedance when $Z < R_Q$ and high-impedance when $Z > R_Q$.

We can now take a look at the quantum LC oscillator Hamiltonian where the φ term is considered as the potential energy:

$$\mathscr{H} = 4E_C\hat{n}^2 + \frac{1}{2}E_L\hat{\varphi}^2 = \sqrt{8E_LE_C}\left(a^\dagger a + \frac{1}{2}\right) \tag{1.30}$$

The wavefunction for the groundstate in the φ basis is a Gaussian func-

tion where the width is determined by φ_{zpf}:

$$\psi_0(\varphi) = \frac{1}{(2\pi\varphi_{\text{zpf}}^2)^{1/4}} e^{-\varphi^2/4\varphi_{\text{zpf}}^2} . \tag{1.31}$$

Each subsequent wavefunction can be found analytically using Hermite polynomials (H_m) which are inserted into the function:

$$\psi_m(\varphi) = \frac{1}{(2\pi\varphi_{\text{zpf}}^2)^{1/4}} \frac{1}{\sqrt{2^m m!}} H_m(\varphi/\varphi_{\text{zpf}}) e^{-\varphi^2/4\varphi_{\text{zpf}}^2} . \tag{1.32}$$

These wavefunctions are known as the harmonic oscillator basis and are commonly used as a basis to diagonalize other Hamiltonians later introduced.

We see that by increasing the impedance but fixing our eigenenergy of the ground state, the wavefunction in the φ basis becomes more spread out, where the variance of the wavefunction extends beyond the value of a flux quantum. Irrespective of the resonance frequency, a high-impedance oscillator will have large flux fluctuations with respect to Φ_0 and small charge fluctuations with respect to 2e. The converse is true for a low-impedance oscillator, always satisfying the Heisenberg uncertainty relation. Therefore, the relative impedance of our LC oscillator compared to the resistance quantum decides whether charge or flux fluctuates by an amount more or less than their fundamental units.

1.4.2 What is high impedance?

An important value that is consistently discussed and is based on fundamental units only is the resistance quantum. Resistance quantum defines the boundary where charging effects become observable in SCQC.

Charging effects essentially become destroyed in a low-impedance regime due to quantum fluctuations of charge exceeding the value of a single Cooper-pair (charge number n exceeding 1). Low-impedance circuits are more prevalent naturally and are a consequence of the fine structure constant ($\alpha = \frac{1}{137}$) [37]. While reaching the high-impedance regime requires a large inductance with a low-valued self-capacitance. The idea is simplified by re-

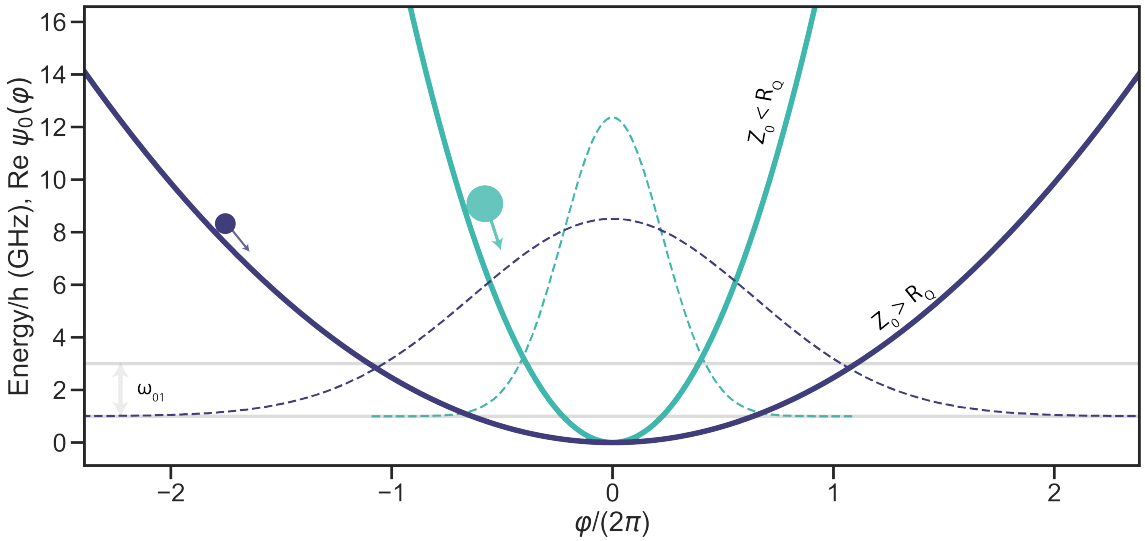

Figure 1.6: The LC oscillator's zpf depends on the ratio between Z_0 and R_Q. When $Z_0 < R_Q$ the variance of the groundstate wavefunction is within a single flux quantum. Keeping the transition frequency fixed, when $Z_0 > R_Q$ the variance now exceeds a single flux quantum. The fictitious particle represents the capacitance as mass and the softness of the harmonic well represents the inductance.

alizing capacitance always accompanies any metallic leads which are necessary for measuring any superconducting circuit, this capacitance is referred to as a "stray" capacitance and is more or less always present.

The value for the boundary between low and high impedance being set at a resistance quantum arises when one does a basic calculation considering the Heisenberg uncertainty relation between energy and time represented by the simple inequality: $\Delta t \Delta E \geq \frac{\hbar}{2}$. The idea is, if we want to observe the charging effects of a capacitor then the charge dynamics we are interested in measuring must occur in less than the charge-decay time ($\tau = RC$) [175]. To arrive at the desired expression we plug in the charging energy of a capacitor ($E_C = (2e)^2/2C$) and replace the uncertainty in time with the time constant for a discharging capacitor τ:

$$\Delta t \Delta E = RC \cdot \frac{4e^2}{2C} \geq \frac{\hbar}{2} \Rightarrow R \geq \frac{\hbar}{4e^2} \,. \tag{1.33}$$

This expression is valid for DC signals, however, we want to observe the charging effects of our circuits operating at several GHz; meaning the resis-

tance is replaced by an inductance that provides a purely reactive impedance. From basic electrical circuits, the ideal inductor provides a reactive impedance with magnitude $|Z| = \omega L$. Using this expression an estimate for the size of the inductance necessary to reach the charging regime in superconducting circuits is:

$$L \geq \frac{R_Q}{2\pi f} = \frac{6.45\ \text{k}\Omega}{2\pi \times 10\ \text{GHz}} \approx 100\ \text{nH}\ . \tag{1.34}$$

Indicating an inductance value on the order of one hundred nano-Henries is necessary to reach an impedance greater than R_Q at 10 GHz. This has been demonstrated already [117] by creating what is known as a superinductance. In this work, we define *ultra*-high impedance as $Z \gg R_Q$. On average we create $L > 1000$ nH which effectively creates an impedance $Z > 60$ kΩ.

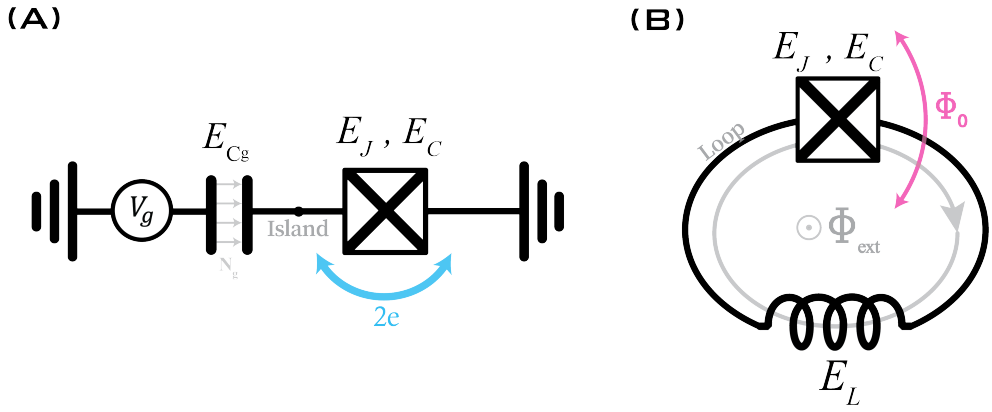

Figure 1.7: (A) The circuit diagram for a Cooper-pair box, which is an island separated from ground by a JJ. Cooper pair number $N = Q/2e$ is the natural basis. (B) The circuit diagram for a "Fluxon box" (or really any flux qubit) which is an inductive loop interrupted by a single JJ. The flux quanta number $m = \Phi/\Phi_0$ is the natural basis.

1.5 Superconducting circuits

A JJ's behavior depends strongly on the surrounding circuitry. The topology of the circuit, whether the two leads of the junction are detached or connected, decides whether degrees of freedom are quantized in discrete values or rendered continuous and well-defined [38].

A superconducting island is created when a superconducting lead is separated from a superconducting reservoir by a single JJ. The island can only

have charge in discrete integer values of 2e. The charge number on the island changes when Cooper-pairs tunnel across the JJ. This fundamental circuit is called the "Cooper Pair Box" [21] or CPB for short which was notably studied in depth at Saclay, Paris throughout the 1990s and early 2000s [15, 33].

The loop scenario has a discrete quantized flux of integer values inside the closed, connected JJ leads. Instead of a quantized Cooper-pair number, the quantum variable is the flux that tunnels in and out of the loop by phase slips across the JJ [124]. The device can be thought of as the dual to the CPB and can be called a "fluxon box" [14].

In both topologies, the quantized variable is stored either by the charge on the island or the flux in the loop. The JJ's role in both cases is the tunneling of the relevant degree of freedom into or out of the storage "box". These two topologies, islands and loops, are the starting points when considering the dynamics of the variety of superconducting circuits which exist.

In this section, the four distinct forms of superconducting circuits, each operating in a distinct regime of zero-point fluctuations within the two different circuit topologies, will be introduced [28, 29]. In essence, the JJ can be shunted by either a capacitor or inductor which is either low or high impedance at the circuit's operating frequency.

Three fundamental types of superconducting qubits are already well known [29], each reflecting a distinct behavior of quantum fluctuations in a Cooper pair condensate: single charge tunneling (charge qubit [133, 181]), single flux tunneling (flux qubit [27]), and phase oscillations (phase qubit [121]/transmon [92]). Yet, the dual nature of charge and flux suggests that circuit atoms come in pairs. In this thesis, we introduce the missing one, named "blochnium" which exploits a coherent insulating response of a single Josephson junction that emerges from the extension of phase fluctuations beyond the 2π-interval [6, 20, 157, 160].

1.5.1 Charge qubit: Cooper-Pair Box

The Cooper-pair box consists of a superconducting island connected to a superconducting reservoir by a single JJ. The superconducting island is capacitively biased by an external voltage source V_g enabling the tuning of

the dimensionless gate charge $n_g = \frac{C_g V_g}{2e}$.

The two energy scales which determine the energy eigenstates are the tunneling energy E_J and the charging energy E_C. The following Hamiltonian describes the CPB [33, 180]:

$$\mathscr{H}_{CPB} = \sum_{N\in\mathbb{Z}} \left\{ 4E_c(N-n_g)^2|N\rangle\langle N| - \frac{E_J}{2}\Big(|N\rangle\langle N+1| + |N+1\rangle\langle N|\Big)\right\} \tag{1.35}$$

where $|N\rangle$ is considered as the pure charge basis. Physically the operator $\hat{N}$ is the charge number operator ($\hat{N} = \frac{\hat{Q}}{2e}$) which returns the integer number of excess Cooper pairs on the superconducting island when acting on the pure charge eigenstate ($\hat{N}|N\rangle = N|N\rangle$ where the pure charge basis is a complete set such that $\sum_{-\infty}^{\infty}|N\rangle\langle N| = 1$.

This Hamiltonian is represented by a matrix where the charging energy terms are diagonal and the Josephson terms are off-diagonal. The Josephson junction can be thought of as breaking the charge degeneracy of the island and providing a link from the superconducting box to the superconducting reservoir. When diagonalized the resulting energy eigenstates are superpositions of pure, discrete charge states:

$$\mathscr{H}_{CPB}|k\rangle = E_k|k\rangle, \quad k \in \mathbb{N}\,. \tag{1.36}$$

The conjugate variable of the pure charge $\hat{N}$ is the phase $\hat{\varphi}$ which represents the phase difference between the two electrodes on either side of the tunnel barrier.

To write the CPB Hamiltonian solely in the phase basis the Josephson junction term must be transformed to $|\varphi\rangle$ from $|N\rangle$. The transformation between basis amounts to applying Fourier transformations [36, 38]:

$$|\varphi\rangle = \sum_{N=-\infty}^{\infty} e^{iN\varphi}|N\rangle \quad \text{and} \quad |N\rangle = \frac{1}{2\pi}\int_0^{2\pi} d\varphi e^{-iN\varphi}|\varphi\rangle\,. \tag{1.37}$$

To transform to $|N\rangle$ is a discrete transformation while to transform to $|\varphi\rangle$ is continuous. To go along with these definitions it is instructive to define

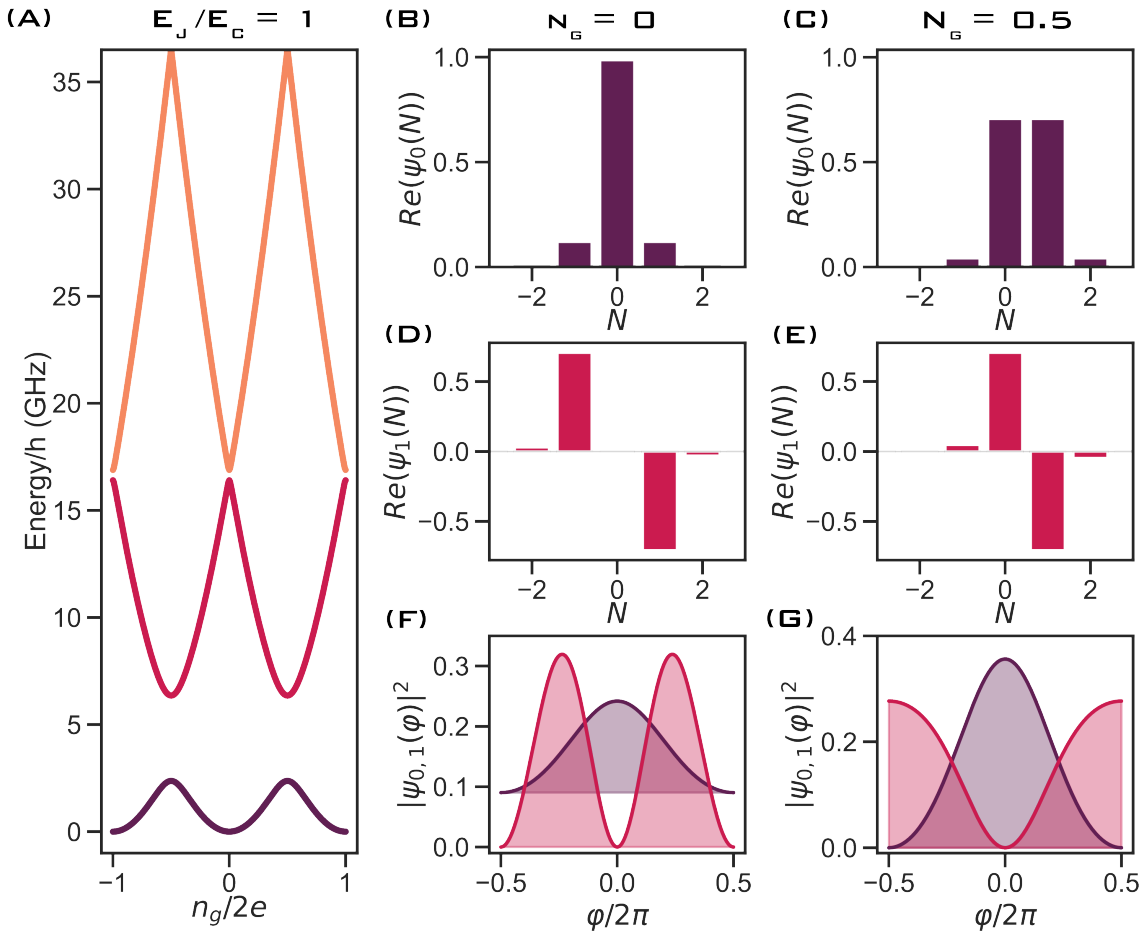

Figure 1.8: (A) The eigenspectrum of the CPB with $E_J/E_C = 1$. (B,D) The first two discrete wavefunctions in the charge number basis N when $n_g = 0$. (C,E) The first two discrete wavefunctions in the charge number basis N when $n_g = 0.5$. The wavefunctions are centered around the gate charge value. (F,G) The wavefunctions in the phase basis.

Kronecker and Dirac deltas:

$$\delta nm = \frac{1}{2\pi}\int_0^{2\pi} e^{-i(n-m)\varphi}d\varphi \quad \text{and} \quad \langle\varphi|\varphi'\rangle = 2\pi\delta(\varphi-\varphi') = \sum_n e^{-in(\varphi-\varphi')} \tag{1.38}$$

After realizing these relations among conjugate variables, a transform of the Josephson energy term from an expression dependent on N to just φ starts with defining a 'translation' operator: $e^{i\hat{\varphi}} = \frac{1}{2\pi}\int_0^{2\pi} e^{i\varphi'}|\varphi'\rangle\langle\varphi'|d\varphi'$ such that operating with $e^{i\varphi}$ on the pure charge state amounts to translating

N by 1:

$$e^{i\hat{\varphi}}|N\rangle = |N+1\rangle \ . \tag{1.39}$$

The rest is straightforward, representing the $\mathscr{H}_{JJ}$ terms via the translation operator and using the completeness relation:

$$\begin{aligned}\sum_{N=-\infty}^{\infty} -\frac{E_J}{2}\Big\{|N\rangle\langle N+1|+|N+1\rangle\langle N|\Big\} &= \sum_{N=-\infty}^{\infty} -\frac{E_J}{2}\Big\{e^{i\hat{\varphi}}|N\rangle\langle N|+e^{-i\hat{\varphi}}|N\rangle\langle N|\Big\} \\ &= -\frac{E_J}{2}(e^{i\hat{\varphi}}+e^{-i\hat{\varphi}}) = -E_J\cos(\hat{\varphi})\end{aligned} \tag{1.40}$$

The results solely expressed in the φ picture recover the standard JJ energy.

Finally, $-\frac{id}{d\varphi} = \hat{N}$, meaning the re-expression of the CPB Hamiltonian in the phase-only basis is completed and defined as:

$$\mathscr{H}_{\text{CPB}} = 4E_c\Big(-i\frac{d}{d\hat{\varphi}} - n_g\Big)^2 - E_J\cos(\hat{\varphi}) \ . \tag{1.41}$$

This equation is known as the Mathieu equation and has periodic solutions repeating every $\varphi/2\pi$ and can be represented as Bloch-wave solutions.

Both basis are completely equivalent except the pure charge basis is a bit more intuitive and easier to solve. Experience teaches us to diagonalize the CPB in the N basis and perform a Fourier transformation for the wavefunctions in the phase basis.

In figure 1.8, the charge wavefunctions are well-defined and centered around the offset charge value n_g. When the offset charge is zero, the groundstate is almost completely comprised of the N=0 state while the first excited state is the superposition of one charge on the island and one charge off the island. Therefore a transition from the ground to excited state corresponds to a charge hopping on or off the superconducting island which corresponds to a single Cooper-pair tunneling through the JJ. The actual physical process of exciting this qubit is associated with a single-charge tunneling event and is characteristic for charge qubits for when $E_J/E_C \sim 1$.

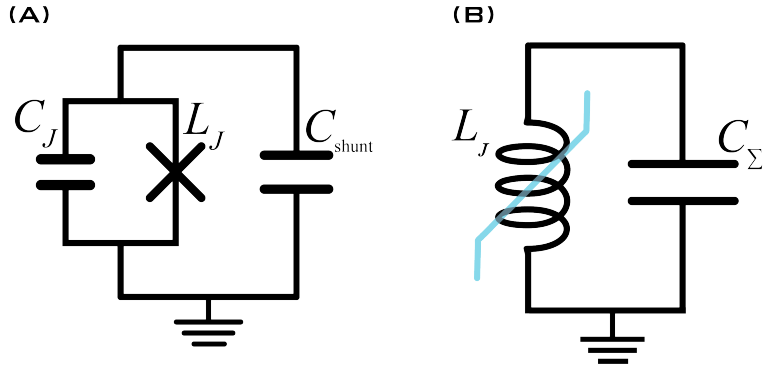

Figure 1.9: (A) The transmon qubit is a small junction with intrinstic capacitance C_J and Josephson inductance L_J shunted by a large exterior capacitance C_{shunt}. (B) The simplified circuit diagram represents the small junction as a non-linear inductance shunted by a single large valued capacitor C_Σ.

1.5.2 Plasma Oscillations: Transmon

The transmon is a charge qubit in virtue yet with different energy scales compared to the CPB. Transmon adds a large shunting capacitance (C_{shunt}) such that the total capacitance is much larger than the intrinsic junction capacitance C_J and is usually denoted as a single capacitor value, C_Σ.

The transmon parameter regime is rigorously defined as when the difference between $\alpha = \omega_{01} - \omega_{12}$ *trans*itions to negative values; where α is the anharmonicity. This is how the *trans*mon gets the name and occurs when the ratio of $E_J/E_C > 20$ [92].

The transmon Hamiltonian is that of a charge qubit:

$$\mathscr{H}_{tm} = 4E_c(\hat{N} - n_g)^2 - E_J \cos(\hat{\varphi}) \tag{1.42}$$

however, when $E_J \gg E_C$, the lower eigenstates have virtually no charge dispersion and are well below the Josephson cosine potential amplitude such that a Taylor series expansion of the Josephson potential is used to obtain the effective Hamiltonian:

$$\mathscr{H}_{tm_{eff}} = 4E_c\hat{n}^2 + \frac{1}{2}E_J\hat{\varphi}^2 - \frac{1}{4!}E_J\hat{\varphi}^4 - O(\hat{\varphi}^6) \tag{1.43}$$

The legitimacy of the Taylor expansion is seen by the wavefunctions localized in a single JJ well potential in the phase picture; meaning the phase

difference is defined between $-\pi < \varphi < \pi$. The quadratic term is perturbative and accounts for the weak non-linearity of the JJ which distinguishes this circuit from a HO and makes the transition energies unique and individually addressable. The operators in the effective picture are in the

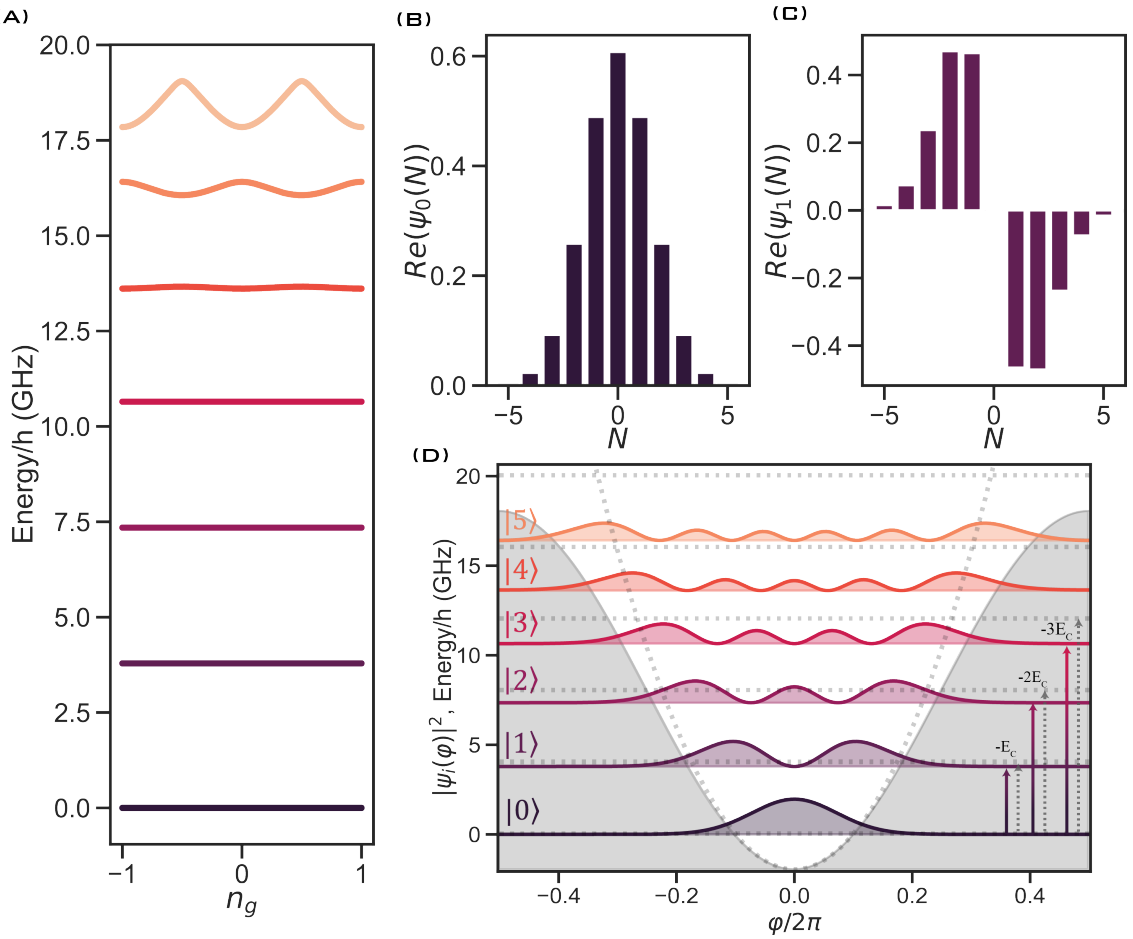

Figure 1.10: (A) The energy eigenstates of the transmon when $E_J/E_C = 50$. (B,C) The wavefunctions in the pure charge basis for the first two energy states. (D) The phase basis wavefunctions localized to a Josephson potential. The dashed lines are the HO potential and the HO energy levels. The transmon transitions from the ground state differ from the HO's by $-kE_C$ where k is the eigenstate index (shown is k=1,2,3).

LC oscillator basis introduced prior except E_L is replaced by E_J. Explicitly defining the operators for transmon as: $\hat{\varphi} = \frac{1}{\sqrt{2}}\left(\frac{8E_C}{E_J}\right)^{1/4}(a + a^\dagger)$ and $\hat{n} = \frac{i}{\sqrt{2}}\left(\frac{E_J}{8E_C}\right)^{1/4}(a^\dagger - a)$ and inserting the operators directly into the effec-

tive model the Hamiltonian which is now defined as:

$$\mathscr{H}_{tm_{eff}} = \sqrt{8E_J E_C}(a^\dagger a) - \frac{E_c}{12}(a + a^\dagger)^4 \ . \tag{1.44}$$

The first term is none other than the plasma frequency associated with small oscillations within a Josephson well as previously seen in the classical JJ model. The quartic term represents the non-linearity of the JJ now represented as a weakly non-linear inductance.

Once expanding the nonlinear fourth power terms the perturbative correction to the eigenenergies becomes:

$$\mathscr{H}_{tm_{eff}} = \left(\sqrt{8E_J E_C} - E_C\right) a^\dagger a - \frac{E_c}{2} a^\dagger a^\dagger a a \ . \tag{1.45}$$

Simulating the spectrum demonstrates the difference between the transition out of the ground state to level n from the plasma frequency is $-nE_C$; where the charging energy is normally on the order of one hundred MHz.

The transmon wavefunctions are now a large superposition of charge states while the phase difference between the two leads is well-defined. Transition energies of the qubit are approximately the plasma frequency and correspond to plasma oscillations of the phase difference.

1.5.3 Flux qubit: Fluxonium

The superconducting flux qubit has the topology of a loop where a JJ is shunted by a capacitance and a linear inductor. When the impedance of the inductance approaches R_Q for frequencies comparable to the transition energy, a fluxonium is formed. The large valued shunting inductance is coined a "superinductance" [117].

The fluxonium can also be thought about as an LC-oscillator shunted by a small JJ. This idea is convenient because fluxonium's operators are traditionally written in an LC-oscillator basis. The fluxonium's loop is threaded by the external flux that tunes the transition frequencies. The parameter regimes for fluxonium qubits are very large with each different combination of the three energy scales resulting in different/unique spectra. The most studied parameter regime appears to be $E_J/E_C > 1, E_L/E_C \sim 1$. By circuit

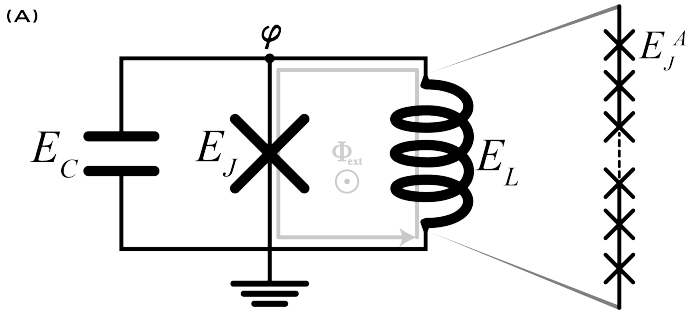

Figure 1.11: The three circuit elements in parallel are well described by one degree of freedom, φ. The loop, formed by the inductance and JJ, is threaded by external flux to tune the transition frequencies. The energy scales E_J, E_C, E_L are changed to access different parameter regimes. The inductive shunt is comprised of large area JJ in series where $E_J^A \gg E_J$.

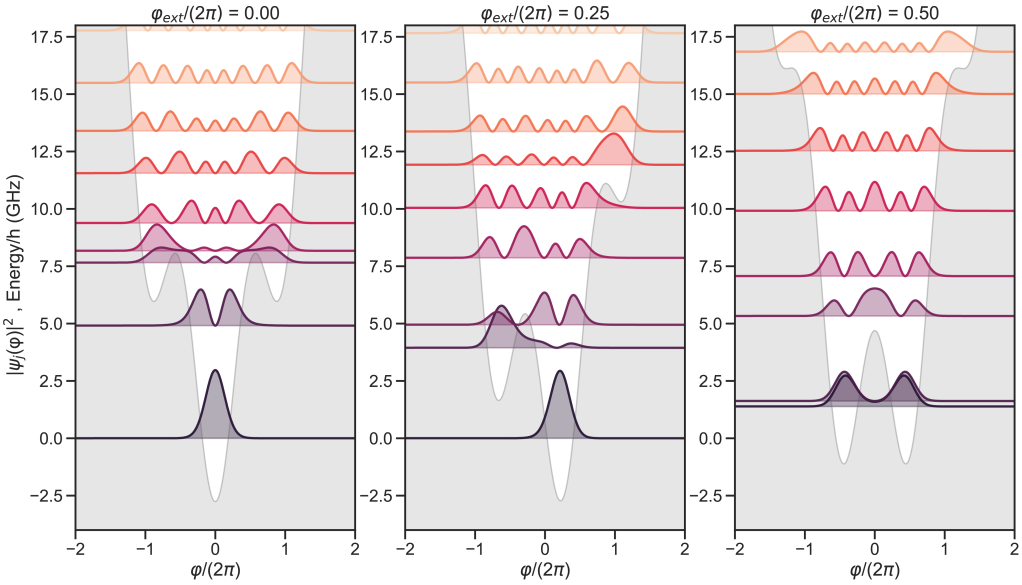

Figure 1.12: The wavefunctions of a fluxonium qubit with $E_J = 4$ GHz, $E_C = 1$ GHz, and $E_L = 0.5$ GHz. Each wavefunction is offset by the corresponding energy eigenvalue and is superimposed with the potential at the corresponding external flux bias.

quantization, the Hamiltonian can be written with one degree of freedom, φ, the phase difference across the small JJ:

$$\mathscr{H}_F = 4E_C\hat{n}^2 - E_J\cos(\hat{\varphi} - \varphi_{\text{ext}}) + \frac{1}{2}E_L\hat{\varphi}^2 \ . \tag{1.46}$$

The charging energy is normally a summation of the entire circuit's capacitance seen by the small JJ and not solely attributed to the small JJ's self-capacitance. This charging energy term can be thought of as analogous to the kinetic energy of a fictitious particle where the mass of the particle is the capacitance. Whereas the potential energy is the sum of the Josephson cosine term and the inductive harmonic well.

The fluxonium qubit will be studied in depth along the course of this thesis in a lesser explored energy scale regime where $E_J/E_C \sim 1, E_L/E_C < 1$. In this regime, the lower energy dynamics can be described by a phase slip Hamiltonian:

$$\mathscr{H}_s = \sum_{m=-\infty}^{\infty} \left\{ 2\pi^2 E_L (m - \varphi_{\text{ext}}/2\pi)^2 |m\rangle\langle m| - \frac{\varepsilon_s}{2}\{|m\rangle\langle m+1| + |m+1\rangle\langle m|\} \right\} \tag{1.47}$$

where flux tunnels in and out of the loop at a frequency given by ε_s. The variable m is now the Josephson well index where a state is localized in the mth well and a transition corresponds to changing wells thus adding a 2π-phase factor to the phase difference across the small JJ.

When the fluxonium is biased at half of a flux quanta, the dynamics of the qubit can always be explained in this form. The two lowest eigenstates are nearly degenerate in energy, where the splitting is the single phase-slip frequency. In fact, the fluxonium's lowest eigenstates are symmetric and anti-symmetric superpositions of the wavefunction being located in the left or the right Josephson well, and the phase-slip energy ε_s is the tunneling rate between the two wells. Fluxonium is most commonly biased at this flux point; making the fluxonium's lowest transition associated with a single flux tunneling event.

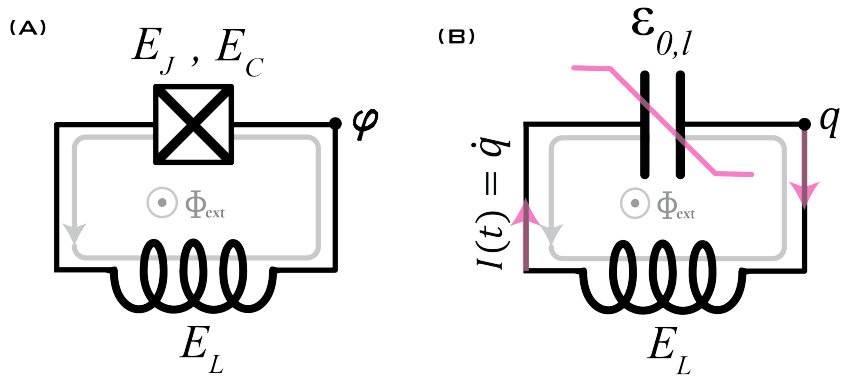

Figure 1.13: (A) The standard fluxonium qubit circuit diagram with the degree of freedom φ. (B) The blochnium circuit diagram consists of a non-linear capacitance shunted by a large inductance. The degree of freedom, in this case, is the quasicharge, q [141].

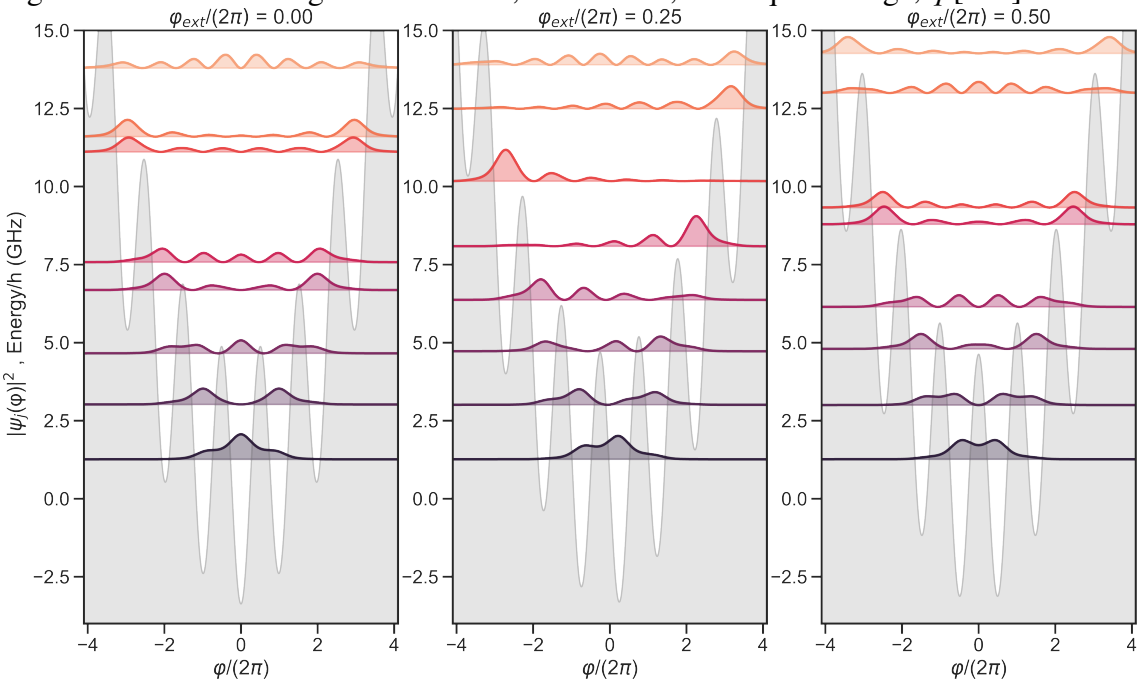

Figure 1.14: Fluxonium wavefunctions in the phase representation for the blochnium qubit regime at three different external flux bias values. The groundstate wavefunctions are delocalized into multiple wells at all flux points.

1.5.4 Quasicharge Oscillations: Blochnium

The blochnium is the main result of this thesis and is the fourth type of qubit which consists of shunting a JJ with the largest shunting impedance possible such that the charge is localized to less than 2e.

Blochnium has the same topology as a fluxonium, however, the lower-level transitions lose external flux sensitivity due to the delocalized wavefunctions in the phase basis. This qubit can be thought of as dual to transmon where the lowest eigenfunctions are comprised of a large superposition of charge states but in blochnium's case, the lower transitions exist in multiple Josephson wells simultaneously.

The delocalization of the eigenfunctions enables a new Hamiltonian emerging which describes the dynamics of the system as:

$$\mathscr{H}_B = \sum_{m\in\mathbb{Z}} \left\{ 2\pi^2 E_L \left(m - \frac{\varphi_{ext}}{2\pi} \right)^2 |m\rangle\langle m| + \sum_{\ell=0}^{\infty} \frac{\varepsilon_{0,\ell}}{2} \left\{ |m\rangle\langle m+\ell| + |m+\ell\rangle\langle m| \right\} \right\}. \tag{1.48}$$

This Hamiltonian enables states which are superpositions of discrete flux quanta in the loop to transitions to other states comprised of large superpositions of discrete flux quanta.

The conjugate variable in this case is no longer charge but is instead a continuous form of charge called quasicharge (q). The potential becomes the quasicharge energy dispersion of the small JJ and the kinetic energy is proportional to E_L. With correctly selected energy scales the first few transitions become localized in a single potential well where quasicharge is the well-defined variable existing between $-0.5 < q/2e < 0.5$. Bound to a single harmonic-like potential well the transitions are thought of as quasicharge oscillations which develop the idea of a JJ acting like a nonlinear capacitor.

1.5.5 Periodic table of artificial atoms

The naturally occurring atoms are categorized and sorted based on several defining features such as electron affinity and atomic radius. The main sorting category highlighted so far in this thesis for superconducting circuits is the topology and degree of quantum zero-point fluctuations of either

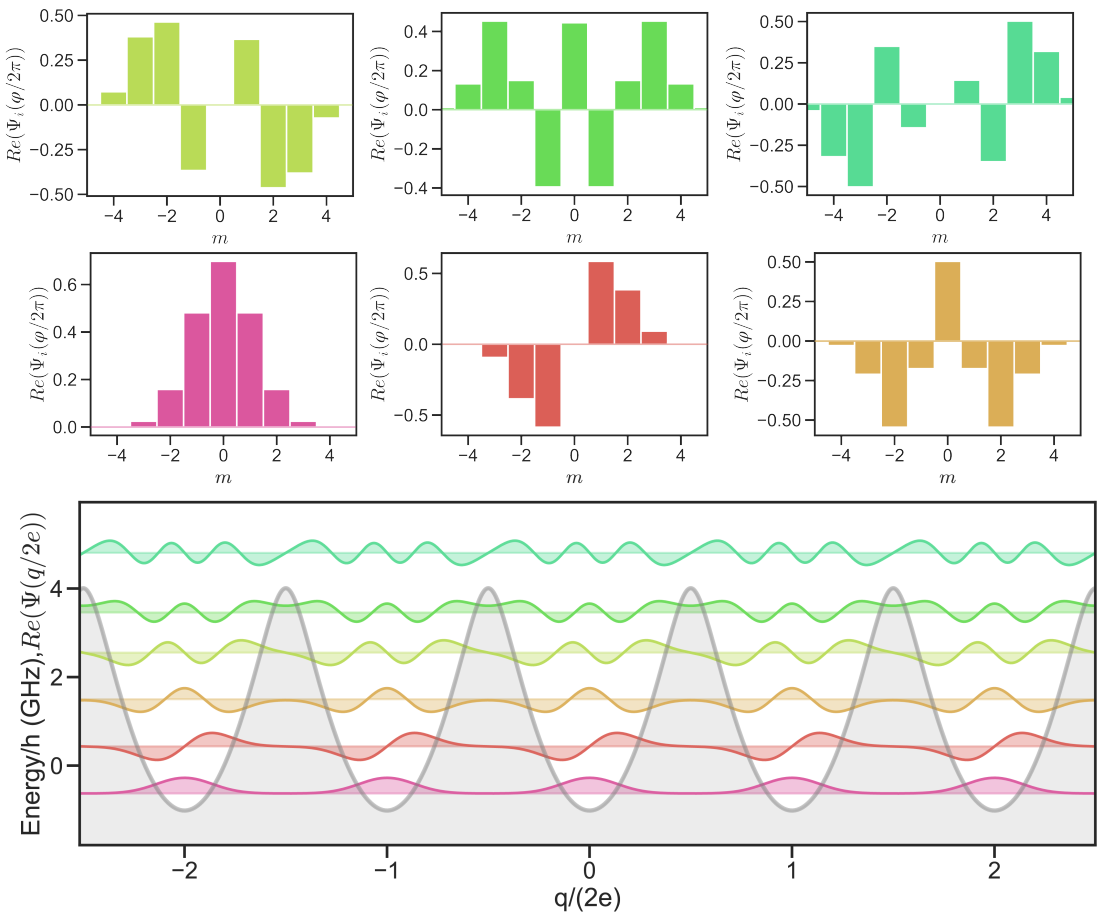

Figure 1.15: The quasicharge description of a circuit with the circuit parameters: $E_J = 4$ GHz, $E_C = 7$ GHz, and $E_L = 0.02$ GHz at Φ_{ext}/Φ_0=0. (A-F) The discrete flux-number wavefunctions show the superposition of flux quanta in the loop at once for the first six eigenstates. (H) The wavefunctions in the quasicharge "extended-zone" space ($q \in \pm\infty$) and are periodic every $q = 2ek$. The first few eigenvalues are situated within the first bloch-band and the transitions can be thought of as quasicharge oscillations.

phase across the JJ or charge on an island. Another way to sort Josephson-

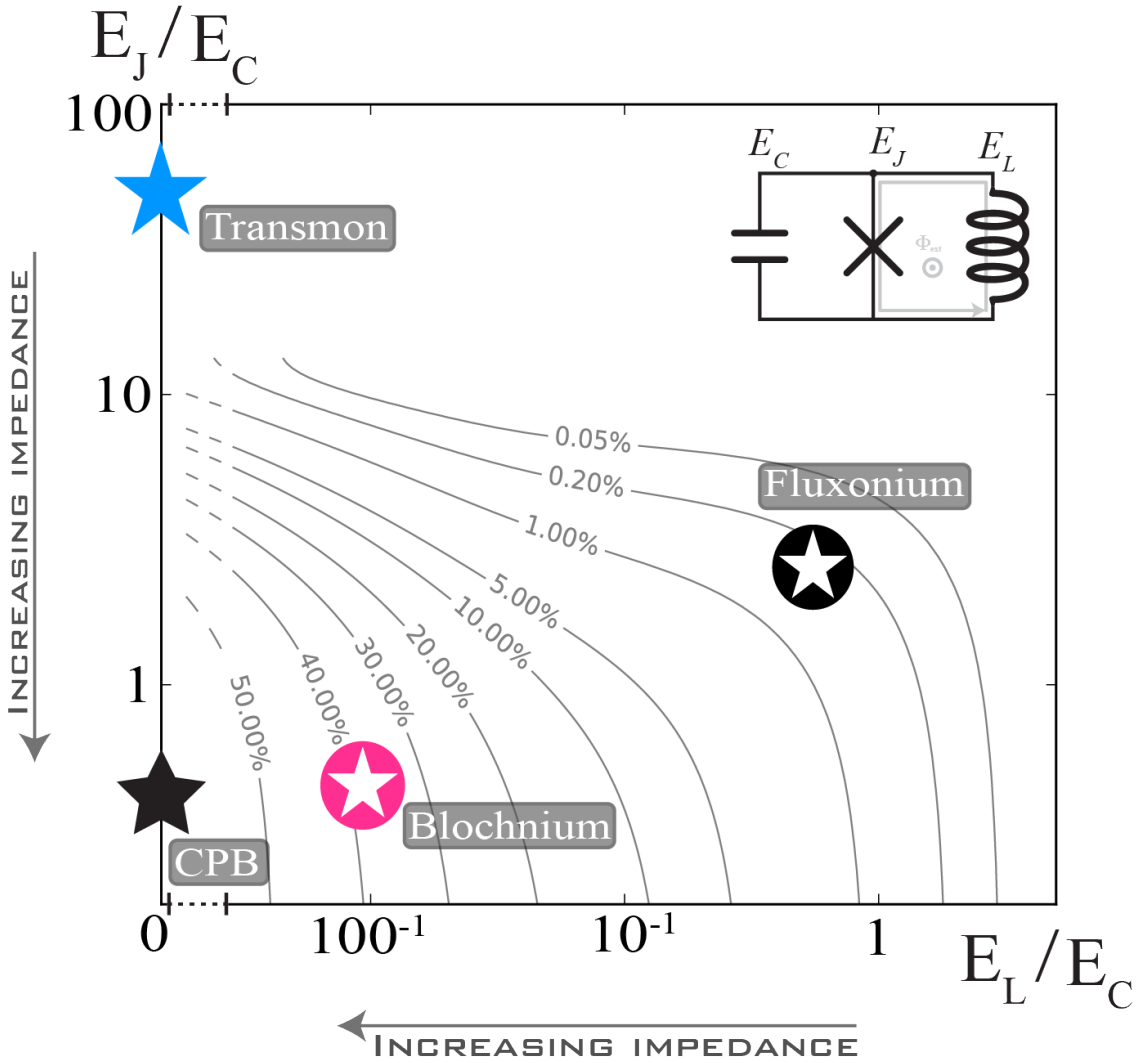

Figure 1.16: The four fundamental qubit types are sorted by the ratio of their energy scale parameters. The background outlines the probability to find the groundstate wavefunction outside a single Josephson well.

based artificial atoms is by the ratio of the respective energy scales; in particular E_J/E_C and E_L/E_C. The ratio of Josephson energy to the charging energy indicates the degree of phase localization of the wavefunctions within a single Josephson well; when $E_J \gg E_C$ the fictitious particle becomes localized in a single well. While the ratio of the inductive energy to the charging energy indicates the availability of the wavefunctions to spread out into

multiple Josephson wells at a single time; when $E_C \gg E_L$ the probability of finding the fictitious particle in multiple wells increases.

The four fundamental qubit types are shown in figure 1.16 sorted by their energy scale ratios. The two charge qubits have no inductive term E_L and are located on the detached y-axis, yet the ratio E_J/E_C still separates them where the CPB has localized charge and the transmon has a localized phase. In figure 1.17 the discrete wavefunctions of the charge qubits are shown in (A,C). The CPB has a localized wavefunction around the external charge bias of $n_g = 0$ and $E_J/E_C = 1$ for the simulation. The well-defined charge on the island means the transition frequencies are sensitive to the external gate charge and are shown in figure 1.18 (A). The transmon on the other hand has a wavefunction comprised of a superposition of many charge states where the simulated value is $E_J/E_C = 40$. The large superposition of charge states creates eigenenergies that are *insensitive* to the external gate charge.

In figure 1.17 the wavefunctions of the flux-like qubits are shown in (B,D) where each simulation had an external flux bias at half a flux quantum. The fluxonium has a wavefunction split into the two adjacent Josephson wells and is a superposition of the fictitious particle being either in the left or right wells. This simulation was done for $E_J/E_C = 4$ and $E_L/E_C = 0.5$. The spectrum of fluxonium with these energy combinations is shown in figure 1.18 (B); where the transition energies are clearly modulated by the external flux bias. The blochnium on the other hand has wavefunctions delocalized into many Josephson wells at once where the simulated value is $E_J/E_C = 0.5$ and $E_L/E_C = 0.005$. The probability to find the fictitious particle outside of the interval $-\pi < \varphi < \pi$ is larger than 40% at all external flux bias points. This large phase delocalization creates eigenenergies that are *insensitive* to the external flux bias.

The blochnium is situated by the CPB illustrating the delocalized (localized) phase (charge) due to the high impedance nature of the junction's environment, regardless of the topology. While the transmon and the fluxonium are lesser impedance versions creating a more localized phase.

There are other qubit varieties that have been created, however, these four sufficiently demonstrate the different zpf possible in a superconducting circuit which is due to shunting a JJ with a low or high-impedance capacitor

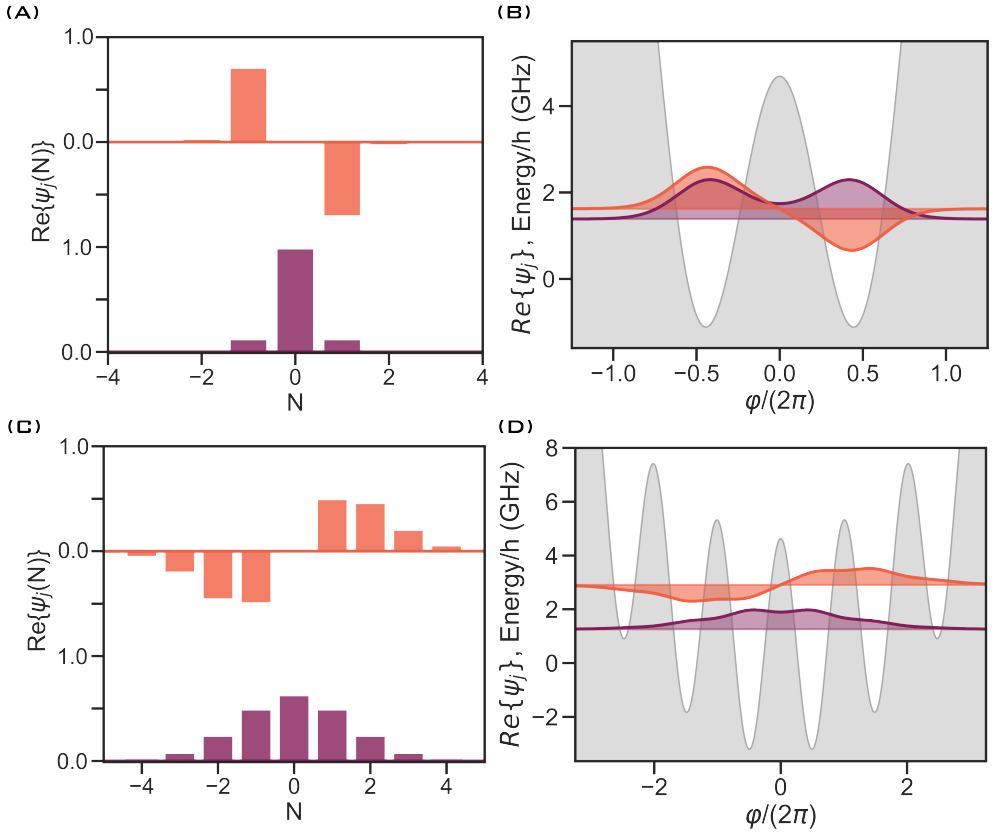

Figure 1.17: (A) The discrete CPB wavefunctions for $E_J/E_C = 1$ while biased at $n_g = 0$. (B) The fluxonium wavefunctions for $E_J/E_C = 4$ and $E_L/E_C = 0.5$ while at half of a flux quantum. (C) The discrete transmon wavefunctions for $E_J/E_C = 40$. (D) The fluxonium wavefunctions for $E_J/E_C = 0.5$ and $E_L/E_C = 0.005$.

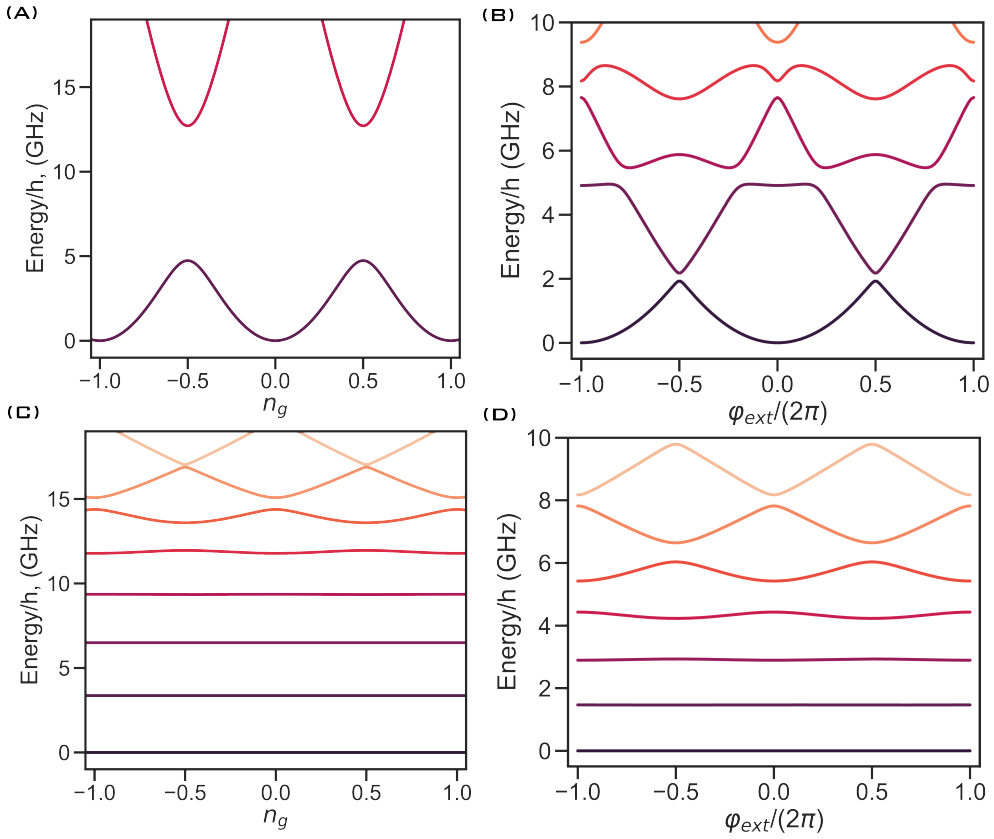

Figure 1.18: The CPB - (A) and the transmon - (C) eigenspectrums as a function of n_g. The fluxonium - (B) and the blochnium - (D) eigenspectrums as a function of $\varphi_{\text{ext}}/2\pi$. When the zpf of the variable (φ or n) associated with the respective external tuning parameter (φ_{ext} or n˙g) is made large, the eigenenergies become less sensitive to fluctuations in the external tuning parameter.

or inductor at the circuit operating frequency. This discussion demonstrates the unique ability to engineer a quantum mechanical system's behavior with superconducting circuits.

Furthermore, the ability to engineer zpf gives the option to create strong interactions with light. Normally, the light-matter interaction is weak due to the small value of the fine structure constant: $\alpha = Z_{\text{vac}}/8R_Q$ [37]; which in part is due to the small dipole moment of normal atoms. In SCQC, we can reach regimes where $\alpha \sim 1$, creating light-matter coupling strength comparable to the artificial atom's transition frequency.

1.6 Thesis overview

The results of this thesis are focused on increasing the impedance of superconducting circuits to values much greater than R_Q. We focus on maximizing the inductance density of a wire using ultra-packed JJ arrays while simultaneously minimizing the parasitic capacitance to the ground. We develop a dry etching technique compatible with high-quality factor resonators in chapter 4 and high-coherence qubits.

Parasitic chain modes in fluxonium qubits are created in shunting inductances which have a non-trivial capacitance to ground, as will be discussed in chapter 6, which will lay the framework and motivation for applying our dry etching technique to a variety of high impedance circuits which would otherwise be negatively affected by the parasitic modes ultra-strong coupling to the qubit mode. Utilizing this technique, JJ transmission lines with tens of thousands of JJs can have characteristic impedance $Z_\infty > 26\,\text{k}\Omega$ (chapter 4) and superconducting qubits with $Z > 160\,\text{k}\Omega$. Furthermore, we characterize our ultra-high impedance circuits before and after etching highlighting the circuit's Q and the qubit's coherence which both are not degraded by the dry etching techniques (chapter 7). Finally, we apply this technology to create the first-ever quasicharge qubit (chapter 8) and explore the applications of ultra-high impedance transmission lines to study Bloch oscillations in small JJ's (chapter 9).

This thesis's results shed light on a JJ's insulating character when embedded in ultra-high impedance circuitry. We find the experimental spec-

trum of blochnium agrees with a duality mapping onto transmon, which replaces the external flux by the offset charge and introduces a new collective quasicharge variable in place of the superconducting phase [93, 124]. Our results unlock the door to an unexplored regime of macroscopic quantum dynamics in ultrahigh-impedance circuits with direct applications in quantum computing and metrology.

Throughout the work done in this thesis, we will be discussing three distinguishable regimes of looped-based qubits. The distinguishing characteristic is the ratio of the zero-point fluctuations of the phase to zero-point fluctuations of the charge for the ground state wavefunction as can be seen in figure 1.19.

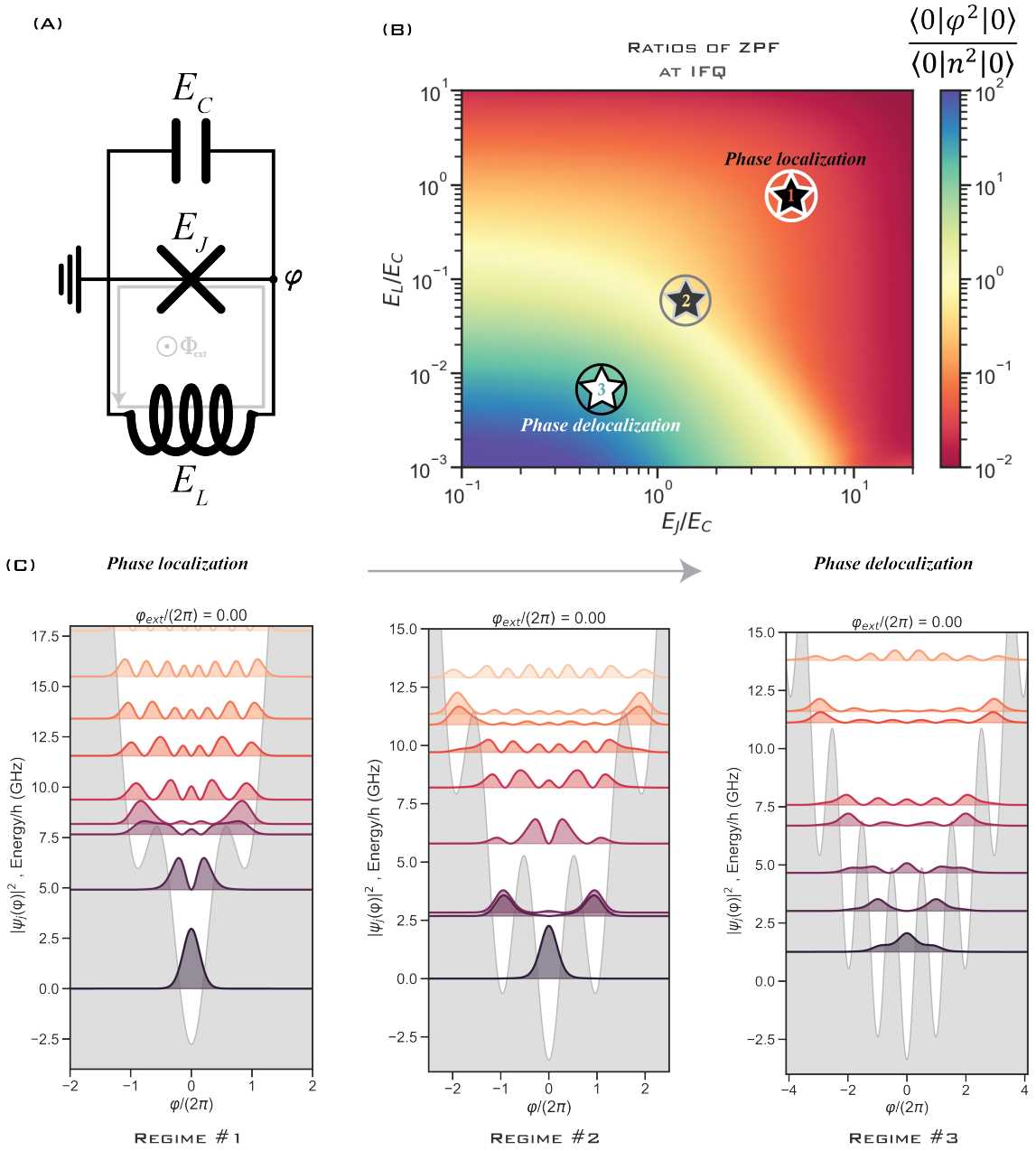

Figure 1.19: (A) The basic circuit studied throughout this thesis. (B) The three distinguishable energy scale combinations of loop-based circuits. The energy scale combinations are distinguished by the ZPF ratio of phase to charge for the groundstate wavefunction. (C) Wavefunctions at zero-external flux bias (IFQ) demonstrate the varying degree of phase delocalization by changing the energy scales of the basic circuit. The three energy scale combinations are discussed in chapter 5

.

2
Experimental techniques

"Tell me and I forget, teach me and I may remember, involve me and I learn."— Benjamin Franklin

In this chapter, the experimental techniques necessary to realize the results of this thesis are discussed. In the process, we will also introduce several physical ideas about certain constraints. We will begin by discussing the nano-fabrication techniques used to make Dolan bridge [45] based Josephson junctions. An outline of the procedure is highlighted with the demonstration of numerous devices in different forms, many devices not thoroughly discussed in this thesis are highlighted in literature in references: [34, 44, 102]. Next, an etching technique is introduced which is employed for Dolan bridge JJ devices which is necessary for the realization of ultra-high impedance superconducting circuits.

We will then discuss the various resonators or waveguides used to house and measure our superconducting circuits. Finally, an introduction to the basic cryogenic set-up as well as how to actually measure resonators using well-established microwave engineering techniques is discussed in detail.

The point of this chapter is to give a realistic view of the experimental procedures, materials, and various apparatuses. This way we can connect

the later experimental results to the various components of this chapter.

2.1 Overview of the necessities

To successfully engineer a superconducting circuit components of nano-fabrication, microwave engineering, and cryogenic technology are all combined to create a suitable device in an environment where quantum effects are measurable in the microwave frequency range.

Firstly, superconducting circuits are created by nano-fabrication which have dimensions ranging from $d \sim 100$ nm to $d \sim 10$ mm. These circuits are operated with microwave frequency electric signals whose wavelength $\lambda \sim 10$ cm for a signal at 10 GHz. Due to the fact $\lambda \ll d$ our circuits can mostly be treated using the lumped element approximation instead of a truly distributed circuit. For example, this means a wire of several tens of μm in length can be considered a single inductor. However, when the dimensions of the circuit become extended into the mm range the speed of light (v) in the system must also be considered. The general condition for treating a circuit with the lumped element approximate model circuit works for all circuits when :$f \ll \frac{v}{\lambda}$ [169].

Our end goal is to measure the quantum mechanical effects; specifically the interactions of microwave light and a superconducting circuit which is often called an "artificial atom" [120]. To prohibit thermal noise from washing out quantum dynamics, the ambient environment which houses the circuit must meet the criteria: $\hbar\omega >> k_B T$. In other words, the transition energy of the atom must be greater than the thermal energy. A 10 GHz signal is proportional to a temperature of ~ 500 mK; this requires the circuit to be cooled inside a He3-He4 dilution refrigerator where temperatures are capable of reaching ~ 10 mK.

Finally, to properly characterize and measure the time-domain dynamics of superconducting circuits we need ultra-fast pulses and data acquisition operating with nanosecond precision at microwave/radio frequency while all being simultaneously synchronized. These capabilities are possible using microwave electronics with the ability to process incoming data at 1 Gigasample/second; that is 1 billion points per second.

With these conditions satisfied the measurement of observing fragile states of quantum superpositions of light and matter in engineered superconducting circuits is possible. The remainder of this chapter discusses the various experimental techniques details necessary to accomplish this feat.

2.2 Nano-fabrication

The devices in this thesis are fabricated using already established nano-fabrication techniques [57]. This procedure is quite simple and is very reproducible on the condition that there exists consistency with e-beam lithography, and physical vapor deposition with oxidation while also exercising caution over human factors to minimize any errors or uncertainties induced by the creator.

Once creating a successful sample, the procedure should be kept as consistent as possible. Below is an outline of the basic procedure followed for producing JJ-based superconducting circuits.

2.2.1 Lithograghy

The first step is simply to dice the substrate to specified dimensions and clean the sample thoroughly using only acetone and isopropanol (IPA). The diced substrates are ultrasonically agitated with the quality insurance of tossing any samples which have too many specs of dust on top of the polished surface.

Once cleaving and cleaning the Si or sapphire wafer a bilayer of e-beam resist is spun on top. The first layer of resist is MMA EL-13 which is spun at 3500 rpm for 60 seconds. This first layer of resist is approximately 800 nm thick. The sample is then baked at 180 degrees Celsius for 60 seconds to harden. Next, a layer of PMMA-A3 is spun on top of the first baked layer at 1500 rpm for 60 seconds. This layer is $\sim$200 nm thick and completes the bilayer. The substrate spun with the bilayer of resist on top is then baked for 30 minutes at 180 degrees Celsius.

Understanding the differences in the resist composing the bilayer helps build intuition for the technician fabricating. The MMA EL-13 resist is a "softer" yet thicker layer compared to the PMMA layer. Softness refers

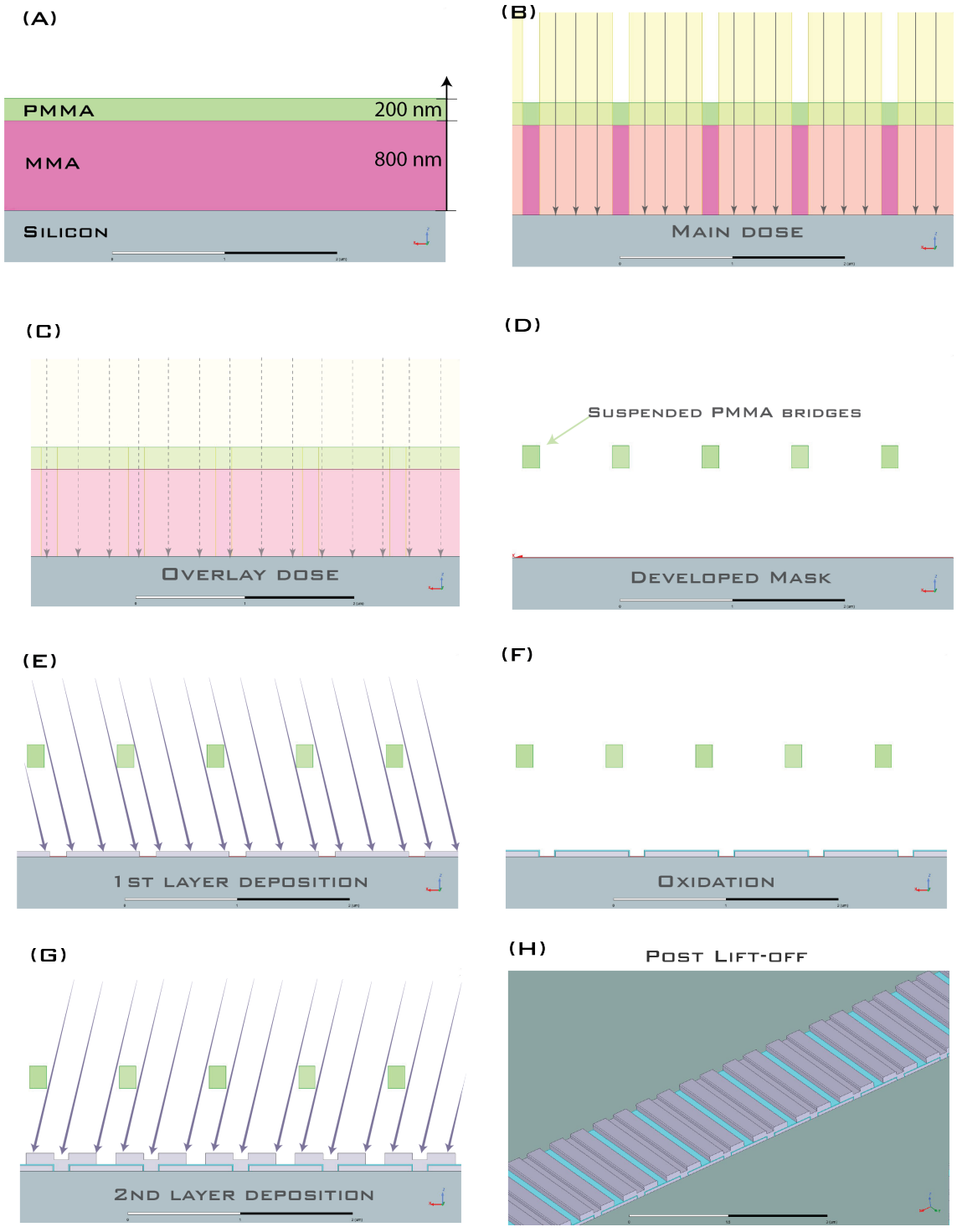

Figure 2.1: The various fabrication steps to create Dolan bridge JJs. The outline shows the cross-sectional view of a slice through the edge of the bridge mask.

to the required e-beam dose necessary to create a mask. As an analogy, the PMMA layer is the stencil for the pattern we want to make while the MMA layer suspends the stencil layer above the substrate sufficiently high such that layers of metal can be deposited at an angle onto the substrate. A key feature is the MMA around the exposed PMMA layer is broader in width and becomes rounded which will ultimately create a cavern of space necessary for a shifted circuit pattern.

Once the substrate is prepared with the bilayer it is time for e-beam lithography. The system used to create devices is an Elionix GLS-100 keV e-beam lithography system. The main pattern is normally written at 1 nA of e-beam current with varying doses dependent upon feature size. The e-beam writes a pattern by exposing small pixels of the entire design. A "dose" from the e-beam is created by a single pixel being exposed to the beam current for a certain length of time, the units are then Coulombs per area. The general findings through trial and error indicate a feature size less than 1 μm^2 requires a dose $> 2000\ \mu C/\mu m^2$ while large features usually require doses around $1000\ \mu C/\mu m^2$.

Due to the differences between the two resists and the fact we need to make room for the shifted pattern two doses are commonly used. The main dose is used to create the "stencil" in the PMMA layer which the metal pattern will take the shape of; while the second dose commonly referred to as the "overlay" is smaller, usually around 10 percent of the main dose. Too large of an overlay dose can deform the PMMA pattern; the overlay is more or less used to just clean up the MMA on the borders of the main patterns ultimately creating room for the shifted pattern.

Once the e-beam write is complete the mask is developed in an IPA/DI water 3:1 ratio mixture cooled to 6 degrees Celsius. The sample is submerged for 120 seconds while being slowly swayed side to side by the creator. In this step, the exposed areas of resist are removed. To stop development a filtered nitrogen gun is used to blow dry the developer off. After development, the sample can be gently washed in IPA to clean the residuals left over which are around or on your pattern but this can be skipped if it is already clean. The merit of success on this step is to have a uniformly spun device that, after development, has no fallen Dolan bridges and all leads are

connected as per the design.

The process of creating a mask is similar to that of traditional photography and printmaking. First, a picture is snapped with a specific exposure time depending on the intensity of ambient light. The film is then taken and developed in a solution for a fixed amount of time and is later used as the stencil for projecting the image of the final photo onto the canvas. In this analogy, we have already snapped the photo and developed our film. Now we must deposit the metal through the resist mask and onto our substrate to create the final "image".

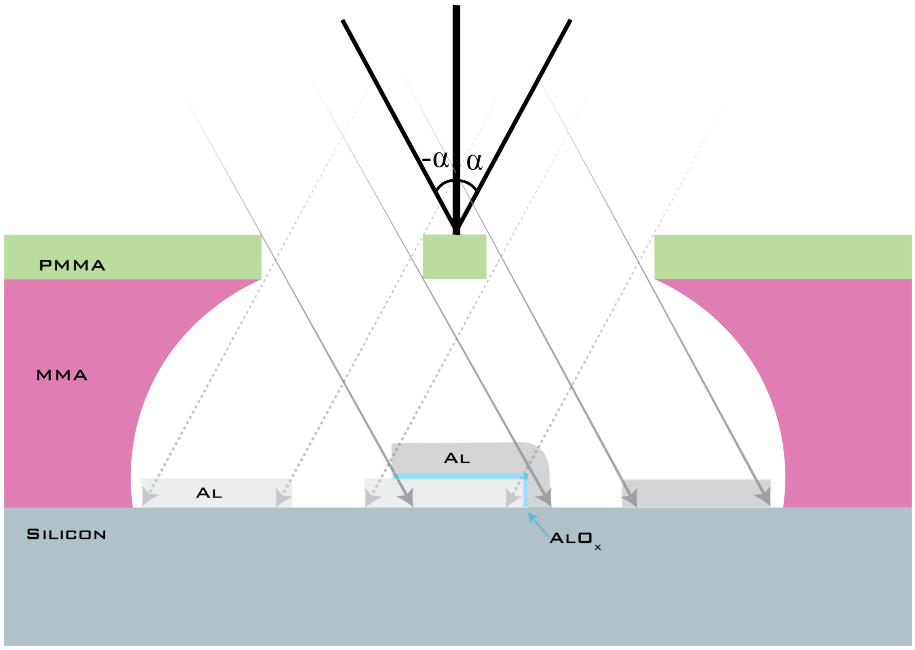

Figure 2.2: A cross-sectional view of the deposition of a single junction with the PMMA bridge forming the shadow required to make Dolan bridge JJs.

2.2.2 Deposition

The developed sample is now loaded into a Plassys e-beam evaporator for the actual deposition of aluminum; which is the most commonly used material in superconducting circuits. The device has a specific load orientation with respect to the axis of rotation of the sample mount that must be adhered to for the correct deposition angle and pattern shift. The loaded sample is usually pumped overnight; for $\sim$ 16 hours by a turbo pump which

gives the sample sufficient time to outgas and pump down to $\sim$ 1e-7 mBar. The long pump time is technically unnecessary but we have seen greater reproducibility of our sample's plasma frequencies once switching to the standard practice of pumping for longer than 12 hrs. After pumping, the sample is deposited following an automated recipe which is used for each device deposition.

A descum process is first performed where we expose the sample to a light plasma etching of an Argon oxygen mixture for $\sim$30 sec at each deposition angle. This step is used to clean up any residual organics on the substrate surface without damaging the device mask. The next step is a titanium pump where we now open the interlock between the loading chamber and the material chamber. In this step, we evaporate titanium which substantially lowers the pressure and acts as a pump to further reduce pressures to $\sim$3e-8 mBar. This step helps establish a constant chemistry composition of both chambers prior to evaporating the aluminum layers onto the substrate.

The sample holder is rotated to the first angle where 20 nm of 99.999 percent purified aluminum is deposited, rather quickly, at 1 nm/sec. The deposition angle (α) is determined from the trigonometric relation:

$$\alpha = \tan^{-1}\left\{\frac{\text{shift}}{\text{resist- thickness}}\right\} \quad [\pm\text{degrees}]. \tag{2.1}$$

The oxide barrier is created next in situ by using a static oxidation procedure of the freshly deposited aluminum film. The pressure is ramped to 100 mBar of an oxygen-argon mixture in about 20 minutes while the sample sits in the static gas-filled environment for 10 minutes. The oxidizing gas is pumped out and the next layer of aluminum, which is 40 nm thick, is deposited at the second angle; thus forming the junctions.

One last static oxidation is performed at 10 mB of pressure in the oxygen-argon mixture to ensure a clean oxygen capping layer. The sample is then brought to atmosphere, unloaded, and submerged into a bath of acetone at 60 degrees Celsius for around an hour so the resist is dissolved in the acetone. This process "lifts-off" the aluminum-coated resist while leaving behind the metal deposited through the mask onto the substrate. After an hour has passed a quick sonication for a few seconds is performed to clear

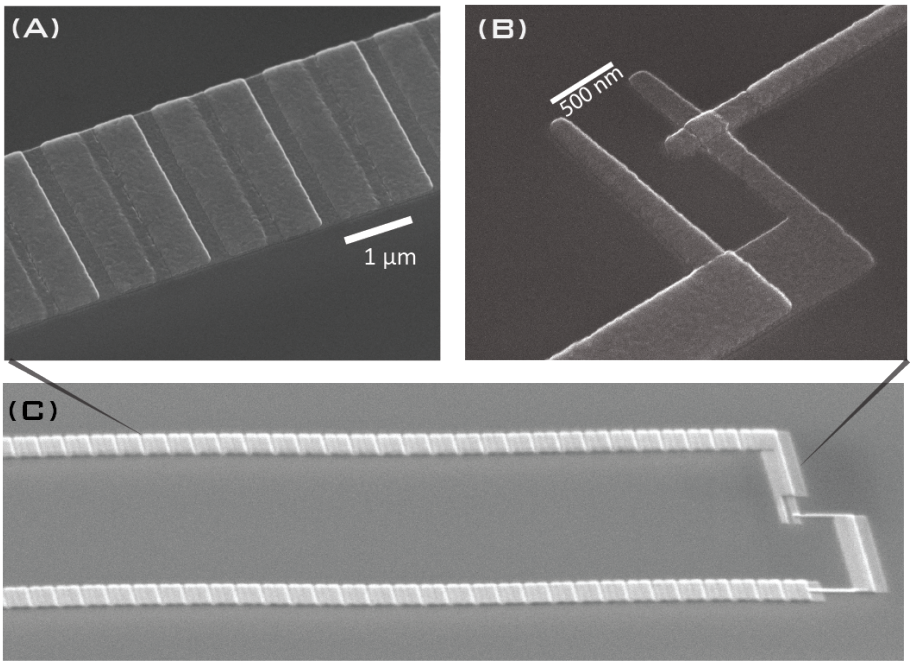

Figure 2.3: SEM images showing the final products created following the outlined procedure of: (A) a chain of JJ, (B) a weak/small JJ, (C) a larger snapshot of both.

the device. The sample is removed and dried with nitrogen gas.

Granted good lithography; the sample is now fresh and ready to measure. Usually, devices are not viewed using SEM imaging after conception. The SEM images of devices are often done after measurement since the SEM can modify the parameters of junctions.

2.3 Devices

The devices in this section are a mixture of circuits that have several hundreds of JJs to several tens of thousands of JJs. The Dolan bridge process is robust and can create devices spanning millimeters while having small feature sizes on the order of one hundred nanometers.

2.3.1 JJ transmission line devices

JJ chains comprised of $\sim$35,000 junctions in series were fabricated as shown in 2.4. The impedance of each device was tuned during the fabri-

cation process by the junction size. The wave dispersion and Q-factors of the standing modes are used to characterize the device and extract junction parameters in combination with SEMing the junction areas.

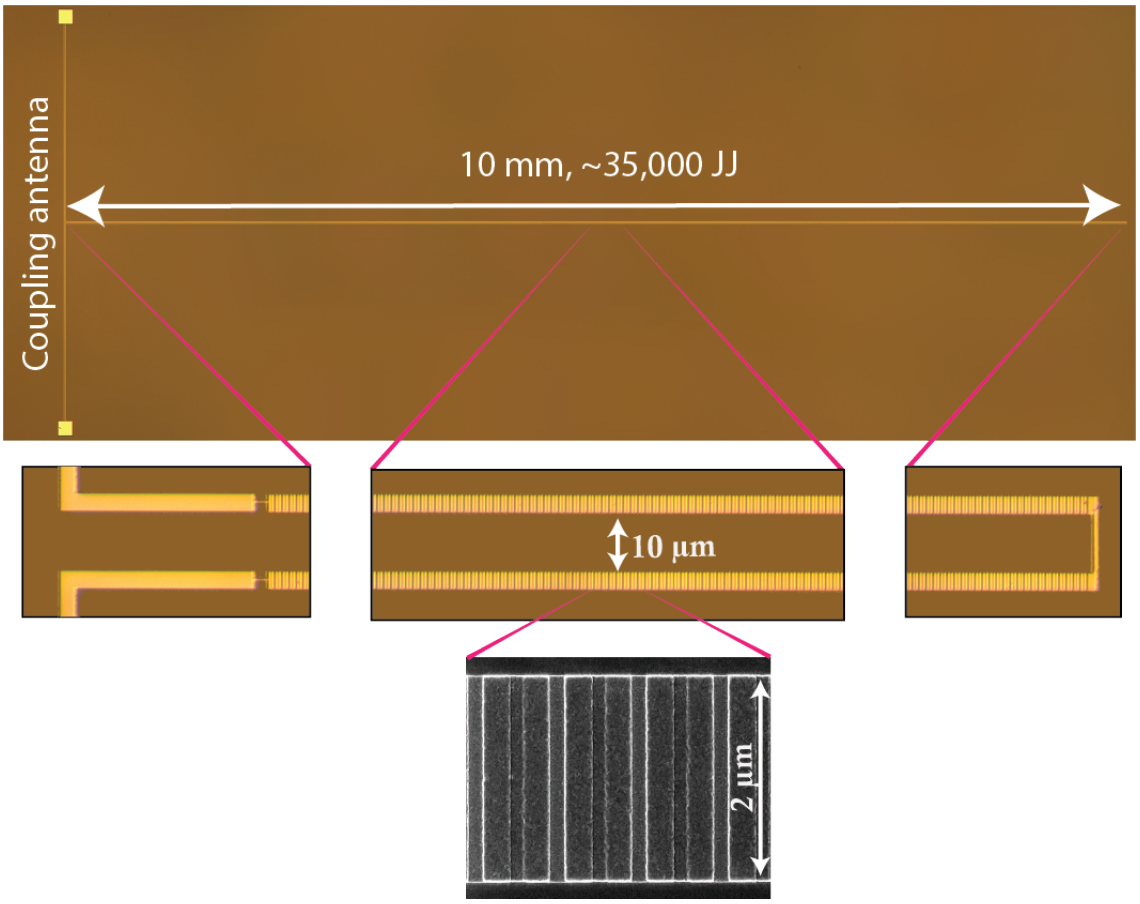

Figure 2.4: A JJ transmission line; 10 mm in length and comprised of $\approx$ 35,000 JJ in series. Each array is fabricated using the Dolan bridge technique. The junctions on a single device all have the same width and distance apart. These parameters are changed to tune the impedance of the line.

Changing the impedance of the JJ transmission line amounts to changing the width of the individual JJs. In our work [103], widths of the junctions ranged between $\sim$300 nm - 3 μm. Another way to tune the impedance of the device is to change the unit cell dimension of each JJ. The unit cell determines the density of JJs in an array. The usual density is 600 nm/junction which was pushed to 350 nm/junction for ultra-high impedance devices. Changing the density of junctions while fixing the length increases the total

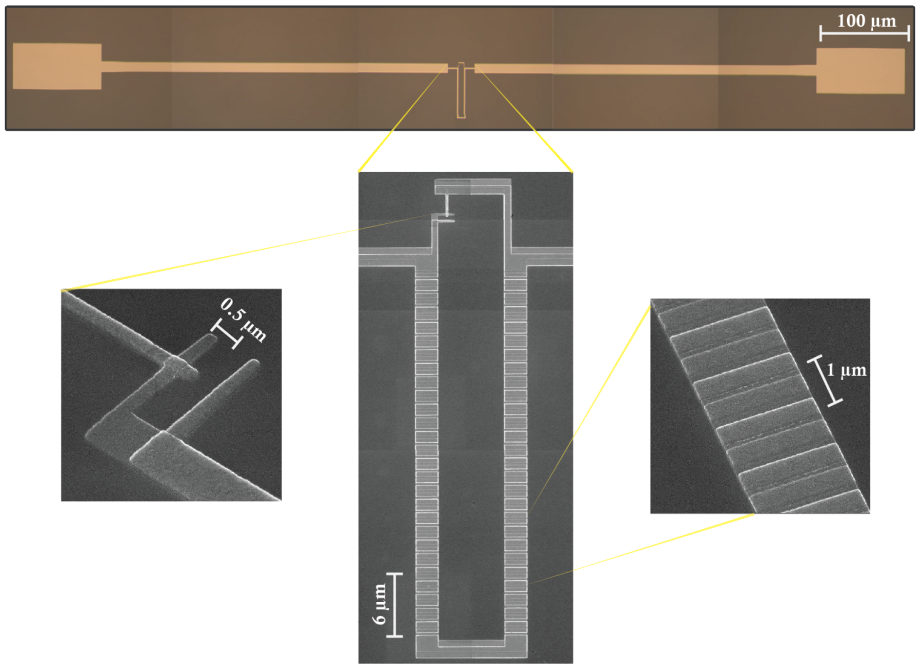

Figure 2.5: An optical microscope image of fluxonium devices fabricated extensively for [135]. An SEM image of the small junction and an SEM image of several JJs in series which are apart of the array.

inductance while decreasing the capacitance to ground per junction. Recently the impedance was also tuned by applying an external magnetic field [101].

2.3.2 Qubit devices

Fluxonium qubit devices fabricated in this work usually require an array ranging from $N \sim 80$ - $N \sim 500$ junctions in total. The challenging part of qubit fabrication is making a circuit with a small JJ with the correct target dimensions to achieve the energy scales as per the design. The small JJ in the fluxonium usually has an area of about 100 nm x 100 nm. This small feature size can be challenging.

2.3.3 Etched devices

A highly selective dry etching technique is used to remove the relatively high permittivity silicon substrate around the devices. By etching the silicon

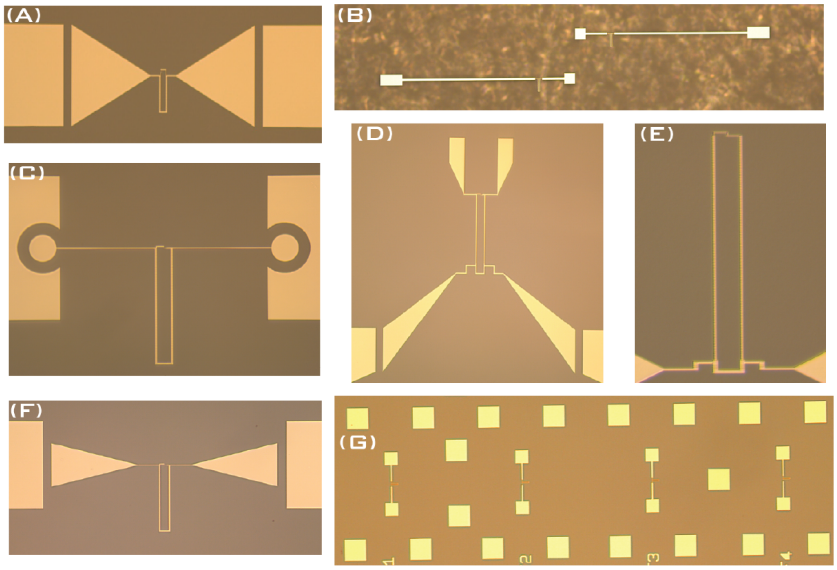

Figure 2.6: Different samples fabricated for: (A)[34], (B) [44], (C-G) for other on going experiments.

away from the aluminum circuit the stray electrostatic coupling between various leads becomes reduced. The devices in this thesis are etched in two different manners.

XeF_2 Etch: The first etch technique employed is an isotropic XeF_2 dry etch [190]; where fluorine atoms react with silicon (Si) when incident on the substrate. The isotropic nature of this etch attacks silicon non-directionally and underetches the mask. In this case, the device itself acts as a mask since aluminum (Al) and aluminum oxide ($AlO^{\cdot}x$) are non-effected by the XeF_2 dry etch [3]. The XeF_2 dry etchant is almost entirely selective of Si over Al (1000:1) [26] and has the chemical reaction:

$$2XeF_2 + Si \rightarrow 2Xe + SiF_4 \tag{2.2}$$

Prior to etching, no additional post-processing to the device was necessary once lifting off the resist since the Al device itself acts as the mask. Due to the XeF_2 etching isotropicity the etchant removes Si under our devices almost at the same rate as down into the substrate. This effect is what is refered to as an underetch. Our device's thin circuit components are completely detached and separated from the Si substrate while the large features

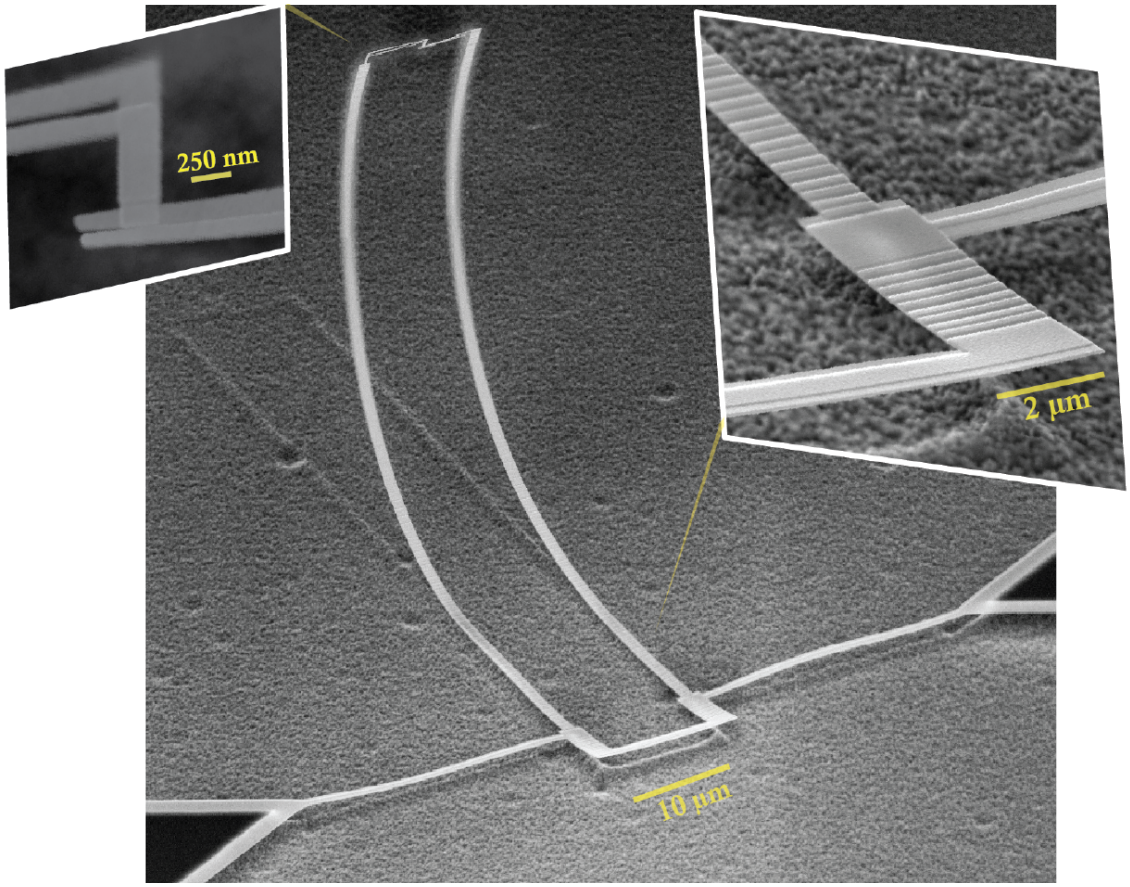

Figure 2.7: A fluxonium like qubit which has peeled off the Si substrate due to the under etching effect of the isotropic XeF_2. Note the faint outline of where the circuit used to be attached to the Si substrate. The small JJ is at the top of the standing circuit where the bottom of the loop is attached to capacitive leads.

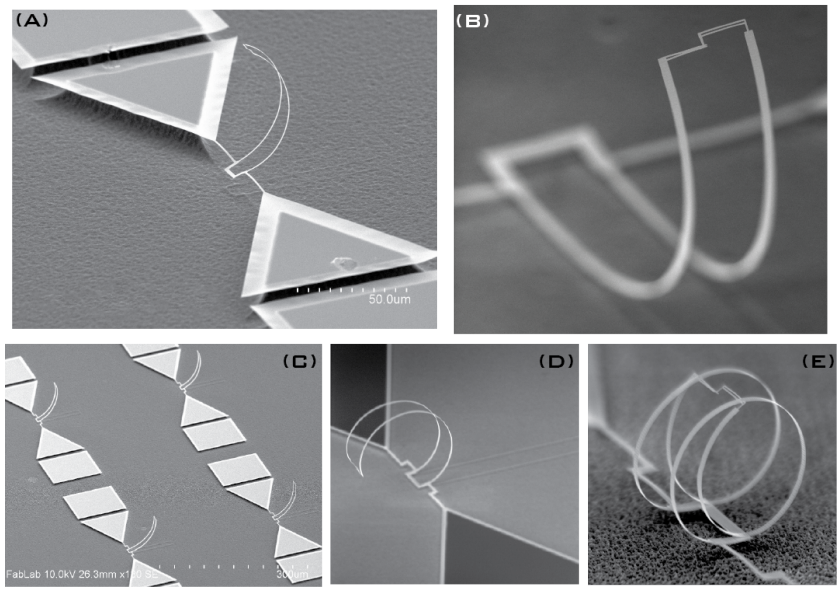

Figure 2.8: A variety of SEM images of different XeF_2 qubits. The qubits can stand up in vacuum vertically (A-D) to different degrees or even roll completely over (E) forming a spinodal like inductance. (C) Demonstrates the repeatability of the etch effect on devices on the same chip.

remain attached to the substrate effectively acting as anchor points securing the device. Due to the strain relaxation of the long thin JJ chains the circuit effectively peels off the substrate and stands almost vertically in vacuum. In fact, this is a common technique used to release micro-structures from substrates to create free-standing on-chip cantilevers [50, 108] and other on-chip mechanical resonating structures [138].

Using the XeF_2 etch technique, observations suggest deep etching is not necessary for samples to become detached from the substrate and surrounded primarily by vacuum. The amount of etching necessary to make a vertically standing chain is only a few micrometers thanks to the underetch and really only depends on the width of the JJ chains. However, we find etching extra deep ($d > 10\mu m$) does not degrade the structure's integrity as long as it still has sufficient anchoring to a larger, attached, object.

To much surprise, this etching technique is robust, fast, and with careful handling, the samples usually last over multiple cooldowns.

SF_6 Etch: In order to etch only *around* our sample, not underneath, an anisotropic etch with a resist mask that covers parts we do not want etched

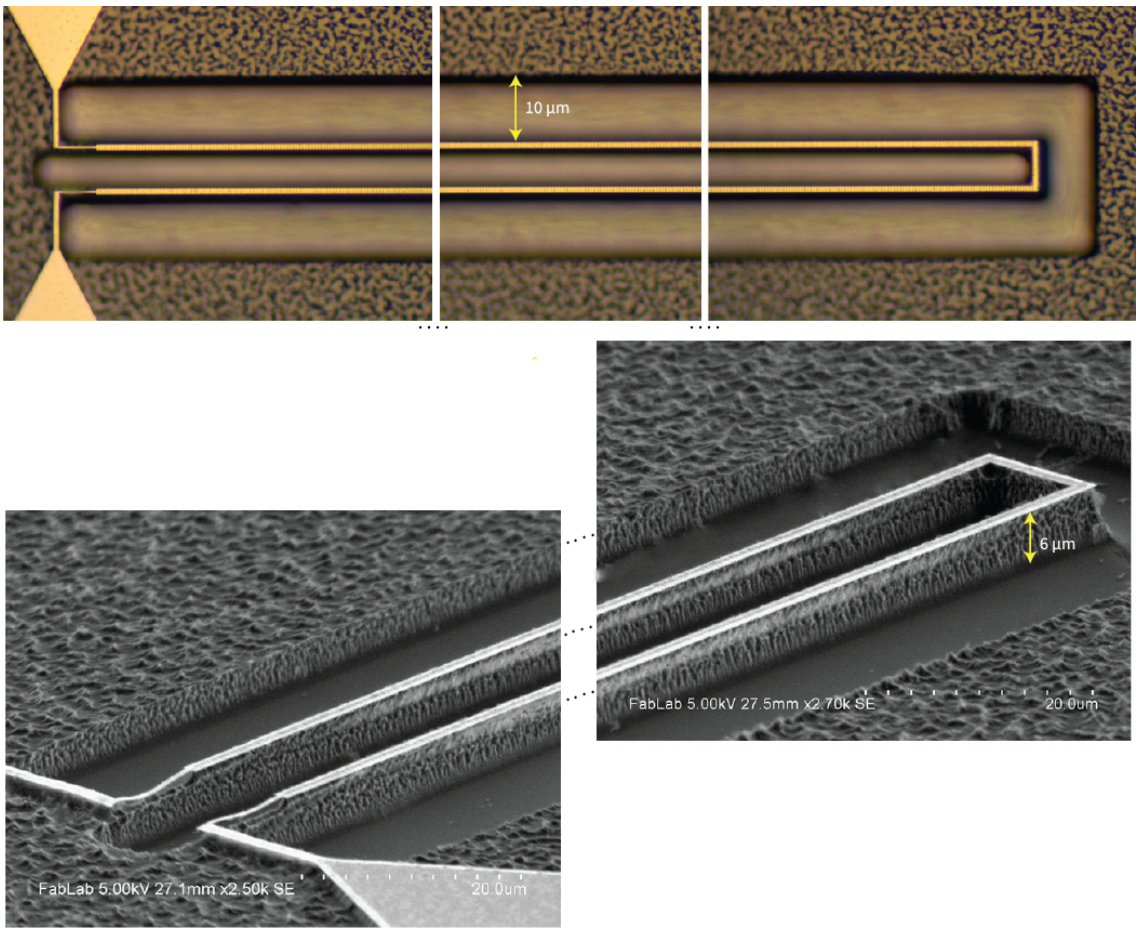

Figure 2.9: An optical image (top) of a selectively etched JJ transmission line and an SEM image of the same device (bottom).

must be utilized. Our technique uses a plasma dry etch technique of SF_6. At very low power and flow this process becomes anisotropic and etches down into the exposed Si and minimally under-etches our devices. The following reaction describes the chemical reaction of the dry etch [48]:

$$4SF_6 + 6Si \rightarrow 4S + 6SiF_4 \ . \tag{2.3}$$

Our procedure amounts to an added post-processing procedure where the devices has multiple layers of MMA spun ontop such that the thickness is of the resist is $\sim 5\mu$m. The spun device is then exposed where the Si should be removed and the patterned resist mask then has 10 nm of Al deposited on top at a very sharp angle such that the shift of deposited material misses the exposed Si region. The device is then etched accordingly. Using this technique only regions of Si exposed to the SF_6 etch will be removed. We can etch down removing $\sim 7\ \mu$m with a trench width of $\sim 10\ \mu$m. This technique also avoids any free-standing leads which avoids any unforeseen possible thermalization issues of completely releasing JJ chain. In the fabrication world, this technique is commonly used for deep etching of devices to produce micro-electrical-mechanical systems [154].

2.4 Cryogenics

The dilution refrigerator operating at a minimal temperature is crucial. The brand used in this thesis is BlueFors. This refrigerator uses a dilute mixture of He^3/He^4 to reach temperatures under 10 mK; that is -272.09° C which is colder than the temperature of deep space. This temperature is just barely above absolute zero and is completely necessary to freeze out all thermal degrees of freedom which would otherwise wash out the quantum effects in the microwave frequency range. Using a dilution refrigerator satisfies the criteria that $hf \gg k_B T$.

The BlueFors dilution unit is an engineering feat in its own right. Luckily the dilution refrigerator technology has advanced significantly in the last few decades. There is no need to fill up Helium reservoirs on a consistent basis and in fact, the only bi-weekly maintenance necessary for a healthy fridge is to fill up a liquid nitrogen dewar cold trap which acts as a filter

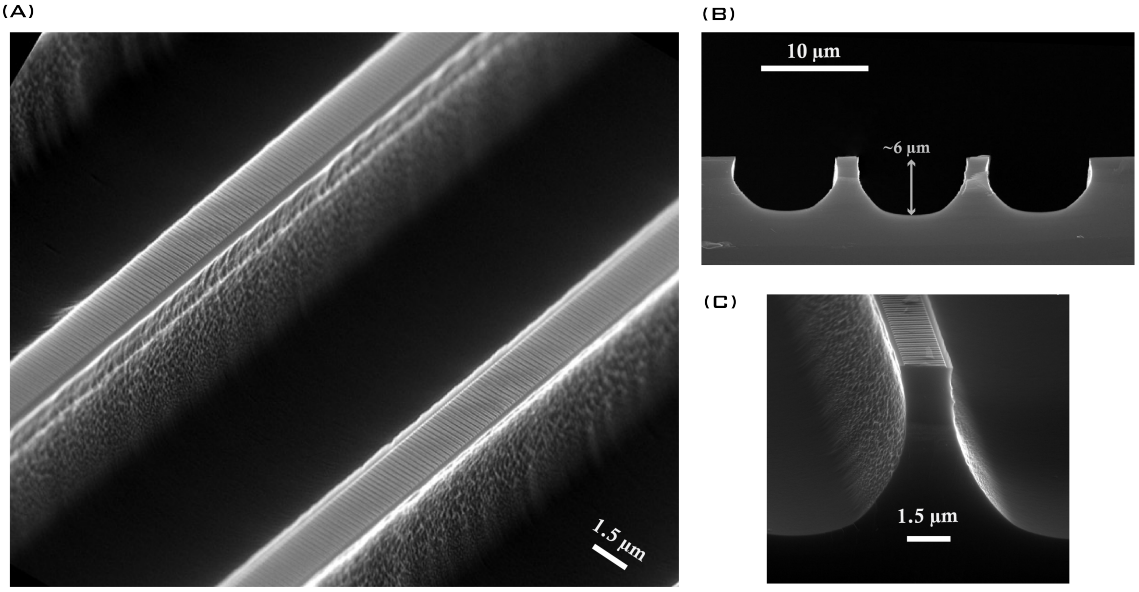

Figure 2.10: A transmission line etched by SF_6. (A) An SEM image showing the two parallel JJ arrays where the differential modes propagate. (B) A crossectional image of the device snapped. The etch has created trenches in the silicon surrounding the device to a depth d 6 μm. (C) A zoomed crossectional image showing the chain suspended above the silicon while still being attached to the silicon mesa.

removing impurities from the He-mixture.

The fridge cools down in about 36 hours and is operated through simple software which has premade scripts to aid in the cooling process. Eliminating the need to engineer and troubleshoot dilution units has enabled the common lab to prosper without costly time delays from figuring out why the fridge won't cool down properly. With that being said, it is critical for the proper maintenance of the dilution unit components with a careful understanding of the thermalization of various microwave components along with proper microwave hygiene.

Without the proper thermalization, the dilution unit does not guarantee a cold sample. Thermalization of cables and attenuators is especially critical. The fridge consists of different temperature stages, each with a different cooling rate, and can only withstand a certain thermal load. Therefore, proper distribution of power dissipating microwave components must be thermally anchored at different stages to ensure proper cooling. This is true for both RF and DC measurement lines.

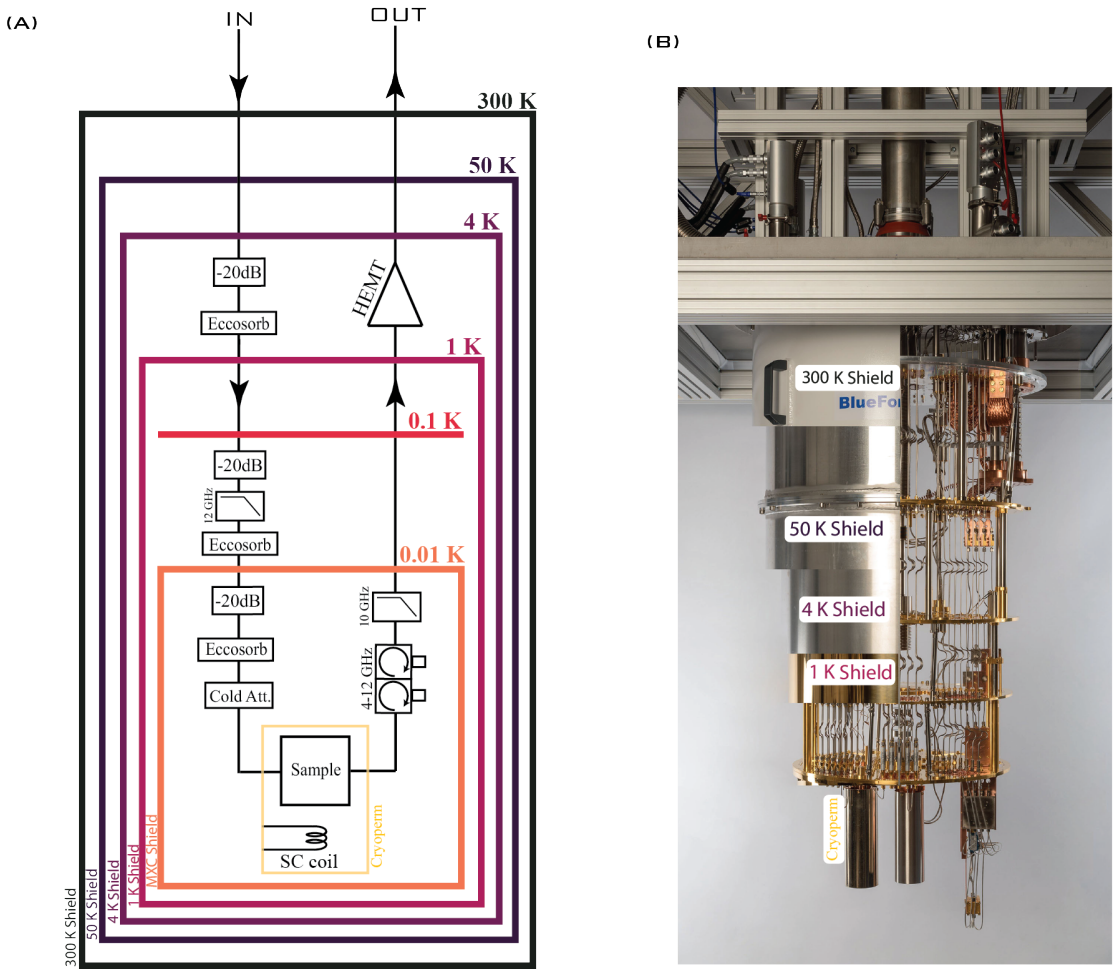

Figure 2.11: (A) The different temperature stages of a dilution refrigerator with the input and output lines shown. The basic setup for RF measurements is shown. The temperature of each component is the same as the stage directly above. (B) A reproduction from [97] where the dilution refrigerators stages and shields are all shown. The picture is multiple shot superimposed to show the different temperature shields overlapping.

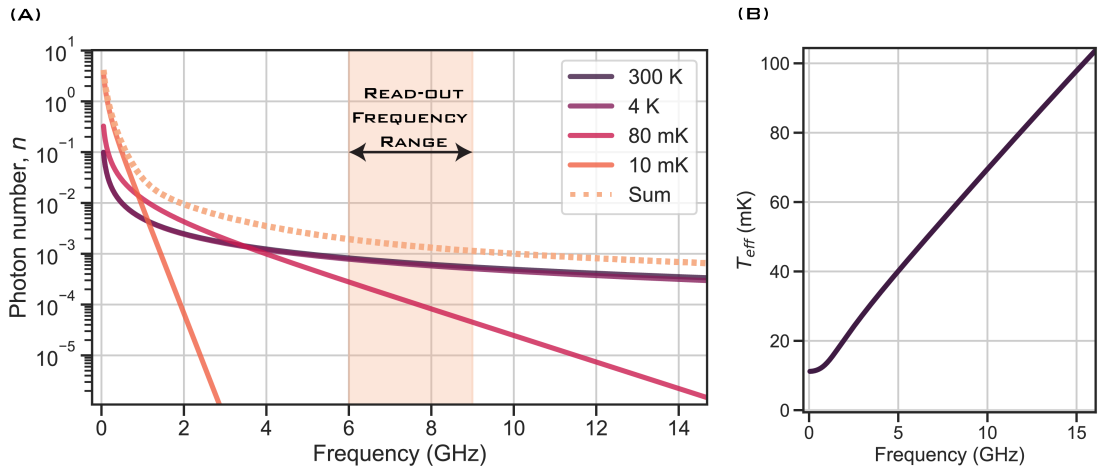

Figure 2.12: (A) Photon number at a given frequency for each temperature stage corresponding to -20 dB attenuators at 4 K, 100 mK, and 10 mK. The photon number is found by using Boltzmann's distribution and each is represented as a black body at some temperature which can also radiate into the lines. (B) The effective temperature at a given frequency.

To reduce the "black-body" temperature of the measurement lines, which enter the fridge at 300 K, cold attenuators are inserted along the line. The attenuator distribution found most optimal is to thermally anchor -20 dB attenuators to the 4 K, 100 mK, and 10 mK stages. The line becomes thermalized due to power dissipation by a very cold object which itself contributes to the thermal noise at frequencies proportional to its temperature [51]. The idea of cascading attenuators at different temperatures starts from a black body spectrum at 300 K which enters the fridge along with the signal of interest. This spectral density is dissipated by each cold attenuator therefore effectively reducing the spectral noise of the incoming signal. The average photon occupation is calculated using Bose-Einstein statistics and microwave cascading calculations [151] while also considering the Black-body spectrum of the thermalized attenuator. Expectedly, at lower frequencies, average photon numbers are larger and the sum in the read-out frequency range is limited by the contribution mostly from the 4K stage. Thermal photon occupation at read-out frequency can contribute to dephasing and is important to optimize.

Now using the average photon number contributed by each stage, the

effective temperature can be extracted. Using this attenuation distribution, a readout in the range of 6-8 GHz has an effective temperature between $T_{\text{eff}} \sim 40-60$ mK attributed to an average photon number of $n_{th} \sim 1 \times 10^{-3}$.

Furthermore, proper shielding from the multitude of noise-causing agents must be considered when optimizing the measurement conditions for our devices. Major sources considered in state-of-the-art set-ups include shielding from high-frequency stray photons and magnetic field shielding. In this scenario, high-frequency amounts to anything above 20 GHz and becomes especially important for light comparable to the superconducting gap of Al which is approximately 40 GHz. Shielding from high-frequency photons comes in the form of Eccosorb filters which have large attenuation in this range. Magnetic field shielding takes the form of a high-μ cylinder which encloses the sample on the base plate. We also enclose the RT can with high-μ material to ensure external ambient magnetic fields do not cause low-frequency drifts of the flux biasing of our devices.

2.5 3D copper box sample holders

The fabricated samples are loaded and mounted into one of the varieties of 3D copper boxes shown in 2.13. The edges of the chips are thermally anchored by pressing them firmly into small strips of indium. The actual device is located in the middle of the chip and has relatively large distances to the walls of the copper housing which act as ground; indicating the electric fields from coupling antennas are less dense and therefore are less susceptible to concentrated fields around lossy TLSs.

2.5.1 3D copper cavities

The fundamental transverse-electric mode of the copper cavity is used as a way to measure the state of the qubit. The coupling antennas of the fluxonium are used to couple to the electric field inside the cavity where the fundamental mode is used as "readout".

The dimensions of the cavity determine the resonant modes; where the largest dimension determines the lowest mode frequency. The modes of a

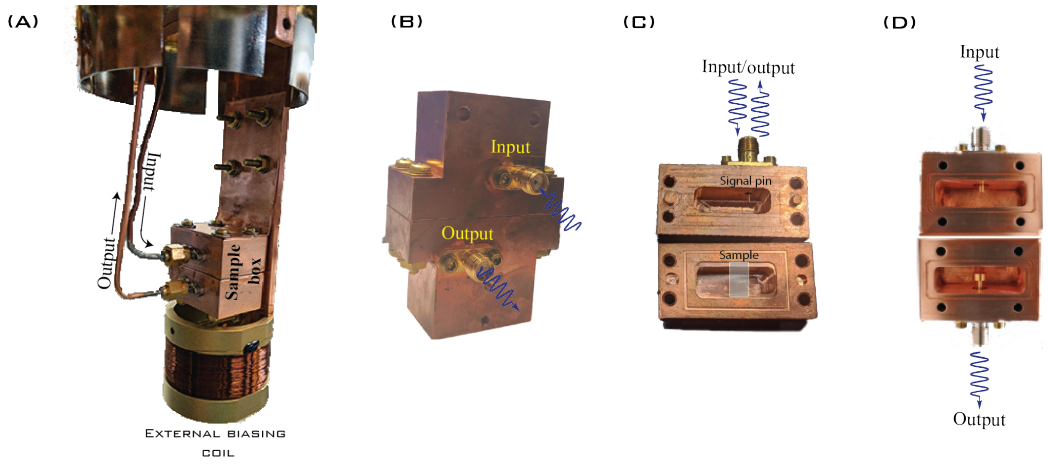

Figure 2.13: A variety of copper boxes acting as a 3D cavity or 3D waveguide. (A) A sample box mounted directly to the fridge's cold finger which has an external biasing coil underneath. A 3D copper cavity can be measured in (B) transmission configuration (two ports) and in (C) reflection configuration (one port). The box can also act as a 3D waveguide (D).

3D cavity are found as [151]:

$$f_{nmk} = \frac{c}{2\pi}\sqrt{\left(\frac{n\pi}{l_x}\right)^2 + \left(\frac{m\pi}{l_y}\right)^2 + \left(\frac{k\pi}{l_z}\right)^2} \tag{2.4}$$

In this case, we want to use the lowest frequency mode to couple to the circuit's dipole antenna, meaning the lowest mode should be a transverse electric-field mode (TEM). The walls of the copper cavity are electrical ground and a pin sticks in from the SMA cable input. The electric field mode has a spatial dependence that is strongest in the middle and decreases sinusoidally to zero at the edges. The chip can be positioned at different points away from the exact center to adjust the external coupling to the input or output bias pins. A subtle detail to point out is the SMA connectors are non-magnetic brass which helps to create a "cleaner" magnetic environment.

The cavity can be used for reflection or transmission measurements. Reflection is when the second port is terminated with a 50 Ω terminator cap while the input port has a pin of variable length that determines the line width of the cavity. Transmission measurements have the second port added

when the signal enters and exits at different ports each with a separate coupling to the chip. Usually, the signal-out port has stronger coupling to enable the readout of the qubit at lower powers.

To properly prepare a cavity for cooling down the coupling to the external pin is extracted for each port separately. This way we can determine the cavity's approximate line width before cooling down. The shape of the cavities resonance should be Lorentzian [87].

2.5.2 3D copper waveguides

We measure 2D samples in this box which, in this work, are either JJ transmission lines or inductively coupled qubits. Each sample has on-chip readout modes which are used to read out the state of the qubit instead of the 3D cavity mode. These boxes have a bandpass frequency where frequencies

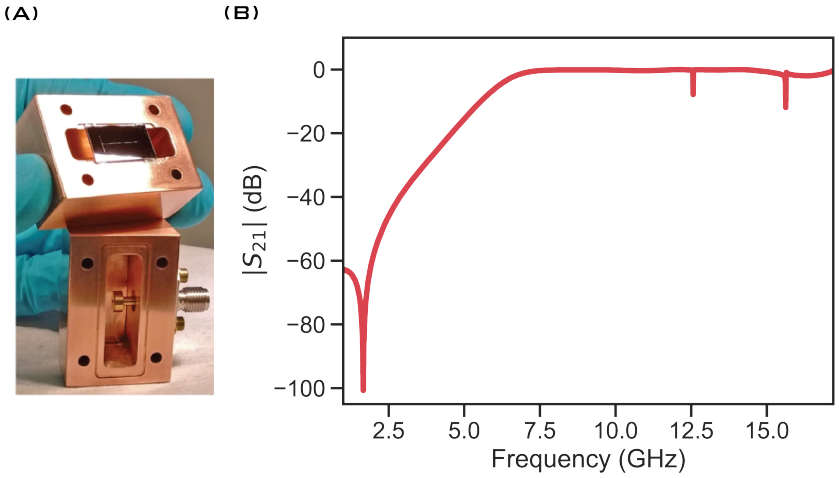

Figure 2.14: (A) A sample is prepared for a cool down and is thermally anchored to the box via indium. (B) The transmission spectrum of microwaves through the waveguide. A passband for $f > 5$ GHz where signals above 5 GHz are transmitted without reflection.

approximately greater than 5 GHz are able to pass through from port to port with little reflection. Below this is the cutoff, the 3D waveguide has significantly reduced transmission.

On-chip resonators made by thin film deposition are used to inductively couple to qubit devices. These resonators share a mutual inductance with the qubit by sharing several JJs. These compact resonators have a lumped

inductance and a lumped capacitance which also serves to couple the samples to the incoming microwave signals from the large input microwave launchers. The advantage of a 2D resonator is the reduced footprint and the ability to easily change the geometry from device to device. 2D resonators also enable qubit devices to have large charging energies since the large area coupling antennas are no longer necessary.

2.6 Microwave electronics

The microwave signals to excite, control, and measure devices are produced at room temperature and rely on fast pulses ranging between 1-1000 ns. Microwave frequency signals typically range between 0.01 - 20 GHz with a power range between -40 - 22 dBm. A fast voltage pulse is generated by an arbitrary wave generator (AWG) which is used as the pulse envelope for the microwave frequency generator. When the voltage pulse is a Gaussian wave packet, the signal entering the fridge is: $s(t) = \{A\cos(\omega_{RF}t) + B\sin(\omega_{RF}t)\} \times \exp\{-t^2/4w^2\}$; where w is the pulse width and A, B are the signal quadrature amplitudes. Another RT microwave components used

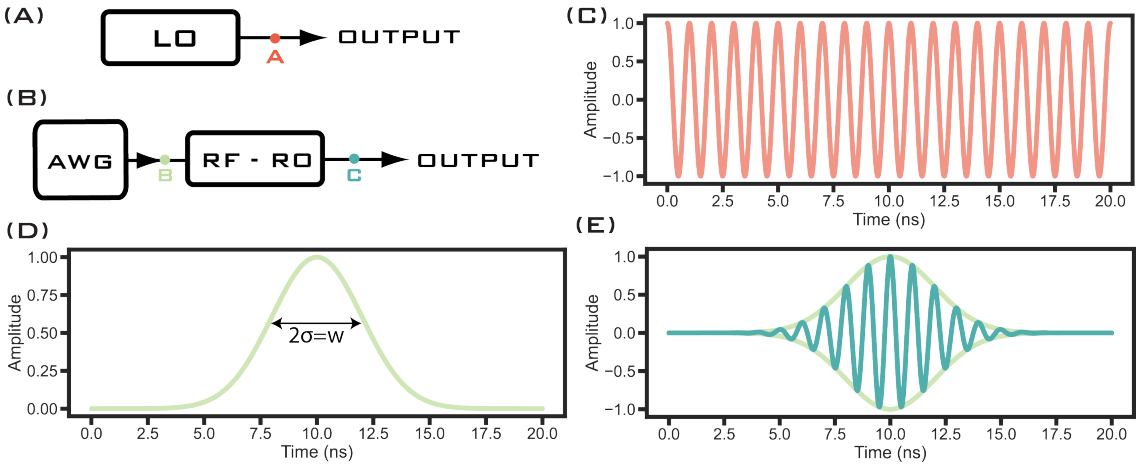

Figure 2.15: (A,C) Continuous RF output signal from a generator. (B) An AWG produces a voltage pulse (D) of variable width. This pulse is mixed with a continuous signal which produces a wave packet (E). The pulse is the modulating signal while the RF signal is the carrier wave.

for measurement are power splitters which takes a single input and makes two outputs with a usual power loss of approximately one-half or -3 dB. RF

mixtures are also used to combine two signals with detuned frequencies to produce an intermediate frequency (IF) signal. The two input frequencies, in this case, are the RF signal and a local oscillator (LO) signal which when combined via the mixer produces a signal at $\omega_{IF} = \omega_{RF} \pm \omega_{LO}$. The generated signal now passes through the fridge and is ultimately converted into a digital demodulated value of voltage in the IQ plane. The setup is capable of collecting 1 Giga-samples per second making the time resolution 1 ns per point. We use a phase-insensitive analog-to-digital acquisition which utilizes a LO-RF frequency detuning of 50 MHz. All signal generators and ADCs are frequency locked to a 10 MHz reference atomic clock. The specific ADC used is an Alazzar card. The measurement is controlled with the GUI measurement software called Labber. For fast measurements in

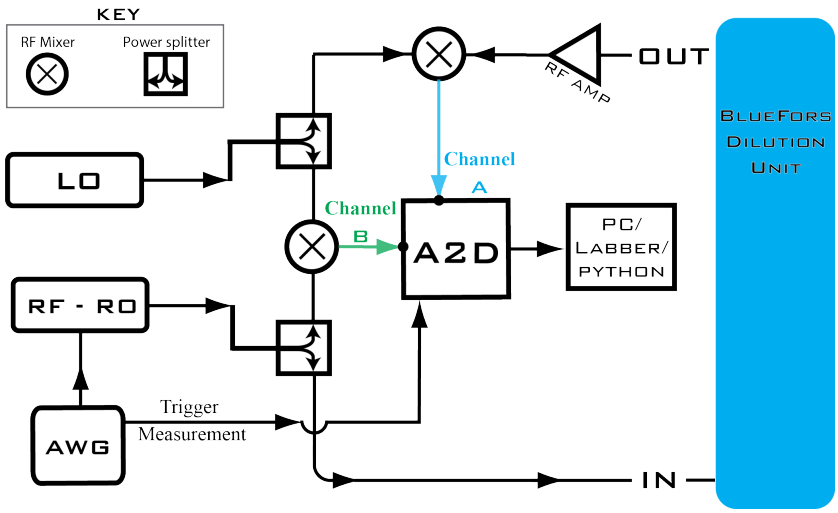

Figure 2.16: Baisc room temperature microwave set-up for measurements using a single RF source only.

the frequency domain only, a vector network analyzer (VNA) is often used. Calibration at temperatures above the base ($\sim$ 800 mK) is necessary to remove the background created by the cables and various filters/circulators in the readout/driving lines.

2.7 Data aquisition

Once the devices are prepared and loaded into our cryogenic microwave setup with all other components set up and functioning properly we can now perform measurements.

We first send in a microwave signal which is modulated with a voltage pulse at the resonator frequency. After the electrical signal passes by and interacts with the resonator a new amplitude and phase will be acquired and this is measurable. A generic cosinusoidal signal microwave signal $s(t)$ with amplitude A_{RO} at frequency ω_{RO} will pass through the measurement line and acquire phase θ_{RO} [96] expressed as:

$$s(t) = A_{RO}\cos\{\omega_{RO}t + \theta_{RO}\} = Re\{A_{RO}e^{i\theta_{RO}}\}\ . \tag{2.5}$$

Our data acquisition technique converts the signal into a point in the complex voltage plane using heterodyne demodulation. The newly acquired amplitude and phase of the signal will be detectable in the complex voltage IQ plane. The goal of the measurement is to extract any newly acquired signal due to the presence of the resonator which is represented as the complex number:

$$\{A_{RO}e^{i\theta_{RO}}\} = I + iQ \tag{2.6}$$

This measurement scheme relies on comparing the read-out signal which has passed through the fridge with a reference signal which has not passed through the fridge. The digitizer has two separate inputs, channel A for the signal which interacted with the chip and channel B for the reference signal that never leaves room temperature. The digitizer also has a time domain measurement resolution which is $\Delta t = 1$ giga-sample/sec or 1 billion points per second. This resolution defines a total measurement time as $t_m = n_m\Delta t$ where n_m is the total number of points in a single measurement trace or "record". Signals arriving at channels A and B in 2.16 do not have the same phase at all times; after signal A passes through the fridge and reference signal B both arrive at their respective mixers each signal will have a phase difference with the LO, defined by ϕ. Once channel A and channel B become modulated with the LO using analog mixers the signals can be

expressed as:

$$\begin{aligned} I_{IF_A} &= A_{IF_A} \times \cos\{\omega_{IF} \cdot n_m \Delta t + \phi + \theta_{RO}\} \ , \ Q_{IF_A} = B_{IF_A} \times \sin\{\omega_{IF} \cdot n_m \Delta t + \phi + \theta_{RO}\} \\ I_{IF_B} &= A_{IF_B} \times \cos\{\omega_{IF} \cdot n_m \Delta t + \phi\} \ , \ Q_{IF_B} = B_{IF_B} \times \sin\{\omega_{IF} \cdot n_m \Delta t + \phi\} \end{aligned} \tag{2.7}$$

where $\omega_{IF} = 50$ MHz. Now the electrical signal with some amplitude and phase oscillating at 50 MHz enters the digitizer board where the analog to digital conversion (ADC or A2D) takes place. The ADC takes the incoming signal ($I_{IF_A}, Q_{IF_A}, I_{IF_B}, Q_{IF_B}$) and creates a "digitized" point for each channel every Δt and multiples them by either cos or sin argument of IF frequency times the time step.

Following this, the signal used as a reference (channel B) is:

$$\begin{aligned} I_B &= \frac{2}{M} \sum_{N=1}^{M} I_{IF_B} \times \cos\{\omega_{IF} \cdot n_m \Delta t\} = \frac{1}{M} \sum_{N=1}^{M} A_{IF_B} \times \cos\{\phi\} \\ Q_B &= \frac{2}{M} \sum_{N=1}^{M} Q_{IF_B} \times \sin\{\omega_{IF} \cdot n_m \Delta t\} = \frac{1}{M} \sum_{N=1}^{M} B_{IF_B} \times \sin\{\phi\} \end{aligned} \tag{2.8}$$

While the signal which passes through the fridge and interacts with the resonator (channel A) is:

$$\begin{aligned} I_A &= \frac{2}{M} \sum_{n=1}^{M} I_{IF_A} \times \cos\{\omega_{IF} \cdot n_m \Delta t\} = \frac{1}{M} \sum_{n=1}^{M} A_{IF_A} \times \cos\{\phi + \theta_{RO}\} \\ Q_A &= \frac{2}{M} \sum_{n=1}^{M} Q_{IF_B} \times \sin\{\omega_{IF} \cdot n_m \Delta t\} = \frac{1}{M} \sum_{n=1}^{M} B_{IF_A} \times \sin\{\phi + \theta_{RO}\} \end{aligned} \tag{2.9}$$

Where M is the total number of discretization points per single measurement record. Measurement length or the number of points per record depends on the length of the Gaussian pulse sent by the AWG. A second pulse linked with the beginning of the readout Gaussian pulse is sent directly to the A2D which initiates data collection. When triggered by this pulse the A2D effectively demodulates the incoming signals to a zero-frequency signal where each point in the demodulated record is represented as: $z = I + iQ$ in the complex plane.

The magnitude and phase of the normalized summation of points in the

record are expressed as:

$$\begin{aligned} \text{magnitude} &= \sqrt{I_A^2 + Q_A^2} \\ \text{phase} &= \tan^{-1}\left\{\frac{Q_B}{I_B}\right\} - \tan^{-1}\left\{\frac{Q_A}{I_A}\right\} \end{aligned} \tag{2.10}$$

We see that the phase is the difference between the arguments of reference channel B and signal channel A. This way the arbitrary phases between the LO and the respective channel signals are accounted for and we are able to recover the average magnitude and phase:

$$\begin{aligned} \text{magnitude} &= |\bar{z}| = \sqrt{\bar{A}_{IF_A}^2 + \bar{B}_{IF_A}^2} \\ \text{phase} &= \bar{\theta}_{RO} \end{aligned} \tag{2.11}$$

producing a single point in the IQ plane represented as $\bar{z} = |\bar{z}|e^{-i\bar{\theta}_{RO}}$; this average value is considered the result of a single measurement record.

This technique is then repeated between $10^3 - 10^6$ times creating an ensemble of points representing the outcome for a measurement with fixed parameters. These points are again averaged together for a final data point in the IQ plane. The final averaged records have a value defined as:

$$\langle \bar{z} \rangle = \frac{1}{K}\sum_{k}^{K} \bar{z}_k \tag{2.12}$$

where k is an integer that represents the number of records incorporated for the measurement. Specific measurement parameters are then swept and this procedure is repeated for each unique measurement condition.

2.8 Basic measurement

The data acquired from a resonator measurement where the RF frequency was swept through the resonance can be most simply analyzed as an RLC parallel circuit; the analysis considered here is close to the work of [162] and will help build the intuition of how to make sense of the A2D data. The analysis naturally starts by first considering the impedance as a function of

frequency for the RLC circuit. In this case, a resistor is added to represent dissipation channels that cause energy loss in one form or another; where each possible loss channel can be added in parallel and become solely represented as a single resistor.

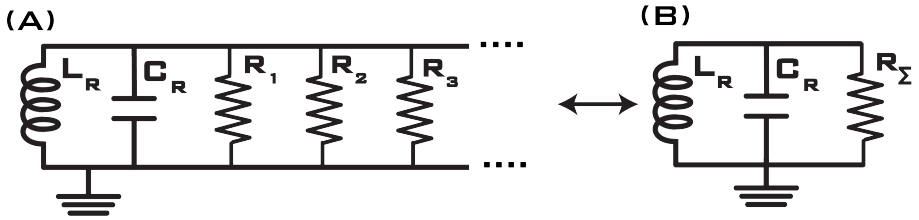

Figure 2.17: Parallel loss channels can be combined to a single loss source R_Σ.

The system is described by the standard damped oscillator equation of motion where the parallel RLC circuit has an impedance [125]:

$$Z_s[\omega] = \frac{1}{Y_s[\omega]} = \left\{ i\omega C + \frac{1}{i\omega L} + \frac{1}{R} \right\}^{-1} . \tag{2.13}$$

This representation of a superconducting resonator allows for the quality factor of the resonator to be defined as:

$$Q = \omega_0 \frac{\text{average energy stored}}{\text{dissipated power}} . \tag{2.14}$$

Using this simple relation with the definition of power dissipation by a resistor:

$$P = \frac{RI^2}{2} = \frac{V^2}{2R} , \tag{2.15}$$

along with the energy stored in the reactive elements:

$$E_C = \frac{1}{4} V^2 C \ , \ E_L = \frac{1}{4} \frac{V^2}{\omega_0^2 L} \tag{2.16}$$

the formula for the quality, Q takes the form:

$$Q = \frac{\omega_0}{2} \times R \left\{ C + \frac{1}{\omega_0^2 L} \right\} = \omega_0 RC . \tag{2.17}$$

The quality factor is found as the ratio of the imaginary (reactive) part of the impedance to the real part:

$$Q = \left.\frac{Re[Y]}{Im[Y]}\right|_{\omega=\omega_0} \tag{2.18}$$

This equation is true for the parallel configuration since taking the limit $R \to \infty$ there would be no current traveling through the resistor, meaning no power dissipated. While in the series configuration of an RLC circuit if R is large then Q is small and so the inverse of the ratio above would hold true or the expression for the admittance would be exchanged for the expression for the impedance. The Q can also be expressed as a function of a decay constant, τ: $Q = \omega_0 \tau$. In other words, the number of oscillation cycles a resonance can undergo before losing energy in the form of power dissipation at the resonant frequency is Q. Finally, Q can also be found by using the line-width of the resonance (κ) in spectroscopy and is expressed as: $Q = \frac{\omega}{\kappa}$.

The quality factor just considered is called the internal quality or Q_{int} of the circuit. This Q is dominated by the loss mechanisms which are solely due to the properties of the circuit and does not consider losses of energy to the external world. Loses due to the coupling of the superconducting resonator to the external world is a separate type of quality factor called the external quality or Q_{ext}.

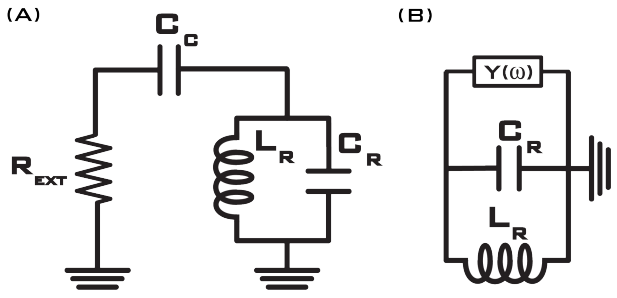

Figure 2.18: (A) An LC oscillator is coupled to and external resistor by a capacitor. (B) The equivalent parallel RLC circuit.

The external quality factor is the measure of how well the circuit is coupled to the external circuitry which in this case is the 50 Ω measurement

line. For this consideration, the standard LC circuit is now capacitively coupled to a resistor. The value of the resistor is not necessarily 50 Ω and is variable depending on Q_{ext} while C_c is normally a simulatable quantity. The shunt impedance is now defined as [62]:

$$Z_s[\omega] = R_{\text{ext}} + \frac{1}{i\omega C_c} = \frac{\omega^2 C_c^2 R_{\text{ext}}^2 + i\omega C_c}{1 + \omega^2 R_{\text{ext}}^2 C_c^2} \approx \omega^2 C_c^2 R_{\text{ext}}^2 + i\omega C_c \ . \quad (2.19)$$

The last approximation is made valid since the second denominator term is much less than 1. The impedance of the LC oscillator is just the characteristic impedance, $Z_0 = \sqrt{\frac{L}{C+C_c}}$ simplifying the expression for Q to:

$$Q = \frac{Im[Y(\omega)]}{Re[Y(\omega)]} = \sqrt{\frac{C+C_c}{L}} \frac{1}{\omega^2 C_c^2 R_{ext}^2} \ . \quad (2.20)$$

The takeaway is the external quality factor is inversely proportional to the coupling capacitance and the external variable resistance found by the Q. Typical values for Q_{ext} range between several hundred to several thousand and can be changed by moving the position of the sample within the 3D housing.

The parallel addition of the two types of quality factors defines the total Q as [59]:

$$Q_{\text{tot}} = \left(\frac{1}{Q_{\text{int}}} + \frac{1}{Q_{\text{ext}}} \right)^{-1} \ . \quad (2.21)$$

The scatter parameters are what we measure experimentally and are represented by the matrix equation [151]:

$$\begin{pmatrix} V_1^- \\ V_2^- \end{pmatrix} = \begin{pmatrix} S_{11} & S_{12} \\ S_{21} & S_{22} \end{pmatrix} \begin{pmatrix} V_1^+ \\ V_2^+ \end{pmatrix} \ .$$

The actual measurement is either S_{11} or S_{21}. The ratio of the voltage sent by port 1 to the voltage reflected back from port 1 is $S_{11} = \frac{V_1^-}{V_1^+} = \frac{Z-Z_0}{Z+Z_0}$ and is called reflection. While the ratio of the voltage transmitted to port 2 after sending a signal out of port 1 is $S_{21} = \frac{V_2^-}{V_1^+}$ and is called transmission. Another

geometry exists called "hanger" where S_{21} is measured however the sample is not directly attached to either port and is instead hanging between ports coupled by a capacitance to both input/output. In this work, we use either reflection or hanger geometry to measure our samples.

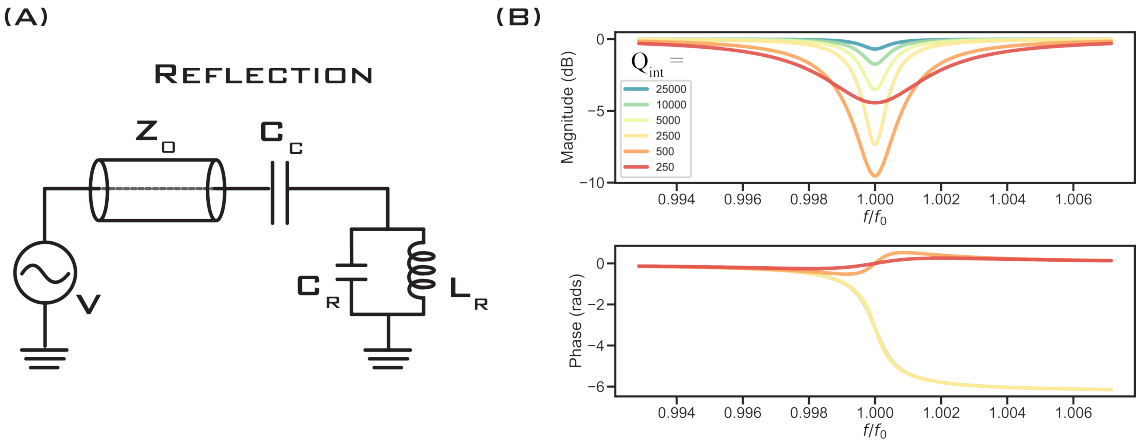

Figure 2.19: (A) Circuit diagram for reflection measurement geometry. (B) The magnitude and phase of the resonator measured for different Q_{int} while keeping $Q_{\text{ext}} = 1,000$.

Once measuring the resonator, the characteristic features including the resonance frequency, Q_{int}, and Q_{ext} are extracted. For a fit using the reflection configuration [125]:

$$S_{11}(\omega) = \frac{2i(\omega-\omega_0)/\omega_0 - Q_{\text{ext}}^{-1} + Q_{\text{int}}^{-1}}{2i(\omega-\omega_0)/\omega_0 + Q_{\text{ext}}^{-1} + Q_{\text{int}}^{-1}} \tag{2.22}$$

or a measurement using the hanger configuration:

$$S_{21}(\omega) = \frac{2i(\omega-\omega_0)/\omega_0 + Q_{\text{int}}^{-1}}{2i(\omega-\omega_0)/\omega_0 + Q_{\text{ext}}^{-1} + Q_{\text{int}}^{-1}} \ . \tag{2.23}$$

The magnitude and phase of the scattering parameters when measuring S_{j1}, for j=1,2 are defined as [60]:

$$\begin{aligned} \text{Magnitude} &= 20 \times \log_{10}\left(|S_{j1}|\right) \text{ [dB]} \\ \text{Phase} &= \tan^{-1}\left\{\frac{Im[S_{j1}]}{Re[S_{j1}]}\right\} \text{ [Radians]} \ . \end{aligned} \tag{2.24}$$

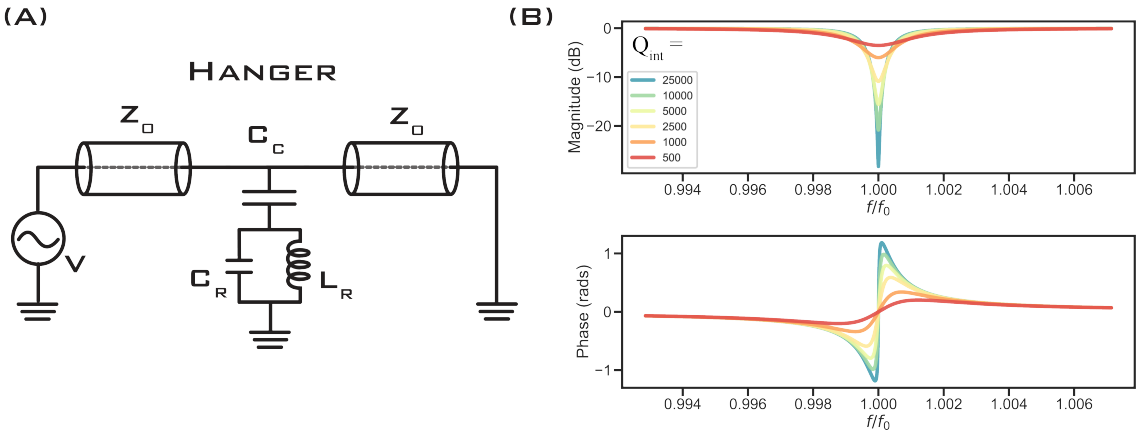

Figure 2.20: (A) Circuit diagram for hanger measurement geometry. (B) The magnitude and phase of the resonator measured for different Q_{int} while keeping $Q_{\text{ext}} = 1,000$.

and can also be analyzed by fitting a circle of the measured trace to the real and imaginary components of each expression.

The usual configuration uses more than one RF source to perform the full characterization of a device. The standard RT microwave measurement is shown in 2.21. In the next chapter, we will discuss full-on measurements of superconducting qubits coupled to the resonators.

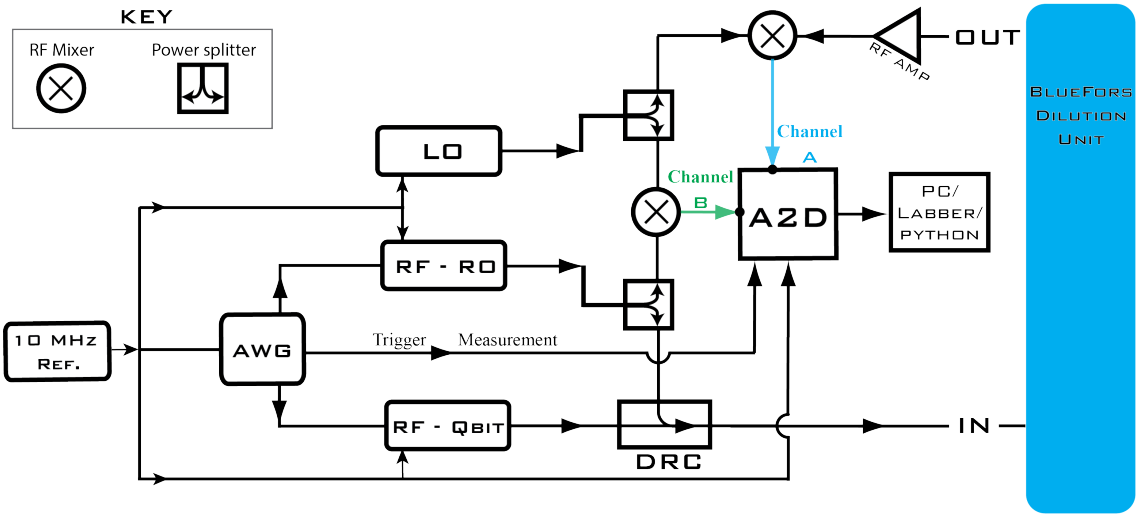

Figure 2.21: Baisc room temperature microwave set-up for measuring a resonator and a qubit. Multiple RF sources are needed.

3

Quantum information with superconducting circuits

"Note that because of the quantum nature of the discussed problem one cannot say that the present state of knowledge is exactly equal to zero." — Harry J. Lipkin, The Journal of Irreproducible Results

3.1 Quantum states

The development and understanding of an electrical quantum circuit starts with exploring the most fundamental constituent: a single "artificial" atom. The transition between the lowest two eigenstates is most commonly used as the two-level system which creates the quantum bit known as a qubit. The dynamics of a qubit can be understood by using the formalism developed to describe a spin in the Pauli basis. The qubit, in the simplest consideration, is a two-level system (TLS) and is made from two orthonormal state vectors defined as:

$$|0\rangle = \begin{bmatrix} 1 \\ 0 \end{bmatrix}, |1\rangle = \begin{bmatrix} 0 \\ 1 \end{bmatrix} . \tag{3.1}$$

The quantum nature of the states provides the ability to create superpositions of the $|0\rangle$ and $|1\rangle$, which can represent any state on the surface of a sphere by a linear superposition of $|0\rangle$ and $|1\rangle$. This sphere is commonly called a Bloch sphere and is used to visualize the state of two-level systems [137]. Any superimposed state can be represented by a state vector [91]:

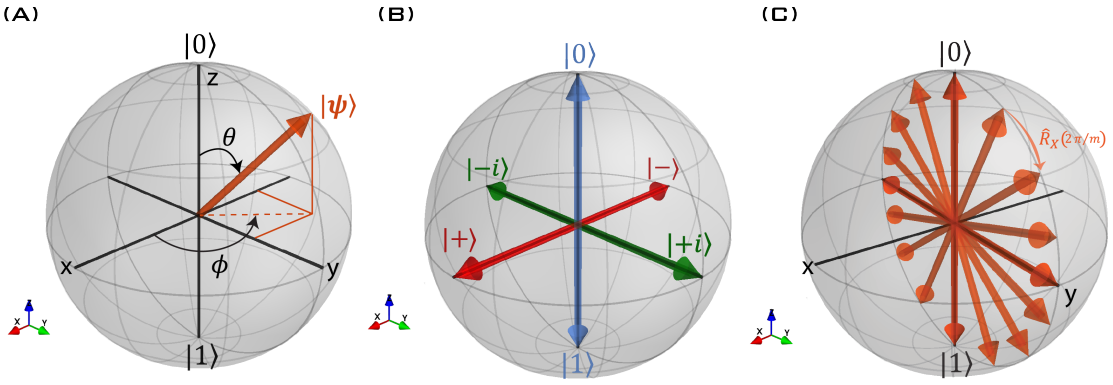

Figure 3.1: (A) The Bloch sphere representation of a two-level state. (B) The eigenstates correspond to the x (+,-), the y (+i,-i), and the z (0,1) axis. (C) The rotation of a state around the x-axis is applied m times. Each displacement corresponds to operating on the state by the rotation operator $R_x(2\pi/m)$.

$$|\psi\rangle = \cos\frac{\theta}{2}|0\rangle + e^{i\phi}\sin\frac{\theta}{2}|1\rangle \ . \tag{3.2}$$

The two angles, θ, and ϕ, are with respect to the z-axis and x-axis, respectively. The amplitudes of $|0\rangle$ and $|1\rangle$ are normalized such that: $|a|^2+|b|^2 = |\cos(\theta/2)|^2+|\sin(\theta/2)|^2 = 1$. Now $|\psi\rangle$ can be represented by the Bloch vector:

$$u(\hat{x},\hat{y},\hat{z}) = \hat{x}\sin\theta\cos\phi + \hat{y}\sin\theta\sin\phi + \hat{z}\cos\theta \ . \tag{3.3}$$

This vector is used when describing arbitrary rotations/dynamics on the TLS. Basic operations that can be applied to a single qubit are the four Pauli matrices defined as:

$$\mathbf{X} = \hat{\sigma}_x = \begin{bmatrix} 0 & 1 \\ 1 & 0 \end{bmatrix}, \mathbf{Y} = \hat{\sigma}_y = \begin{bmatrix} 0 & -i \\ i & 0 \end{bmatrix}, \mathbf{Z} = \hat{\sigma}_z = \begin{bmatrix} 1 & 0 \\ 0 & -1 \end{bmatrix}, \mathbf{I} = \hat{\mathbb{I}} = \begin{bmatrix} 1 & 0 \\ 0 & 1 \end{bmatrix} \tag{3.4}$$

The TLS Hamiltonian can now be defined as two energy levels with a transition frequency $\omega_q/2\pi$:

$$\mathscr{H}_q = \frac{1}{2}\omega_q \hat{\sigma}_z \,. \tag{3.5}$$

Furthermore, rotation operators are created by exponentiation of the Pauli matrices. These operators can be used to define all arbitrary rotations about the $\hat{x}$, $\hat{y}$, or $\hat{z}$ axis on the Bloch sphere and are defined as [156]:

$$\begin{aligned}
R_x(\theta) &= e^{-i\theta\mathbf{X}/2} = \cos(\theta/2)\mathbf{I} - i\sin(\theta/2)\mathbf{X} = \begin{pmatrix} \cos(\theta/2) & -i\sin(\theta/2) \\ -i\sin(\theta/2) & \cos(\theta/2) \end{pmatrix} \\
R_y(\theta) &= e^{-i\theta\mathbf{Y}/2} = \cos(\theta/2)\mathbf{I} - i\sin(\theta/2)\mathbf{Y} = \begin{pmatrix} \cos(\theta/2) & -\sin(\theta/2) \\ \sin(\theta/2) & \cos(\theta/2) \end{pmatrix} \\
R_z(\theta) &= e^{-i\theta\mathbf{Z}/2} = \cos(\theta/2)\mathbf{I} - i\sin(\theta/2)\mathbf{Z} = \begin{pmatrix} e^{-i\theta/2} & 0 \\ 0 & e^{i\theta/2} \end{pmatrix}
\end{aligned} \,. \tag{3.6}$$

When a state is rotated about the y-axis or the x-axis by $\pi/2$, an equal superposition of $|0\rangle$ and $|1\rangle$ states can be used to create another set of orthonormal vectors on the equator of the Bloch sphere:

$$\begin{aligned}
|+\rangle &= \frac{1}{\sqrt{2}}(|0\rangle + |1\rangle)\,, \quad |-\rangle = \frac{1}{\sqrt{2}}(|0\rangle - |1\rangle) \\
|+i\rangle &= \frac{1}{\sqrt{2}}(|0\rangle + i|1\rangle)\,, \quad |-i\rangle = \frac{1}{\sqrt{2}}(|0\rangle - i|1\rangle)\,.
\end{aligned} \tag{3.7}$$

A bit flip is when the state of the TLS has the $|0\rangle$ amplitude swapped with the $|1\rangle$ amplitude and is represented by σ_x. An easy example is $\hat{\sigma}_x|0\rangle = |1\rangle$ and $\hat{\sigma}_x|\pm\rangle = |\pm\rangle$ where we see it is possible to have a bit flip from the 0 $\rightarrow$ 1 but this operation has no effect on the $\pm$ state. While a phase flip is represented by σ_z which changes the phase factor by -1. Other operators worth defining is the $\hat{\sigma}_+$ and $\hat{\sigma}_-$ which represent a change of state of the TLS no matter the position in the Bloch sphere; where $\hat{\sigma}_+ = |1\rangle\langle 0|$ and $\hat{\sigma}_- = |0\rangle\langle 1|$ such that: $\sigma_\pm = \sigma_x \pm i\sigma_y$.

Using the TLS Hamiltonian and considering the time evolution of the state given a prepared input state $|\psi(0)\rangle$; we can define $|\psi(t)\rangle$ using the

time-dependent Schrödinger equation $|\psi(t)\rangle = e^{-i\mathscr{H}t}|\psi(0)\rangle$ as:

$$|\psi(t)\rangle = a|0\rangle e^{-2i\pi f_0 t} + b|1\rangle e^{-2i\pi f_1 t} = a|0\rangle + b|1\rangle e^{-2i\pi(f_1 - f_0)t} \ . \tag{3.8}$$

The transition frequency is $f_{01} = f_1 - f_0$ and is the frequency at which the TLS phase is precessing around the z-axis; or in other words, how the phase is increasing as time evolves. The state evolution as a function of time can be eliminated by applying the unitary transformation [1]:

$$i\frac{\partial|\psi(t)\rangle}{\partial t} = i\frac{\partial}{\partial t}\left(e^{iH_q t}\right)|\psi(0)\rangle + i\frac{\partial|\psi(0)\rangle}{\partial t}e^{iH_q t} \tag{3.9}$$

such that the state is static in time and is now in the rotating frame [96].

To excite or "drive" the qubit transition a signal at the f_{01} frequency is applied to the system. The incoming signal is a voltage source oscillating as a function of time at the RF source drive frequency f_d and with a voltage amplitude A(t). The excitation applied to the TLS is represented as $V_d(t) = A(t)(\cos(\phi)\sin(2\pi f_d t) + \sin(\phi)\cos(2\pi f_d t))$ while the signal is coupled to the qubit with strength g. The Hamiltonian in the rotating frame with a drive tone detuned from the qubit by $\delta = \omega_q - \omega_d$ takes the form after simplification using the rotating wave approximation [11, 86]:

$$\begin{aligned}\mathscr{H}' = \frac{1}{2}\delta\hat{\sigma}_z - gA(t)\Big\{&(\cos(\phi)\cos(\delta t) - \sin(\phi)\sin(\delta t))\hat{\sigma}_x \\ &+(\cos(\phi)\sin(\delta t) - \sin(\phi)\cos(\delta t))\hat{\sigma}_y\Big\} \ .\end{aligned} \tag{3.10}$$

When the driving frequency is off resonance with the qubit such that $\delta \neq 0$ the Bloch vector precesses about an angle. The width of the precession on the Bloch sphere is determined by the value of ϕ. In each representation, the blue vector is the axis of rotation. When $\delta = 0$, equation 3.4.4 becomes simplified to:

$$\mathscr{H}' = gA(t)\Big\{\cos(\phi)\hat{\sigma}_x - \sin(\phi)\hat{\sigma}_y\Big\} \ . \tag{3.11}$$

For $\phi = 0$ the state will rotate about the x-axis while for $\phi = \pi/2$ the state

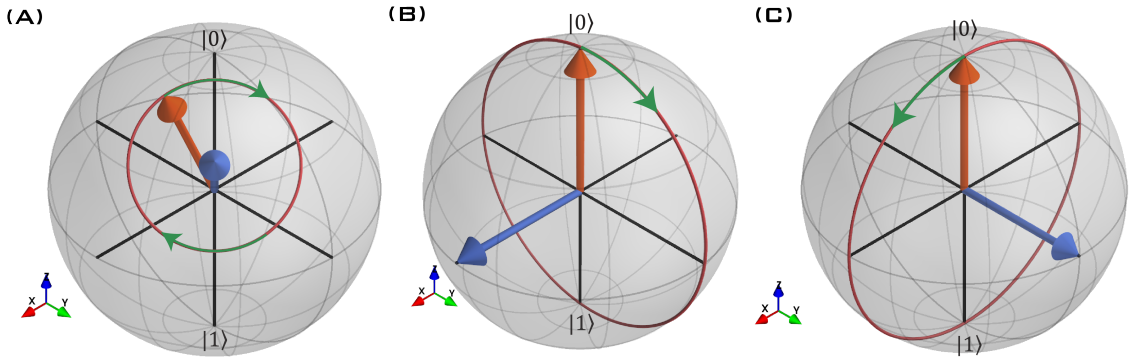

Figure 3.2: (A) The state vector precesses about a fixed point on the Bloch sphere when the qubit is driven at a tone that is not perfectly resonant with the TLS transition frequency. (B) When driven on the qubit frequency with $\phi = 0$ the state will rotate about the x-axis. (C) When driven on the qubit frequency with $\phi = \pi/2$ the state will rotate about the y-axis.

will rotate about the y-axis. The total arc length the state moves is determined by the term $gA(t) = \Omega_R$, which is the "drive strength" [86]. If the TLS is strongly coupled to the signal or the amplitude A is large then the state is modified and precesses faster. While if the pulse has fixed amplitude and coupling strength, then the longer the signal lasts the more the state will rotate and accumulate phase about the respective axis of rotation. Since any rotation on the Bloch sphere can be decomposed into rotations about the x or y-axis, all possible states on the Bloch sphere can be created using sequences of on-resonant drives with varying phases. Furthermore, the amplitude and duration of the drive tone are experimental parameters both controllable by the room-temperature electronics.

3.2 Density matrix formalism

The two-level state can be represented as a density operator [191]:

$$\hat{\rho} = \frac{1}{2}(\mathbb{I} + u \cdot \sigma) \, . \tag{3.12}$$

Where a more practical form to write the density operator in a matrix representation [55]:

$$\hat{\rho} = |\psi\rangle\langle\psi| = \begin{pmatrix} \hat{\rho}_{00} & \hat{\rho}_{01} \\ \hat{\rho}_{10} & \hat{\rho}_{11} \end{pmatrix} = \begin{pmatrix} \cos^2\frac{\theta}{2} & e^{-i\phi}\cos\frac{\theta}{2}\sin\frac{\theta}{2} \\ e^{i\phi}\cos\frac{\theta}{2}\sin\frac{\theta}{2} & \sin^2\frac{\theta}{2} \end{pmatrix} \quad (3.13)$$

This representation creates an easy connection between the density matrix and the Pauli matrices such that:

$$\mathbf{X} = \hat{\rho}_{10} + \hat{\rho}_{01}\,,\ \mathbf{Y} = -i(\hat{\rho}_{10} - \hat{\rho}_{01})\,,\ \mathbf{Z} = \hat{\rho}_{00} - \hat{\rho}_{11}\ . \quad (3.14)$$

The diagonal components of the density operator, $\hat{\rho}_{00}$ and $\hat{\rho}_{11}$, sum to unity and quantify the populations in the ground and excited states, respectively. The off-diagonal elements, $\hat{\rho}_{01}$ and $\hat{\rho}_{10}$, are called coherence and quantify the relative phases between the ground and first excited states which are zero for a mixed state.

The density matrix formalism is particularly instructive when understanding quantum measurements. Measuring a qubit amounts to projecting the state onto the z-axis which simply means taking the expectation value of $\hat{\sigma}_z$. This means a measurement in the z-basis amounts to taking the trace of the matrix product of the density matrix with $\mathbf{Z}$ [191]:

$$\langle \mathbf{Z} \rangle = \mathrm{Tr}(\hat{\rho}\mathbf{Z}) \quad (3.15)$$

Whenever the qubit is not completely in the $|0\rangle$ or $|1\rangle$ state the measured projected vector will be inside the Bloch sphere and lay on the z-axis.

The density matrix is an important tool to introduce basic ideas about the decoherence of a quantum system using the Linbladian master equation formalism [71]:

$$\frac{d\hat{\rho}}{dt} = -\frac{i}{\hbar}[\mathscr{H}, \hat{\rho}] + \sum_j \left(L_j \hat{\rho} L_j^\dagger - \frac{1}{2} L_j^\dagger L_j \hat{\rho} - \frac{1}{2} \hat{\rho} L_j^\dagger L_i \right) \quad (3.16)$$

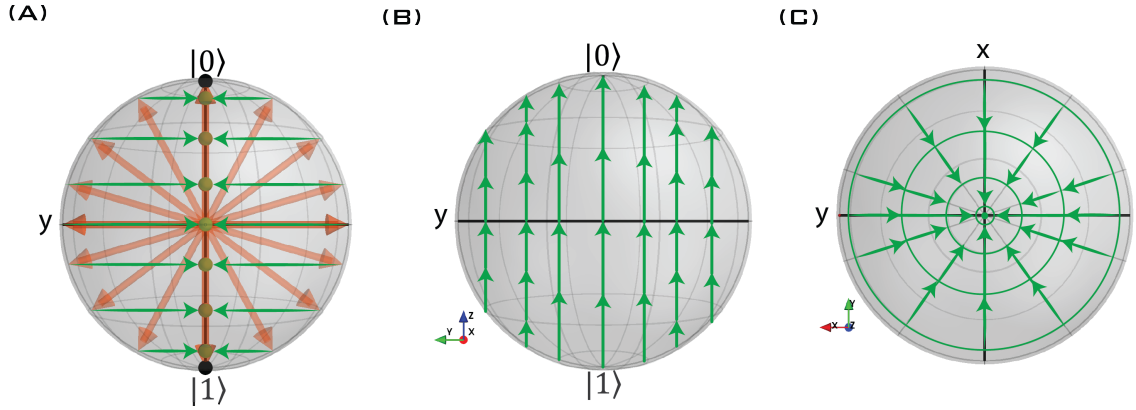

Figure 3.3: (A) Measuring the quantum state in the z-basis corresponds to projecting the Bloch vector onto the z-axis. (B) The diagonal elements of the density matrix follow a vector field which increases the latitude of the Bloch vector only. When the thermal energy is much less than the ω_q the state will relax to the ground state $|0\rangle$. (C) Off-diagonal elements of the density matrix create a vector field that brings the Bloch vector to the center of the sphere [55]. These processes are spurred by a slight change in ω_q which also causes a spiral in the trajectory of the quantum state.

3.2.1 Energy relaxation

For qubit relaxation processes $L_j = L_1 \rightarrow \sqrt{\Gamma_1}\hat{\sigma}_-$. The variable Γ_1 represents the decay rate of the TLS and gives the energy relaxation time $T_1 = 1/\Gamma_1$. Plugging in the defined variables:

$$\frac{d\hat{\rho}}{dt} = -\frac{i\omega_q}{2}[\hat{\sigma}_z, \hat{\rho}] + \Gamma_1\left(\hat{\sigma}_-\hat{\rho}\hat{\sigma}_+ - \frac{1}{2}\hat{\sigma}_+\hat{\sigma}_-\hat{\rho} - \frac{1}{2}\hat{\rho}\hat{\sigma}_+\hat{\sigma}_-\right). \tag{3.17}$$

Now we can explicitly solve for the rate equation of the density operator resulting in simple differential equations for each term:

$$\frac{d\hat{\rho}_{00}}{dt} = \Gamma_1\hat{\rho}_{11}, \frac{d\hat{\rho}_{11}}{dt} = -\Gamma_1\hat{\rho}_{11}, \frac{d\hat{\rho}_{10}}{dt} = -i\omega_q\hat{\rho}_{10} - \Gamma_1\hat{\rho}_{10}, \tag{3.18}$$

when integrated we find that energy relaxation of the two-level system decays exponentially with a rate Γ_1. Expressing the density operator as a function of time with the newly acquired matrix elements gives:

$$\hat{\rho}(t) = \begin{pmatrix} \hat{\rho}_{00} + (1 - e^{-\Gamma_1 t})\hat{\rho}_{11} & \hat{\rho}_{01}e^{-\Gamma_1 t/2} \\ \hat{\rho}_{10}e^{-\Gamma_1 t/2} & \hat{\rho}_{11}e^{-\Gamma_1 t} \end{pmatrix}. \tag{3.19}$$

In the rotating frame the ω_q term can be ignored when driven exactly on resonance.

An important observation is an excited state not only decays exponentially at a rate of Γ_1 for the diagonal elements but also has off-diagonal time-dependent elements showing the relaxation processes cause the qubit to dephase as well at a rate given by $\Gamma_1/2$. In the absence of other dephasing mechanisms, the qubit loses the prepared superposition in a characteristic time given by $2T_1$.

3.2.2 Dephasing

For qubit dephasing processes, $L_j = L_2 \rightarrow \sqrt{\Gamma_\phi/2}\hat{\sigma}_z$. The variable Γ_ϕ sets the dephasing time $T_\phi = 1/\Gamma_\phi$.

$$\frac{d\hat{\rho}}{dt} = -\frac{i\omega_q}{2}[\hat{\sigma}_z, \hat{\rho}] + \frac{\Gamma_\phi}{2}\left(\hat{\sigma}_z\hat{\rho}\,\hat{\sigma}_z - \hat{\rho}\right) \tag{3.20}$$

In this case, the diagonal terms will be zero and the off-diagonal terms will be defined as:

$$\begin{gathered}\frac{d\hat{\rho}_{00}}{dt} = \frac{d\hat{\rho}_{11}}{dt} = 0\,,\ \frac{d\hat{\rho}_{01}}{dt} = -i\omega_q\hat{\rho}_{01} - \Gamma_\phi\hat{\rho}_{01}\,, \\ \frac{d\hat{\rho}_{10}}{dt} = -i\omega_q\hat{\rho}_{10} - \Gamma_\phi\hat{\rho}_{10}\,.\end{gathered} \tag{3.21}$$

Integrating this set of differential equations finds the dephasing mechanism of a qubit also decreases exponentially at a rate of Γ_ϕ and is only given by the off-diagonal components:

$$\hat{\rho}(t) = \begin{pmatrix} \hat{\rho}_{00} & \hat{\rho}_{01}e^{-\Gamma_\phi t} \\ \hat{\rho}_{10}e^{-\Gamma_\phi t} & \hat{\rho}_{11} \end{pmatrix}\,. \tag{3.22}$$

3.2.3 Decoherence

Usually, relaxation and dephasing occur simultaneously, the combined rate is called decoherence. Decoherence's decay rate is given by: $\Gamma_2 = \Gamma_1/2 + \Gamma_\phi$ [96], and is most commonly referenced as a new characteristic time called T_2. The expression for T_2 using the relaxation and dephasing

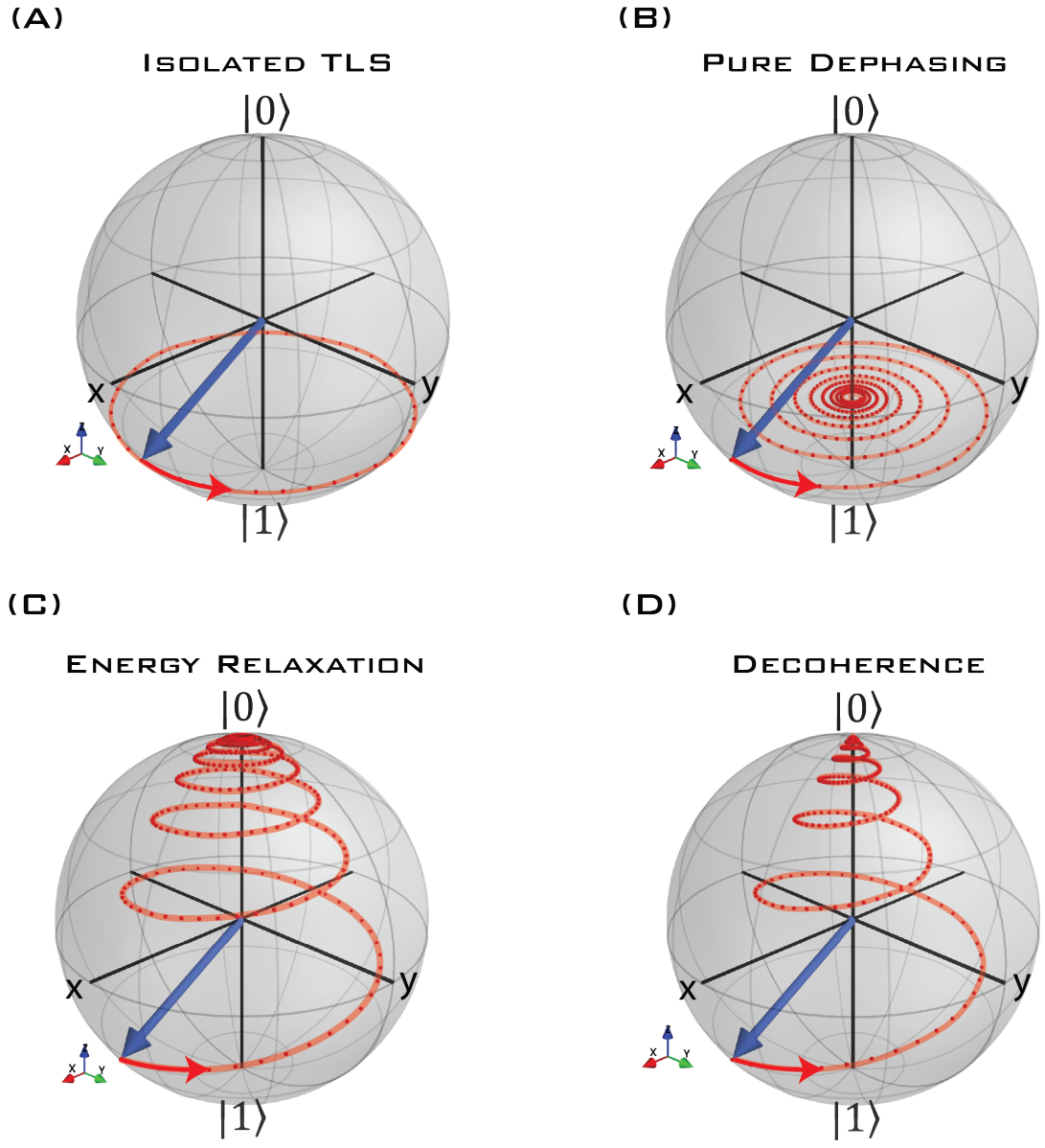

Figure 3.4: (A) An isolated TLS, not in the RWA, will rotate about the z-axis at the transition frequency. (B) Pure dephasing shows the qubit will spiral inside the Bloch sphere until the x and y components are zero. This term can be seen as the off-diagonal terms of the density matrix. (C) Energy relaxation of a state causes decay back to the ground state while also dephasing due to the off-diagonal elements. (D) Decoherence is the combination of pure dephasing and energy relaxation. The spiral of the state in (D) spins faster than in (C).

time constants is:

$$\frac{1}{T_2} = \frac{1}{2T_1} + \frac{1}{T_\phi} \ . \tag{3.23}$$

Experimentally, T_1 and T_2 are the measured quantities while T_ϕ is extrapolated for.

In summary, T_1 is used to quantify how long a quantum state can remain excited before relaxing to the ground state while T_ϕ is used to quantify how long a quantum state can remain in a coherent superposition before the information is lost. T_2 is the parallel combination of both sources which causes the prepared quantum state to lose the information encoded within the state. The way this information is lost due to energy relaxation is primarily from internal dissipative processes while dephasing mechanisms are due to any small deviation in the qubit transition frequency caused by low-frequency fluctuations of environmental factors. Both mechanisms will be covered in detail in the fluxonium chapter.

3.3 Coupling between an atom and a photon

To measure the quantum state of a two-level system, without destroying the quantum state, an auxiliary linear bosonic read-out is coupled to the system. The read-out commonly referred to as a resonator couples to the two-level system and perturbs/hybridizes with the qubit state. Specifically, the resonator frequency changes depending on which state the qubit is in [11]. Furthermore, when the resonator's frequency is within the vicinity of the qubit transition a splitting/hybridization occurs proportional to the atom-resonator coupling strength g. The strength of coupling is a measure of how strongly the two systems can interact and is usually $g < 100$ MHz. The generic form of a Hamiltonian which describes a TLS coupled to a photon mode with coupling strength g, is defined by the Rabi Hamiltonian [11, 96, 115]:

$$\mathscr{H}_R = \frac{\omega_q \hat{\sigma}_z}{2} + \omega_r a^\dagger a + g(a + a^\dagger)\hat{\sigma}_x \ . \tag{3.24}$$

The Rabi Hamiltonian is used when g is comparable to transition frequencies ($g \sim \omega_q$), however, the coupling is normally much less. Therefore, a unitary transformation to the rotating frame of the qubit rotating at ω_q ef-

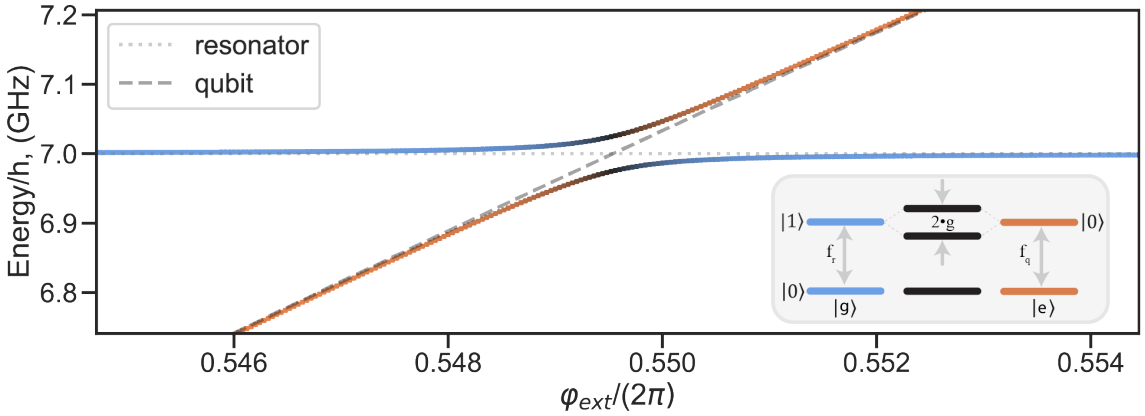

Figure 3.5: A flux-dependent TLS coupled to a resonator anti-cross (or hybridize). The grey dashed line represents the pure qubit transition energy while the grey dotted line represents the undisturbed resonator frequency. The coupling strength g dictates how far the modes are pushed when $f_r = f_q$. (Inset) A picture of the energy levels at the flux point where the unperturbed transitions intersect. The middle black diagram is of the dressed, hybrizied picture.

fectively getting rid of the higher frequency terms. The result is a simpler Hamiltonian which only considers one excitation exchange at a time and is called the Jaynes-Cummings (JC) Hamiltonian [10]:

$$\mathscr{H}_{JC} = \frac{\omega_q \hat{\sigma}_z}{2} + \omega_r a^\dagger a + g(\hat{\sigma}_+ a + \hat{\sigma}_- a^\dagger) \ . \tag{3.25}$$

The first term represents the TLS, the second term represents the resonator, and the third term describes the light-matter interaction which occurs between the resonator photons and the qubit excitations.

In atomic systems, this interaction is created between the dipole moment of the atom and the electric field present in the cavity housing the atom [71, 112]. The dipole interaction between the atom and the cavity photon dictates the strength of the coupling. The operators $\sigma_+ a$ and $\sigma_- a^\dagger$ describe the atom-cavity photon exchange while g is proportional to the inverse rate where an excitation in the qubit decays into an excitation in the cavity and vice versa.

When the TLS and the read-out are far-detuned in frequency, this Hamiltonian is further simplified and re-expressed as the dispersive Hamiltonian

[13]:

$$\mathscr{H}_{\text{disp}} = \omega_r a^\dagger a + \frac{\omega_q \hat{\sigma}_z}{2} + \frac{\chi}{2}\hat{\sigma}_z a^\dagger a \ . \tag{3.26}$$

The dispersive Hamiltonian provides insights on exactly the mechanism of

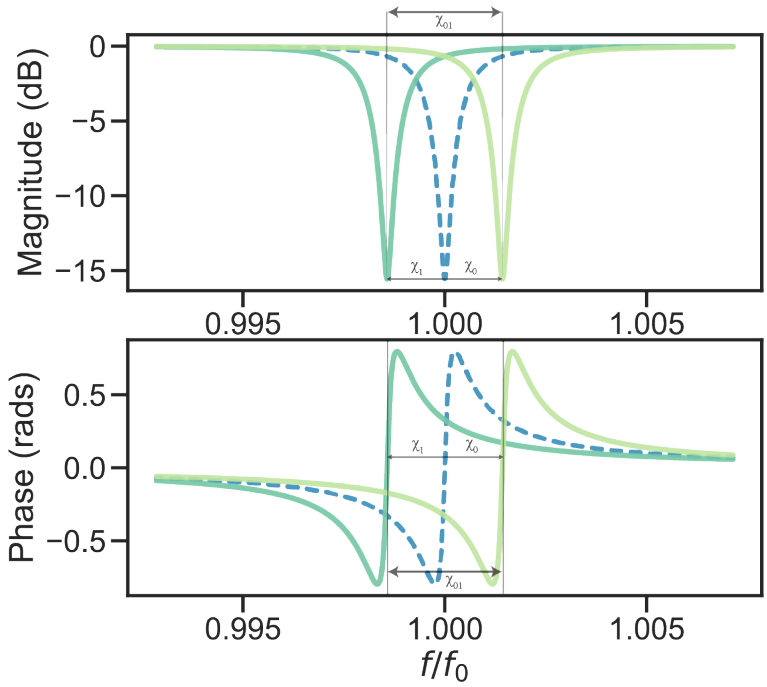

Figure 3.6: The resonator frequency shifts by an amount χ depending on the state of the qubit. The difference between the resonator magnitude or phase from when the qubit is not excited from when the qubit is excited is the signature of a qubit transition.

qubit-state measurement by probing the read-out. In essence, the resonator frequency shifts by an amount χ when the qubit is in the excited state. In this fashion, the read-out frequency is probed while sweeping the second (qubit) tone, when the qubit transition frequency is hit, the resonator's signal becomes modified – the resonator's frequency shifts causing the measured read-out signal to form either a dip or peak in. This process is how two-tone spectroscopy is performed. Other quantities can be swept besides the qubit frequency, for example, changing pulse delays, allowing for time domain characteristics and other quantum measurements can be extensively performed to fully characterize the device.

3.4 Basic quantum measurements

This section highlights the basic measurements used to characterize quantum circuits. The experimental results discussed throughout this thesis use these basic measurement techniques to analyze a variety of devices.

3.4.1 One-tone spectroscopy

The most basic measurement consists of sending in a single microwave tone and measuring the returned signal. This type of measurement is performed firstly to find the read-out frequency of the resonator coupled to the qubit. This technique is generally used to probe any resonance frequencies sufficiently coupled to the incoming microwaves.

Usually, in fluxoniums, the qubit transitions are far detuned from the read-out frequency and are filtered out by a resonator coupled to the external signal, therefore using one-tone spectroscopy for measuring qubits is not feasible. The case when the qubit anti-crosses with the resonator is indeed visible in one-tone but this is unique to only a few external bias points and the qubit transitions quickly fade in a one-tone measurement once passing through the frequency vicinity of the read-out mode.

3.4.2 Two-tone spectroscopy

Once finding the read-out frequency the next task is to map the qubit transitions. This is done by fixing a tone at the read-out resonance while sweeping the frequency of another, second tone. When the second tone hits the resonance frequency of the qubit, the read-out frequency undergoes a dispersive shift where the resonance frequency of the read-out shifts slightly by an amount χ and is due to the coupling between the qubit and the read-out. Two-tone spectroscopy can be performed with second tones of variable power with frequencies ranging between $f \sim$10 MHz and 20 GHz. Two-tone spectroscopy is performed either with a continuous second tone or by a pulsed second tone. Low-power continuous irradiation of the qubit produces sharper transition lines but may cause slight shifts of the true resonance frequency of the qubit transition by Stark-like shifts.

3.4.3 Rabi oscillations

A two-level system can be made to oscillate between the ground and the first excited state depending on the length and the amplitude of the incoming excitation pulse. The frequency of oscillation is also dependent on the coupling strength between the read-out and qubit.

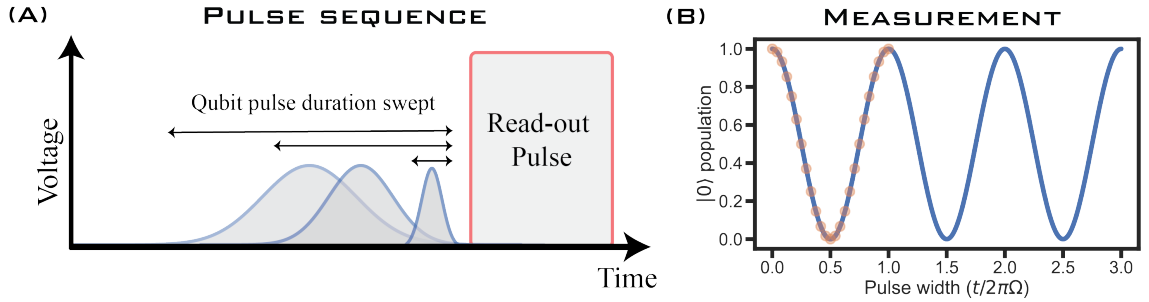

Figure 3.7: (A) Pulse sequence for a Rabi measurement. The pulse width is increased for every orange point in (B). The power delivered at the qubit frequency increases when the pulse width becomes larger. The x-axis in (B) is the time duration of a pulse. At t=0 the qubit is not excited while when the pulse width hits a "pi-pulse" excites the qubit into the first eigenstate.

Assuming the qubit drive is exactly on resonance, the state evolution comes from equation 3.11 where the qubit will oscillate between the ground and first excited state at a frequency Ω_R and the dynamics evolve according to the Hamiltonian [191]:

$$\mathscr{H}_{\text{Rabi}} = \frac{1}{2}\Omega_R \hat{\sigma}_x \tag{3.27}$$

where the population in the two states evolve according to the unitary operation [105]:

$$\hat{U}(t) = \exp\left(\frac{-it}{2}\Omega_R \hat{\sigma}_x\right) = \begin{bmatrix} \cos(\Omega_R t/2) & -i\sin(\Omega_R t/2) \\ -i\sin(\Omega_R t/2) & \cos(\Omega_R t/2) \end{bmatrix} \tag{3.28}$$

such that given the ground state and first excited state populations, will evolve according to $p_0(t) = \frac{1}{2}\{1+\cos(\Omega_R t)\}$ and $p_1(t) = \frac{1}{2}\{1-\cos(\Omega_R t)\}$. Using this relation, we define a π-pulse as the duration/length of a pulse which rotates the Bloch vector around the x- or y-axis by π. This pulse flips the qubit population between p_0 (g) and p_1 (e). The duration of time

the qubit pulse should last to excite swap the ground and first excited state populations is $t_\pi = \frac{\pi}{\Omega_R}$.

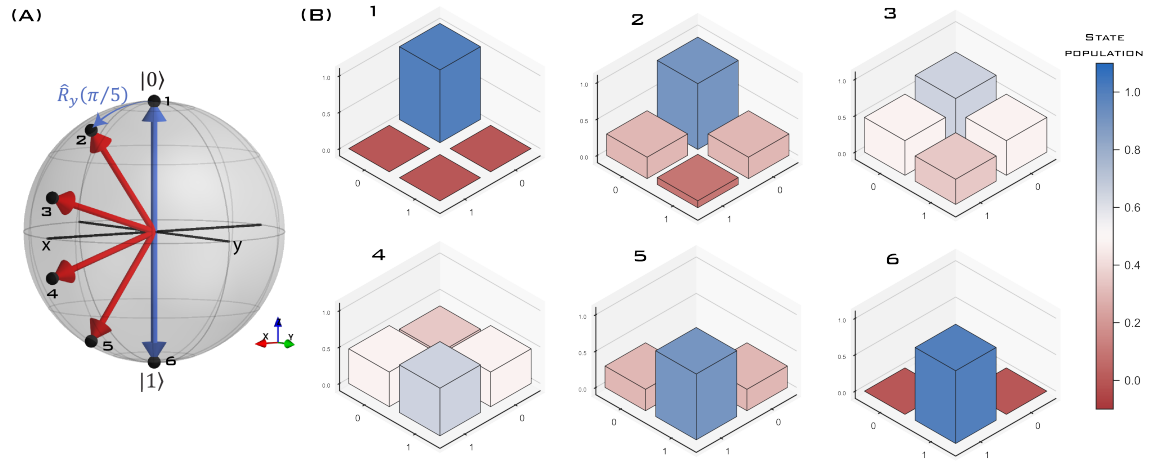

Figure 3.8: A Rabi measurement where the state is excited with different pulse widths to excite certain amounts of the population in each state. The Bloch vector is rotated about the y-axis.

In actual measurements of Rabi oscillations, the signal decays with time due to loss mechanisms. The measurement is fit to a decaying oscillation with a generic form:

$$\mathrm{f}(t_i) = A_0 + A_1 \cos(\Omega_R t_i + A_2) e^{-t_i/T_R} \tag{3.29}$$

where $A_0, A_1, A_2, \Omega_R, T_R$ are fit parameters. Ω_R is the valuable parameter that gives the Rabi frequency and is converted to time determining the pulse length for a pulse sequence to excite the qubit into the first excited state.

When driving the qubit slightly off-resonance with detuning δ the Rabi-frequency becomes increased modified to [22]: $\Omega_R = \sqrt{\Omega^2 + \delta^2}$, where Ω is the Rabi frequency when driving exactly on resonance.

3.4.4 Ramsey fringes

To measure a Ramsey fringe, the superposition of the $|g\rangle$ and $|e\rangle$ states are prepared and allowed to freely evolve according to: $\mathscr{H}_{\text{Ramsey}} = -\frac{1}{2}\delta\hat{\sigma}_z$. The variable δ is known as the detuning, introduced in equation which is the difference between the actual qubit transition frequency and the frequency

of the excitation pulse sent into the system.

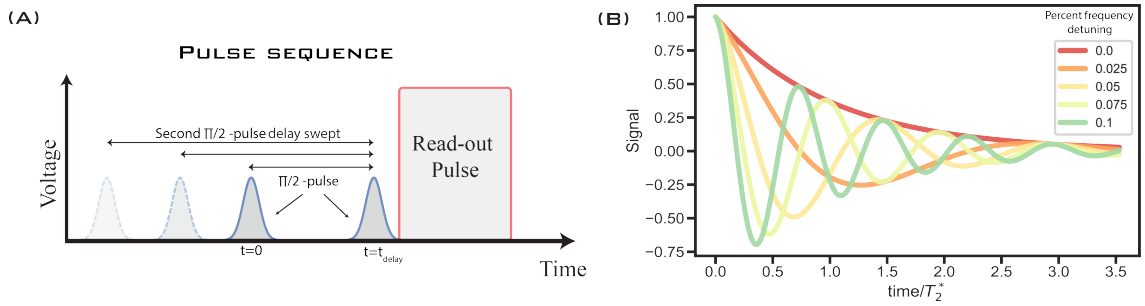

Figure 3.9: (A) The standard Ramsey pulse sequence used to measure T_2^*. Two $\pi/2$ pulses are measured with the difference in time between the two pulses increased. The second pulse is the one moving. (B) Several standard Ramsey measurements where the qubit detuning frequency is changed.

A Ramsey measurement is performed by first preparing the state in an equal superposition by applying a Hadamard gate which is just a $\pi/2$ rotation about the x or y-axis on the Bloch sphere. A $\pi/2$-pulse is found in the Rabi experiment as the duration $t_{\pi/2} = \frac{\pi}{2\Omega_R}$. This first pulse prepares the superposition of states onto the equator of the Bloch sphere. Next, the newly prepared state is allowed to evolve for some variable amount of time before another $\pi/2$ rotation is performed on the evolved qubit state. If no time elapses then the qubit state is prepared in the excited state, however, when increasing the time delay between the two $\pi/2$ pulses we find the vector to accumulate a phase proportional to the qubit-excitation detuning. The populations then evolve as: $p_0(t) = \frac{1}{2}\{1-\cos(\delta t)\}$ and $p_1(t) = \frac{1}{2}\{1+\cos(\delta t)\}$. The actual measurement of Ramsey oscillations decays with time due to low-frequency noise which causes dephasing effects due to a fluctuating qubit transition frequency. The Ramsey measurements are fit to a decaying oscillation envelope with a generic form almost exactly the same as the Rabi measurements except the function depends on different quantities. The fit function is defined as:

$$\mathrm{f}(t_i) = A_0 + A_1\cos(\delta t_i + A_2)e^{-t_i/T_2^*} \tag{3.30}$$

where $A_0, A_1, A_2, \delta, T_2^*$ are fit parameters where δ is used to find the exact qubit drive frequency. This quantity can be used to quantify small variations

in the qubit frequency over a long period of time. The other valuable parameter extractable is the decay constant T_2^* which is known as T_2- Ramsey and is a measure of the qubit's coherence.

3.4.5 T_1

Energy relaxation or T_1 is used to describe the process which produces an excitation or relaxation of the two-level system due to coupling to a noise source at the frequency of the transition between $|g\rangle$ and $|e\rangle$. Unwanted relaxation of the TLS is induced by longitudinal coupling to a noisy environment, which is represented as a noise source coupled to the TLS as [159]:

$$\mathscr{H}_{\text{TLS}} = \frac{\omega_q}{2}\hat{\sigma}_z + \frac{1}{2}V_x\hat{\sigma}_x \tag{3.31}$$

where $V_x\hat{\sigma}_x$ causes population flips proportional to the time-dependent noise source V_x.

Measurements of energy relaxation are performed by applying a π-pulse at the qubit frequency with an increasing time delay between the excitation pulse and the read-out measurement. The signal decays exponentially and is fit to the equation:

$$\text{f}(t_i) = A_0 + A_1 e^{-t_i/T_1} \tag{3.32}$$

where A_0, A_1, A_2, T_1 are fit parameters and T_1 is the decay constant of the excited state of the qubit.

In SCQC, the dissipative processes caused by coupling to a noisy environment are treated by adding resistors in parallel/series to different circuit elements which have an admittance/impedance evaluated at the qubit transition frequency. This admittance/impedance is also used to express the spectral density of the noise source. The noise spectral density ($S_x(\omega_{ij})$) of each relaxation source can be represented as:

$$S_x(\omega_{ij}) = \hbar\omega \times \left(\coth\left[\frac{\hbar\omega_{ij}}{2k_BT}\right] + 1\right)\text{Re}[Y(\omega)]\ . \tag{3.33}$$

The qubit in turn couples to the noise source with a strength given by the relevant matrix element which is susceptible to the noise. The power spectral

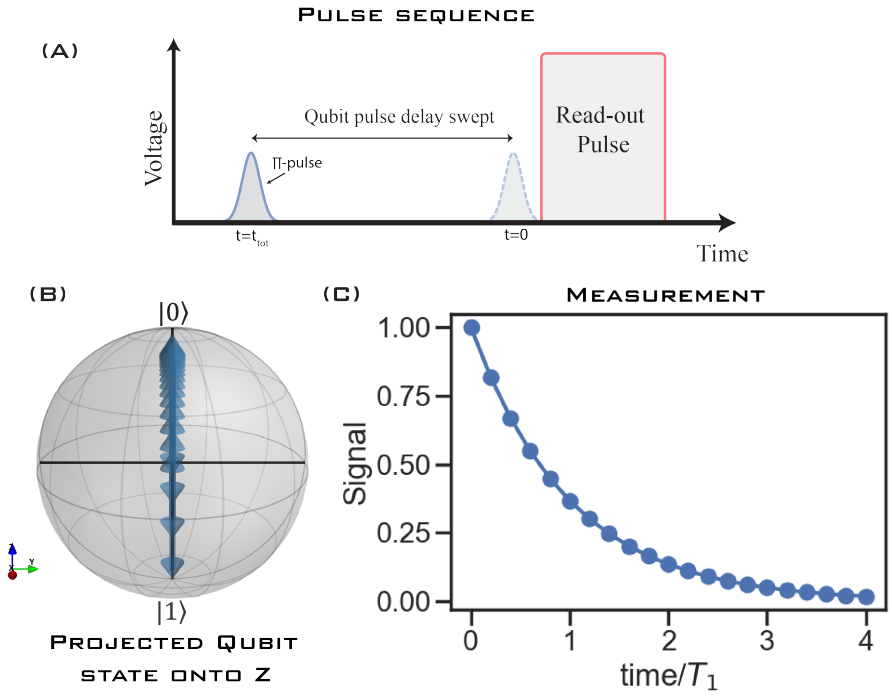

Figure 3.10: (A) The pulse sequence for a T_1 measurement. (B) The projected state onto the z-axis of the Bloch sphere after measurement. (C) The exponential decay profile for a relaxing qubit.

density is often small so the use of perturbation theory to represent the transition rates induced by the noise term between our two states is expressed by Fermi's Golden rule where Γ_{ij} denotes the transition rate from state i to j, and using Fermi's Golden rule takes the form:

$$\Gamma_{ij} = \frac{1}{\hbar^2}|\langle j|\mathscr{O}|i\rangle|^2 S_x(w_{ij}) \ . \tag{3.34}$$

This expression is used to quantify the energy relaxation rate for different processes to which the qubit is exposed. The matrix element $|\langle j|\mathscr{O}|i\rangle|^2$ is the "quantum" link to the classical noise spectral variable where the operator is the coupling Hamiltonian between the qubit and the environment. The coupling to the environment comes in the form of current or voltages induced by the noise source. Commonly, $|\langle j|\mathscr{O}|i\rangle|^2 = -\varphi_0^2|\langle j|\hat{\varphi} I_{\text{env}}|i\rangle|^2$; representing the noise as a voltage source would be completely equivalent.

The qubit can be excited or deexcited with the ratio of the rates given as the statistical quantity:

$$\frac{\Gamma_{01}}{\Gamma_{10}} = \frac{S_x[-\omega_{01}]}{S_x[\omega_{01}]} = e^{-\hbar\omega_{01}/k_B T} \ . \tag{3.35}$$

Where T is the effective temperature of the qubit coupled to the environmental thermal bath at thermal equilibrium. The spectral density of a current noise produced by a wire in the quantum regime shows the asymmetry to the excitation/relaxation spectral density effectively by suppressing excitation when the frequency is much less than the thermal energy. This process can be represented by a parallel addition of the decay rate of the atom being excited (0 to 1) or deexcited (1 to 0) represented as:

$$1/T_1 = \Gamma_{01} + \Gamma_{10} \ . \tag{3.36}$$

Common sources of energy relaxation in SCQC include capacitive loss, inductive loss, and relaxation into the environment. The way to quantify each decay channel follows the procedure of representing each reactive element as having both real and imaginary permittivity/permeability and is covered in depth in the later chapters.

3.4.6 T_2

Low-frequency noise in various forms is the main cause of dephasing which creates a slowly varying qubit transition frequency [104]. Normally slow variations to an external control knob are the source that can cause the qubit frequency to jitter [70]. Having the read-out frequency jitter can also contribute to dephasing mechanisms since this in turn causes the qubit frequency to jitter. These processes are represented in the two-level system as a generic Hamiltonian:

$$\mathscr{H}_{\mathrm{TLS}} = \frac{\omega_q}{2}\hat{\sigma}_z + \frac{1}{2}V_z\hat{\sigma}_z \,. \tag{3.37}$$

Where the qubit now couples to a noise source that has off-diagonal contributions to the qubit state also known as transverse coupling. This fluctuating noise V_z causes the transition frequencies of the qubit to shift and effectively causes the phase to accumulate in a none coherent manner. The additional phase accumulated between the two states over a time t:

$$\phi_z = \int_0^t V_z(t')dt' \,. \tag{3.38}$$

Due to the natural 1/f quality of the spectral densities considered, the low-frequency variations, on the time scale of measurement, have the largest contribution. In the absence of qubit relaxation the qubit would undergo pure dephasing in a time:

$$T_\phi = \frac{2}{S_Z[\omega = 0]} \tag{3.39}$$

. But due to the unavoidable presence of relaxation the experimental quantity measurable is the decoherence time T_2.

The actual measurement of T_2^* was already discussed but understanding how the decay time constant is produced can help illustrate what decoherence measurements represent. Consider a noise source that perturbs the qubit transition frequency by $\delta\omega$. Two traces are taken in this measurement and are averaged together such that trace 1 has $\delta\omega = 0$ and trace 2 has $\delta\omega = \theta$. Then the measurement would average to a population in the

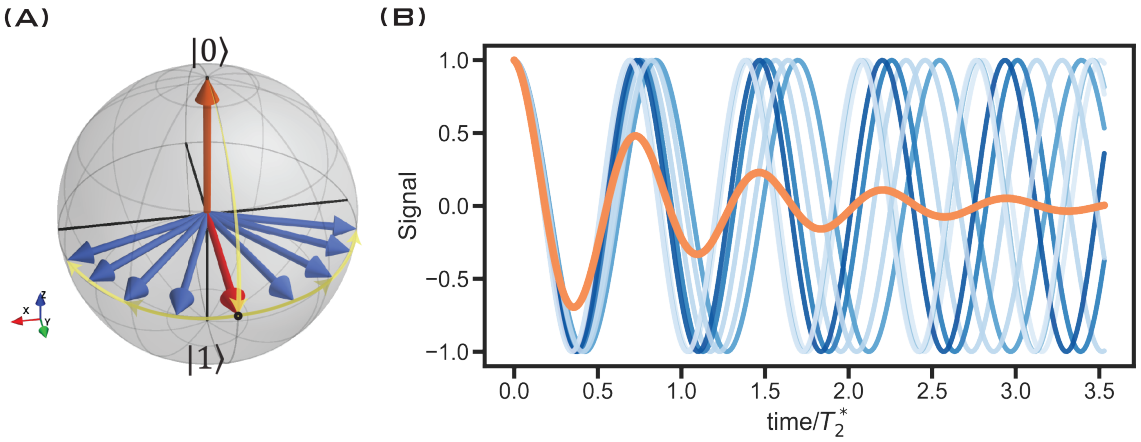

Figure 3.11: (A) The state on the Bloch sphere is prepared onto the equator where noise causes the vector to rotate around the z-axis. The noise is random in nature and each measurement will have a different accumulation of phase. (B) The measurement consists of many average traces (shown in blue) which lose phase coherence as the time between qubit rotations is increased. This causes the curve to have a decay envelope. The quantum state decays to the middle of the Bloch sphere at long times.

ground state as:

$$\begin{aligned} p_0(t) &= \frac{1}{2}\left\{\frac{1}{2}\{1-\cos(\delta t)\}+\frac{1}{2}\{1-\cos(\delta t-\theta)\}\right\} \\ &= \frac{1}{2}\left\{1-\cos(\delta t-\theta/2)\cos(\theta/2)\right\} \end{aligned} . \tag{3.40}$$

This example shows the amplitude of the signal is changed by $\cos(\theta/2)$ which is caused by a slightly modified qubit transition frequency. When many traces are averaged together then at large times, the oscillating signal decays to $p_0 = 1/2$ where the phase of the states becomes completely unresolvable. On the Bloch sphere, $p_0 = p_1 = 1/2$ is a point at the very center where the coordinates are $(x,y,z) = (0,0,0)$.

Another type of T_2 measurement can be performed by applying a π-pulse between the two $\pi/2$ pulses. The added π-pulse shifts the noise frequency window to higher values and are used as a "refocusing" technique acting to undo the accumulated phase and, this acts as a protective protocol. This measurement technique is called Hanh-echo or T_2^E. The measured signal decays exponentially, in this case, to the middle of the Bloch sphere and is

fit to the equation:

$$\mathrm{f}(t_i) = A_0 + A_1 e^{-t_i/T_2^E} \tag{3.41}$$

where A_0, A_1, A_2, T_2^E are fit parameters where T_2^E is the decay constant of the excited state of the qubit. This protective protocol can be extended to adding more *pi* pulses between the two $\pi/2$ pulses [22].

The line width of the qubit signal in two-tone spectroscopy can also indicate a ball park estimate of the value for T_2. The line width κ_q of the qubit transition is inversely proportional to T_2 such that $\kappa_q \sim 1/\pi T_2$ [1, 104].

4

Josephson junction transmission lines

"Don't reinvent the wheel, just realign it."
— Anthony J. D'Angelo

Ultra-high impedance SCQC requires inductance far exceeding the standard geometrical inductance of a conventional wire while also maintaining minimal stray capacitance. In this chapter, we first discuss why a conventional wire, with aspect ratios similar to JJ chains, are unable to achieve $Z > R_Q$ in the GHz frequency range. The kinetic inductance of Cooper pairs is introduced which is the key to substantially increasing the total inductance of a wire. The discussion shifts next to JJ wires and the characterization of their electrical properties. Finally, we discuss how to create ultra-high impedance JJ transmission lines by minimizing the stray capacitance (capacitance to ground). The results show conclusively that JJ transmission lines with $Z_\infty \gg R_Q \sim 25.8$ kΩ are possible while still remaining well into the superconducting state for GHz range frequency signals.

4.1 Introduction

Transmission line resonators can be described as a classical telegraphers line [54]. The circuit is represented as a series of LC oscillators each with

a single unit cell (Δx) represented as an inductance $\Delta x \cdot l$ and a capacitance $\Delta x \cdot c$ as seen in figure 4.1 B. The total length of the wire is $X = \Delta x \cdot N$ with l and c the inductance per unit cell and capacitance per unit cell, respectively. In the analysis, each cell is treated as identical with exactly the same inductance and capacitance – void of any disorder. The transmission line under investigation is a single wire which is bent at the halfway point. This geometry creates electrostatic coupling between adjacent parts of the wire which is represented as the capacitance between unit cells directly across from one another; this capacitance is called the ground capacitance.

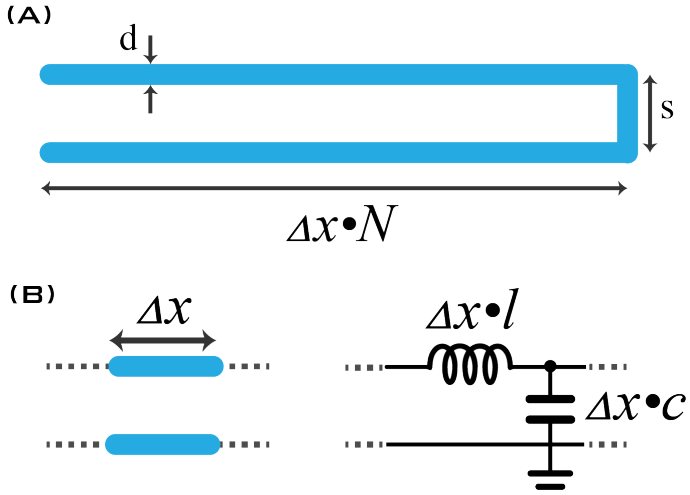

Figure 4.1: (A) A telegrapher transmission line made of a single wire which is folded at the midpoint. This configuration creates open-short boundary conditions. (B) The transmission line can be approximated as discrete unit cells which each has a specific inductance and capacitance.

Disregarding dispersive effects for the moment, many standing modes will emerge when solving the basic wave equations of a lossless transmission line using the fundamental voltage and current laws; in this introduction, we only consider the differential modes. When the transmission line has open-short boundary condition the voltage and current are found as a sum of an incoming wave and a reflected wave [151]:

$$\begin{aligned} V_x &= V_0(e^{ikx} - e^{-ikx}) \\ I_x &= \frac{V_0}{Z_\infty}(e^{ikx} + e^{-ikx}) \end{aligned} \quad . \tag{4.1}$$

These modes are dependent on the length, using the expression for the impedance at x=-X and dividing voltage by current:

$$Z(x) = \frac{V_x}{I_x} = Z_\infty \frac{e^{-ikX} - e^{ikX}}{e^{ikX} + e^{-ikX}} = -iZ_\infty \tan(kX) \ . \tag{4.2}$$

Solutions emerge in this case when $k = \frac{\pi}{2X} + \frac{n\pi}{X}$ while also defining the characteristic impedance is defined as $Z_\infty = \sqrt{2l/c}$. The geometrically constrained variable k is known as the wavenumber which fulfills the boundary constraints of the circuit; the variable n is an integer-valued variable indexing the number of modes and ranges from 0 to 2N.

Furthermore n resonate modes exist and are defined as: $\omega_n = v(\frac{\pi}{2X} + \frac{n\pi}{X})$, where v is the speed of light in the transmission line. The speed of light can be redefined as $v = \Delta x/\sqrt{2lc}$ and makes the expression for the standing modes resonance become:

$$\omega_n = \frac{1}{\sqrt{2lc}} \left(\frac{\pi}{2N} + \frac{n\pi}{N} \right) \ . \tag{4.3}$$

When the product of the wavenumber and the total length (kX) increases, the impedance of a transmission line grows faster than a lumped element inductor to the point where the impedance diverges at the first fundamental mode of the resonator (when $kX = \frac{\pi}{2}$). This condition is exactly the behavior of the resonant mode of an LC-oscillator and exists for all k values which make $Z(\omega)$ diverge. This standard result demonstrates the impedance of a transmission line resonator is frequency dependent and behaves as an inductance approximately up to the first fundamental mode. The line impedance, $Z(\omega) \approx -iZ_\infty kX = -i\omega L$ which is exactly the expression for the lumped-element inductance. The transmission line resonances can be thought of as distributed modes that contain the collective behavior of all lumped elements in the system. The number of resonant modes in a transmission line is the same as the number of lumped elements involved within the model. If there are many modes then the lumped element model is sufficient for the large wavelengths compared to a single unit cell.

4.2 Transmission line resonators

When a transmission line is created from a normal wire with geometrical inductance in the specific transmission line configuration shown in figure 4.1, it becomes apparent the impedance is limited to the order of the vacuum impedance. This is a consequence due to the inductance and capacitance scaling proportionally and inversely proportionally with the total length of the wire, respectively. This scaling effectively negates one another when attempting to increase the impedance and becomes a dilemma for any microwave engineer who desires to create high-impedance transmission lines that present R_Q at GHz frequency.

To illustrate this point let's examine two wires shorted at one end while separated by a distance s with a diameter d. This conventional transmission line has inductance per unit length and capacitance per unit length defined as [151]:

$$\begin{aligned} \frac{L}{N\Delta x} &= \frac{\mu_0}{\pi} ln(s/d) \\ \frac{C}{N\Delta x} &= \frac{\pi\varepsilon_0\varepsilon_r}{ln(s/d)} \end{aligned} \quad . \tag{4.4}$$

The results for specific inductance and capacitance produce the characteristic impedance:

$$Z_\infty = \sqrt{\frac{L}{C}} = \frac{ln(s/d)}{\pi}\sqrt{\frac{\mu_0}{\varepsilon_0\varepsilon_r}} \, . \tag{4.5}$$

The equations show the total inductance and total capacitance wire length scaling cancel and are left with a weak logarithmic dependence on the separation and diameter of the wire. The characteristic impedance then is always on the order of $Z_\infty = \sqrt{\mu_0/\varepsilon_0} \approx 377\Omega$, only to be reduced further by having a dielectric material with $\varepsilon_r > 1$ present. Conclusively, we see to achieve characteristic impedance greater than R_Q there is a need to destroy the scaling dilemma; which has multiple engineering solutions in fact.

One such solution is to harness a new contribution to the inductance which is much more than the geometrical inductance of a wire in this configuration and is called "kinetic" inductance. Another solution would be to

reduce the capacitance of the wire to the minimal value possible. Naively it is often thought this solution is readily available by just moving the adjacent wires far apart but this has a weak logarithmic dependence which barely increases the characteristic impedance. In fact, the separation necessary to achieve $Z_\infty \sim R_Q$ is much larger than the wavelength which means the line would lose energy by radiating at ω_0 and would again lead to $Z_\infty \sim Z_{\text{vac}}$ when $\omega \to \omega_0$ [114]. Interestingly, there is another way to produce $Z_\infty \sim R_Q$ by using nano-fabricated geometrical coiled wires [145]. The results in [145] prove a coiled wire with a diameter and separation of less than 300 nm on a perforated silicon substrate only 3 μm thick produces an impedance greater than the resistance quantum almost entirely from the geometric inductance created by tightly spiraling the wire.

4.3 Kinetic inductance

The way around the dilemma presented in the last section is commonly addressed by creating the transmission line out of an inductance that does not rely on the geometrical inductance alone and instead harnesses the power of kinetic inductance.

For a wire of cross-sectional area A and electron density ρ the kinetic inductance of normal electrons with charge e and mass m have energy stored in their inertia given by:

$$L_{\text{kinetic}} = \frac{m}{e^2 \rho} \frac{1}{A} \, . \tag{4.6}$$

However, electrons in normal conductors collide in short time scales too soon for L_{kinetic} to have any significant impacts for frequencies below the THz range. This issue is remedied in a superconductor; the story changes since the time before a collision, $\tau \to \infty$. The expression for kinetic inductance associated with Cooper pairs is modified since now the charge carriers are pairs of electrons where the new expression becomes [2, 175]:

$$L_{\text{kinetic}} = \frac{2m}{4e^2 \rho} \frac{1}{A} = \frac{\hbar R_{\text{sheet}}}{1.74 \pi k_B T_C} \, . \tag{4.7}$$

This equation demonstrates large kinetic inductance is present in disordered

superconductors whose normal resistance is large. A further enhancement arises from the suppression of T_C, both properties exclusively present in "dirty" superconducting wires such as TiN or grAl [64, 127]. In another view, the Cooper pair density (ρ) is suppressed yet to support the same amount of supercurrent fewer charge carriers are present therefore the kinetic inductance must be enhanced.

Likewise, a synthetically disordered superconductor made out of a chain of JJs can be utilized, where the order parameter (or the density of Cooper pairs) becomes reduced in the oxide layer between the two superconducting leads. The wire is then constructed from a chain of JJs which is called a superinductance [114, 123].

When the area of the JJs in the array is large enough, such that the current passing through them is much less than the critical current values, the equation for Josephson inductance, L_J, becomes linearized. For typical JJ in arrays used throughout this thesis, the critical current values are in the range of several tens of nA putting the inductance for a single junction on the order of 1 - 10 nH. The linear Josephson inductance expression per single chain junction becomes:

$$L_J^A \approx \frac{\Phi_0}{2\pi I_c^A} \approx 1 - 10 \text{ nH} \approx 1 - 10 \times 10^4 \mu_0 \ . \tag{4.8}$$

Furthermore, the capability to fabricate compact-large area JJ arrays with unit cells reaching as small as 350 nm/junction is possible; creating an inductance per μm in the range of tens of nH.

To summarize, we can directly compare JJ arrays and conventional wires in the transmission line geometry described. Assuming both capacitances of the conventional and JJ wires scale the same way, only the inductance/length of the wire needs to be considered. The geometrical transmission line has inductance limited to roughly the vacuum permeability, $\mu_0 = 1\ \mu$ H/meter while a JJ chain has about $L_{\text{tot}}^A \approx 10$ mH/meter; meaning we are increasing the inductance per unit length by around a factor of 10^4 times; conclusively proving the advantage of the JJ array which utilizes kinetic inductance to for achieving $Z_\infty > R_Q$.

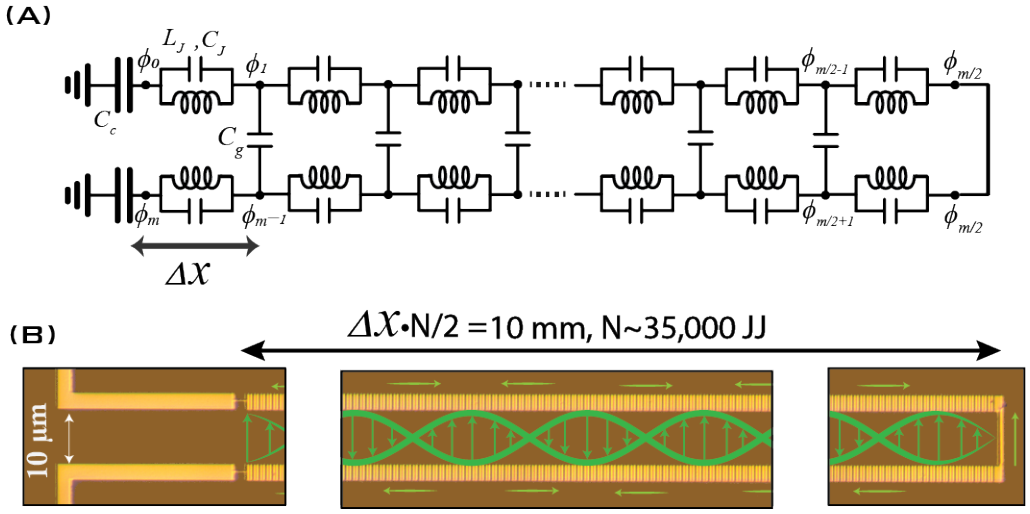

Figure 4.2: (A) The discrete lumped element circuit representation of a JJ transmission line. The superconducting island phase ϕ is the degree of freedom. The transmission line is coupled to an external signal by a capacitance C_c and has capacitive coupling between adjacent JJ stripes C_g. (B) An optical image of a JJ transmission line device that hosts a differential standing mode between the two JJ arrays is shown in green. A current flows along the JJ wire while a differential voltage is created between the two stripes.

4.4 Josephson Junction transmission lines

The Josephson junction transmission line is comprised of thousands of JJ connected in series where the total length (X) of the line is given by the unit cell ($\Delta x = a$) times one-half the total number of junctions ($N/2$). Each unit cell is exactly one junction and includes the junctions self-capacitance C_J and the junctions capacitance to ground C_g. The unit cell can be thought of as the smallest dimension in the system where each cell is an individual oscillator with a plasma frequency $\omega_p = 2\pi\sqrt{8E_J E_{C_J}} = 1/\sqrt{L_J C_J}$. Similar systems have also been explored using JJ which exhibits flux-tunable E_J [152, 187].

The electrostatic capacitive coupling of each unit cell to the one directly across from itself is what is defined as C_g. This coupling capacitance gives rise to differential standing modes in the array. The differential modes are excited by external signals coupled to the device by the capacitance C_c at the open end. Each junction has superconducting islands on either side with the degree of freedom ϕ_m for the mth island.

The boundary conditions of the JJ transmission lines, first considered, are open-closed where the open end has the coupling antenna and the other is shorted by a superconducting connection. Since there are N oscillators in our system, in theory, it can support up to N standing modes. Experimentally, up to the first one hundred modes or so are usually.

4.5 Spectroscopy

JJ transmission lines are first characterized by measuring S_{11} of the sample inside the 3D waveguide. This most basic measurement of reflected signal enables the resonant frequencies within the bandpass to be measured and extracted. Two-tone spectroscopy is utilized for frequencies above and be-

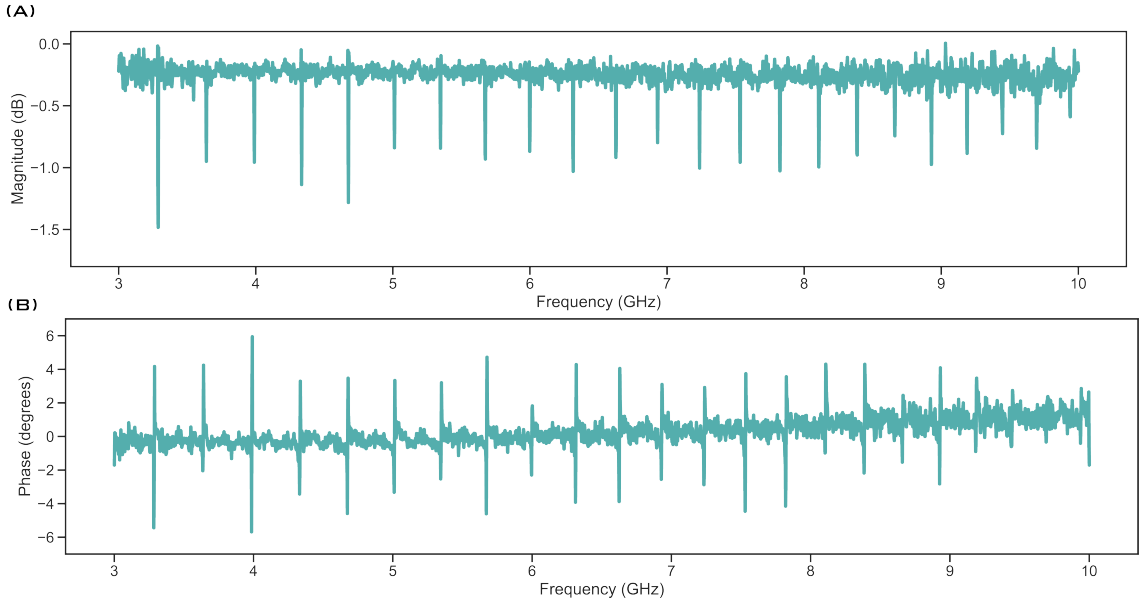

Figure 4.3: One-tone spectroscopy of a device demonstrating the calibrated magnitude in (A) and phase is shown in (B). Each magnitude dip is a standing wave mode resonance supported by the JJ waveguide.

low the waveguide bandpass to overcome the inability to measure the modes in single-tone spectroscopy due to a diminishing probe signal strength. Two-tone spectroscopy in the waveguide is possible due to the weak non-linearity present in the array JJs. The quartic term in the expansion of the Josephson potential creates a cross-Kerr interaction between different modes. The photons in the pumped tone (n_j, f_j) create a shift of the resonant frequency in

the measured tone (f_i) [98, 103, 187]:

$$\delta f_i \approx n_j \frac{f_i f_j}{N E_J} \ . \tag{4.9}$$

The dispersive shift of the measure mode is used as the signal. Using this technique, we are capable to probe all standing modes ranging from about 100 MHz - 18 GHz.

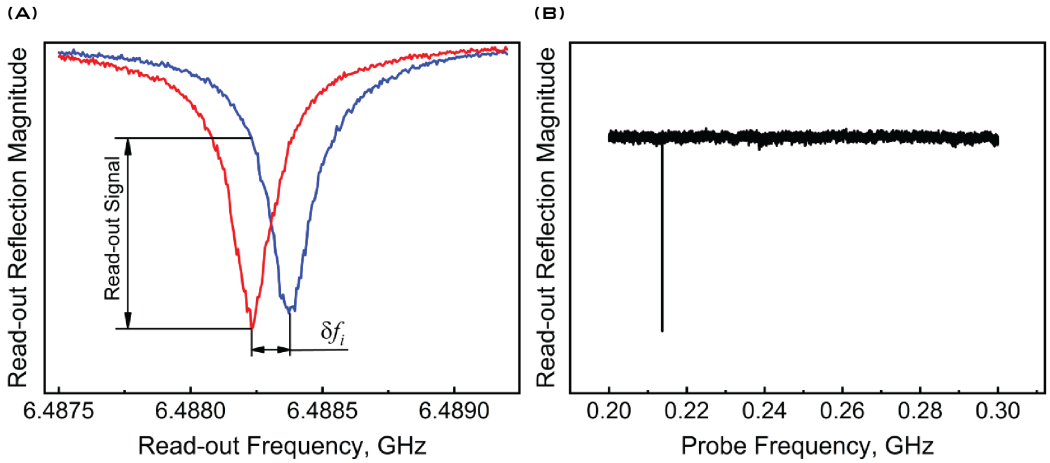

Figure 4.4: (A) The red dip is the read-out mode while the probe tone is on resonance while the blue dip is the probe tone off-resonance with a standing wave mode at 215 MHz. (B) The resulting read-out reflection magnitude versus the probe frequency. The sharp dip indicates the dispersive shift of the read-out resonance caused by the cross- Kerr effect.

4.6 Extracting transmission line parameters

Once measuring all transmission line modes possible via one- and two-tone spectroscopy, the resonance frequencies are extracted and fit to the mode dispersion model [63, 103, 126]:

$$\omega(k_n) = \frac{vk}{\sqrt{1+\left(\frac{vk}{\omega_p}\right)^2}} = \frac{2ka\sqrt{E_J E_{C_g}}}{\sqrt{1+k^2a^2\frac{E_{C_g}}{2E_{C_J}}}} \tag{4.10}$$

where v is the velocity of light and k is the wavenumber each defined in this system as:

$$\begin{aligned} v &= \frac{a}{\sqrt{2L_J C_g}} = 2a\sqrt{E_J E_{C_g}} \\ k_n &= \frac{\pi}{2X}(2n+1) = \frac{\pi}{Na}(2n+1) \end{aligned} \quad . \tag{4.11}$$

The dispersion of the modes at low frequency is linear with $\omega(k_n) \approx vk$. While at higher frequencies the dispersion relation is no longer linear and experiences a cut-off at the plasma frequency. The modes approaching the plasma frequency begin to bunch together where the increase of the mode density is noticeable. The mode dispersion is fit using v and ω_p as the fit parameters with equation 4.10. The fit results can be made into junction parameters by the following relations:

$$\begin{aligned} L_J \times C_J &= 1/\omega_p^2 \\ L_J \times C_g &= a^2/2v^2 \end{aligned} \tag{4.12}$$

where we fit assuming a consistent value of $C_J = 45$ fF/μm^2 while knowing the area of the junctions in the array. This assumption is validated by extensive SEM imaging of devices to extract the areas of the JJ in the array. Taking the ratio of the two products, while knowing the unit cell precisely and assuming C_J, the parameter C_g is extracted by using the ratio $(\frac{v}{a\omega_p})^2 = \frac{C_J}{2C_g}$. While the inductance per junction is found by the ratio $L_J = \frac{1}{C_J}(\frac{2\pi}{\omega_p})^2$.

Another parameter extraction technique based on the spectroscopy of the standing modes is using the density of states (DOS) defined as [102]:

$$\rho(\omega) = \frac{1}{2\pi v(1-(\omega/\omega_p)^2)^{3/2}} \ . \tag{4.13}$$

Fitting to DOS has the advantage of not having to perfectly index the modes since this expression does not depend on the wavevector k.

The wave impedance (Z_∞) of the transmission line can then be found

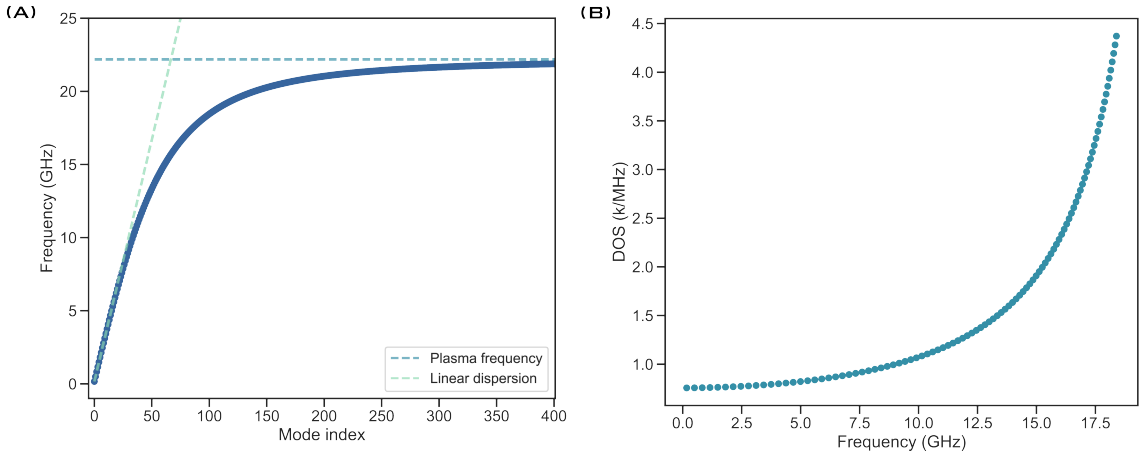

Figure 4.5: (A) The dispersion relation of the JJ transmission line is shown as a function of the mode index. The dispersion relation is first linear but as the mode frequencies become closer to the plasma frequency of the junctions the modes become bunched. The plasma frequency acts as the cut-off of higher frequency modes and causes the mode space to significantly decrease. (B) The density of states (DOS) shows the modes become spaced occurring in increasingly smaller intervals.

using the extracted parameters and is defined as:

$$Z_\infty = \sqrt{\frac{2L_J}{C_g}} = \frac{2R_Q}{\pi}\sqrt{\frac{E_{C_g}}{E_J}}\,. \tag{4.14}$$

The measurements in the first experiment were on samples where the impedance of the JJ transmission line was scaled by changing the area of the individual JJs. The samples area ranged from $3\mu\text{m} \times 0.4\mu\text{m}$ to $0.25\mu\text{m} \times 0.4\mu\text{m}$, shown in figure 4.6 (A,G). In some cases, the unit cell was decreased from 600 nm to 350 nm, a comparison is shown in figure 4.6 (C,D).

Logging the plasma frequency of each device can help establish consistency of the fabrication process. The experimental value found for the plasma frequency of the JJ in the array by the aforementioned fitting procedure is more or less the average plasma frequency across all of the array junctions. The plasma frequency has been observed to also evolve depending on the age of the sample and how long the device is left in ambient conditions. Over time the oxide becomes more opaque and more opaque the longer the junction is left in atmospheric conditions. The plasma fre-

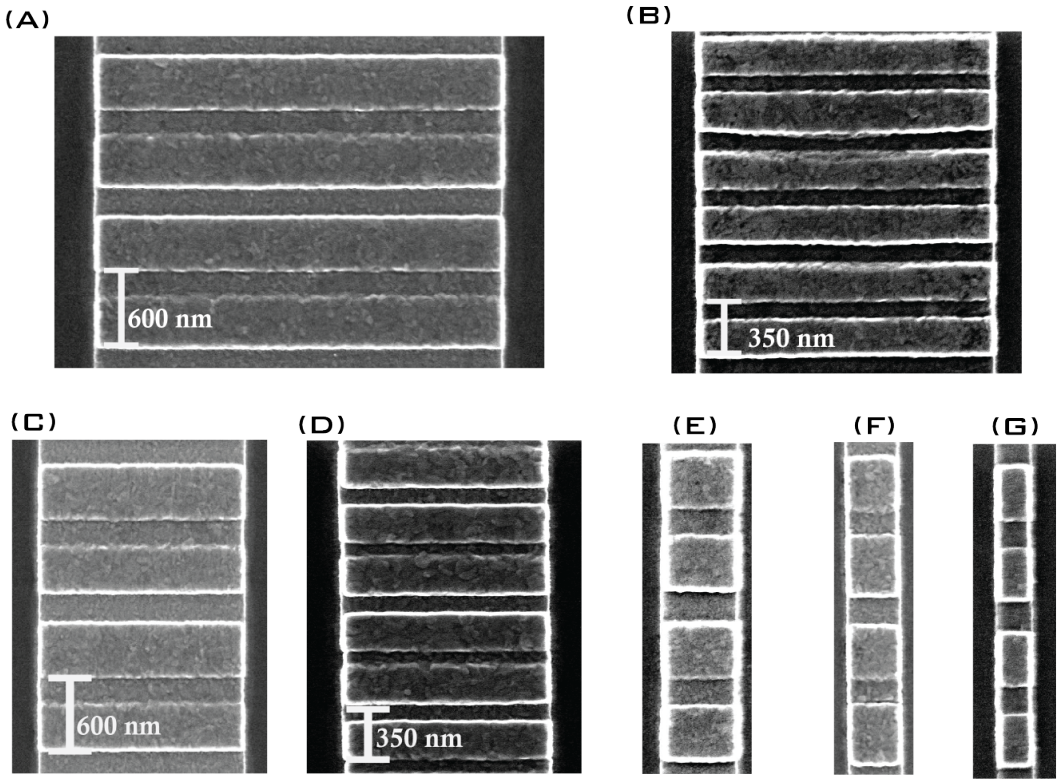

Figure 4.6: SEM images of the variety of JJ arrays with different areas. The images only show a few junctions that were a part of the mm-long junction arrays. Each image is approximately scaled with respect to one; (C) compared to (D) demonstrates reducing the unit cell to change the impedance. While (A,C,E,F,G) demonstrate changing the width of the junctions to change the impedance.

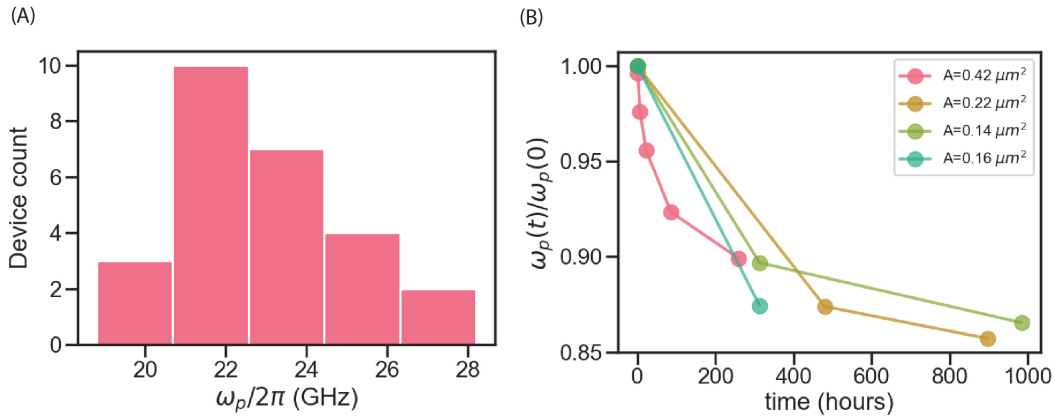

Figure 4.7: (A) The different plasma frequencies measured for JJ arrays. (B) The evolution of the plasma frequency as the device ages. The plasma frequency appears to decrease to around 85% of the original value.

quency of our devices are consistently between 20 - 27 GHz with 23 GHz being the most occurring. The device's plasma frequency decreases with time; apparently down to $\approx 85\%$ of the original value. Shown in figure 4.7(B) are the aging plasma frequencies for JJ transmission lines made with different areas A and measured several times after creation.

The collection of samples measured in [103] is summarized in table 4.6. Devices a-f have the chains separated by 10μm with only the area (E_J/E_{C_J}) modified. Devices g-i have the separation between the two chains modified to smaller values. Characteristic impedance ranges from 7-23 kΩ. The largest impedance device has JJs with $E_J/E_C = 7$. This ratio's low value has measurable consequences revealed through fitting each mode's quality factor.

	$\omega_p/2\pi$(GHz)	$v(\times 10^6$ m$/s)$	$Z_\infty(\mathrm{k}\Omega)$	E_J/E_{C_J}	$\sqrt{E_{C_g}/E_{C_J}}$
a	23.8	1.28	17.0	20.2	20.2
b	20.8	1.12	19.0	15.8	20.2
c	22.3	1.16	21.3	11.3	19.4
d	20	1.04	23.1	9.3	19.4
e	19.3	0.99	23.6	8.7	19.3
f	20.8	0.83	19.0	7	15
g	27.0	2.76	7.4	440	38.4
h	24.8	1.88	12.6	80	28.4
i	22.3	1.68	13.8	65	28.2

4.7 Quality factors

Each resonance measured in one tone can be fit to the expression for reflection:

$$S_{11}(\omega) = \frac{2i(\omega-\omega_0)/\omega_0 - Q_{\text{ext}}^{-1} + Q_{\text{int}}^{-1}}{2i(\omega-\omega_0)/\omega_0 + Q_{\text{ext}}^{-1} + Q_{\text{int}}^{-1}} \,. \tag{4.15}$$

This expression for S_{11} is a complex number where the signal plotted in the complex plane traces out a circle $\mathrm{Re}[S_{11}] + i\ \mathrm{Im}[S_{11}]$ when the microwave tone traces through the mode frequency. The magnitude and the phase of the signal along with the circle in the complex plane can be fit to the collected data in order to extract the resonance frequencies, internal quality factors, and external quality factors of each mode.

The measurement of Q-factors across different area devices indicates larger area JJ with $E_J/E_{C_J} > 20$ have Q_{int} which decrease with increasing mode frequency (sample a and b in figure 4.9)indicating dielectric loss as the main limiting mechanism. Modeling the junction capacitance (C_J) as a lossy dielectric gives the expression [126]:

$$Q_{\text{int}}(\omega) = 2Q_{\text{cap}}\frac{\omega_p}{\omega}\left(1-\left(\frac{\omega_p}{\omega}\right)^2\right) . \tag{4.16}$$

The fit value for Q_{cap} is on the order of $10^3 - 10^4$ which is consistent with other experimental values found in [66, 140].

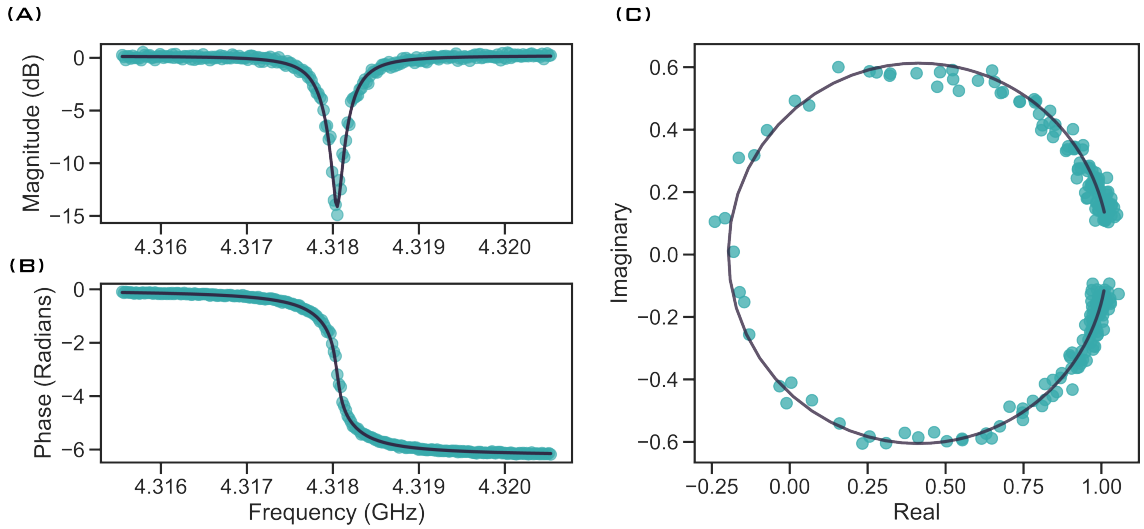

Figure 4.8: The quality factors of the modes are extracted by fitting the magnitude and phase of the reflected signal. The signal is also fit in the real and imaginary plane; in this case, a resonance creates a circle.

While the modes with smaller ratios of E_J/E_{C_J} have broadened linewidths and have lower Q_{int} which at first are frequency independent (sample c in figure 4.9) and further reducing the $E_J/E_{C_J} < 10$, the Q_{int} begins to increase with mode frequency (sample e and f in figure 4.9). The loss mechanism's dependence on mode frequency appears to be due to phase slips among the junctions in the array. The Q_{ext} dependence is more or less independent on E_J/E_{C_J} and only depends on the size of the coupling antenna and the position where the sample is located inside the 3D box. The slight increase in the external quality factor is most likely due to the increase in impedance which causes signal reflection from the extreme impedance mismatch.

This study concludes, tuning E_J/E_{C_J} to increase the impedance of the array of junctions while maintaining low loss has a limit given approximately by the ratio $E_J/E_{C_J} \sim 20$ and $Z_\infty \sim 16\,\text{k}\Omega$. To further increase the impedance of the line with sufficiently large enough E_J/E_{C_J} other techniques must be explored.

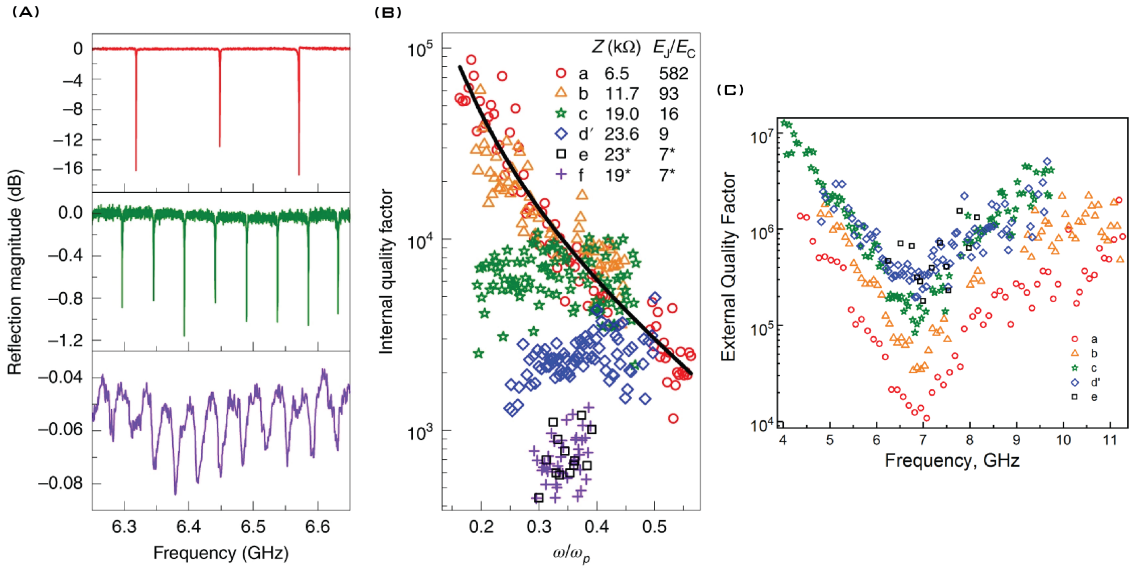

Figure 4.9: Reproduction from [103]. (A) The linewidth of the standing modes increase as E_J/E_{C_J} decreases. The red plot trace is for $E_J/E_{C_J} = 582$ while the purple trace is for $E_J/E_{C_J} = 7$. (B) The internal quality factor as a function of normalized mode frequency. Large ratio of E_J/E_{C_J} shows a decreasing Q_{int} with increasing mode frequency. The black line is a best-fit line for the expected Q_{int} limited by dielectric loss. This trend disappears for devices that have $E_J/E_{C_J} < 20$ indicating a new loss mechanism dominating at lower modes. (C) The Q_{ext} versus mode frequency across measured devices are more or less consistent.

4.8 Increasing characteristic impedance by etching

The technique used to further increase Z_∞ presented in this section is to consider modifying the capacitance between the two adjacent JJ chains by selectively etching the silicon substrate away. The goal is to quantify how much C_g can be reduced while maintaining the same quality factor mode dependence for $E_J/E_{C_J} > 20$. Through basic electrostatics, we can conclude the permittivity of the dielectric substrate unnecessarily enhances C_g by the electric fields in the Si substrate [87]; which is a consequence due to the relative permittivity (ε_r) being around an order of magnitude larger than the vacuum permittivity for conventional silicon and sapphire substrates. Due to the larger-than-vacuum permittivity, the substrate enhances the electric field between the two stripes and enlarges the differential capacitance.

Earlier when considering the classic two-wire transmission line we derived the results which show the capacitance reduces very slowly ($\sim 1/\ln(s)$) when increasing the wire separation so this appears as an impractical solution. Plus the separation should not be so large that the electrostatic capacitive coupling between the two stripes becomes so weak that the differential modes are no longer viable.

With this limitation in mind, an anisotropic dry etch which removes the silicon substrate between and around the device is used. The dry etching technique utilizes the following chemical process:

$$4\mathrm{SF}_6 + 6\mathrm{Si} \rightarrow 4\mathrm{S} + 6\mathrm{SiF}_4 \ . \tag{4.17}$$

After etching the sample is still attached to the substrate but is suspended on top of mesas or pillars which sit several micrometers above the Si substrate.

To get an intuition and understand how etching impacts the coupling between the two adjacent JJ stripes a simulation was performed using ANSYS Maxwell 3D finite element analysis to find the differential capacitance per unit length of the stripes depending on the depth and width of the etched silicon trenches. As a sanity check, we also used an analytic solution which is found for 2D planar coupled stripes [176]. The simulation results are compared to the analytic method for the normal substrate conditions and when the substrate is completely removed (figure 4.10).

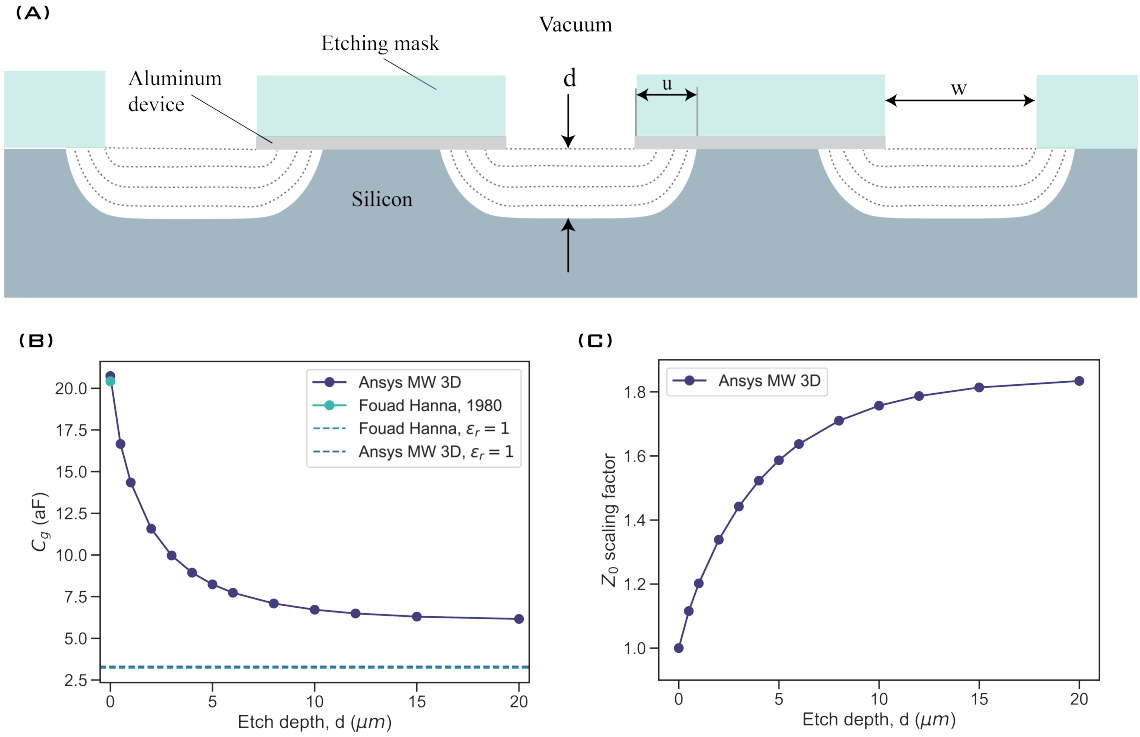

Figure 4.10: (A) The schematic showing the selective etching technique using SF_6. The etching mask is layers of MMA with a thin layer of $\sim$ 10 nm of aluminum deposited on top. The areas where the mask was patterned using e-beam lithography are etched away. (B) Finite element analysis simulation results showing how C_g scales with etching depth. The structure in (A) is simulated for a finite length of wire where the etch depth d is changed. The results are compared to the analytical solution for used for 2D planar coupled stripes [176] with and without the dielectric present. (C) The impedance scaling factor is inferred from the simulation. Etching the trenches can scale the impedance by roughly a factor of 1.8.

4.9 Unetched versus Etched comparison

To properly understand the effects of etching, we characterize a sample before and after the dry etching technique. The sample is probed by wire-bonding the leads directly to a sample box instead of having the sample capacitively coupled to a 3D waveguide like what was done in the measurements discussed in the previous sections. This way the sample can be probed using both RF and DC measurement techniques exclusively or together at the same time.

The sample has one lead directly wire-bonded to the input pin while the other lead is wire-bonded directly to the copper box which is ground. The sample under study is 2 mm long and has unit cells of 400 nm per junction putting a total number of 10,000 JJ in series. The JJs have an area of 1.5 μm by 0.25 μm designed specifically for a large enough E_J/E_{C_J} to avoid quantum phase-slips in the array. Using microwave spectroscopy the spectrum of the unetched device was measured. The modes are fit to the dispersion and DOS expressions to extract an $E_J/E_{C_J} = 56 \pm 2$ with a characteristic impedance $Z_\infty = 16.37 \pm 0.38$ kΩ.

The same device is then selectively etched to create trenches between and on both sides of the array with trench width w = 10 μm and a depth d=$\sim 5\mu$m. Using the same microwave spectroscopy technique as the unetched version, the modes were again extracted and fit using the dispersion and DOS expressions. The etched version had an $E_J/E_{C_J} = 42 \pm 2$ with a characteristic impedance $Z_\infty = 24.81 \pm 0.27k\Omega$. The etched device's impedance increased by a factor of 1.52 while maintaining $E_J/E_{C_J} > 20$.

	$\omega_p/2\pi$(GHz)	L_J (nH)	C_g (aF)	Z_∞(kΩ)	E_J/E_{C_J}
Unetched	23.22±0.23	2.53±0.05	18.88 ± 0.42	16.37 ± 0.38	56 ± 2
Etched	20.09± 0.21	3.36± 0.03	10.91± 0.17	24.81 ± 0.27	42 ± 3

The Q_{int} is found to decrease with increasing frequency for both samples indicating dielectric loss as the main source contributing to the measured internal quality factor. The $Q_{\text{int}} \sim 10^4$ for the first measurable modes in one-

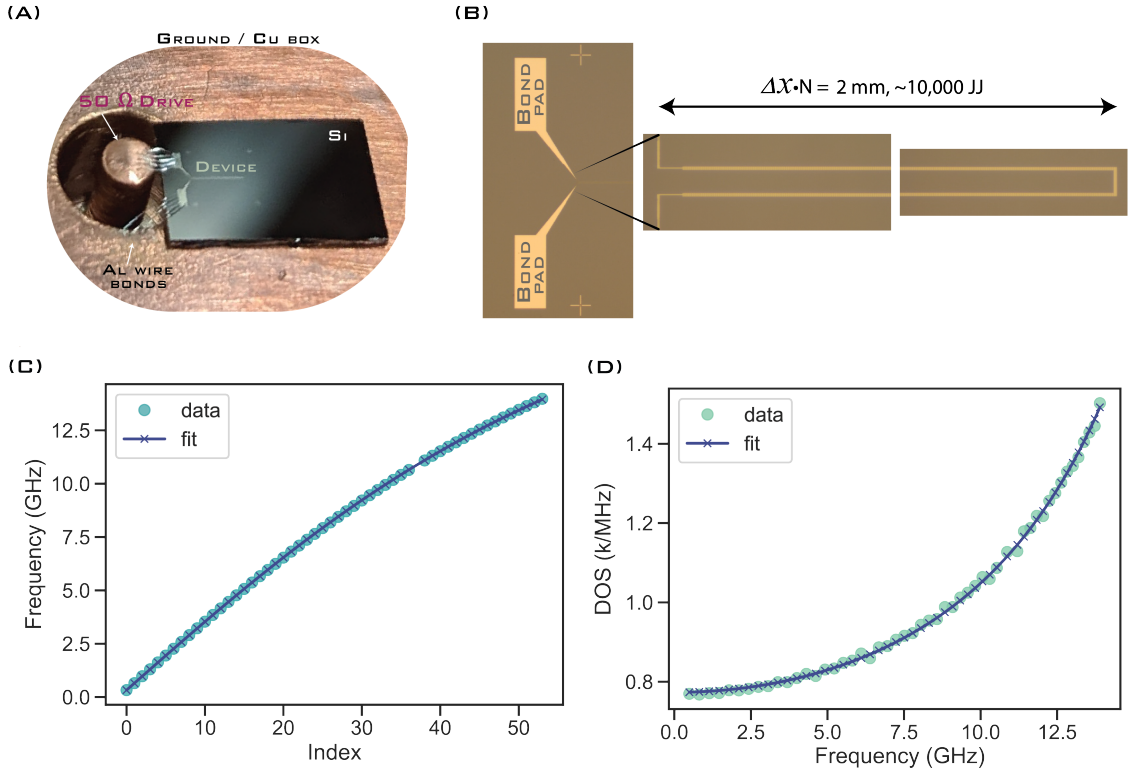

Figure 4.11: (A) The *unetched* JJ waveguide sample wire bonded to the 50 Ω drive pin and to the Cu box. (B) An optical image zoom-in on the unetched device. (C) The dispersion and (D) the DOS of the JJ waveguide modes extracted from microwave measurements. In both (C) and (D) the fits are superimposed.

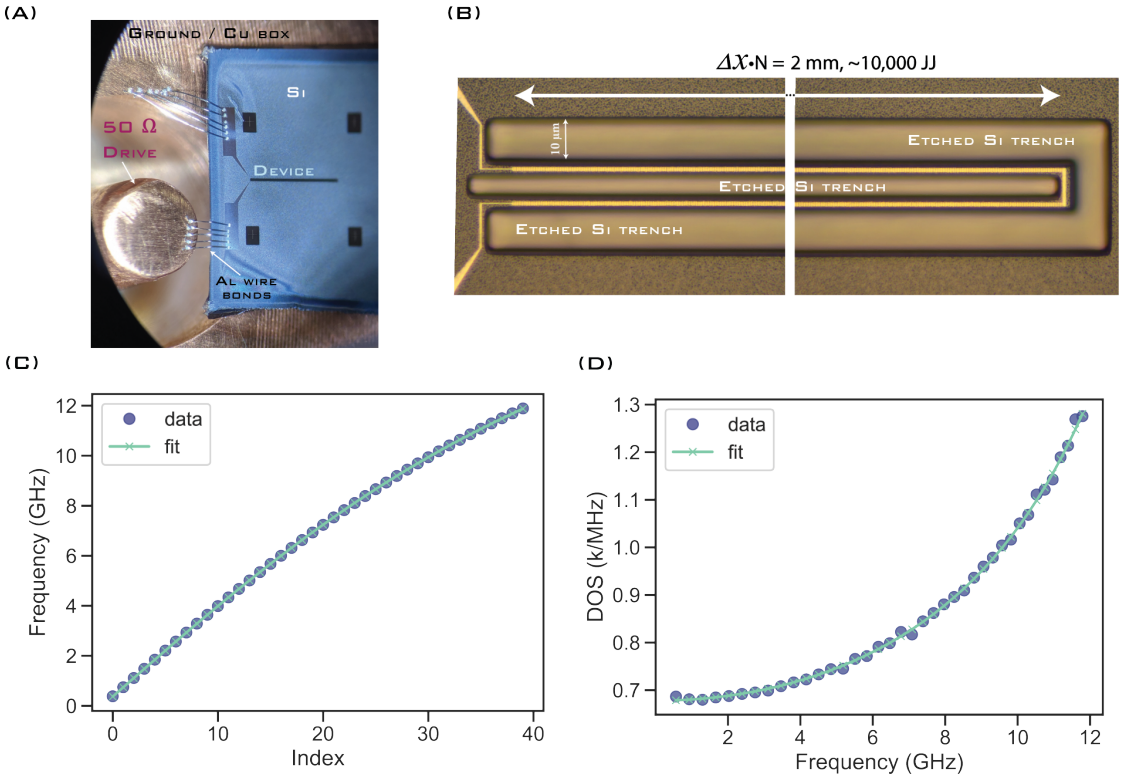

Figure 4.12: (A) The *etched* JJ waveguide sample wire bonded to the 50 Ω drive pin and to the Cu box. (B) An optical image zoom-in showing the etched trenches between and on the sides of the array. This device is shown in SEM in chapter 2. (C) The dispersion and (D) the DOS of the etched JJ waveguide modes extracted from microwave measurements. In both (C) and (D) the fits are superimposed.

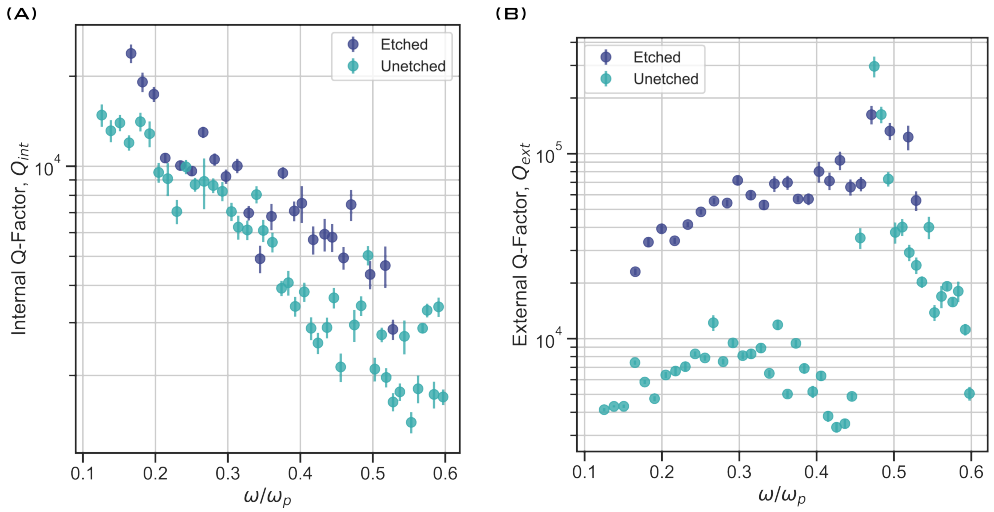

Figure 4.13: (A) The internal quality factors of both the unetched and etched versions of the same device. Both have Q_{int} which decreases with increasing mode frequency. (B) The external quality factors of the devices before and after etching. Notice the difference in the Q_{ext} associated with an increase in Z_∞.

tone indicating the selective etch procedure does not produce extreme modifications of junction quality. Likewise, the E_J/E_{C_J} ratio further indicates the internal quality factor is not limited by phase slips among the junctions in the array as was the case for the prior experiment when $E_J/E_{C_J} < 20$.

The characteristic impedance of the etched device was indeed comparable to unetched devices in [103] (sample f in figure 4.9) however those devices had $E_J/E_{C_J} \sim 9$ with $Q_{\text{int}} < 10^3$. Therefore, this result demonstrates the wave impedance of JJ transmission lines with high-quality factors, and wave impedance can be created by removing the high dielectric silicon around the JJ array. This technology can be utilized for experiments that require large E_J/E_{C_J} and wave impedance simultaneously which are rather conflicting constraints.

Due to the wire bonds the Q_{ext} scales differently than the devices in the 3D waveguide and increases with frequency. The sample holder box seems to have a resonance mode where the Q_{ext} has a peak in figure 4.13 (B). The lower frequency mode dependence makes sense due to the wire bonds acting as an inductance such that the impedance grows as a function of ω up to the box mode. The difference of Q_{ext} between the unetched and etched versions

of the device indicates the impedance mismatch between the input pin and the device grows as well causing more reflection of the signal.

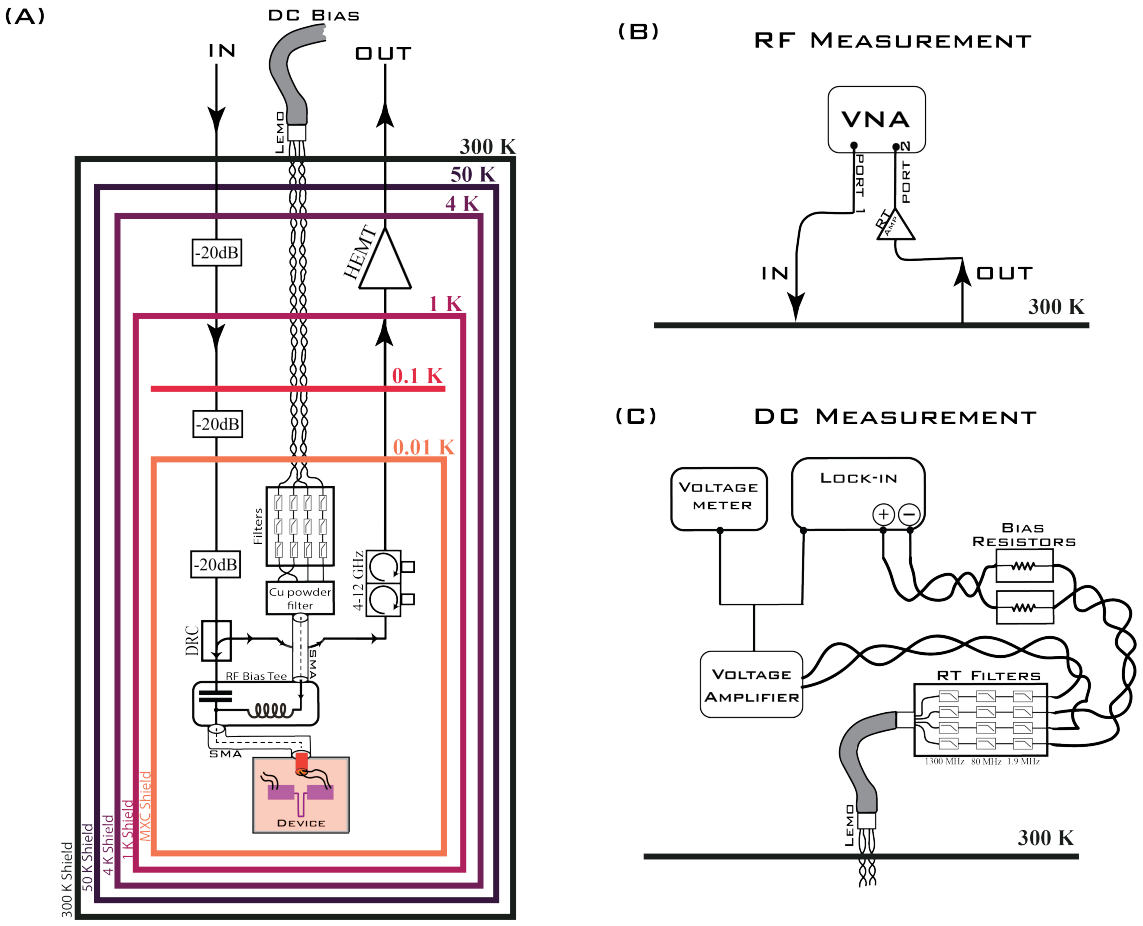

Figure 4.14: (A) The cryogenic setup for the DC and RF measurements. Both measurement techniques can be performed individually or simultaneously due to the RF-bias tee. (B) The RF spectrum is measured with a VNA. (C) The DC differential measurements are made using a Lock-in while also monitoring the voltage. A large valued bias resistor at RT is used to create a current-biased sample.

4.10 DC Measurements

The etched sample was then measured in a DC-only experiment; measuring the standard I-V and dV/dI characteristics. The measurements show a critical current value of the array as $I_0 = 14$ nA in both the I-V and dV/dI measurements.

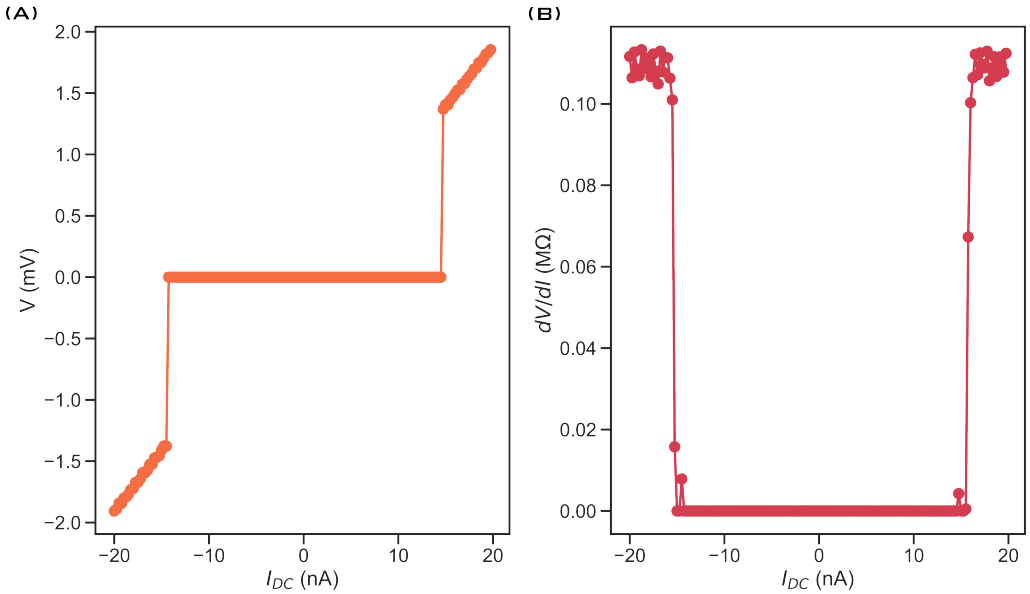

Figure 4.15: (A) The bias current I_{DC} versus the measured voltage of the device. The value for critical current, I_0, is taken when the voltage signal jumps to a non-zero value and then retains the Ohm law linear scaling for $I_{DC} > I_0$. (B) The differential resistance (dV/dI) measurements of the same device. This measurement is performed by a Lock-in measurement technique yet both measurements in (A) and (B) show the same value for $I_0 = 14$ nA.

Hybrid RF and DC experiments were then performed by doing low power one tone spectroscopy of a differential mode and a common mode as a function of I_{DC}. The frequency of the mode shifts to the left due to the modification of the array junctions inductance and then abruptly disappears at the value of I_0 measured in the DC-only experiment. This result shows a promising consistency between the two measurements and opens the possibility for other hybrid DC-RF experiments utilizing etched chains in the future. The differential mode's Q-factor was fit for each value of the bias current I_{DC}. The data shows a decrease of Q when increasing the current. The external Q-factor decreases much less than the internal Q-factor. The mode broadens when increasing the bias current and can be due to heating.

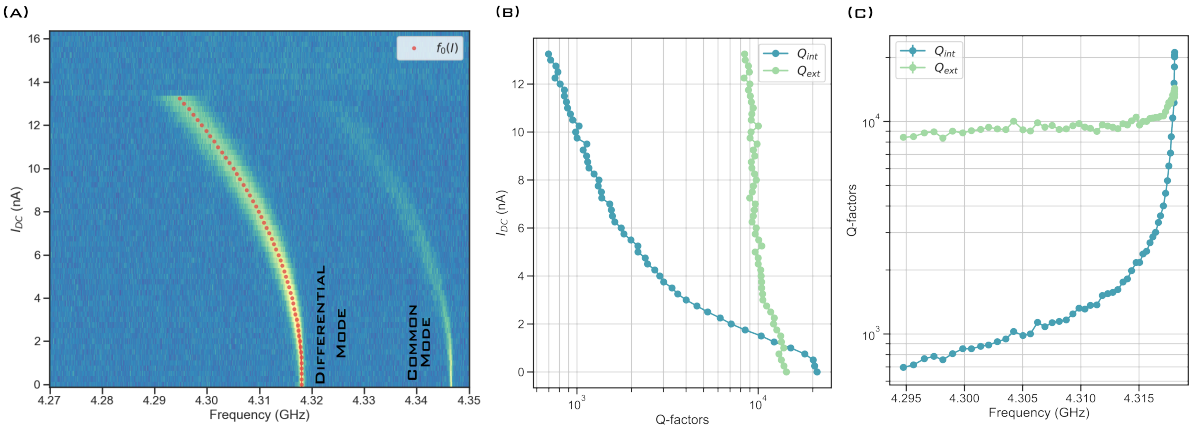

Figure 4.16: (A) A differential and common mode are measured using a VNA RF source while also sweeping the bias current I_{DC}. The color plot is the magnitude of the VNA trace for S_{11}. For each value of I_{DC} the RF trace is fit using equation 4.15. The Q_{int} and Q_{ext} are then extracted at all current bias points (B,C). Interestingly, the mode disappears for $I_{DC} \sim 14$ nA which is the measured critical current in the previous DC only measurements.

4.11 Outlook

JJ transmission lines are an interesting experiment in their own right but also enable us to probe the chain properties exclusively in a wide RF range while also measuring the DC properties of the device.

In summary, the data demonstrates how chain parameters evolve when etching and prove this technique as a viable option to produce superconduct-

ing transmission lines with ultra-high impedance. The strategy employed here uses tightly packed arrays of etched JJs that have a large E_J/E_{C_J} ratio. The selective etching technique of the Si around the device pushed the impedance up by a factor of 1.5 while maintaining high Q-factors when compared to the unetched version. As an added bonus, the JJ chains still show DC superconductivity in the I-V curves and can be measured using RF and DC signals simultaneously. In the future, the characteristic impedance can be pushed even larger if more Si is etched away at much larger depths.

5
Fluxonium

"You must understand that there is more than one path to the top of the mountain."— Miyamoto Musashi

5.1 Overview

The fluxonium superconducting qubit has the topology of a loop (flux qubit) and consists of a small JJ shunted by a superinductance [117]. The loop is threaded by an external flux bias used to tune the transition frequencies which are periodic with respect to a single flux quantum, Φ_{ext}/Φ_0. This chapter explores the basic formalism to describe the dynamics of a fluxonium qubit. Different properties arise from the variety of possible energy scale combinations found for $E_J \in (1, 10)$ GHz, $E_C \in (0.5, 10)$ GHz, and $E_L \in (0.05, 1)$ GHz. Along with the basic fluxonium formalism, three clearly distinguishable energy combinations will be highlighted in a contrasting manner demonstrating the ability to engineer a wide range of diverse spectra while also accessing the ability to enter different intrinsically protected regimes.

In particular, the first energy scale combination to be discussed in detail is defined as $E_J > E_C > E_L$. A fluxonium with these energy scales can be

thought of as a small JJ in parallel with an LC oscillator. When the external flux bias is at an integer value of flux quantum (IFQ, defined as $\Phi_{\text{ext}}/\Phi_0 = \mathbb{Z}$), the lowest energy transition exists within a single Josephson well and is called a "plasmon". The transitions then evolve smoothly with external flux bias into hybridized low-frequency transitions at half an integer value of flux quantum (HFQ, defined as $\Phi_{\text{ext}}/\Phi_0 = \mathbb{Z}/2$). The transitions at HFQ are due to quantum phase slips which are transitions between neighboring Josephson wells. These transitions are called "fluxons" [116].

The second energy scale combination to be discussed is defined where $E_J \sim E_C \gg E_L$. This parameter regime is dominated by the fluxon-type transitions for the lower-level eigenstates which are present at all external flux bias points. The first few transitions are well described by a phase-slip Hamiltonian where the loop supports circulating currents [43, 117, 124].

The third and final energy scale combination to be discussed is defined where $E_C > E_J \gg E_L$. This is a special parameter regime where the transitions are the hybridization of fluxon- and plasmon-type transitions at all external flux points. This is due to the wavefunctions spreading out over multiple Josephson wells simultaneously, wherein the conjugate picture, the charge wavefunction becomes localized with zero-point fluctuations of n taking on values less than a single Cooper-pair charge. This energy scale combination will be the sole focus of a later chapter where a dual description is introduced [93, 141] yet is worth introducing with the fluxonium formalism first.

5.2 Basic formalism

The fluxonium has a single degree of freedom, φ across the small junction, used to describe the dynamics. The general Hamiltonian, accurate in all parameter regimes, is defined as:

$$\mathscr{H}_f = 4E_C(\hat{n} - n_g)^2 - E_J \cos\hat{\varphi} + \frac{1}{2}E_L(\hat{\varphi} - \varphi_{\text{ext}})^2. \tag{5.1}$$

Optimally, the inductance (E_L) is composed of N large area JJs connecting to the small JJ leads forming a loop that enables flux tunability. Since the array provides a connection between the two islands separated by

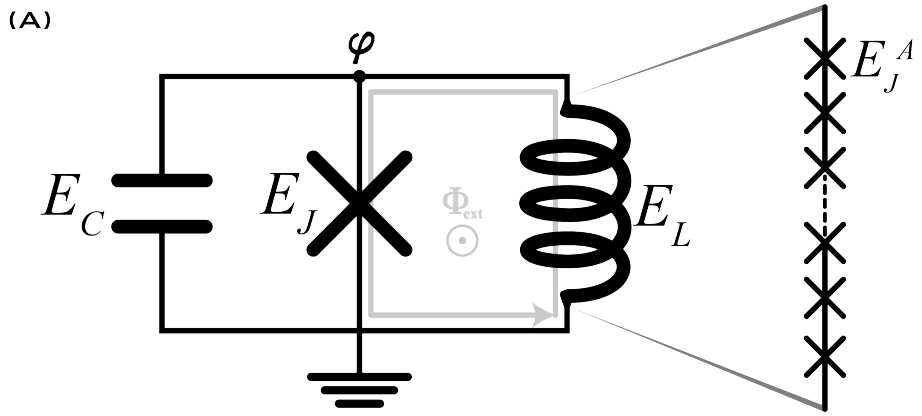

Figure 5.1: The three circuit elements in parallel are well described by one degree of freedom, φ. The loop, formed by the inductance and JJ, is threaded by external flux to tune the transition frequencies. The energy scales E_J, E_C, E_L can be changed from device to device to access and explore the different properties arising from the wide variety of energy scale combinations. In this work, $E_J \sim 4$ GHz while E_C, E_L are changed through fabrication and device design. The inductive shunt is comprised of large area JJ in series where $E_J^A \gg E_J$.

the small junction, the circuit becomes insensitive to external offset charge [117]; meaning n_g can be set to zero. Mathematically, a unitary gauge transformation of the form $\hat{U}\psi\hat{U}^\dagger$ where $\hat{U} = e^{in_g\hat{\varphi}}$ gets rid of the offset charge term without affecting the eigenenergies. The array of JJs is dubbed superinductance [114] and is defined by the two characteristics: zero DC resistance and $Z > R_Q$ in the GHz frequency range. Conventionally the transformation $\hat{\varphi} \to \hat{\varphi} + \varphi_{\text{ext}}$ provides a more convenient yet completely equivalent form for $\mathscr{H}_f$ where the cosine term now shifts with external flux instead of the inductive potential shifting. The array junctions are treated as a linear inductance not only because of the large area (current flowing through each is much less than the critical current value) but also because the phase difference across each junction is much less than 2π. In fact, each junction has a phase difference of φ/N and due to the sheer number of junctions comprising the array (N>50) the total inductance can be linearized in the following way:

$$E_{J_{\text{tot}}}^A = \sum^N E_J^A \cos\left(\frac{\hat{\varphi}}{N}\right) \approx \sum^N E_J^A \left(1 - \frac{\hat{\varphi}^2}{2N^2}\right) = NE_J^A \left(1 - \frac{\hat{\varphi}^2}{2N^2}\right). \quad (5.2)$$

The constant term is dropped and the usual inductive energy scale is re-

vealed for an array of N junctions as: $\frac{E_{J_{\text{tot}}}^{A}}{N} = E_L$.

Intuition can be gained by an analogy between the fluxonium system and a fictitious quantum particle where the φ variable is analogous to the spatial coordinate and $n = -i\frac{\partial}{\partial\varphi}$ is analogous to the momentum. The external flux modifies the landscape of the potential which is the sum of the E_J and E_L terms. The amplitude of the cosinusodial term in the potential is given by E_J while E_L determines the sharpness of the parabolic scaling of the potential with φ. E_C is thought of as the inverse mass, scaling the kinetic energy term; indicating the charging energy shifts the energy eigenvalues up or down by a constant value. Interestingly, φ is defined for all values: $\varphi \in (-\infty, \infty)$ with the potential energy $U(\varphi) \neq U(\varphi + 2\pi)$. This property is due to the inductive scaling with φ^2 which clearly breaks the 2π periodicity of the usual JJ potential.

The fluxonium potential is tunable, smoothly transforming with the external flux bias φ_{ext} and has two symmetry points when the external flux bias is equal to integer or half-integer values of a flux quanta. These points are explicitly denoted as IFQ $= n\Phi_0$ (integer-flux quantum) and HFQ $= n\Phi_0 + \frac{1}{2}$ (half-flux quantum). The potential at IFQ has the absolute minimum centered and symmetric at $\varphi/2\pi = 0$ (figure 5.2) and the potential at HFQ has the absolute minimums split into two wells each centered at $\varphi/2\pi \approx \pm 1/2$. The potential between these two points is always asymmetric with respect to the origin and transforms continuously between the symmetrical points forming half a period. Similarly to the potential, the eigenvalue transitions and matrix elements also smoothly evolve between these two points providing a unique spectrum at every external flux value point.

5.2.1 Eigenspectrum and wavefunctions

The fluxonium Hamiltonian is conventionally diagonalized using the harmonic LC oscillator Fock basis [122] since all states are bounded by the harmonic potential created by the inductor. The operators are explicitly ex-

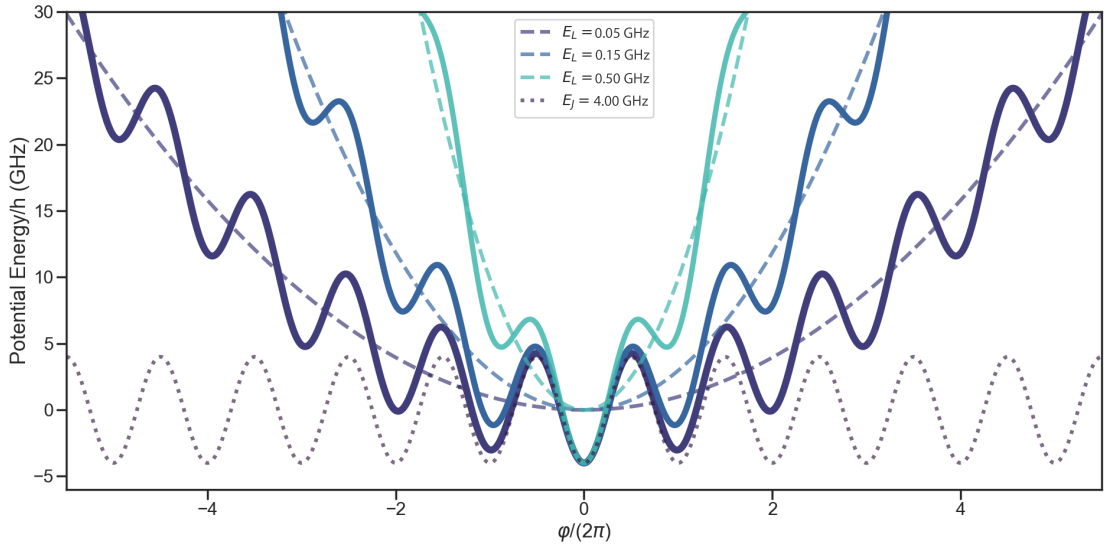

Figure 5.2: The fluxonium potential for different values of E_L at IFQ. For lower values of E_L the harmonic φ^2 contribution forms a wider, softer potential. The dashed lines indicate the harmonic contribution while the dotted line is the Josephson potential contributed solely by the small JJ; in this case, $E_J = 4$ GHz. The solid line is the addition of both contributions forming the fluxonium potential energy.

pressed as:

$$\begin{aligned} \hat{\varphi} &= \frac{\varphi_{zpf}}{\sqrt{2}}(a + a^\dagger) = \frac{1}{\sqrt{2}}\left\{\frac{8E_C}{E_L}\right\}^{1/4}(a^\dagger + a)\,, \\ \hat{n} &= \frac{n_{zpf}}{\sqrt{2}} i(a^\dagger - a) = \frac{i}{\sqrt{2}}\left\{\frac{E_L}{8E_C}\right\}^{1/4}(a^\dagger - a) \end{aligned} \tag{5.3}$$

Where $a, a^\dagger$ are the HO raising and lower operators each with a Hilbert space dimension exceeding fifty oscillator states. The commutation relation between the phase and charge operators is $[\hat{\varphi}, \hat{n}] = i$. With the considerations presented above and the explicit operator definitions, the fluxonium Hamiltonian takes the form:

$$\boxed{\mathscr{H}_f = 4E_C\hat{n}^2 - E_J\cos(\hat{\varphi} + \varphi_{\text{ext}}) + \frac{1}{2}E_L\hat{\varphi}^2} \tag{5.4}$$

Plugging in the operator definition in the harmonic oscillator basis, $\mathscr{H}_f$ is now diagonalizable using the QuTip software [88] by utilizing the built-in functions and operators. For ease of calculation the cosine term can be recast as the translation operator [198] which is the off-diagonal element that mixes the diagonal harmonic oscillator LC Fock modes. Defining $\hat{T} = \exp(-i\hat{\varphi}) = \exp\left\{\frac{-i\varphi_{zpf}}{\sqrt{2}}(a^\dagger + a)\right\}$ such that $\cos(\hat{\varphi} + \varphi_{\text{ext}}) = \frac{1}{2}\left\{\hat{T}e^{i\varphi_{\text{ext}}} + \hat{T}^\dagger e^{-i\varphi_{\text{ext}}}\right\}$. The fluxonium Hamiltonian becomes:

$$\mathscr{H}_f = 4E_C\hat{n}^2 + \frac{1}{2}E_L\hat{\varphi}^2 - \frac{E_J}{2}\left\{\hat{T}e^{i\varphi_{ext}} + \hat{T}^\dagger e^{-i\varphi_{ext}}\right\} \tag{5.5}$$

and is diagonalized at many φ_{ext} values to find the eigenspectrum versus external flux.

Furthermore, it is instructive to plug the operators in the harmonic oscillator basis directly into the fluxonium Hamiltonian and simplify to find:

$$\mathscr{H}_f = \sqrt{8E_LE_C}\{a^\dagger a + 1/2\} - E_J\cos\left\{\frac{\varphi_{zpf}}{\sqrt{2}}(a^\dagger + a) + \varphi_{\text{ext}}\right\}. \tag{5.6}$$

This form reinforces the idea of the fluxonium being a small JJ shunted by an LC oscillator. The non-linear cosine term in $\mathscr{H}_f$ can be expanded due to the addition of the phases $\varphi + \varphi_{\text{ext}}$:

$$\cos(\hat{\varphi} + \varphi_{\text{ext}}) = \cos(\hat{\varphi})\cos(\varphi_{\text{ext}}) + \sin(\hat{\varphi})\sin(\varphi_{\text{ext}}). \tag{5.7}$$

which provides a clear definition for the off-diagonal matrix elements. The Hamiltonian in matrix form is defined as:

$$\begin{aligned}\langle m|\mathscr{H}_f|n\rangle = \sqrt{8E_LE_C}(m+1/2)\delta_{mn} \\ - E_J\cos(\varphi_{\text{ext}})\cdot\langle m|\cos\left(\frac{\varphi_{zpf}}{\sqrt{2}}(a^\dagger + a)\right)|n\rangle \\ - E_J\sin(\varphi_{\text{ext}})\cdot\langle m|\sin\left(\frac{\varphi_{zpf}}{\sqrt{2}}(a^\dagger + a)\right)|m\rangle;\end{aligned} \tag{5.8}$$

where δ_{mn} is the Kronecker-delta equating to 1 when m=n and zero otherwise. The off-diagonal matrix elements can be analytically evaluated with

Laguerre polynomials [4, 122]:

$$\begin{aligned}\langle m|\cos(\varphi)|m+2n\rangle &= (-2)^{-n}\sqrt{\frac{m!}{(m+2n)!}}\times(\varphi_{zpf})^{2n}e^{-\varphi_{zpf}^2/4}\times L_m^{2n}\left(\frac{\varphi_{zpf}^2}{2}\right)\\ \langle m|\sin(\varphi)|m+2n+1\rangle &= (-2)^{-n}\sqrt{\frac{m!}{(m+2n+1)!}}\times(\varphi_{zpf})^{2n+1}e^{-\varphi_{zpf}^2/4}\times L_m^{2n+1}\left(\frac{\varphi_{zpf}^2}{2}\right)\end{aligned} \tag{5.9}$$

where $m,n\in\mathbb{N}$. Providing an alternative method for constructing the $\mathscr{H}_f$ matrix needed for diagonalization if Qutip is inaccessible.

In all cases, $\mathscr{H}_f$ is diagonalized with the energy eigenvalues of each state at the defined external flux points being returned. The difference between the relevant eigenstates is the transition energy where, usually, the basic transitions out of the ground state or out of the first excited state are considered.

The eigenvalues returned after diagonalization of the fluxonium Hamiltonian in the harmonic oscillator basis give the eigenenergies, however, the eigenfunctions are the coefficients needed to construct the fluxonium wavefunctions from the linear superposition of the harmonic oscillator wavefunctions defined as:

$$\psi_m(\varphi)=\frac{1}{(2\pi\varphi_{zpf}^2)^{1/4}}\frac{1}{\sqrt{2^m m!}}H_m(\varphi/\varphi_{zpf})e^{-\varphi^2/4\varphi_{zpf}^2}\ . \tag{5.10}$$

Where m in this equation is the integer index of the harmonic oscillator state. To explicitly construct the fluxonium wavefunction of the jth energy level the eigenfunction is defined as: $\Psi_j(\varphi)=\sum_{m=0}^{m=M}c_m\psi_m(\varphi)$, where c_m is the mth component of the eigenvector given for the jth eigenstate after diagonalizing $\mathscr{H}_f$ and $\sum_m|c_m|^2=1$. The value of φ_{zpf} (or equivalently the amount of phase delocalization) dictates how many harmonic oscillator states are necessary to include when diagonalizing $\mathscr{H}_f$.

To represent the wavefunctions in the conjugate basis, Q, a discrete Fourier transformation must be applied to the wavefunctions in the phase (φ) representation. The transformation is discrete due to the finite φ points which

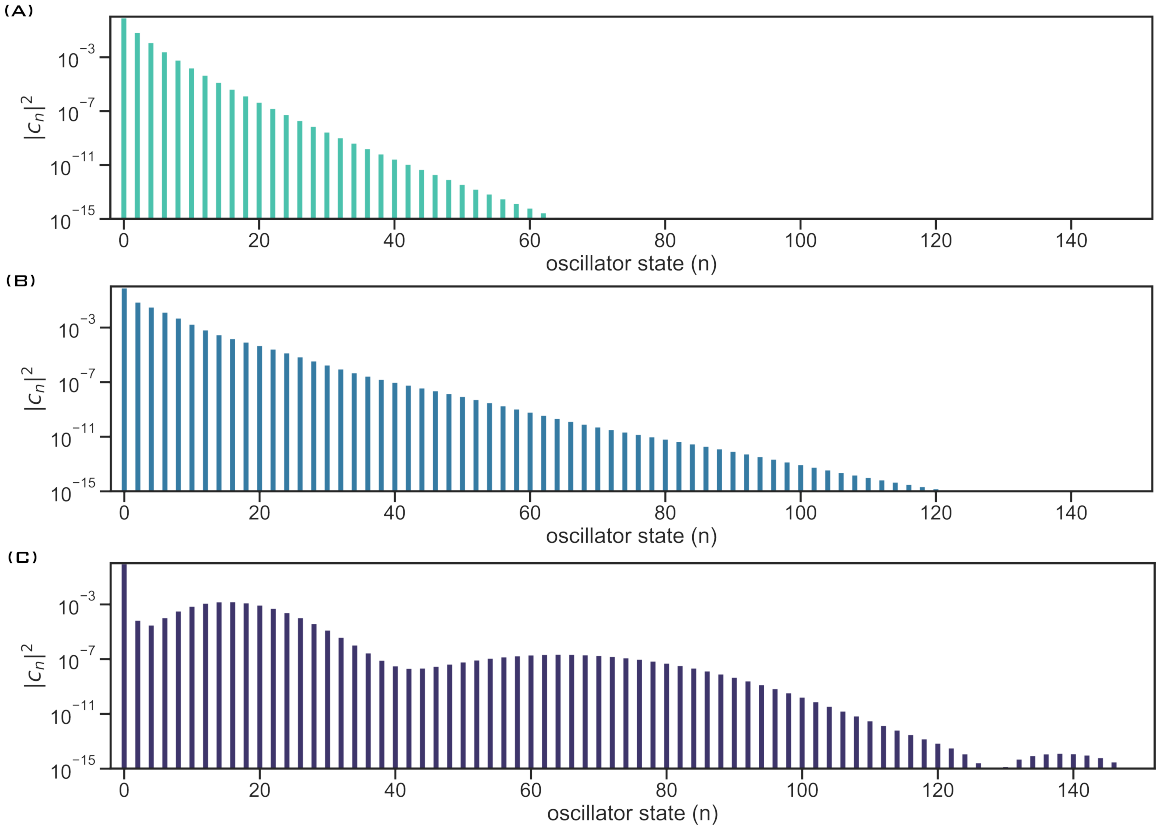

Figure 5.3: The harmonic oscillator state coefficients used to construct the fluxonium wavefunctions at half flux quantum for the energy parameter combination of: (A) phase localization (B) phase slip (C) phase delocalization. The amount of harmonic oscillator states necessary to accurately construct the wavefunctions increases as the phase becomes more delocalized.

are used when simulating the $\Psi_f(\varphi)$ and is expressed as:

$$\Psi_f(Q) = \frac{1}{2\pi}\sum_{k}^{K}\Psi_f(\varphi)\cdot e^{iQ_k\varphi_{\text{ext}}}\ . \tag{5.11}$$

The dual representation of the wavefunctions in the continuous charge basis helps illustrate the Heisenberg relationship between charge and phase in the sense a localized wavefunction in the charge representation is due to a delocalized wavefunction in the phase representation and vice-versa. The eigenenergies of the Hamiltonian in both basis are the same however the potential changes form. The potential in the Q basis becomes the charge dispersion of the small JJ.

The fluxonium eigenvalues and eigenvectors can be cast into the diagonal basis such that: $\tilde{\mathscr{H}_f}|k\rangle = E_k|k\rangle$ where k is the index of the eigenstate and $\tilde{\mathscr{H}_f}$ is the unitary transformed fluxonium Hamiltonian which is diagonal. If the charging term is purely diagonal then the commutation relations have the form [169]: $[\hat{\varphi}, \mathscr{H}_f] = 4E_C[\hat{\varphi}, \hat{n}^2] = 8iE_C\hat{n}$. Now taking the inner product of states $|k\rangle$ and $|j\rangle$ gives the relation: $8iE_C\langle k|\hat{n}|j\rangle = f_{jk}\langle k|\hat{\varphi}|j\rangle$ where E_C is in units of Hz. Therefore the matrix elements are proportional to one another through the relation:

$$\langle k|\hat{n}|j\rangle = \frac{f_{jk}}{8iE_C}\langle k|\hat{\varphi}|j\rangle \tag{5.12}$$

Other ways to define this relation when not in the diagonal basis is considered in [122].

The matrix elements between different states are considered as the selection rules for our system and are a way to explain how external coupling strength can induce a transition from $k \to j$ or how an external noise source couples to a qubit transition. These matrix elements will be used time and time again to gain insight on the dynamical properties of the system. Matrix elements are used for perturbation theory, Fermi's golden rule, and dephasing theory and are intrinsic properties of the fluxonium which are ultimately set by the combination of energy scales that can be visualized through wavefunctions.

Now that the fluxonium Hamiltonian, matrix elements, wavefunctions,

and operators are defined simulations of these quantities along with transition energies and time-domain characteristics will be discussed in depth. This discussion will be presented for each energy scale combination introduced earlier and will set the stage for the experimental results discussed.

5.3 Energy scale combinations of fluxonium

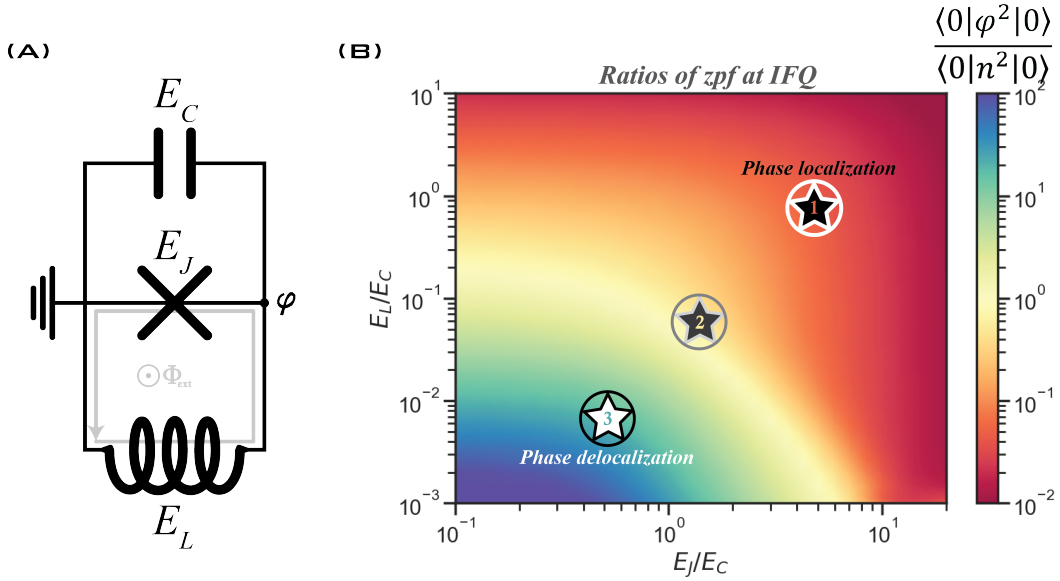

Figure 5.4: (A) Generic fluxonium electrical circuit. (B) A "phase" diagram showing the relationship between E_J/E_C, E_L/E_C, and $\langle 0|\varphi^2|1\rangle/\langle 0|n^2|1\rangle$. The three points are for the three-parameter regimes defined for: (1) $E_J = 4$ GHz, $E_C = 0.8$ GHz, $E_L = 0.5$ GHz; (2) $E_J = 4$ GHz, $E_C = 2$ GHz, $E_L = 0.15$ GHz(2) $E_J = 4$ GHz, $E_C = 8$ GHz, $E_L = 0.05$ GHz.

The different energy scale combinations can be explored through simulation by changing the circuit parameters E_J, E_C, and E_L and analyzing the spectrum and wavefunctions. These simulations illustrate the ability to engineer fluxonium's spectrum and matrix elements by systematically choosing the energy parameters which suit your cause. The wide range of the resulting fluxonium properties can also enable intrinsic protection from decoherence by choosing combinations with small or large matrix elements.

The energy scale combinations selected in this work are partitioned into three sections categorized by the ratio of the zpf's at IFQ. At this flux point, the parameter phase space shows phase localization for $E_J/E_C > 1$ and

$E_L/E_C > 0.1$ (parameter regime 1) which transitions to phase delocalization for $E_J/E_C < 1$ and $E_L/EC < 0.1$ (parameter regime 3). The energy combination on the boundary (gold) is a sort of "goldie-locks" regime where the ratio of zpf's are roughly unity (parameter regime 2) and will be studied in depth in chapter 7.

5.3.1 Energy scale combination #1

The first fluxonium energy scale combination is defined with $E_J = 4$ GHz, $E_C = 0.8$ GHz, $E_L = 0.5$ GHz. This energy scale combination is studied in depth experimentally in [111, 135, 136, 170, 171].

For starters, the fluxonium in this regime while biased with external flux at IFQ is qualitatively characterized as the two lowest states being localized wavefunction in the single Josephson potential centered about zero such that the expectation value of $\varphi_{\text{RMS}}/2\pi \ll 1$. The transition from $|0\rangle \rightarrow |1\rangle$ is the plasmon in this case and can be approximately expressed as [24, 172]:

$$f_{\text{plasmon}} \approx \sqrt{8(E_J + E_L)E_C} - E_C \,. \tag{5.13}$$

When sweeping the external flux bias away from IFQ, a sharp change in transition frequency occurs indicating the eigenstates are more or less localized in the Josephson potential wells which are changing position with changing external flux (figure 5.5 E). The transitions become a weak hybridization between plasmon and fluxon transitions.

When arriving at HFQ, the qubit transition is at a very low frequency where the states occupy the two adjacent potential wells forming a symmetric and anti-symmetric combination of occupying the left and right well, evident by a sharp peak of the $\langle 0|\varphi|1\rangle$ matrix element. The symmetric and anti-symmetric combination of occupying the left and right well can be recast as the superposition of eigenvectors $|L\rangle$ and $|R\rangle$:

$$\begin{aligned} |0\rangle &= \frac{1}{\sqrt{2}}(|L\rangle + |R\rangle) \\ |1\rangle &= \frac{1}{\sqrt{2}}(|L\rangle - |R\rangle) \end{aligned} \tag{5.14}$$

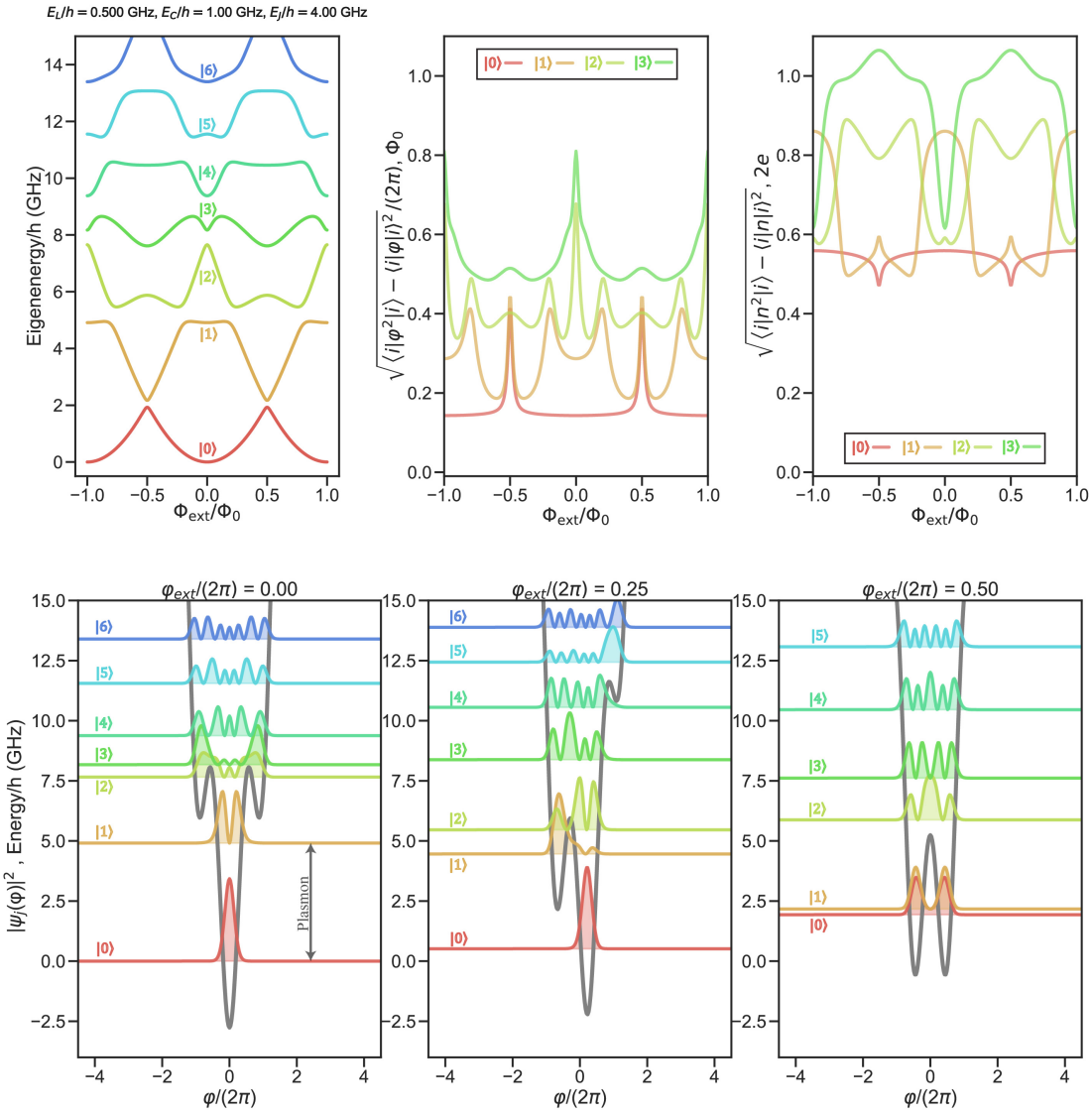

Figure 5.5: (A) The eigenspectrum with energy scale combination #1. This combination has flux sensitivity of the ground state $|0\rangle$ of about 2 GHz. A main defining feature is the flat part of the $|1\rangle$ state at IFQ. This is the plasmon mode which intersects with the fluxon mode at around 5 GHz and causes the splitting between states $|1\rangle$ and $|2\rangle$. (B) The root-mean-square (RMS) deviation of φ for the first four eigenstates. The RMS deviation increases sharply around HFQ for the two lowest eigenstates due to the ability to tunnel between the two adjacent potential wells. (C) The RMS deviation of charge is just greater than e for all eigenstates. Comparing the normalized RMS values of φ and n at all external flux bias points $\varphi_{\text{RMS}} > n_{\text{RMS}}$ for each respective eigenstate; demonstrating this regime has phase-localization. (D) The wavefunctions at IFQ where the plasmon transition is labeled. The plasmon is clear when the states involved in the transition are within the same Josephson well. (E) The system at $\varphi_{\text{ext}}/2\pi = 0.25$. Notice the asymmetry of the potential. (F) At HFQ the two lowest states are separated by very low frequency and are superpositions of circulating current states.

The coupling of the two states can be modeled as the tunneling of a flux quantum in and out of the loop.

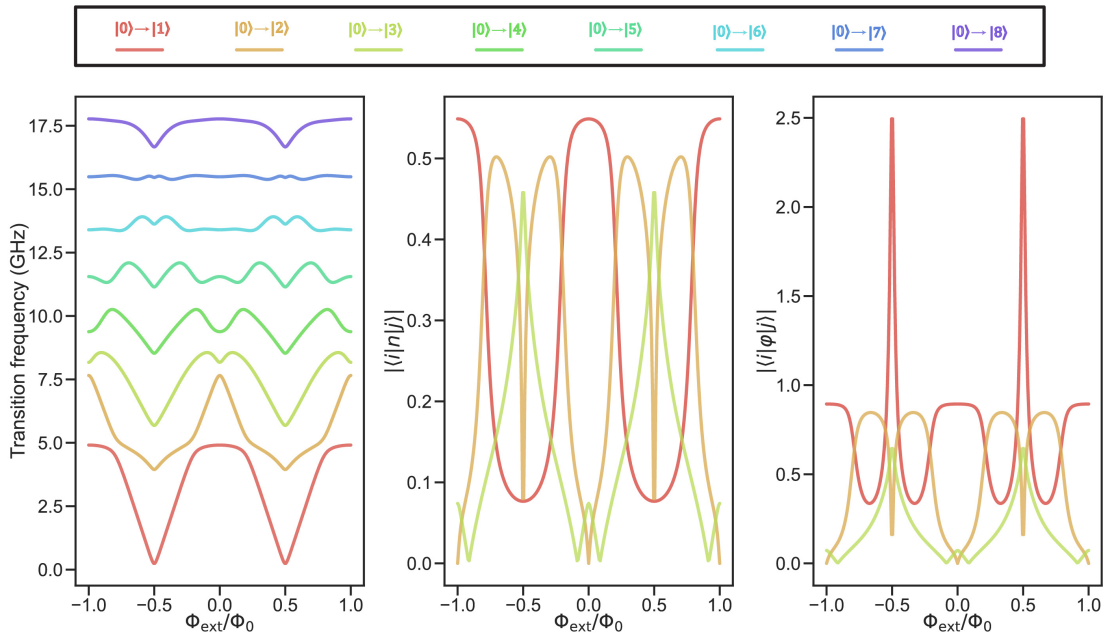

Figure 5.6: (A) The transition spectrum for the first eight transitions out of the groundstate. (B) The charge (n) matrix element for the first three transitions. (C) The phase (φ) matrix element for the first three transitions; notice the value becomes peaked when $\varphi_{\text{ext}}/2\pi = 0.5$.

The Hamiltonian which describes the tunneling of a single flux quanta at an arbitrary external flux bias is given by [114]:

$$\mathscr{H}_s = \sum_{m,m+1} 2\pi^2 E_L (1/2 - \Phi_{\text{ext}}/\Phi_0)^2 |m\rangle\langle m| - \frac{\varepsilon_s}{2}\left\{ |m\rangle\langle m+1| + |m+1\rangle\langle m| \right\} \tag{5.15}$$

where m is an integer which describes the Josephson well number coordinate that the eigenstate wavefunction is localized in (see equation 5.19); while ε_s is the phase slip energy of the small JJ. Using this definition at HFQ, $|L\rangle \rightarrow m = 0$ and $|R\rangle \rightarrow m = 1$ making the phase slip Hamiltonian of the 0 and 1 states:

$$\mathscr{H}_s^{\text{HFQ}} = -\frac{\varepsilon_s}{2}\left\{ |L\rangle\langle R| + |R\rangle\langle L| \right\}. \tag{5.16}$$

Here ε_s is the splitting between the ground and first excited state and is the

frequency of which phase-slips of 2π across the small JJ occur or likewise the frequency which flux tunnels in and out of the loop. This frequency exactly corresponds to the transition frequency f_{01} at HFQ [5, 129] with the origin of the eigenvectors for $|0\rangle$ and $|1\rangle$ in equation 5.14 now becoming clear.

These eigenstates are fluxons which are also considered persistent current states due to the wavefunctions position changing by 2π during a tunneling event, therefore, producing a current due to the phase difference frustration from not having an integer value of flux quanta in the loop. The symmetric and anti-symmetric superposition of states are represented equivalently as current circulating in the clockwise and counter-clockwise directions or as localized states exclusively in the left or right potential well. Re-expressing the two lowest eigenstates one final time in a suggestive way where the circular arrows represent the current direction, takes the form:

$$\begin{aligned} |0\rangle &= \frac{1}{\sqrt{2}}(|\circlearrowleft\rangle + |\circlearrowright\rangle) \\ |1\rangle &= \frac{1}{\sqrt{2}}(|\circlearrowleft\rangle - |\circlearrowright\rangle)\ . \end{aligned} \tag{5.17}$$

The transition at HFQ is considered the optimal operation point for fluxoniums with this energy scale combination due to: the low transition frequency, the desirable protection which arises from a suppressed charge matrix, and the symmetry of the potential that allows for the first-order derivative with respect to external flux to be zero. These properties will be discussed at length in a later section but it is helpful to make connections with these ideas now.

5.3.2 Energy scale combination #2

The second energy scale combination is defined with $E_J = 4$ GHz, $E_C = 2$ GHz, $E_L = 0.15$ GHz. This specific energy scale combination has not been studied in depth however similar fluxonium behavior due to the ratio of E_J/E_C and E_L/E_C being roughly the same has been experimentally explored in [117, 148]. The real main difference between the references and our discussion here comes from the value of transition frequencies.

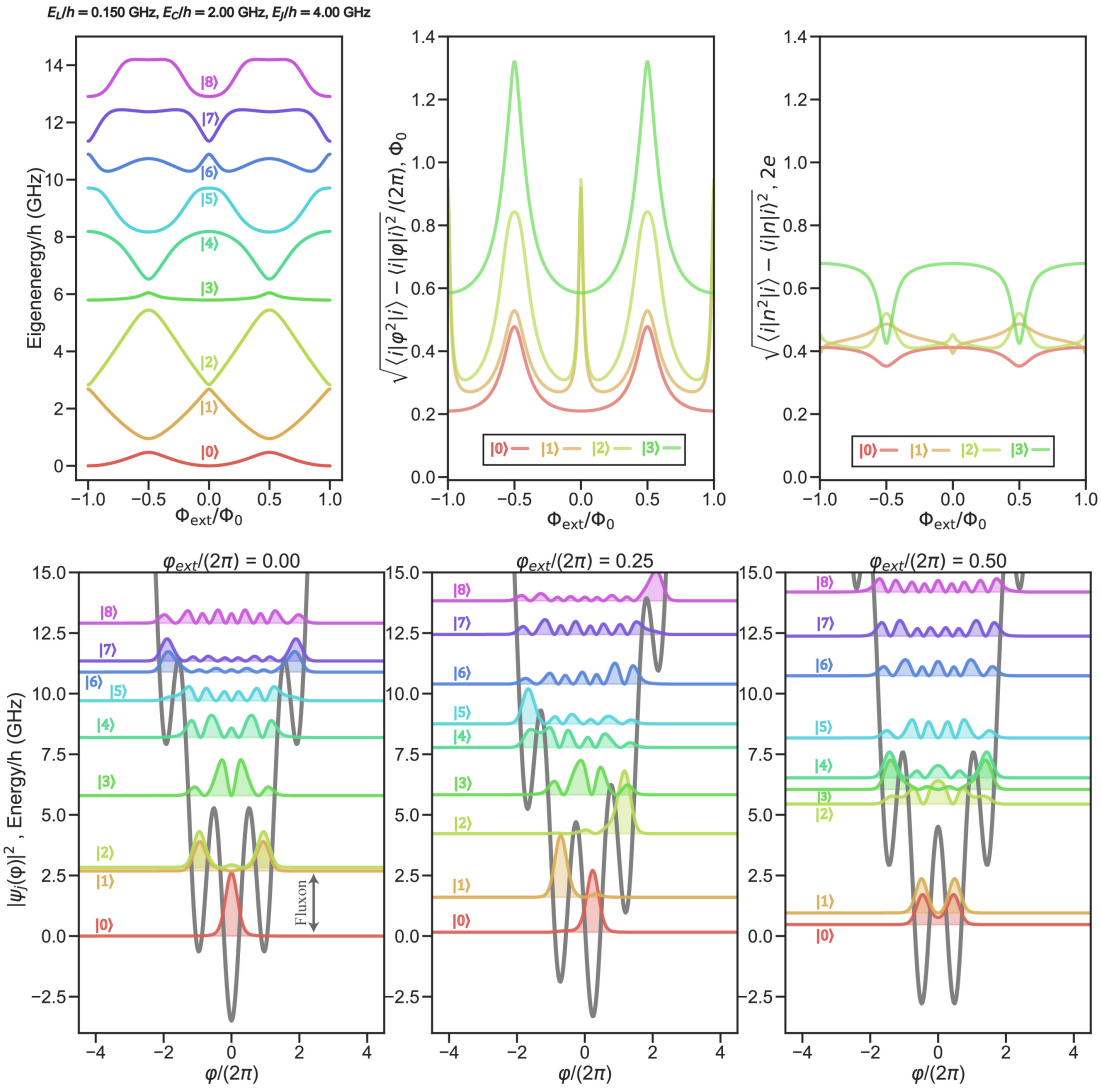

Figure 5.7: (A) The eigenspectrum with energy scale combination #2. (B)The RMS deviation of the φ variable for the first four eigenstates. The RMS deviation increases much smoother around HFQ than the energy combination #1.(C) The RMS deviation of charge is on the order of e. Little change happens for the first three eigenstates as a flux quantum is swept. (D) The wavefunctions of the first seven states at IFQ. The groundstate is localized in the center Josephson potential well while the two next states are located as a superposition of states localized in the left and right potential well from the center. (E) The system at $\varphi_{\text{ext}}/2\pi = 0.25$. The first three states are still localized in their respective wells. (F) HFQ spectrum where the 0 and the 1 eigenvectors are very close in frequency.

The second energy combination has a defining "zig-zag" characteristic shape to the lowest transitions which is a consequence of the primarily fluxon-dominated transitions out of the ground state at all external bias points. However, the plasmon transition recovers by the third or fourth transition and washes out the pure fluxon nature of said transitions. This means, with these energy scales chosen for this discussion, the majority of the first two transitions can be treated with the phase-slip Hamiltonian:

$$\mathscr{H}_s = \sum_{m,m+1,m+2} 2\pi^2 E_L (m-\varphi_{\text{ext}})^2 |m\rangle\langle m| - \frac{\varepsilon_{s_1}}{2}\left\{|m\rangle\langle m+1| + |m+1\rangle\langle m|\right\} - \frac{\varepsilon_{s_2}}{2}\left\{|m\rangle\langle m+2| + |m+2\rangle\langle m|\right\} \tag{5.18}$$

where m is again the integer values of flux quanta in the loop except this time double-phase slips occur at a non-negligible rate almost exclusively at IFQ between the $|1\rangle$ and the $|2\rangle$ states while still having single-phase slips out of the $|0\rangle$ state.

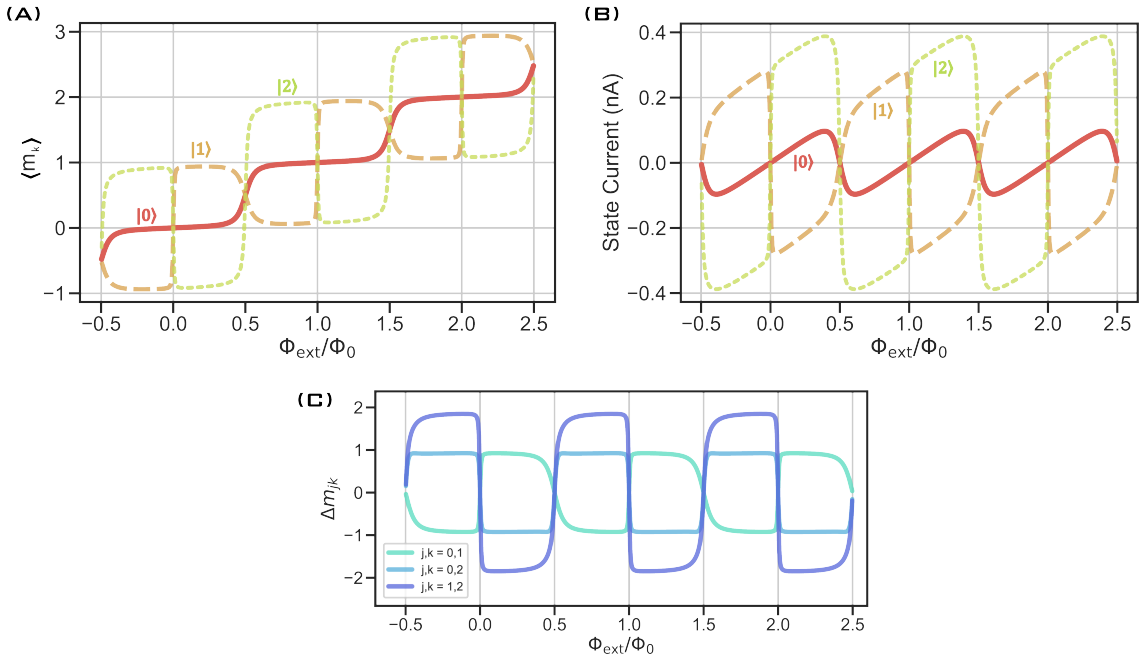

Figure 5.8: (A) The expectation value of the flux quanta occupying the loop. (B) The circulating current in the loop versus external flux. (C) The difference Δm_{jk} associated with transitions $j \to k$.

The fluxon virtue of the lowest eigenstates allows for the expectation value of the state flux, $\langle m_k \rangle = \langle k|m_k|k\rangle$, to be represented as the linear derivative of the energy levels with respect to φ_{ext}. This approximation gives:

$$\langle m_k \rangle = \varphi_{\text{ext}} - \frac{1}{4\pi^2 E_L} \frac{\partial E_k}{\partial \varphi_{\text{ext}}} \,. \tag{5.19}$$

This quantity is called the "Faraday staircase" in [179] and is analogous to the "Coulomb staircase" [9, 15, 65]. The Faraday staircase is shown in figure 5.8 (A) and is important to notice at the flux symmetry points the state currents are zero as well as $\Delta m_{jk} = \langle m_j \rangle - \langle m_k \rangle = 0$ which validates the degeneracy in the absence of phase-slips.

Starting at HFQ, the behavior of the fluxonium with the second energy combination behaves basically identical to the first energy combination; characterized by the two lowest two states having a transition energy given by the frequency of a single phase-slip event. In figure 5.8 at half-integer values of flux quantum the $|0\rangle$ and $|1\rangle$ state expectation value is identical given as by $m = 0.5$ while the persistent current is equal to zero. This is the result of the current circulating in the clockwise or counterclockwise direction.

At IFQ, focusing first at the external flux bias being zero, the ground state is localized in the central Josephson well ($\langle m_0 \rangle = 0$) and is capable of tunneling into the two adjacent wells on either side where the $|1\rangle$ and $|2\rangle$ states are the symmetric and anti-symmetric superpositions of localized states in the two adjacent Josephson wells located at m=$\pm$1. When the ground state to the first or second excited state transition occurs a single phase slip event takes place as is seen in figure 5.8 (C) for $\Delta m_{0,(1\text{or}2)}$.

In the transition spectrum there now exists a small valued splitting between the $|0\rangle \rightarrow |1\rangle$ and the $|0\rangle \rightarrow |2\rangle$ state transitions which are due to the $|1\rangle$ and $|2\rangle$ states now being degenerate. However, this type of degeneracy is not lifted by a single phase-slip event like what happens at HFQ for the two lowest states, but instead, a double phase-slip event occurs changing m by $\Delta m_{1,2)} = \pm 2$. The double phase-slip rate frequency is given by ε_{s_2} and is less than ε_{s_1}. Due to the nature of the transitions at IFQ, the charge matrix element are substantially suppressed indicating a lack of plasmon-like

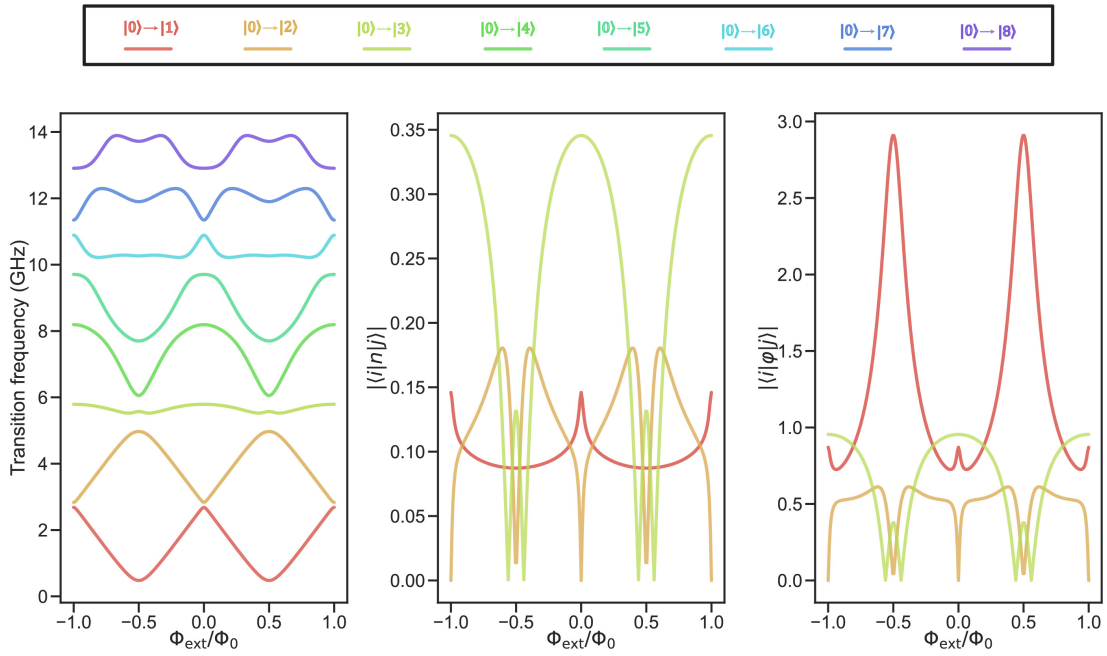

Figure 5.9: (A) The transition spectrum of energy combination #2. The first two transitions are "zig-zag" like while the 0-3 transition is flat indicating the plasmon frequency. (B) The charge (n) matrix element for the first three transitions. (C) The phase (φ) matrix element for the first three transitions.

transitions.

This parameter regime is ideal for creating a qutrit [78] while biased at IFQ since the dynamics of the first three energy levels are protected due to the symmetry of the flux spot and the lack of wavefunction overlap/small charge matrix element. Furthermore, due to the symmetry of the potential forbidden transitions arise between $|0\rangle \rightarrow |2\rangle$ when considering odd parity operators, such as n or φ. Therefore a prepared $|2\rangle$ must decay first through $|2\rangle \rightarrow |1\rangle \rightarrow |0\rangle$.

5.3.3 Energy scale combination #3

The third fluxonium energy scale combination is defined with $E_J = 4$ GHz, $E_C = 8$ GHz, $E_L = 0.05$ GHz. This energy scale combination is studied in depth experimentally in [141]. This parameter regime is a very unique energy scale combination characterized by the complete hybridization of fluxons and plasmons; where there are no external flux bias points where either description is prevalent. This parameter regime has $E_C < E_J \ll E_L$ which essentially enables the ground state wavefunction to spread into multiple Josephson wells at all flux points. The spreading of the wavefuntion creates phase delocalization where there is a finite probability at all times to find $\varphi > \pi$. This parameter regime has an entire chapter devoted to it but is worth understanding first in the fluxonium mind frame.

Due to the low value of E_L ($L_{\text{tot}} > 1\mu$H), the parabolic contribution to the potential becomes much softer while the high E_C allows the eigenstates to tunnel into adjacent wells. This creates a spectrum that is nearly insensitive to the external flux bias for the lower-lying states spread into multiple Josephson wells simultaneously. This becomes further evident by the φ matrix elements being $> \pi$ at all external flux points, an enormous value compared to the other parameter regimes. This qubit's lower transitions can be understood as the superposition of different flux quanta in the loop simultaneously much to the likeness of transmon's superposition of pure charge states simultaneously occupying the superconducting island. This duality will be discussed in depth in the chapter 8.

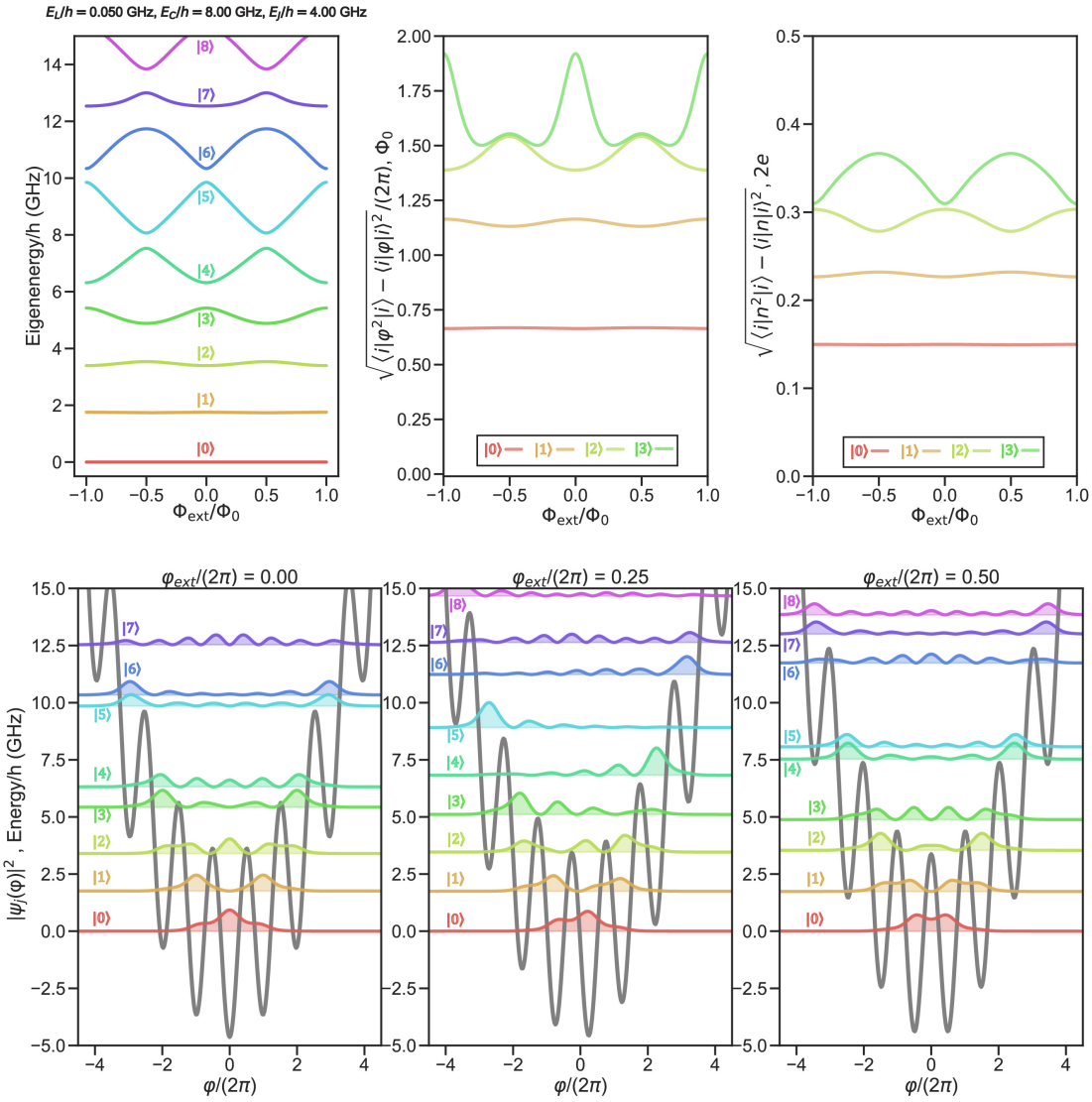

Figure 5.10: (A) The eigenspectrum in parameter regime #3. Notice the flux insensitivity of the three lowest eigenstates. (B) The RMS deviation of the φ variable for the first four eigenstates. The RMS deviation is almost completely flat for the ground state. (C) The RMS deviation of charge is less than e for the first three eigenstates. (D) The wavefunctions of the first seven states at IFQ. (E) The system at $\varphi_{\text{ext}}/2\pi = 0.25$. (F) HFQ spectrum where the 0 and the 1 eigenvectors are located at the bottom of the harmonic potential and are situated in multiple wells.

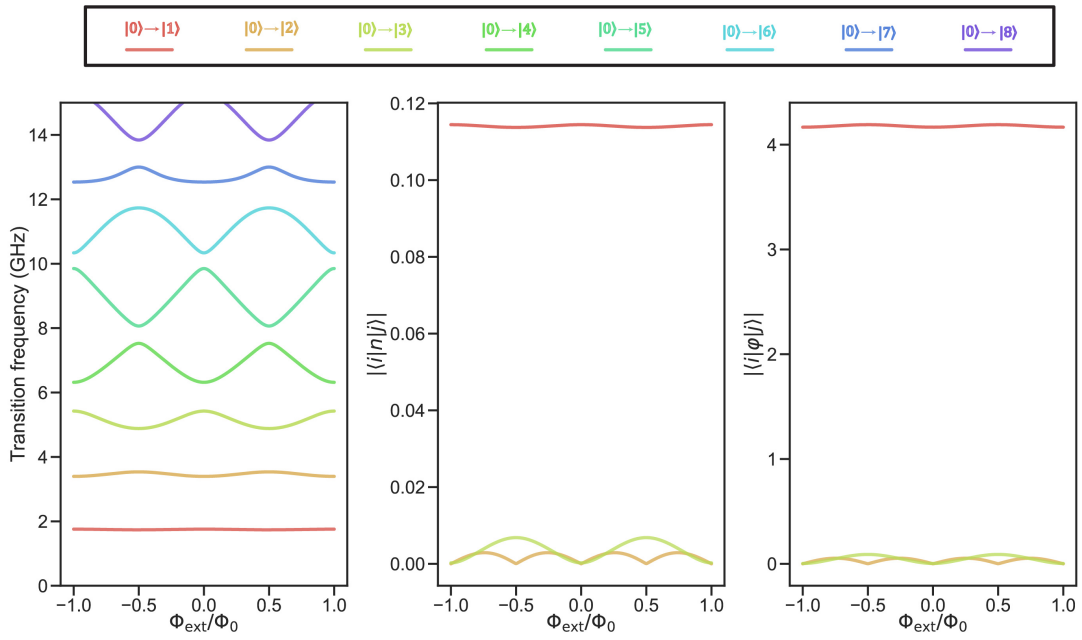

Figure 5.11: (A) The transition spectrum of energy combination #3. The first two transitions are nearly flux insensitive while by the 0→4 the transition recovers flux dependence. (B) The charge (n) matrix element for the first three transitions. (C) The phase (φ) matrix element for the first three transitions. The value for the 0→1 is larger than π.

5.3.4 Parameter regimes discussion

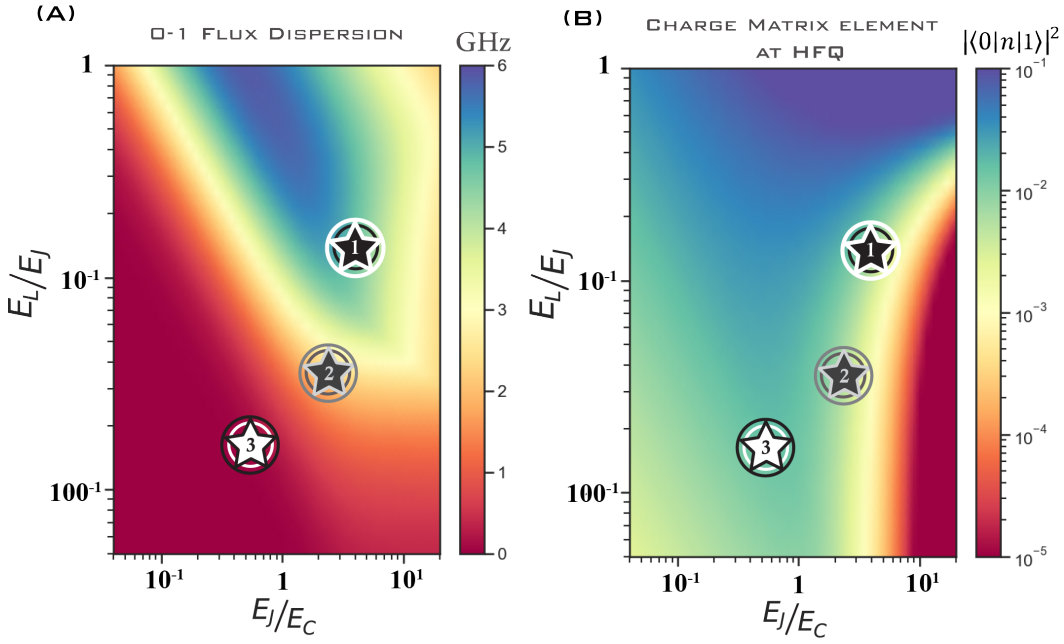

Figure 5.12: Various energy combination maps where the three combinations discussed in depth are highlighted by the stared points. In the simulation, E_J is kept constant at 4 GHz. In (A) the color scale represents the flux dispersion. (B, C) represents the charge matrix elements at HFQ and IFQ respectively.

Other fluxonium energy combinations not explored in this thesis include: "heavy fluxonium" [197], "inductively-shunted transmon" [72], and "C-shunt flux qubit" [193].

In these regimes, E_J is larger while E_C is lower in order to gain phase localization while E_L is variable. By going in the converse direction to phase delocalization, new interesting dynamics still arise further emphasizing the richness of the fluxonium qubit and the ability to dramatically alter the transition frequencies and matrix elements just by engineering the three energy scales to your liking.

5.4 Coupling to fluxonium

In order to read out the quantum state of the fluxonium, a resonator is coupled to the qubit which in turn couples it to the incoming microwave ex-

citations and the environment. The read-out resonator is probed after exciting transitions with a separate second tone which enables the spectra/time-domain dynamics to be measured experimentally.

In this thesis, fluxoniums are capacitively coupled to 3D cavities and inductively coupled to 2D resonators alike. In both cases, the read-out frequency obtains a dispersive shift which produces a measurable signal of the qubit state.

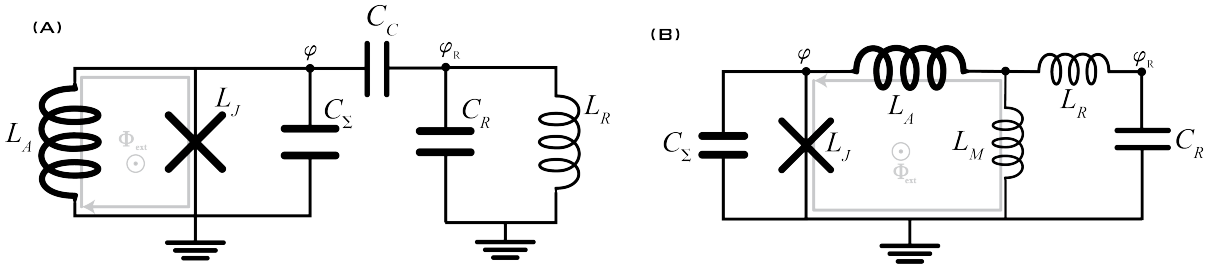

Figure 5.13: The two coupling schemes used in this thesis to couple to the read-out mode. (A) A fluxonium qubit is capacitively coupled to an LC oscillator read-out mode which represents a 3D cavity. The two systems are coupled through the charge on capacitor C_c. (B) A fluxonium qubit inductively coupled to an on-chip 2D read-out mode. The two systems are coupled by the shared current in the inductor L_M.

Depending on the exact dynamics/geometry of the coupling scheme, there can be a mutual charge/ electric field for $\hat{n}$ type coupling or mutual current/magnetic field for $\hat{\varphi}$ type coupling.

5.4.1 Capacitive coupling to a 3D cavity

Coupling a 3D-copper cavity with the fluxonium circuit amounts to having capacitance to the box through an antenna that protrudes from the small junction leads. We couple to the electric field of the 3D-copper cavity's lowest fundamental resonant frequency while the lower frequency qubit is excited by capacitive coupling to the signal input pin instead of the cavity itself. The fluxonium's Hamiltonian $\mathscr{H}_f$ will have new terms added which need to incorporate the coupling between the cavity and the qubit as well as the cavity's own energy corresponding to the read-out mode. For a fluxonium capacitively coupled to a resonator the generic Hamiltonian takes the

form:

$$\mathscr{H}_f + \mathscr{H}_c + \mathscr{H}_g = \mathscr{H}_f + f_r r^\dagger r + i g_r (r^\dagger - r)\hat{n} \tag{5.20}$$

Where f_r is the resonator frequency, g_r is the coupling strength, $\hat{n}$ is the charge operator for the qubit, and r ($r^\dagger$) is the lowering (raising) operator for the resonator. The resonator's Hilbert space is orthogonal to fluxonium's where the diagonalization uses tensor products of the two Hilbert spaces to make a composite new basis.

The governing equations of motion can be derived from basic circuit analysis [136]:

$$\mathscr{L}_f^{\text{cap}} = \frac{C_J + C_\Sigma}{2}\dot{\varphi}^2 + E_J \cos\varphi - \frac{1}{2L_A}\varphi^2 + \frac{C_R + C_c}{2}\dot{\varphi_R}^2 - \frac{1}{2L_R}\varphi_R^2 + C_c \dot{\varphi}\dot{\varphi}_R \tag{5.21}$$

and when transformed into the generic Hamiltonian form the variables become defined as:

$$\begin{aligned} g_r^n &= 2e\left\{\frac{\hbar^2 C_R}{4L_R}\right\}^{(1/4)} \times \frac{C_c}{C_\Sigma C_R} \\ f_r &= \sqrt{\frac{1}{(C_R + C_c)L_R}}\ ,\ C_{\text{tot}}^Q = C_\Sigma + C_c \end{aligned} \quad . \tag{5.22}$$

A consequence of this coupling scheme is the C_c re-normalizes the capacitance shunting the small junction where the total shunting capacitance becomes C_{tot}.

5.4.2 Inductive coupling to a 2D resonator

Another way to consider coupling to the fluxonium is by sharing mutual inductance with an on-chip resonator as was first done in [95, 167]. The resonator in this case is a lumped element LC oscillator where the inductance is made from larger area JJs and the coupling is created by sharing a few mutual array junctions with the resonators. Increasing the coupling between the qubit and resonator amounts to increasing the amount of mutually shared junctions.

For a fluxonium that is coupled to a resonator through $\hat{\varphi}$ the generic

Hamiltonian is expressed as:

$$\mathscr{H}_f + \mathscr{H}_c + \mathscr{H}_g = \mathscr{H}_f + f_r r^\dagger r + g_r^\varphi (r^\dagger + r)\hat{\varphi} \ . \tag{5.23}$$

And by analyzing the circuit the Lagrangian can be found as:

$$\mathscr{L}_f^{\text{ind}} = \frac{C_\Sigma}{2}\dot{\varphi}^2 + E_J \cos\varphi - \frac{1}{2L_A}\varphi^2 + \frac{C_R}{2}\dot{\varphi_R}^2 - \frac{1}{2(L_R+L_M)}\varphi_R^2 + \frac{L_M}{L_A(L_R+L_M)}\varphi\varphi_R \tag{5.24}$$

which is further transformed into the generic Hamiltonian form where the variables take the form:

$$\begin{aligned} g_r^\varphi &= \frac{\Phi_0}{2\pi}\left\{\frac{\hbar^2(L_R+L_M)}{4C_R}\right\}^{(1/4)} \times \frac{L_M}{L_A(L_R+L_M)} \\ f_r &= \sqrt{\frac{1}{(L_R+L_M)C_R}} \ , \ L_{\text{tot}}^A = L_A + L_M \ . \end{aligned} \tag{5.25}$$

This coupling scheme adds the additional inductance shared with the resonator to the total shunting inductance attached to the small JJ. The resonator can of course have inductance that is not shared with the qubit loop. This non-mutual inductance actually reduces the coupling between the qubit and the resonator. Furthermore, increasing the total inductance of the qubit loop can also reduce coupling.

5.4.3 Dispersive shifts

Dispersive shifts (χ) are when the resonator's resonance frequency becomes perturbed by the qubits state after the qubits state is excited from an applied RF tone. The dispersive shift can be calculated directly by diagonalizing the composite qubit-resonator system and seeing the difference of the resonator frequency when the qubit-cavity system is in $|1,0\rangle$ and the $|1,1\rangle$ state; where the first index is the number of excitations in the resonator and the second index is the qubit level excitation. The difference between the two states is the dispersive shift associated with the 0-1 transition. Depending on the coupling strength, g, the dispersive shift can range from several kHz all the way to several tens of MHz. The explicit definition of the dis-

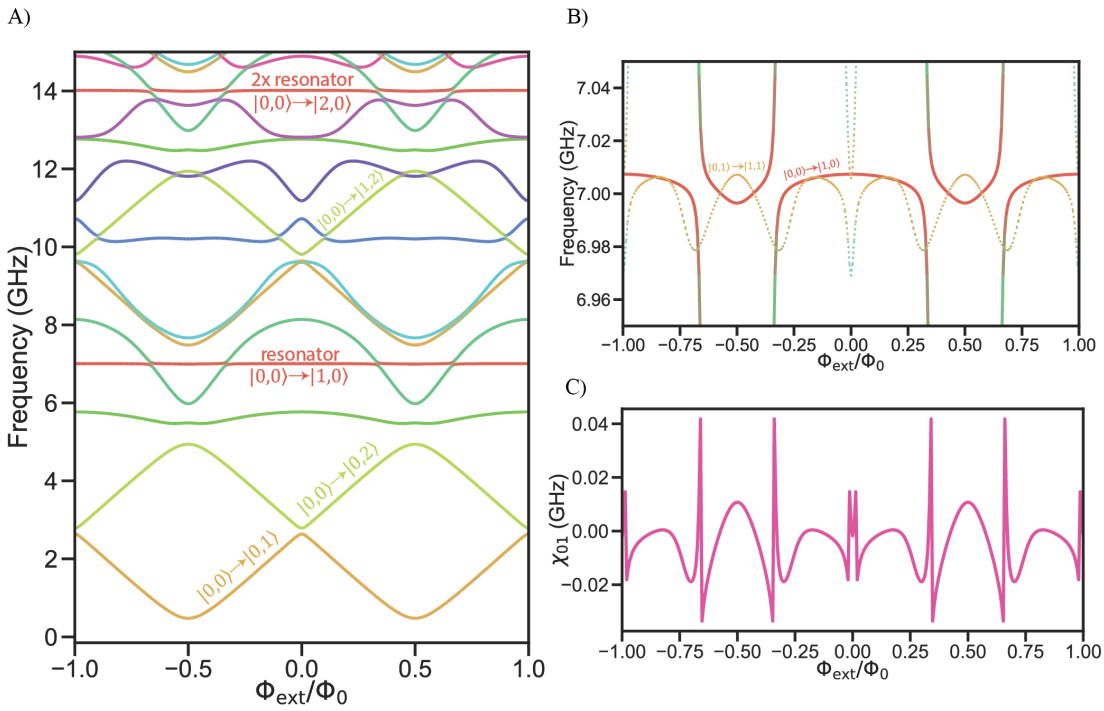

Figure 5.14: (A) The fluxonium-cavity spectrum for a readout mode located at 7 GHz. (B) The zoom-in on the resonator (red solid line) that hybridizes with the intersecting qubit states. The dashed lines correspond to the qubit in the excited state. (C) The difference between the solid red line and the closest dashed orange line in figure (B) gives the dispersive shift for the excited fluxonium qubit by the direct diagonalization method.

persive shift for a resonator given in terms of eigenvalues is:

$$\chi = \{E_{|1,1\rangle} - E_{|0,1\rangle}\} - \{E_{|1,0\rangle} - E_{|0,0\rangle}\} \ . \tag{5.26}$$

The dispersive shift can also depend on the number of photons in the resonator (n_r) so the shift of the resonator frequency for the qubit being in the ground or excited state sometimes needs to include higher resonator photon states for a more rigorous definition of the dispersive shift for large read out powers.

Another way to calculate dispersive shift is to use perturbation theory [198] of the uncoupled fluxonium and resonator states. This method illustrates the fluxonium's dispersive shift is not limited by the qubit-cavity detuning. In fact, the χ_{01} is due to the summation of the perturbing effects which include all transitions out of the ground and first excited states alike. When simulating this effect, it is found the transitions out of the ground state and first excited state which contribute most to the dispersive shift are the ones nearest in frequency to the resonator. The dispersive shift can be found using perturbation for capacitive coupling through the n-matrix element and for inductive coupling using the φ matrix element:

$$\begin{aligned}
\chi_{01}^{n} =& g_{qr}^2 \left\{ \sum_{k\neq 0} |n_{0k}|^2 \frac{2f_{0k}}{f_{0k}^2 - f_r^2} - \sum_{k\neq 1} |n_{1k}|^2 \frac{2f_{1k}}{f_{1k}^2 - f_r^2} \right\} \\
\chi_{01}^{\varphi} =& g_{\varphi r}^2 \left\{ \sum_{k\neq 0} |\varphi_{0k}|^2 \frac{2f_{0k}}{f_{0k}^2 - f_r^2} - \sum_{k\neq 1} |\varphi_{1k}|^2 \frac{2f_{1k}}{f_{1k}^2 - f_r^2} \right\}
\end{aligned} \tag{5.27}$$

The dispersive shift is important to consider, not only to read out the state of the qubit, and to generate the spectroscopy from 10 MHz - 20 GHz, but the dispersive shift also plays a crucial role in coherence and can limit the values of T_2 depending on the ratio of χ to the linewidth (κ) of the resonator; therefore understanding and optimizing the dispersive shift is crucial to improve measurements.

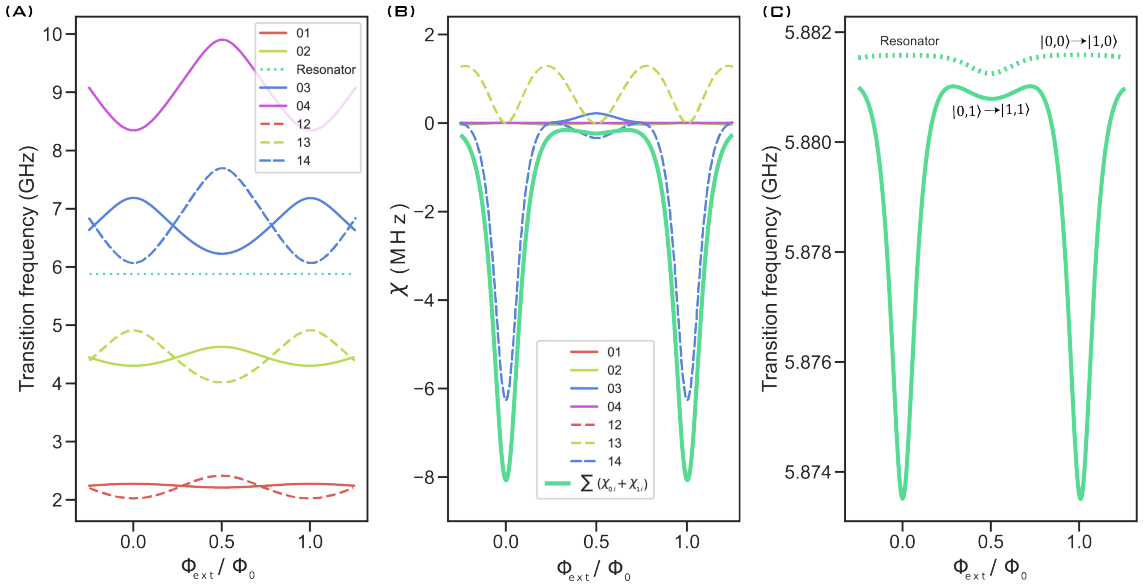

Figure 5.15: (A) The fluxonium-cavity spectrum for a readout mode located at 6 GHz. (B) The contributions to the dispersive shift on the resonator by various transitions out of either the ground or first excited state. (C) The resonator and the calculated dispersive shift through perturbation theory where all contributions are summed in the proper manner from (B).

5.5 Energy loss mechanisms

The decay or relaxation of a qubit is attributed to loss mechanisms paralleling the effect of a resistance on an electrical current in which the resistor dissipates power. However, for a qubit, the dissipation is due to the coupling of the circuit to lossy systems which are resonant with the qubit transition frequency and is given by Fermi's Golden rule introduced in chapter 3 where the lossy systems can be thought of as a bath of energy absorbers at a finite temperature (T). Due to the non-zero coupling to the lossy thermal bath, the qubit has a finite probability of decaying into the ground state after being excited.

The bath of absorbers is modeled as an ensemble of harmonic oscillators with the same transition energy as the fluxonium transition and finite temperature. In general, the lossy absorbers have a noise spectral density at frequency f_{01} that is highly sensitive to the ratio of excitation energy to thermal energy. This term is attached to the spectral density such that the

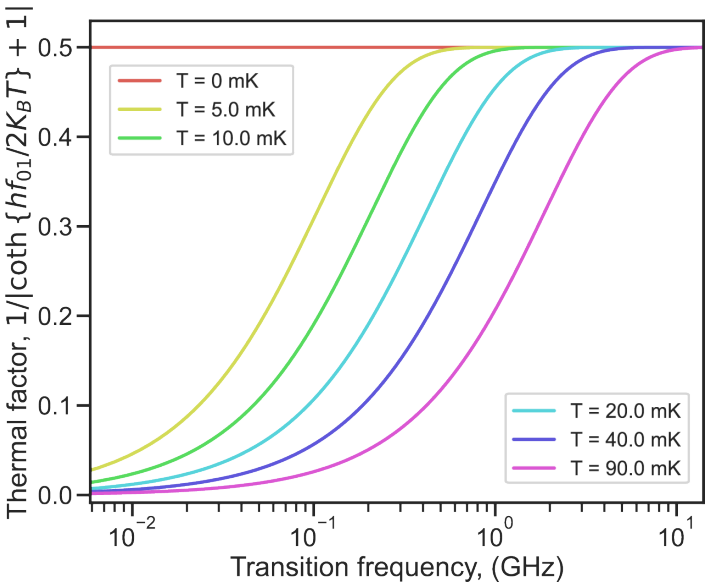

Figure 5.16: The thermal bath of absorbers contributes to energy relaxation depending on the ratio of the state transition energy to the thermal energy. The minimal possible is when T=0 or $hf > k_BT$ for a of contribution is 1/2.

inverse thermal factor is defined as:

$$\frac{1}{T_1} \propto \left\{ \coth\left(\frac{\hbar\omega_{01}}{2k_bT}\right) + 1 \right\}. \tag{5.28}$$

For $T = 0$ the inverse of the thermal factor becomes two and for $T \neq 0$, energy relaxation time becomes dependent on this term when $hf_{01} \sim k_BT$. Ideally, the thermal energy is much less than the transition energy; yet this is not always the case becoming a noticeable factor at 20 mK temperatures for $f_{01} < 500$ MHz.

5.5.1 Purcell limit

The first mechanism considered is the decay of the qubit state into the read-out apparatus. The read-out is coupled to the qubit and when the qubit transition frequency nears the read-out resonator, the qubit excitation has a large chance to spontaneously decay into the resonator which is coupled to the driving ports [18, 153].

To illustrate this effect, the “classical” Purcell effect is firstly considered, where we follow [80] yet for an inductively coupled qubit. In the considered

reduced model the qubit is expressed as an RLC circuit where $T_1 = RC$. Treating everything external to the small junction as the shunting admittance and finding the value for R as $R = Q_{\text{tot}} Z_r$ where Z_r is the impedance of the resonator the expression for T_1 is:

$$\frac{1}{T_1} = \frac{\text{Re}[Y(\omega_{01})]}{C_J} \,. \tag{5.29}$$

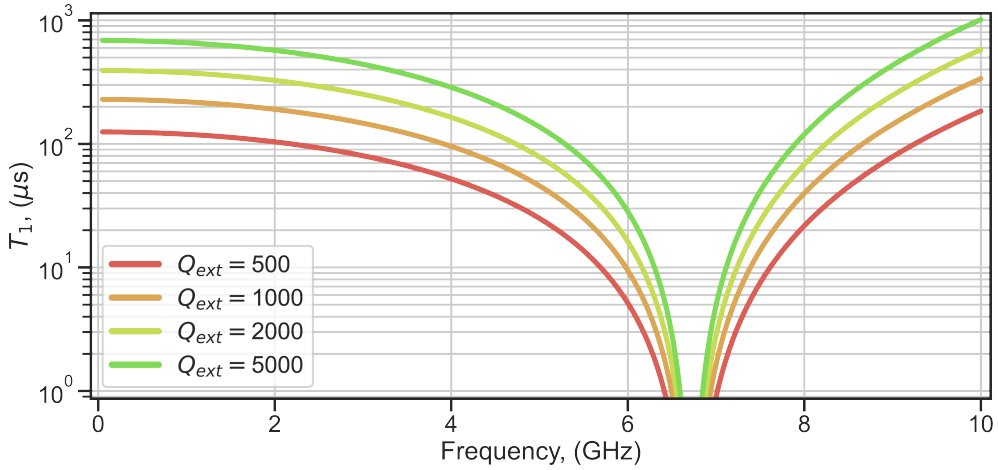

Figure 5.17: The Purcell limit to T_1 for a fluxonium with the second energy scale combination inductively coupled to a resonator at $f_r \sim 7$ GHz with a Q_{int} of 10^4. The plot shows the "classical" consideration for the Purcell effect for different values of the resonators Q_{ext} while sweeping the possible values for f_{01}.

Using Fermi's Golden rule, the quantum expression for the spontaneous relaxation of the qubit into a resonator excitation is:

$$\frac{1}{T_1} = \frac{\omega_{01}}{\hbar} \varphi_0^2 |\langle 0|\hat{\varphi}|1\rangle|^2 \text{Re}[Y(\omega_{01})] \left\{ \coth\left(\frac{\hbar\omega_{01}}{2k_b T}\right) + 1 \right\} \tag{5.30}$$

Where the admittance is found simply by classical circuit analysis producing the dip seen when the qubit frequency approaches the resonators. For the fluxonium, this is usually no matter of concern due to the large detuning between the qubit and the resonator frequencies often by an entire order of magnitude when biased at HFQ.

5.5.2 Dielectric loss

For a lossy capacitor, a complex dielectric constant is introduced: $\varepsilon = \varepsilon_r + i\varepsilon_i$. The complex part will introduce a real component to the normally reactive capacitor. When taking into account the lossy element in between a parallel plate capacitor, the admittance will be defined as:

$$Y_{\text{cap}}[\omega] = i\omega C_{\text{eff}} \rightarrow i\omega(\varepsilon_r + i\varepsilon_i)C = i\omega(1 + i\tan\delta_C)C \ . \tag{5.31}$$

And the quality factor of such a lossy capacitor is then defined as:

$$Q_{\text{cap}} = \frac{Im[Y_c]}{Re[Y_c]} = \frac{\varepsilon_r}{\varepsilon_i} = \frac{1}{\tan\delta_C} \ , \tag{5.32}$$

where $\tan\delta$ is defined as the loss tangent and is commonly used as the quantity to represent the amount of losses. Typical values for Q_{cap} are in the range of $10^5 - 10^6$ for SCQC and the geometry of the capacitance also has been shown to play an important role in losses due to lossy dielectrics [184].

Now defining the spectral density of capacitive loss as:

$$S_{\text{cap}}(\omega) = \hbar\omega \times \left(\coth\left[\frac{\hbar\omega_{ij}}{2k_BT}\right] + 1\right)\frac{\omega C}{Q_{\text{cap}}} \tag{5.33}$$

and using Fermi's golden rule [158], dielectric loss in fluxonium can be modeled as a lossy shunting capacitor with admittance $Y_{\text{cap}}[\omega]$ with a relaxation rate:

$$\begin{aligned}\Gamma_1^{\text{cap}}(\omega_{01}) &= \frac{2}{\hbar}|\langle 0|\hat{\Phi}|1\rangle|^2 S_{\text{diel}}(\omega_{01}) \\ &= \frac{\pi}{2E_C}|\langle 0|\hat{\varphi}|1\rangle|^2\frac{\omega_{01}^2}{Q_{\text{cap}}} \\ &= 32\pi E_C|\langle 0|\hat{n}|1\rangle|^2\frac{1}{Q_{\text{cap}}}\end{aligned} \tag{5.34}$$

where the temperature is set to zero (T=0) in the above expressions. Here, E_C is the effective capacitance energy found experimentally from the fit to the spectrum, and $Q_{\text{cap}} = \tan\delta_C^{-1}$ is the effective quality factor. The dielectric quality factor appears dependent upon frequency such that lower

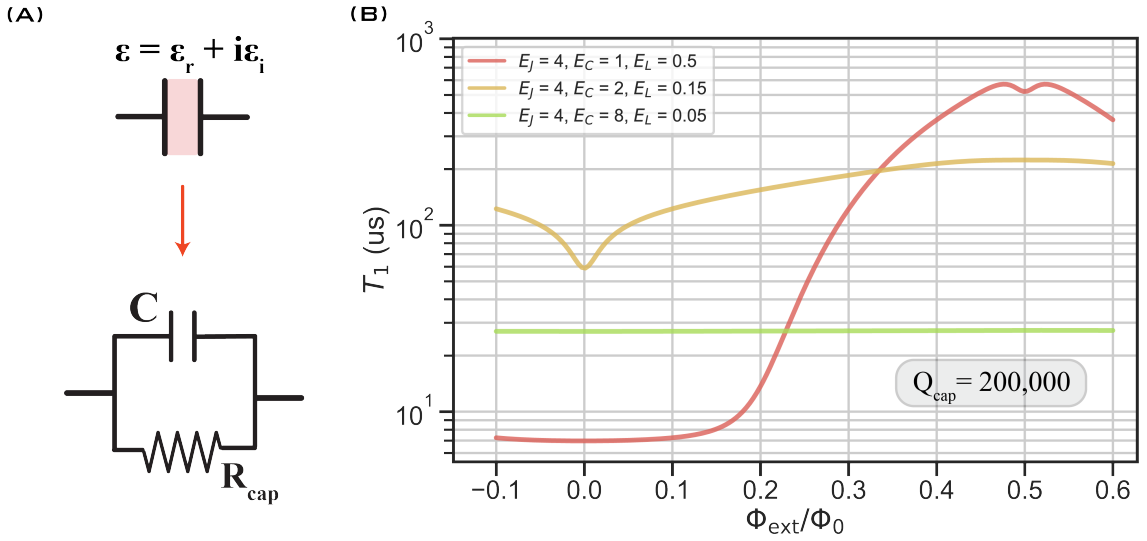

Figure 5.18: (A) A lossy capacitor is represented as a capacitor with a resistor in parallel. (B) The simulated T_1 for dielectric loss in the three energy scale combinations is discussed in the last section. Notice the charge matrix elements impact how the times change with flux.

frequency modes have higher Q-factors [135]. The frequency dependent Q-factor most commonly used in this work is defined as:

$$Q_{\text{cap}} = Q'_{\text{cap}} \left\{ \frac{2\pi \times 6\ GHz}{\omega_{01}} \right\}^{\varepsilon} \tag{5.35}$$

where ε is less than 1 and is taken to be 0.25 in simulations throughout this work.

The dielectric loss associated from the oxide of JJ's in the array may also contribute to dielectric loss. The chain junctions $E^A_{C_J} \approx 0.5 - 1.5$ GHz depending on geometry. Each junction contributes as a parallel loss channel:

$$\begin{aligned} \Gamma_1(\omega_{01}) &= \sum_j^N \frac{\pi}{2E^A_{C_J}} |\langle 0|\frac{\hat{\varphi}}{N}|1\rangle|^2 \frac{\omega_{01}^2}{Q^{JJ}_{\text{cap}}} \\ &= \frac{\pi}{2E^A_{C_J}} |\langle 0|\hat{\varphi}|1\rangle|^2 \frac{\omega_{01}^2}{NQ^{JJ}_{\text{cap}}} \ . \end{aligned} \tag{5.36}$$

If the oxide barrier (amorphous AlOx) was the sole contributor to relaxation then the bound for Q^{JJ}_{cap} from the simulation is Q^{JJ}_{cap}/N , which is the

same order of magnitude found in experiments in chapter 7 as reported in literature $Q_{\text{cap}}^{JJ} \sim 10^4$ [66, 140]. However, previous measurements of relaxation times across many fluxonium qubits with much larger junction array areas than the ones used in this thesis, report the loss tangent from AlOx in the junctions must have a much lower dielectric loss with the associated Q_{cap}^{JJ} an order of magnitude larger than 10^4 [135].

5.5.3 Inductive loss

A lossy inductance is represented in the same manner analogous to a lossy capacitor. Except now, for a lossy inductor $L \rightarrow L(\mu_r + i\mu_i) = L(1 + \tan\delta_L)$ and the circuit model changes such that the resistor, representing relaxation, is in series with the inductance. The quality factor is expressed as:

$$Q_{\text{ind}} = \frac{Re[Z_L]}{Im[Z_L]} = \frac{\mu_r}{\mu_i} = \frac{1}{\tan\delta_L} \,. \tag{5.37}$$

Typical values for inductive Q_{ind} are several orders of magnitude larger than Q_{cap} and range between $10^5 - 10^6$ for JJ arrays. Representing the spec-

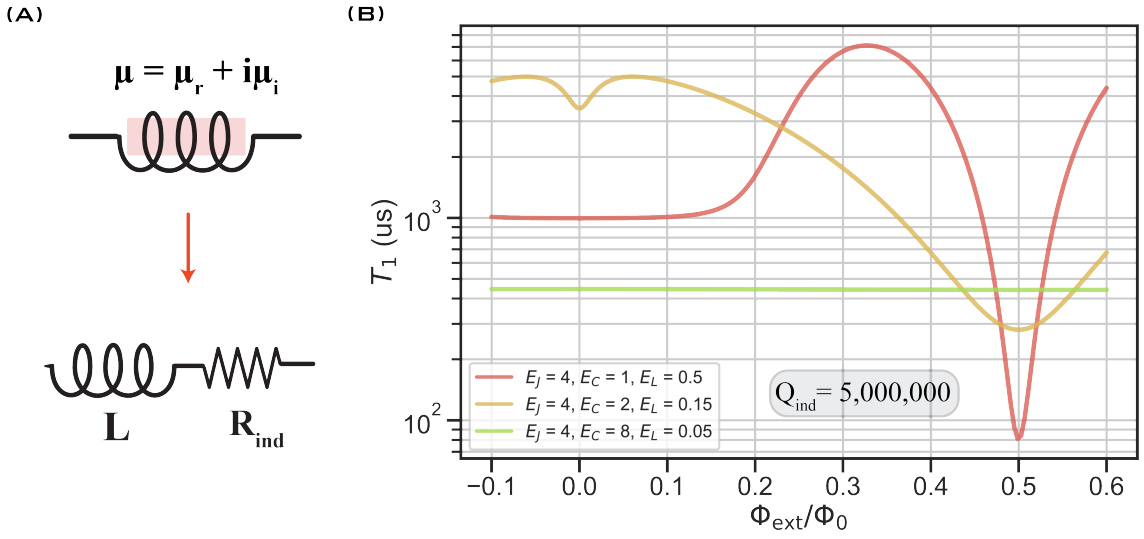

Figure 5.19: (A) A lossy inductance is represented as an inductor in series with a resistor. (B) The simulated T_1 for inductive losses in the three energy scale combinations are discussed in the last section.

tral noise density with the admittance of the lossy inductance as $Y_{\text{ind}} =$

$\tan\delta_L/\omega L = 1/\omega L Q_{\text{ind}}$:

$$S_L(\omega) = \hbar\omega \times \left(\coth\left[\frac{\hbar\omega_{ij}}{2k_BT}\right] + 1\right)\frac{1}{QL\omega} \tag{5.38}$$

and using Fermi's Golden rule the expression for the decay rate from a lossy inductance at T=0 is:

$$\begin{aligned}\Gamma_1^{\text{ind}}(\omega_{01}) &= \frac{2}{\hbar}|\langle 0|\hat{\Phi}|1\rangle|^2 S_{\text{ind}}(\omega_{01}) \\ &= 4\pi E_L|\langle 0|\hat{\varphi}|1\rangle|^2\frac{1}{Q_{\text{ind}}} \\ &= \frac{64E_LE_C}{\pi}|\langle 0|\hat{n}|1\rangle|^2\frac{1}{\omega_{01}^2 Q_{\text{ind}}}\end{aligned} \tag{5.39}$$

For the same relaxation time T_1, the ratio between inductive loss tangent and dielectric loss tangent is:

$$\frac{Q_{\text{cap}}}{Q_{\text{ind}}} = \frac{\tan\delta_L}{\tan\delta_C} = \frac{(\hbar\omega)^2}{8E_CE_L}, \tag{5.40}$$

which is much smaller than unity.

5.5.4 Quasiparticles

Non-equilibrium quasiparticles have been shown to limit qubit's energy relaxation time T_1 [69, 148].

Quasiparticles (qps) tunneling across the small JJ can absorb energy at the qubit frequency and contribute to energy relaxation of the qubit. The relaxation rate for qps tunneling in small JJ is [24]:

$$\Gamma_1^{\text{qp}_J}(\omega_{01}) = \frac{8E_J}{\pi\hbar}|\langle 0|\sin\frac{\hat{\varphi}}{2}|1\rangle|^2\sqrt{\frac{2\Delta}{\hbar\omega_{01}}}\cdot x_{\text{qp}} \tag{5.41}$$

where Δ is the superconducting gap for Al and x_{qp} is the ratio of the number of quasiparticle per Cooper-pair. Measured T_1 versus flux in this thesis indicates that x_{qp} is on the order of 10^{-8}, corresponding to less than a single quasiparticle in the entire system. Quasiparticles often have the signature of

producing a double exponential T_1 trace [69].

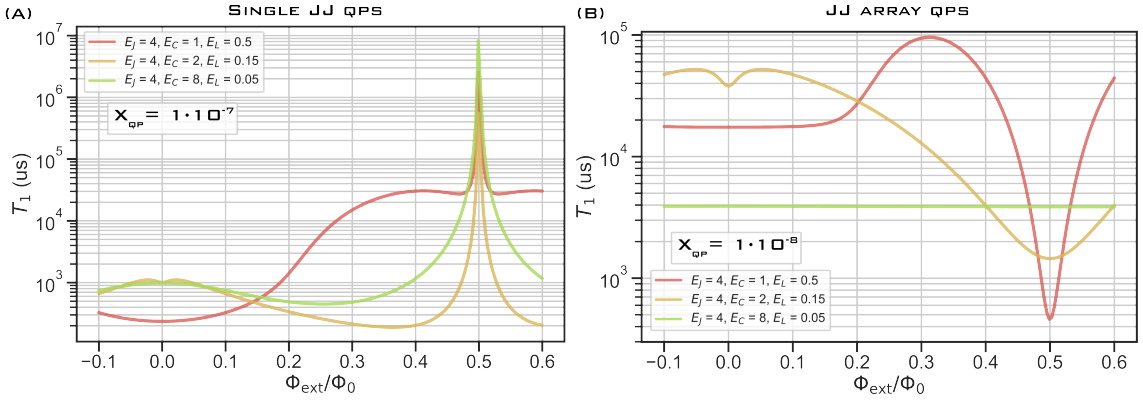

Figure 5.20: The simulated T_1 is limited by qps (A) across the small JJ and (B) in the JJ array. The values chosen for the quasiparticle density are the limiting values found for the measurements in this work and vary between the small JJ and in the array.

At the fluxonium's sweet spot, qp effects from tunneling across the small junction are suppressed by the partiy of the transition which has been observed in [148]. However, quasiparticles in the JJ array must also be considered as a possible cause of energy relaxation [23, 182] and are still present at HFQ with a rate defined as:

$$\Gamma_1^{\mathrm{qp}_A}(\omega_{01}) = \frac{8E_L}{\pi\hbar}|\langle 0|\frac{\hat{\varphi}}{2}|1\rangle|^2\sqrt{\frac{2\Delta}{\hbar\omega_{01}}}\cdot x_{\mathrm{qp}} \tag{5.42}$$

Techniques to mitigate qp effects include filtering the lines with eccosorb which have large attenuation at frequencies greater than the gap of Al which can potentially create qps by absorbing high frequency photons that leak through the line [81].

5.6 Dephasing mechanisims

Low-frequency noise sources are the main contributor to dephasing. These noise sources act as a slow variation to an external parameter which ultimately modifies the qubit frequency ever so slightly causing the relative phase on the Bloch-sphere to rotate. This noise source in fluxonium's are attributed to flux noise, residual cavity photons, and quantum phase-slips in

the JJ array.

5.6.1 Flux noise

An inherent decoherence source in solid-state devices is 1/f flux noise, found to originate from surface defects on the substrate. The spectral density of flux for electronics has clear 1/f scaling where the associated spectral density scales inversely with frequency and is defined as [17]:

$$S_{\Phi}(\omega) = 2\pi \frac{A^2}{\omega} \,. \tag{5.43}$$

Flux noise is found to affect superconducting flux qubits across more than an order of magnitude in frequency [193] where the noise amplitude, A, is found to vary between $10^{-5} - 10^{-6}\Phi_0$ [193] in flux-sensitive devices at cryogenic temperatures. Fluxonium's qubit transition is generally sensitive

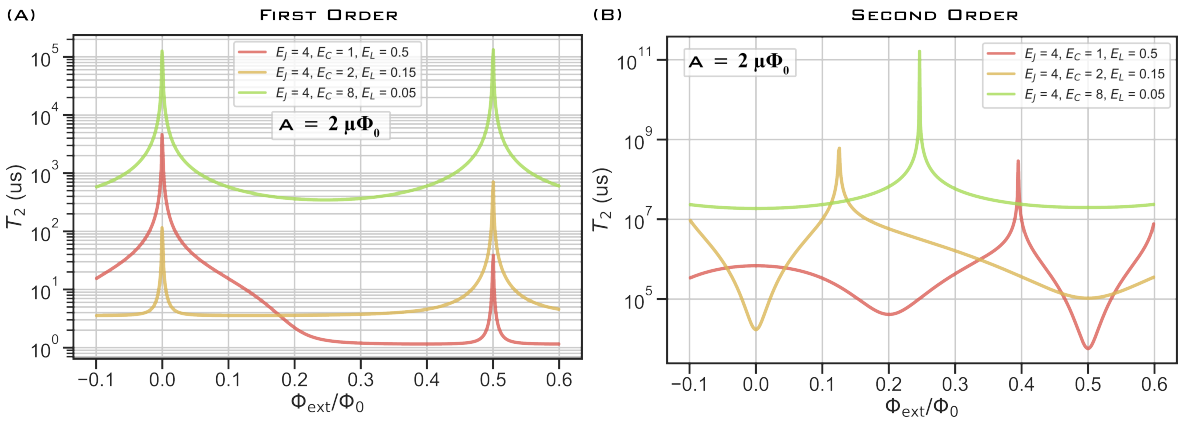

Figure 5.21: The simulated T_2 limited by (A) first order 1/f flux noise and second order 1/f flux noise with a noise spectral amplitude of $2\mu\Phi_0$. The simulation in (A) spikes to infinity at the sweet spots, the simulated curve does not show this due to the finite step of external flux chosen.

to flux noise which causes dephasing proportional to the sensitivity of the qubit transition to the external flux bias given by:

$$\Gamma_{\Phi} = \frac{\partial \omega_{01}}{\partial \Phi_{\text{ext}}} A \sqrt{\ln 2} \tag{5.44}$$

Illuminating the fact, lower flux dispersion protects the qubit's first-order

sensitivity at all flux points.

As the flux is tuned to half-integer flux, the qubit's first-order flux sensitivity goes to zero due to the change in the concavity of the transition. However, the second order sensitivity, $\partial^2\omega_{01}/\partial\Phi^2$, reaches local maxima, giving rise to a small limiting source to qubit's coherence where the relevant dephasing rate is [85]:

$$\Gamma_{\Phi^2} = \frac{\partial^2\omega_{01}}{\partial\Phi^2}A^2 \ . \tag{5.45}$$

5.6.2 Cavity temperature

The thermal dephasing rate due to hot cavity photons follows [196]

$$\Gamma_{\text{th}} = \frac{\kappa}{2}\text{Re}\left[\sqrt{\left(1+\frac{2i\chi_{01}}{\kappa}\right)^2+\frac{8i\chi_{01}n_{\text{eff}}}{\kappa}}-1\right] \ . \tag{5.46}$$

In the limit of low photon number at the cavity frequency, the expression simplifies to:

$$\Gamma_{\text{th}} = \frac{n_{\text{eff}}\kappa}{1+\kappa^2/\chi_{01}^2} \ . \tag{5.47}$$

The ratio of the cavity linewidth to the dispersive shift is the critical factor here. However, when $\chi_{01} > \kappa$, the coherence can still be large as long as the residual photon number is made sufficiently low. Dephasing by residual cavity photons can be understood as the cavity-causing the qubit to shift frequency due to Stark-like effects. This fluctuation to the qubit frequency can, in fact, be caused by parasitic chain modes as well [178].

5.6.3 Quantum phase-slips in the array

Reducing E_L by minimizing the junction area can create quantum phase slips in the array which are exponentially suppressed by the ratio E_J/E_{C_J} in large area JJ where the frequency of the phase slips can be expressed as [150, 155]:

$$\varepsilon_s^A = \sqrt{\frac{16E_JE_C}{\pi}}\left(\frac{8E_J}{E_C}\right)^{1/4}e^{-\sqrt{\frac{8E_J}{E_C}}} \ . \tag{5.48}$$

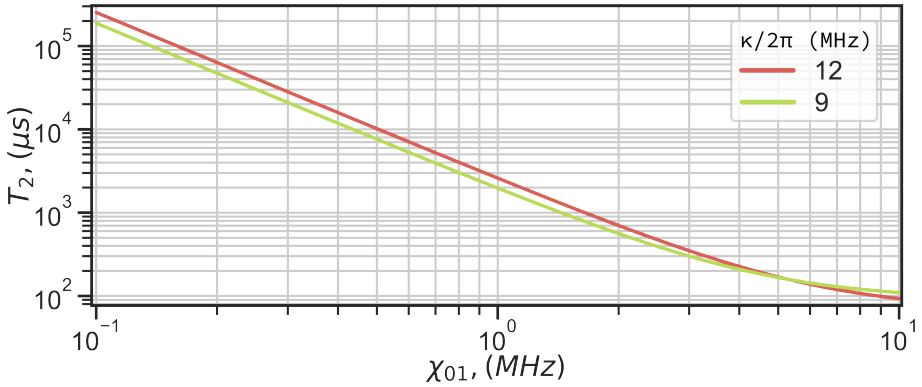

Figure 5.22: A resonator coupled to the qubit at an effective temperature (T_{eff}) has a residual photon number given by the Bose distribution and is more or less determined by the thermalization of the driving line. The ratio of the resonator line width (κ) with the value of χ_{01} gives the sensitivity of the resonator to fluctuating photon number and is the cause for a "jittering" f_{01}.

Using the chain junction impedance $Z_J^A = \sqrt{L_J^A/C_J^A}$ and the array junction plasma frequency $\omega_p = 1/\sqrt{L_J^A C_J^A}$ the slip frequency is put into the form:

$$\varepsilon_s^A = \omega_p \sqrt{\frac{8R_Q}{\pi^2 Z_J^A}} e^{-\frac{4R_Q}{\pi Z_J^A}} . \tag{5.49}$$

This expression is in fact the offset charge dispersion for the eigenenergy of a charge qubit when $E_J/E_C \gg 1$ (transmon regime). The phase-slip energy for array junctions is calculated to be in the kHz frequency range for the common array junction dimension. This value compared to other energy scales is small therefore we can treat the phase slips originating in the superinductance array as a perturbation to the system. Phase slips in the array will add an extra energy term to the usual fluxonium Hamiltonian

$$\tilde{\mathscr{H}}_f = \mathscr{H}_f(\varphi, m_{\text{ext}} - m) + \sum_m \frac{\varepsilon_s^A}{2} \Big[|m\rangle\langle m+1| + |m+1\rangle\langle m| \Big] \tag{5.50}$$

and treating this to first order it was found [116] the frequency contribution to the state energy is the array junction phase slip frequency multiplied by the wave function overlap difference for states 0,1 when displaced by 2π.

This frequency shift can now be converted into a linewidth by considering

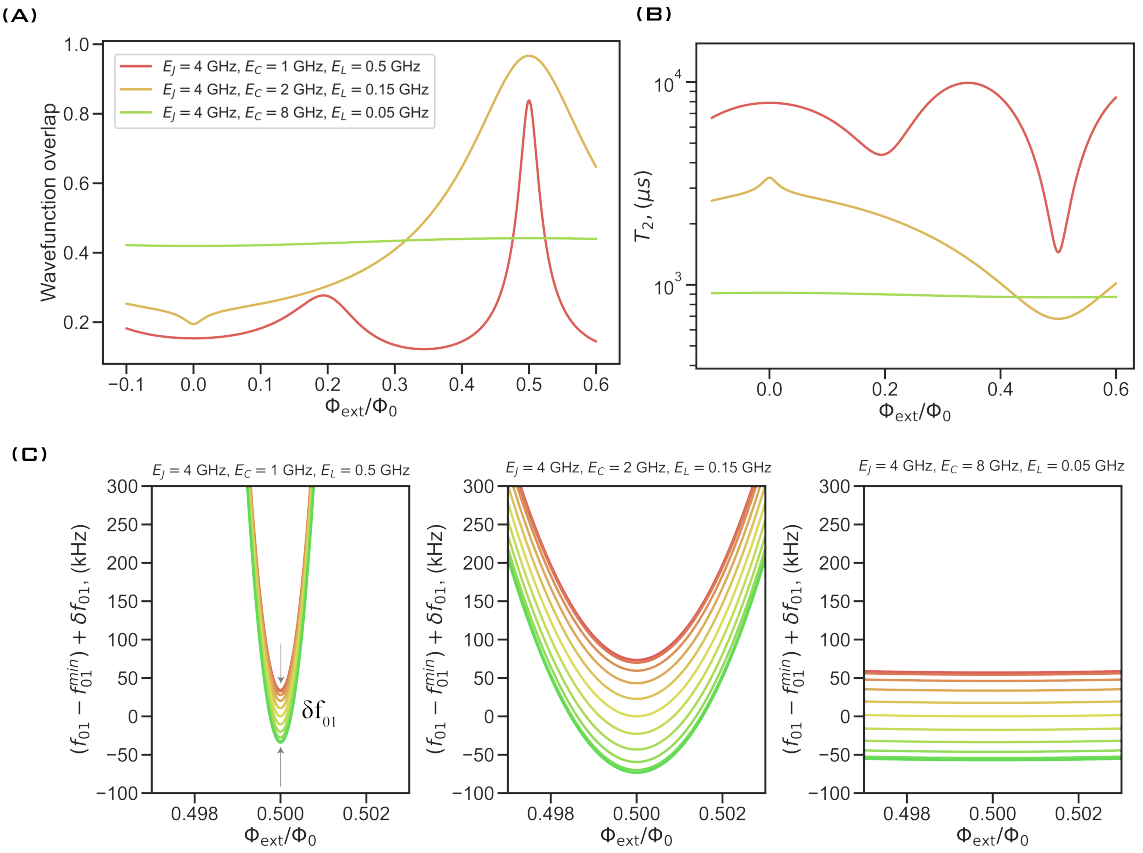

Figure 5.23: (A) The wavefunction overlap as a function of external flux for the three energy scale combinations. (B) The expected T_2 due to CQPS in the JJ array. In the simulation $E_J^A = 40$ GHz and $E_{C_J}^A = 0.85$ GHz; where the number of junctions (N) in the array is changed to create the value of E_L listed. (C) The calculated δf_{01} for each parameter combination. The scale for each is identical and also demonstrates the "sweetness" of each parameter regime at HFQ.

the offset charge Q_j on the jth junction as a random, Gaussian distributed variable such that $\varepsilon_s^A = \sum_j \varepsilon_{S_j}^A e^{2\pi i Q_j/2e}$ [149]. Putting this all together, the linewidth due to phase slips in the JJ array is given by the expression:

$$\delta f_S^A = \sqrt{N/2}\varepsilon_S^A \left| \int d\varphi \Psi_1(\varphi)\Psi_1(\varphi - 2\pi) - \int d\varphi \Psi_0(\varphi)\Psi_0(\varphi - 2\pi) \right| \tag{5.51}$$

where N is the total number of junctions in the array. This quantity is evaluated at any desirable external flux bias point and the dephasing due to this

process is $\frac{1}{T_2} \approx \sqrt{2}\pi\delta f_{01}$. This process becomes enhanced at HFQ where the transition energy is at a minimum [41, 119].

Mitigating CQPS in the arrays is accomplished by making array junctions with $E_J^A/E_{C_J}^A > 50$. This puts a limit on the inductance per unit length for a JJ array which means creating larger inductances without phase slips amounts to increasing the number of junctions. However, we will see in the next chapter, increasing the number of junctions means lowering the parasitic chain modes which will ultra strongly couple to the qubit.

5.7 Current state of the art fluxonium results

The current state-of-the-art single fluxonium results [49, 111, 135, 171] are for the qubit with the energy combination #1 while biased at HFQ. At this external flux point, the qubit transition is several hundreds of MHz and exhibits $T_1, T2 > 1$ ms [171].

While biased at HFQ the fluxonium is a protected qubit in the following way: the combined effect of a low charge matrix element and a low transition frequency offers T_1 protection from the seemingly limiting source for low-frequency fluxoniums which is dielectric loss [135]. Likewise, at HFQ the fluxonium is first-order insensitive to 1/f flux noise since $\frac{\partial \omega_{01}}{\partial \Phi_{ext}} = 0$. With proper thermalization of the line which should account for residual thermal cavity photons and qp sources, the fluxonium can reach $T_2^* > 1$ ms, consistently over multiple cooldowns.

On a quantum engineer note, future improvements to fluxonium could possibly be realized from higher Q substrates or antenna material [132, 146, 165, 185] which have less loss tangent than silicon or aluminum. Furthermore, improvements to the thermalization of the line to reduce thermal photons could help improve T_2. Finally noting, during the time of writing this thesis, performing two fluxonium gates experimentally has seen recent progress with fluxoniums in references: [7, 44, 56, 192].

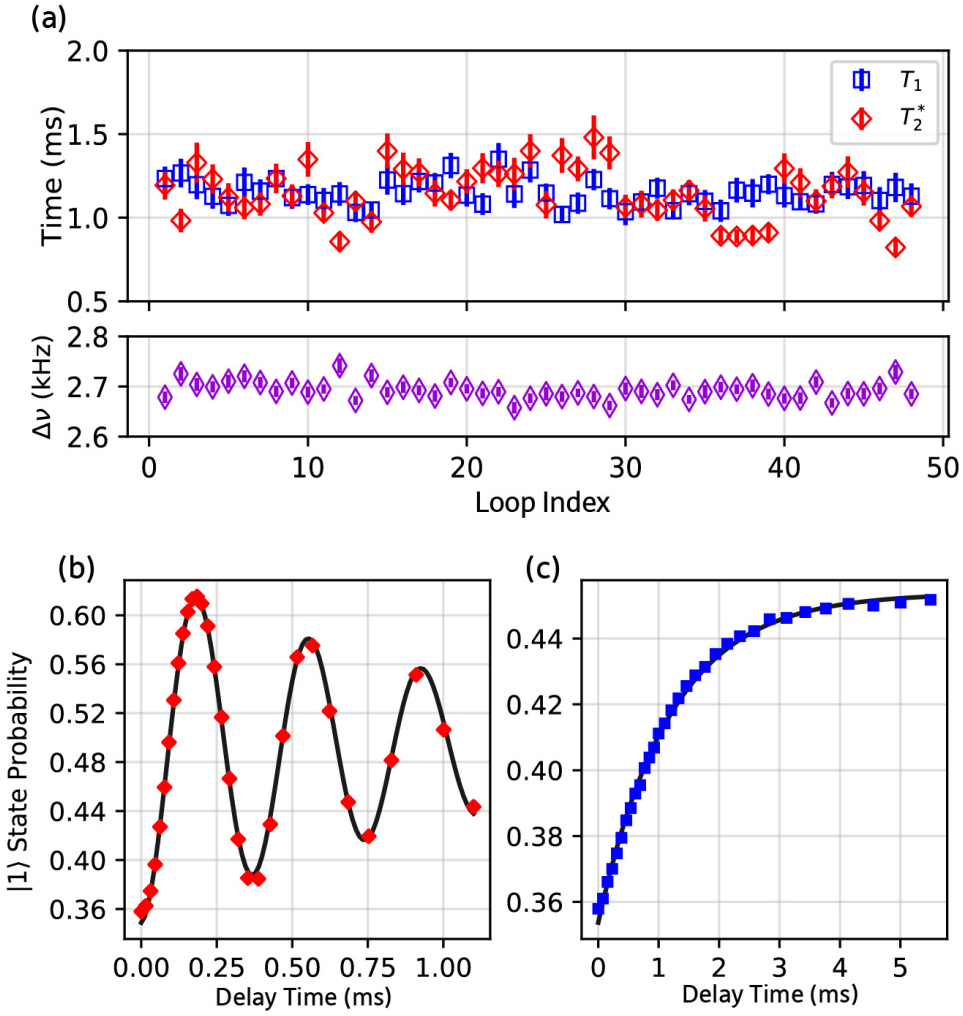

Figure 5.24: Figure reproduced from [171]. The fluxonium used in this experiment has energy combination 1. The time domain statistics show a remarkable coherence, consistently above 1 ms.

6
Parasitic chain modes

"..parasites seldom altogether abandon a monarch so long as the crown still glitters upon his head." — William Beckford, The Episodes of Vathek

In reality, large values of pure inductance are nearly impossible to achieve in the GHz frequency range due to non-negligible capacitance to ground (C_g) that any wire of finite dimension accumulates. Even a wire constructed with a maximal inductance density, using packed JJ arrays, struggle to achieve total inductance values of $L_{\text{tot}} > 500$ nH; before values of capacitance to ground begin creating the fundamental issue addressed in this chapter: the finite length inductance with self-capacitance forms a self-resonant mode (also called a parasitic mode) $f_{m=0} < 10$ GHz which ultra-strongly couples to the qubit spectrum. The problem becomes even more complex for larger and larger values of inductance since the first parasitic mode is now accompanied by many additional standing wave parasitic modes, all hosted by the JJ array.

In this chapter, a phenomenological/generic model to fit the fluxonium spectrum coupled to chain modes is introduced. The model accurately fits the spectrum from several hundreds of MHz all the way to 20 GHz and

reveals the inductance's parasitic modes hosted in the JJ array are ultra-strongly (g $\sim \omega$) coupled to the fluxonium qubit modes. The spectrum becomes dramatically altered by the presence of the coupled modes and is no longer completely fittable using the standard fuxonium Hamiltonian where the usual three energy scale values E_J, E_C, and E_L become effectively dressed by the chain mode.

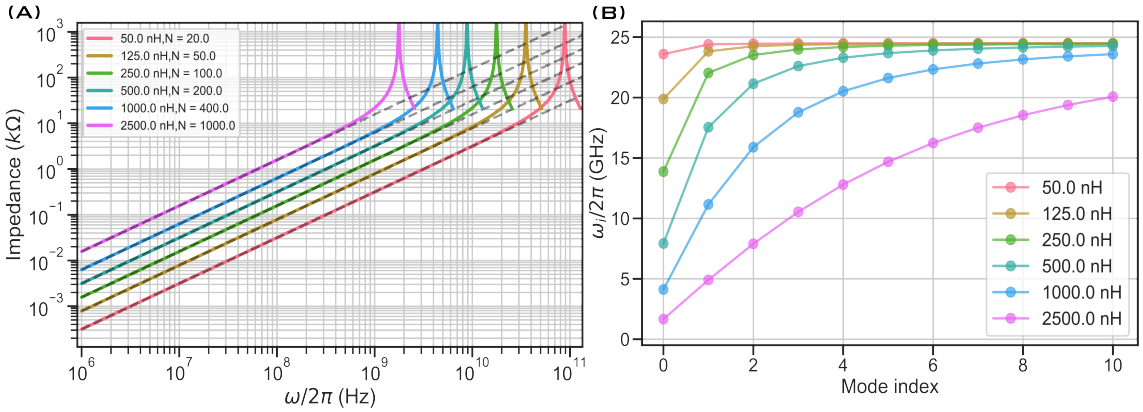

Figure 6.1: The operating frequency of an inductance decreases when increasing the total inductance values due to the ground capacitance accumulated by increasing the length. Increasing the inductance amounts to increasing the number of array JJs (N) and in turn $C_{\text{tot}} = N/2 \times C_g$ ultimately reducing the frequency where the first parasitic chain mode occurs. In (A), an inductance with $C_g = 20$ aF/JJ is simulated. (B) The increase in inductance has the consequence of the reduction of the first parasitic mode frequency which is now accompanied by the appearance of higher harmonic modes.

6.1 Total inductance value limit

The total inductance value achievable before the first chain mode becomes an issue is chiefly limited by the amount of parasitic capacitance C_g. The capacitance to ground is dominated by the electrostatic coupling between the two adjacent JJ arrays. The most basic consideration is to treat the shunting inductance as a transmission line resonator where the first mode is approximately:

$$Z(\omega) = Z_\infty \tan\left(\frac{2\pi f X}{v}\right) \longrightarrow f_0 = \frac{1}{4N\sqrt{L_J^A C_g^A}}. \tag{6.1}$$

In this equation, N is the total amount of junctions, X is the total length of the transmission line resonator, Z_∞ is the characteristic impedance, and v is the speed of light. Typical values for capacitance per JJ is C_g^A $15-22$ aF while typical inductance per JJ is L_J^A $1-3$ nH. Using these values we estimate the first mode for total inductance $L_{\text{tot}} > 500$nH to be less than 10 GHz. The first parasitic mode is accompanied by many other modes which become meaningful, especially for $L_{\text{tot}} > 1000$ nH where the second mode is situated around 10 GHz and the first mode is less than 5 GHz. The mode dispersion follows the same cut-off as the JJ transmission lines introduced in chapter 4. With this in mind, a fluxonium with $L_{\text{tot}} > 500$nH

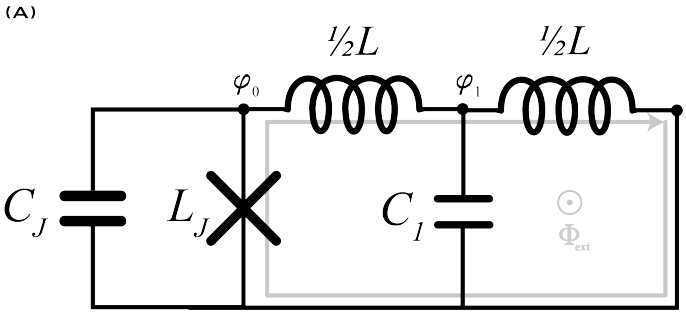

Figure 6.2: To introduce a single chain mode, the inductance is split into two parts by the parasitic chain mode capacitance C_1. Through circuit quantization, the expressions for the Hamiltonian of the circuit can be found with the addition of a new degree of freedom which now includes the phase of the chain mode. The expressions are equivalent in both the flux and the charge gauge.

must, realistically, have the pure shunting inductance accompanied by a self-resonant mode of the shunting JJ array. Furthermore, the coupling strength is non-trivial and cannot be treated simply as a perturbation to the spectrum. Although, chain modes are interesting in their own right, when coupled to a fluxonium spectrum the parasitic chain modes highly distort and complicate fits, and therefore a new model which incorporates the chain modes needs to be developed such that the recovery of the "true" fluxonium energy scale parameters can be extracted from the experimental spectrum.

6.2 Single chain mode fluxonia

The simplest case is when a single mode is coupled to the fluxonium. With the right circuit model, the Hamiltonian can be found using circuit quantization with the addition of one new capacitance (C_1) inserted between two inductors that are half of the original value as shown in figure 6.2. A new degree of freedom must be added across the parasitic capacitance and is defined as φ_1. The value of C_1 is approximately the summation of each junction's capacitance to ground, $C_1 \sim NC_g/2$.

Before diving into the exact circuit analysis, a naive approach is considered to demonstrate the impact of the chain's capacitance on the energy scale parameters found by the standard fluxonium fit. The presence of C_1 is first analyzed by means of finding the equivalent shunting impedance seen by the small junction with C_1 shifted towards the small junction as shown in figure 6.3. Setting the impedance of the two circuits in figure 6.3 equal

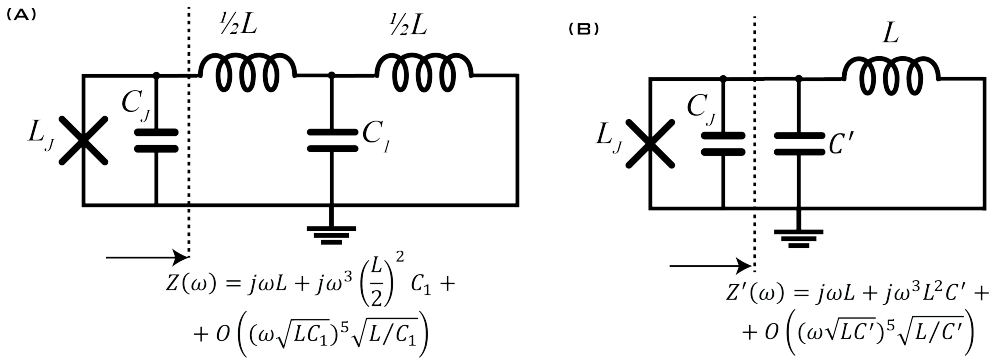

Figure 6.3: The effect of the chain capacitance C_1 on the small junction's charging energy can be approximated by setting the impedance of the circuit in (A) to the impedance in circuit (B) and solving for $C^{'}$.

to one another: $Z(\omega) = j\omega L + j\omega^3(\frac{L}{2})^2 C_1 = j\omega L + j\omega^3 (L^2)^2 C^{'}$ providing the expression for the modified capacitance seen by the small junction as $C^{'} = \frac{C_1}{4}$. This simple model indicates the shunting capacitance felt by the small junction is no longer just C_J but is modified by the lumped capacitance of the chain and is expressed as: $C_\Sigma = C_J + \frac{C_1}{4}$. The true JJ capacitance is then increased by the addition of one-fourth of the parasitic capacitance C_1 or equivalently by $NC_g/8$. Therefore, the charging energy (E_C^Σ) of the small

JJ using the fluxonium-only Hamiltonian ($\mathscr{H}_f$) is modified to:

$$E_C^{\Sigma} \approx \frac{E_C}{1 + E_C/4E_{C_1}} \,. \tag{6.2}$$

Now considering the fluxonium in figure 6.2 with the extra degree of freedom, φ_1, across the parasitic capacitance; the Hamiltonian can be derived in both the charge and flux gauge alike. These gauges are completely equivalent for the same values of $E_J, E_C, E_L, E_C^M, E_L^M$ but only when $L_\varphi = 2L_n$. Through circuit quantization the Hamiltonians in both gauges are found to be:

Flux-coupled fluxonia-chain mode Hamiltonian:

$$\mathscr{H}_{Jm}^{\varphi} = 4E_C\hat{n}^2 - E_J\cos(\hat{\varphi} - \varphi_{\text{ext}}) + \frac{1}{2}E_L\hat{\varphi}^2 + \sqrt{32E_LE_C^m}m^\dagger m + (8E_L^3E_C^m)^{1/4}(m + m^\dagger)\hat{\varphi} \tag{6.3}$$

Charge-coupled fluxonia-chain mode Hamiltonian:

$$\mathscr{H}_{Jm}^{n} = 4E_C\hat{n}^2 - E_J\cos(\hat{\varphi} - \varphi_{\text{ext}}) + \frac{1}{2}E_L\hat{\varphi}^2 + \sqrt{8E_L(E_C + 4E_C^m)}m^\dagger m + iE_C\left(\frac{128E_L}{E_C + 4E_C^m}\right)^{1/4}(m^\dagger - m)\hat{n} \,. \tag{6.4}$$

To understand this new Hamiltonian, the spectrum of the fluxonium-chain mode model in each of the three-energy scale combinations is simulated and displayed in figure 6.4 where the bare fluxonium spectrum is shown in (I) with the grey dashed lines giving the parasitic chain mode frequencies and (II) is the fluxonium-chain mode spectrum. The results of the simulation show the chain mode with the first combo has little to no effect on the spectrum under 15 GHz. This is in part due to the shorter chain length (smaller L and C_1). However, once entering into the second energy scale combination ($L_{\text{tot}} \approx 1\mu$H) the chain mode decreases in frequency and drastically alters the spectrum by hybridizing fluxonium transitions below 10 GHz with substantial coupling strength g. The third energy scale combination shows more and more modes emerging below 15 GHz with now the first three parasitic

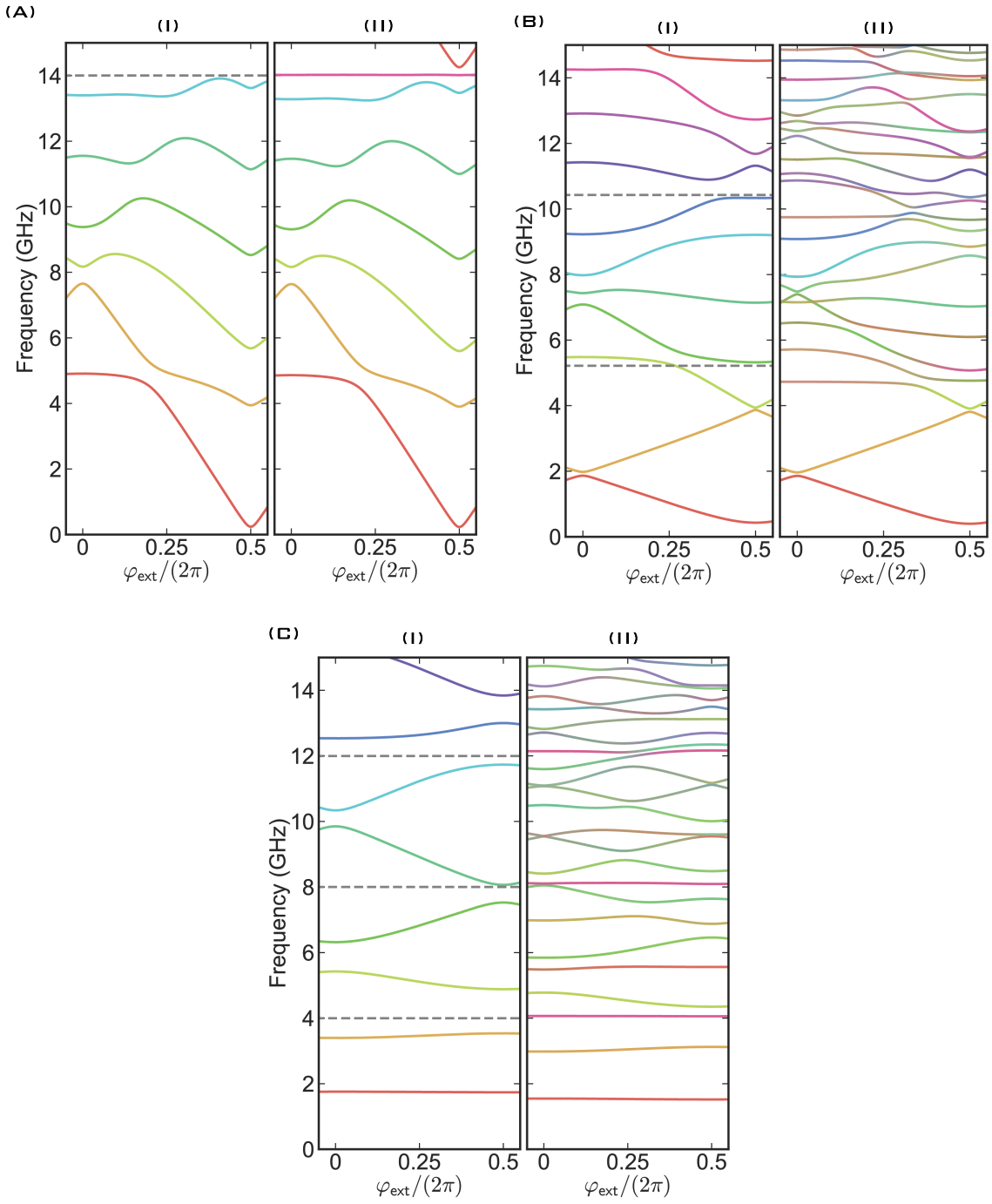

Figure 6.4: (A),(B),(C) are fluxonium spectrums in the 1st, 2nd, and 3rd parameter regimes. (I) of each shows the bare fluxonium spectrum while (II) of each shows the fluxonium-mode spectrum. The dashed line in (I) is the mode position in (II). The mode in (II) is the magenta line.

modes present.

Although the two gauges are completely equivalent, the values of the coupling scale differently. In the flux gauge, g increases with increasing mode frequency creating a divergent coupling in the flux gauge as the limit of the mode frequency $f_m \to \infty$. This creates the situation where chain modes closer to the plasma frequency couple stronger. However, the converse happens for the charge gauge where g decreases with increasing mode frequency such that coupling $g \to 0$ as $f_m \to \infty$. This behavior was also studied experimentally and analyzed in depth for chains with many more modes [126]. The charge gauge is a more intuitive model due to the scaling of the coupling and is used when considering the coupling of chain modes to the fluxonium in the remainder of the analysis throughout this thesis.

6.3 Modification of circuit parameters

By just simulating the fluxonium-chain mode spectrum shown in figure 6.4, the parasitic chain modes clearly have a significant impact on the spectrum which in turn modifies how the fit extracts the circuit parameters. In the following section, the modification of the usual fluxonium energy scales E_J, E_C, E_L is quantified by simulating a predetermined spectrum for fixed energy scales using the fluxoina chain mode Hamiltonian and sweeping values of C_1; this spectrum's first three transitions are then fit with the traditional 3-parameter fluxonium model. The input energy scale parameters used to simulate the fluxonia chain mode spectrum are compared to the energy scale values obtained for the fluxonium-only fit. The simulated spectrum is also fit by the fluxonium-model except with only one free parameter E_C while keeping E_J, E_L fixed.

The simulation fit to the fluxonium-only model shows the modification of all three fluxonium energy scales relative to the original values when sweeping the values of C_1 shown in figure 6.5. Interestingly, we find E_C decreases almost at a constant rate while E_J decreases quite drastically for $C_1 > 1$ fF. E_L is least affected but nevertheless increases slightly for larger values of C_1. The simulation and fit results offer the obvious conclusion that when a parasitic shunting capacitance C_1 is present within the chain, fitting the spec-

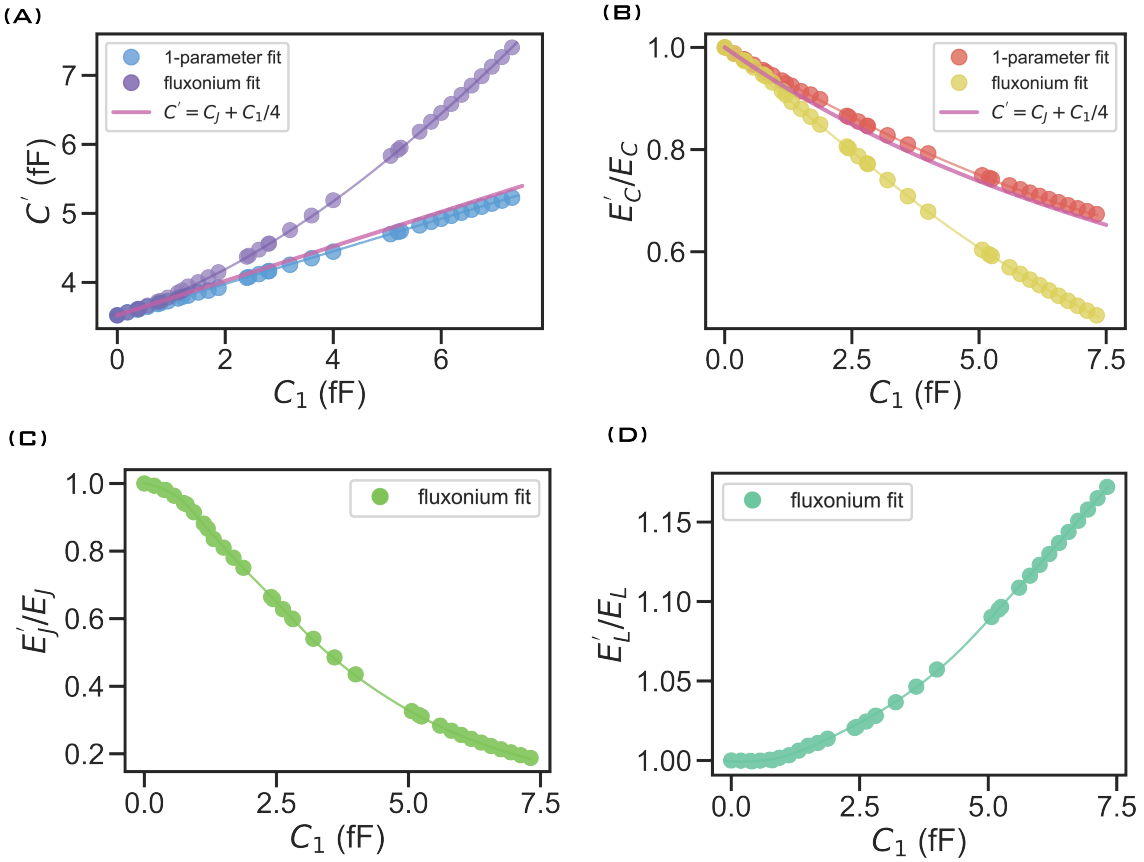

Figure 6.5: A generic fluxonium-chain mode spectrum is simulated and then the lowest transitions are fit using just the fluxonium model to see how $E_J, E_C,$ and E_L scale when changing C_1. The fluxonium-chain mode spectrum is firstly fit using all three energy scales and then again only fitting to E_C. The estimation from the naive approach shown as the magenta line in (A,B) offers a seemingly reliable estimation for the scaling of the charging energy due to the parasitic capacitance.

trum with the conventional fluxonium Hamiltonian is not a reliable source for extracting exact circuit parameters. Instead, effective circuit parameters from the fluxonium model are obtained. This conclusion was also stumbled upon experimentally, due to reliable fabrication the circuit parameters can be (semi-accurately) predicted so when the spectrum fit for a sample gave E_J, E_C, E_L dramatically different than what the fabrication expected it become clear something was amiss for samples with $L > 1\mu$H. Finally, when fitting the simulated spectrum to the fluxonia Hamiltonian with one degree of freedom only, E_C was found to scale approximately by $C = C_J + C'/4$

which is the solution to the analytic "naive" expression showed previously.

It's important to comment this analysis was done for a single chain mode only. In the presence of more than one chain mode, extra capacitance to ground must be introduced per chain mode resulting in more degrees of freedom and new expressions for the frequencies/coupling through direct circuit analysis.

6.4 Generic circuit model for chain mode fluxonias

For fluxonia with more than one chain mode and a flux-coupled resonator, a generic model for the coupled system can be introduced. The system is the fluxonium qubit ($\mathscr{H}_f$) flux coupled to a generic resonator whose Hamiltonian is $\mathscr{H}_r = f_r r^\dagger r$. When multiple chain modes exist there are chain modes added to the generic Hamiltonian term $\mathscr{H}_m = f_m m^\dagger m$ where the charge coupling term is expressed as $\mathscr{H}_c = i g^n_{Jm}(m^\dagger - m)\hat{n}$. The bosonic lowering (raising) for the resonator and chain modes are $r(r^\dagger)$ and $m(m^\dagger)$, respectively, which follow the standard commutation relation for harmonic oscillators raising/lower operators $[r, r^\dagger] = 1$. Each additional mode adds an additional $\mathscr{H}^k_m + \mathscr{H}^k_c$ term where the mode index is now represented by k. This produces the generic fluxonium-chain mode Hamiltonian:

$$\mathscr{H}_{frm} = 4E_C\hat{n}^2 - E_J\cos(\hat{\varphi} - \varphi_{ext}) + \frac{1}{2}E_L\hat{\varphi}^2 + f_r r^\dagger r + g_{Jr}(r^\dagger + r)\hat{\varphi} + \sum_{k=1}^{M}\left\{ f_{m_k} m_k^\dagger m_k - i g_{Jm_k}(m_k^\dagger - m_k)\hat{n} \right\}. \quad (6.5)$$

The Hilbert space of the Hamiltonian with more than one mode becomes dramatically increased since each operator is orthogonal and must be tensor producted together for diagonalization. To remedy this the individual Hamiltonians for the fluxonioum, resonator, and chain modes are diagonalized separately and then recast in a diagonal form where each individual Hilbert space can be truncated before performing the last coupled Hamiltonian diagonaization. The usual harmonic oscillator levels considered for each mode is around N=10.

6.5 Experimental verification of model

In this section, the experimental spectrum of a fluxonium device with four chain modes plus a resonator is accurately fit from 1-20 GHz using the charge-coupled fluxonia-chain mode model. Furthermore, a demonstration of how the fluxonium fit produces effective energy scales which differ significantly from the real circuit parameters is shown with real experimental data.

The device measured is a fluxonium circuit with over N=400 JJ in the array which is inductively coupled to an on-chip resonator through mutually shared inductance. The small JJ is at one end of the device far from the large capacitance associated with the resonator. The spectrum is taken with standard two-tone spectroscopy up to 16 GHz. Using only the lowest two transitions (0-1,0-2), the spectrum is first fit using the fluxonium-only model and the fluxonium-chain mode model resulting in drastically different circuit parameters even though both fits produce spectra identical to what was experimentally measured. Away from the two lowest transitions, the fluxonium model fit begins to deviate from the experimental spectra as seen in figure 6.6. This occurs at around 5-6 GHz, around where the first chain mode is situated. This fact demonstrates that if only the lowest transitions were used to fit an experimentally measured spectrum then the extracted energy scales will drastically differ from the true circuit parameters of the physical device. This produces an unreliable source for circuit parameters if only the lowest transitions are measured in a high-inductance device. The fabricator would indeed be quite confused about the unreliability/unpredictability of their procedure with these results extracted from a spectrum that should be fit with the chain modes incorporated!

Now, only taking a look at the fluxonium-chain mode model and performing a very detailed fit more realistic circuit parameters can be extracted along with chain mode frequencies and couplings. The first mode is situated at $f_{m_1} = 5.61$ GHz with a coupling strength $g = 4.44$ GHz. The ratio of coupling strength to mode frequency is $g/f = 0.79$; making this an ultra-strongly coupled system by definition [16, 173, 194]. The higher frequency spectrum becomes difficult to resolve in spectroscopy partly due

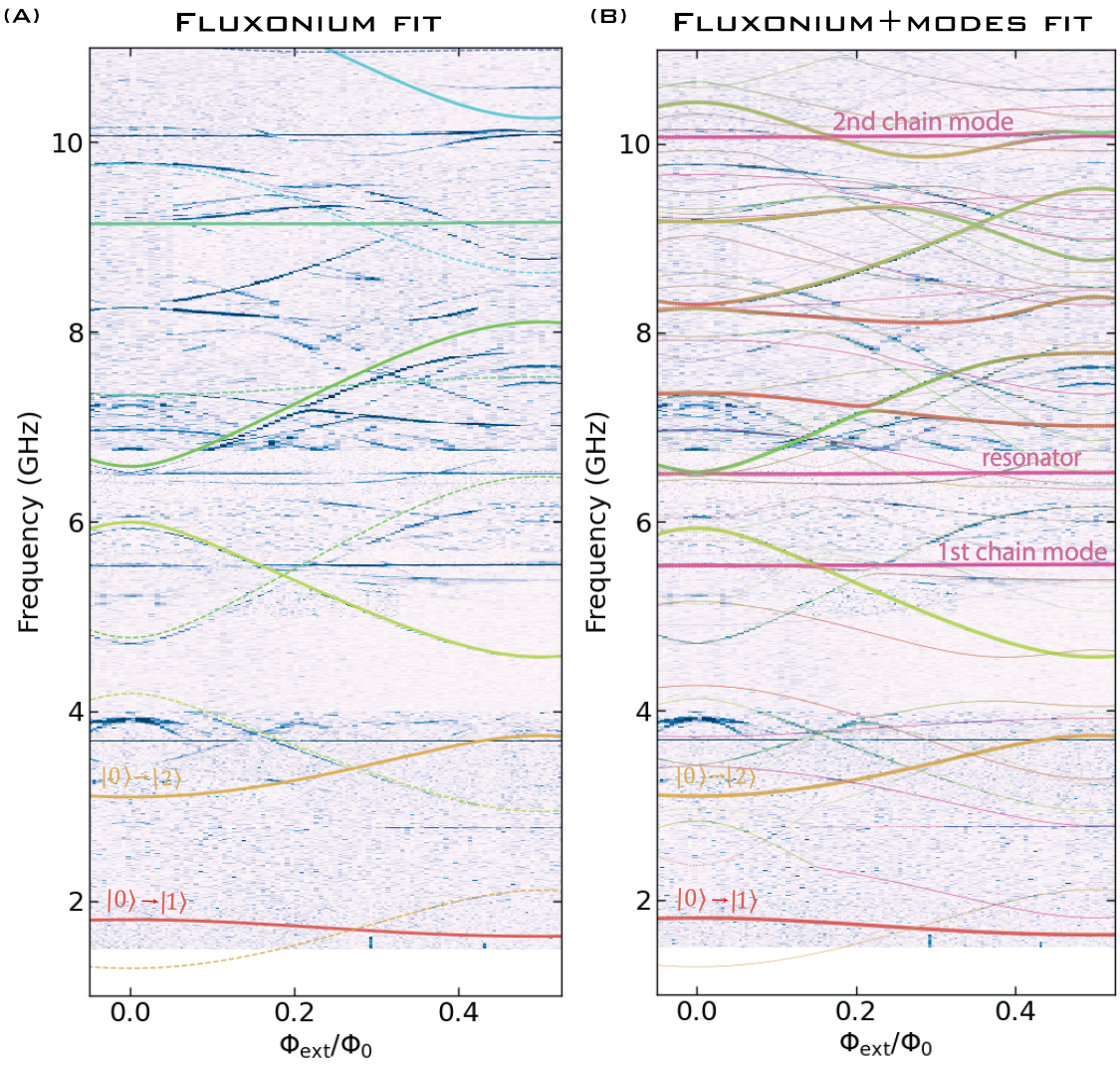

Figure 6.6: The measured spectrum of a fluxonium fit by the fluxonium-only model (A) and by the fluxonium-chain mode model (B). The simulated spectrum in both cases fit the lowest two transitions perfectly yet yields significantly different circuit parameters.

Model	E_J (GHz)	E_C (GHz)	E_L (GHz)
Fluxonium	3.05	5.41	0.073
Mode-fit	4.95	7.29	0.073

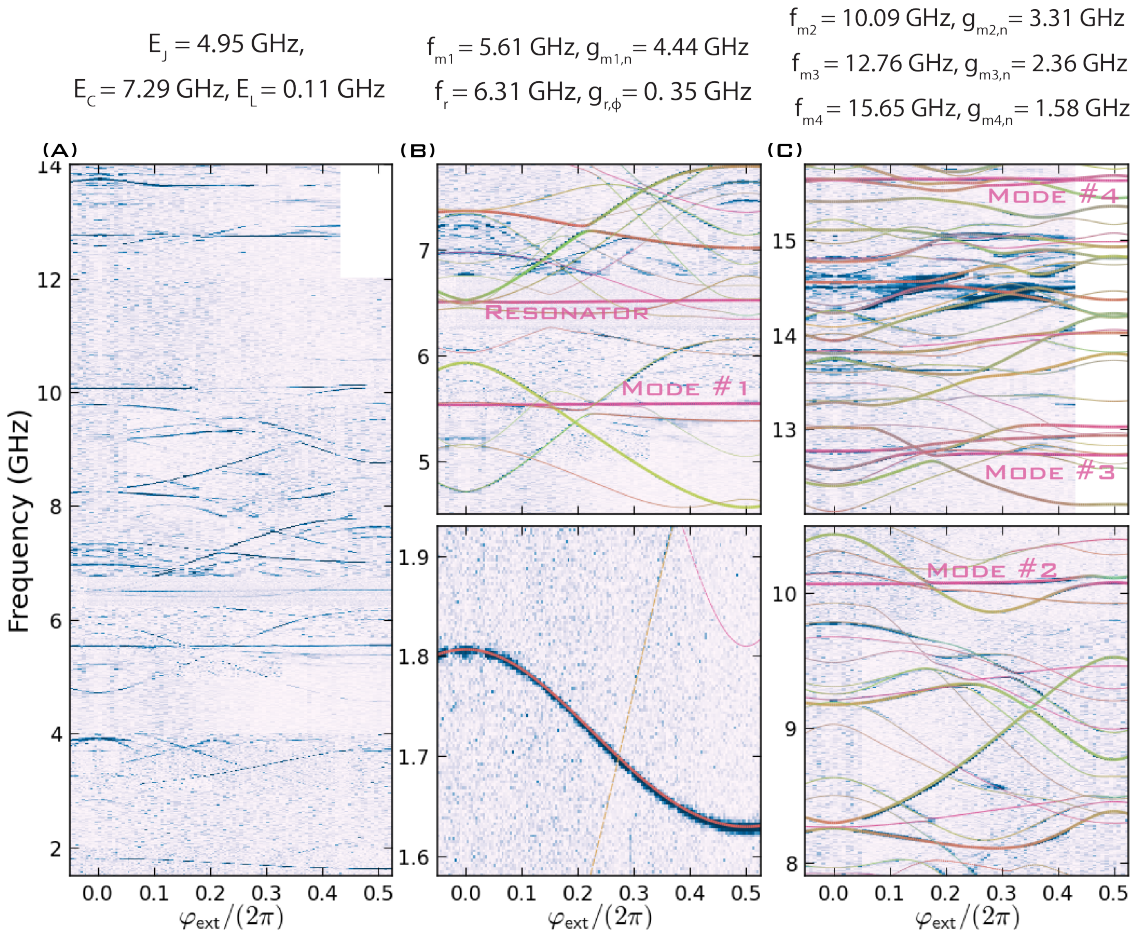

Figure 6.7: (A) The full spectrum of device A. (B-C) Shows the zoomed in fit plus the spectrum. The chain modes and resonators are labeled with the circuit parameters extracted shown as the header.

to the added transitions the chain modes introduce. The spectrum not only has the qubit transitions and the chain modes but also the added transitions between the chain modes and the qubit. This dramatically increases the number of transitions probable in spectroscopy and the higher frequency data hosts a plethora of qubit+chain modes which are hybridized.

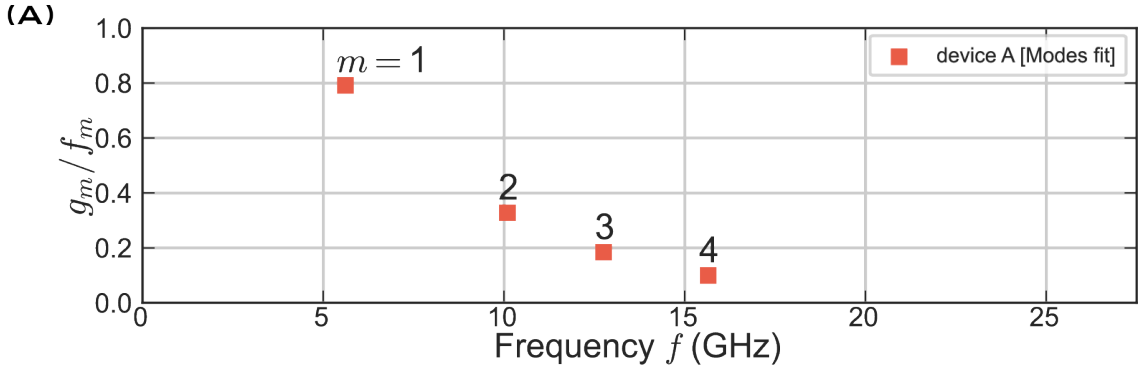

Figure 6.8: The ratio of mode coupling (g) divided by mode frequency. This ratio decreases with increasing mode frequency in the charge gauge. The first several ratios put parasitic chain modes in the ultra-strong coupling regime.

With the generic fluxonium-chain mode Hamiltonian, proper circuit parameters can be extracted. The caveat here is, low-frequency data is not sufficient, the spectrum must be mapped at least up to the first mode for large inductance fluxonium qubits otherwise the parameters will be unknowingly impacted. It's important to note for qubits designed with low E_C, this mapping may not be essential; as we demonstrated the charging energy shunting the JJ is the quantity firstly made effective for $C_1 < 1$ fF so if E_C is already dominated by a large external capacitance then this effect goes unnoticeable.

Although the generic model fits the fluxonium coupled to a resonator and four chain modes simultaneously, the model is still phenomenological and does not capture the microscope parameters of the chain junctions. A more rigorous model should include the capacitance of each JJ in the array to the various other elements to truly capture the physics at play. Several works have modeled chain modes using tensor networks [41] and have also shown the ability to diagonalize the coupled "microscopic" Hamiltonian in the chain mode as the basis [74]. Several theoretical works which derive analytic expressions for chain modes in fluxoniums in references [53, 178]

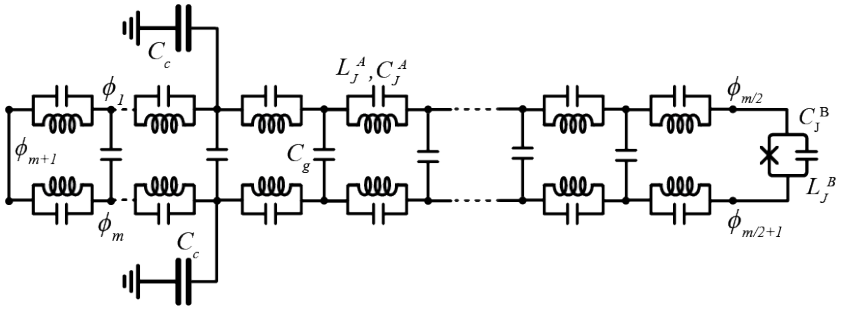

Figure 6.9: (A) The lumped element circuit analyzed. Each island has a degree of freedom ϕ_i where i is the island indexing and ranges from 1 to M=m+1.

also exist and can be extrapolated to the system in this work.

6.6 Classical normal mode analysis

Once fitting to the generic model, the comparison of the results with other models helps verify the correctness and further enables the extraction of finer capacitances – instead of introducing one extra capacitance per mode a more distributed model is considered yet is classical in nature. Here we consider the finite modeling of each JJ in the array as a classical LC oscillator that has capacitance to ground. The model is similar to the previous analysis done for junction arrays in a straight-line array [98, 152]. The Lagrangian for the inductive loop is made from the inductive and self-capacitance components of the Josephson junction as well as the electrostatic coupling between adjacent chains and the coupling capacitance of the bow-tie antenna. The inductive energy, whose energy component is normally $E_J^A(1-\cos(\phi_m-\phi_{m-1}))$, is approximated by only considering the quadratic term for each junction. In the model, the Josephson inductance can be represented by $\frac{E_J^A}{2}(\phi_m-\phi_{m-1})^2$ where $E_J^A=\frac{\Phi_0}{2\pi L_J^A}$. The degree of freedom in the system is the phase ϕ_m and is defined on the node between each junction. The number of array junctions in the system is M and the index m ranges from 1 to M+1 where the first and the last island are connected by the minimum and maximum of the index range. The Lagrangian

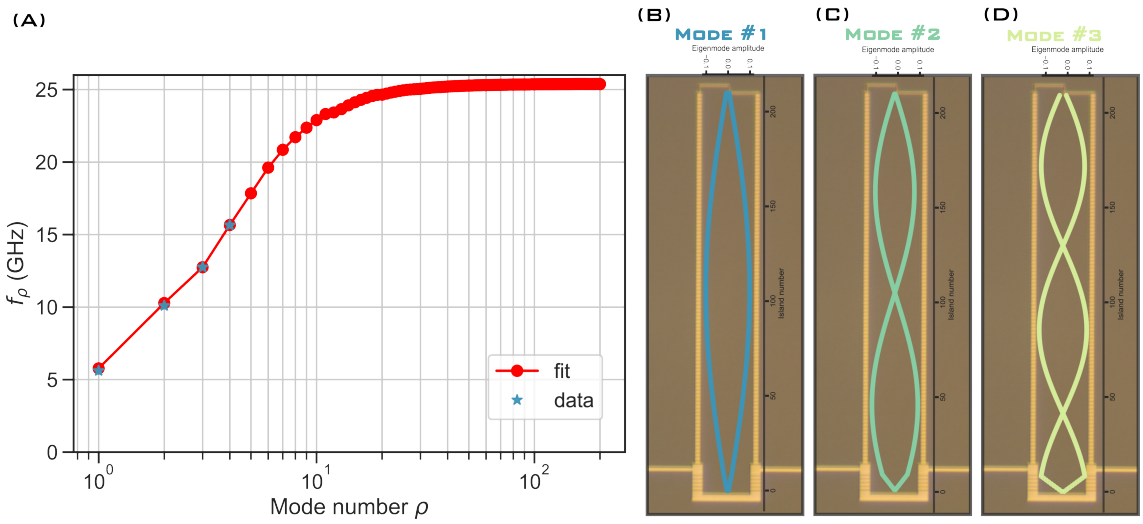

Figure 6.10: (A) The fit to the data using the classical lumped-element approach.(B-D) The eigenmodes structure for the fit chain modes. The amplitude is the normalized phase of each island. The resonator leads adds a unique feature due to the coupling capacitance.

of the chain system is found as:

$$\begin{aligned}\mathscr{L} =& \frac{C_c}{2}(\dot{\phi}_i^2 + \dot{\phi}_j^2) + \sum_{m=1}^{M+1} \frac{C_J^A}{2}(\dot{\phi}_m - \dot{\phi}_{m-1})^2 \\ &+ \sum_{m=1}^{M/2} \frac{C_g}{2}(\dot{\phi}_{M-m} - \dot{\phi}_m)^2 - \sum_{m=1}^{M+1} \frac{1}{L_J^A}(\phi_m - \phi_{m-1})^2\end{aligned} \tag{6.6}$$

where the small junction inductance and capacitance are inserted after construction in the middle at indexes m/2 and (m/2 + 1).

After piecing together the Lagrangian, the conjugate variable to each island phase is called island charge and denoted as Q_m must be solved for following basic Lagrangian mechanics $Q_m = \frac{\partial \mathscr{L}}{\dot{\phi}_m}$. Utilizing matrices the M-dimensional vector $\vec{Q}_m$ can be represented as the capacitive operator $\hat{C}$ acting on the M-dimensional vector $\dot{\vec{\phi}}_m$ such that $\vec{Q}_i = \hat{C}\dot{\vec{\phi}}_i$. The capacitive matrix and inverse inductance matrices are used to construct the Lagrangian matrix: $\mathscr{L} = \frac{1}{2}\dot{\vec{\phi}}^T\hat{C}\dot{\vec{\phi}} - \frac{1}{2}\vec{\phi}^T\hat{L}^{-1}\vec{\phi}$. The eigenfrequncy of the chain is given by the eigenvalue problem [187]:

$$\hat{C}^{-1}\hat{L}^{-1}\vec{\psi}_i = \omega_i^2\vec{\psi}_i \ . \tag{6.7}$$

The results of the eigenfunctions and eigenvalues are solved for the device fit using the fluxonium-chain model. The device consisted of a chain with 418 junctions which have a unit cell size of 350 nm per junction. The junction areas are 1.0 x 0.25 μm^2 with $E_J^A = 46.8$ GHz extracted from the fit for E_L, putting $L_J^A = 3.49$ nH. The intrinsic capacitance of the junction array is $C_J^A = 11.25$ fF found by the conversion $C_J^A = 45$ fF/μm^2. The four extracted mode frequencies are then fit to the lumped-element model finding the ground capacitance $C_g = 21.6$ aF or $E_C^g = 894$ GHz. This value is almost exactly as expected from similar parameters found in JJ transmission line measurements. The other parameters extracted from the fit was the coupling capacitance $C_c = 4.32$ fF or $E_C^c = 4.485$ GHz.

6.7 Finite-element simulation

Finally, the circuit is simulated using finite element software Maxwell 3D to find the all-to-all capacitance matrix. This simulation includes the entire device's geometry with the main difference is the individual chain junctions are bundled together into blocks consisting of 21 junctions per block and 20 blocks in total; 10 on the left and 10 on the right. The simulation is done by setting a finite static voltage from coupler to coupler and simulating the resulting capacitance of each element labeled as shown in figure 6.13. Due to the large differences in the feature sizes in the circuit which ranged from several mm to just above a μm, special care was taken when considering the finite element mesh around and between the junction array where the mesh size was much smaller than the features. The same consideration was taken around the bow-tie antenna. The sample was simulated as a perfect electrical conductor and the substrate was standard silicon.

The simulation result of interest is the average capacitance per junction in each block. The average capacitance per junction in each block to the blocks of the opposing line (to make it clear the left blocks capacitance to the right blocks) reveals that each junction, in fact, has capacitance to more than just the junction directly across. The simulation results show the next nearest few blocks directly across from the simulated block significantly contribute. For example, the left block 2 is seen to have non-negligible

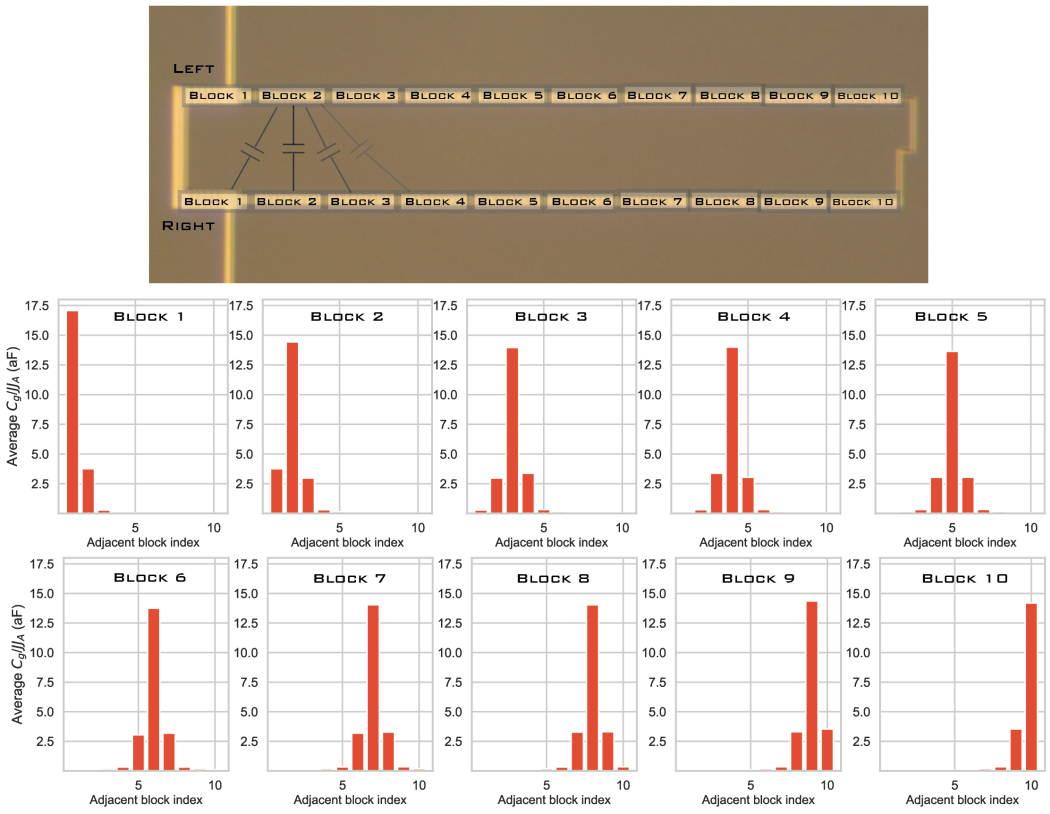

Figure 6.11: The actual measured device superimposed with a visual description of a JJ block. Each square encapsulates 21 chain junctions which make up a single block. The average value for the left to right block capacitances per JJ is shown in the histograms.

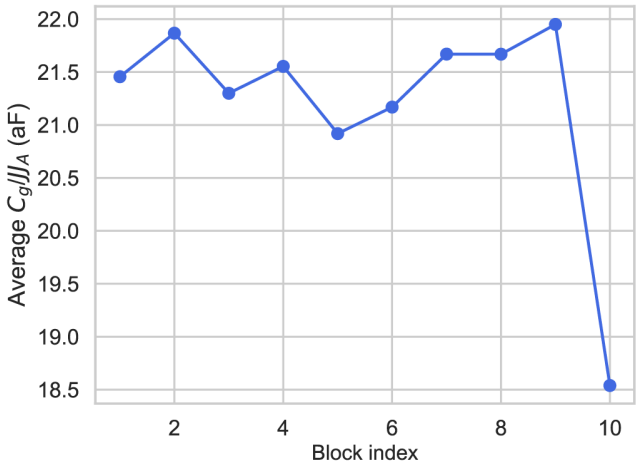

Figure 6.12: The sum of a single histogram which is the average C_g/ JJ. These are the differential capacitances to all opposite facing JJs, the capacitances give an average value which is right on point with the classical mode analysis.

capacitance to the right block 1,2,3,4 as shown in figure 6.11. The total sum of all junction-block to adjacent junction-block for each individual index gives an amount almost exactly the same as the one found in the classical analysis. The average C_g/JJ in each block is centered more or less around 21.5 aF. The last block shows a decrease of roughly 16 percent from the average value. The exact reason is speculated to be that there are simply no chain junctions on one side while also being sufficiently moved away from the resonator capacitance.

Finally, the simulation allows for the extraction of the junction island capacitance to the other circuit components not involved with the differential chain modes. The results show junctions couple to the near-side bow-tie antenna when on the far side away from the small JJ while the junctions by the small JJ end couple more strongly to the antenna. The value of this capacitance is actually less than the differential capacitance yet could contribute to coupling to noise sources. The total average capacitance of each block is shown to drop and stabilize further away from the bow-ties.

Using these results to simulate the all-to-all behavior of the complex capacitance matrix could prove insightful for optimizing the geometry of future devices. On a positive note, the summed C_g per junction in each block

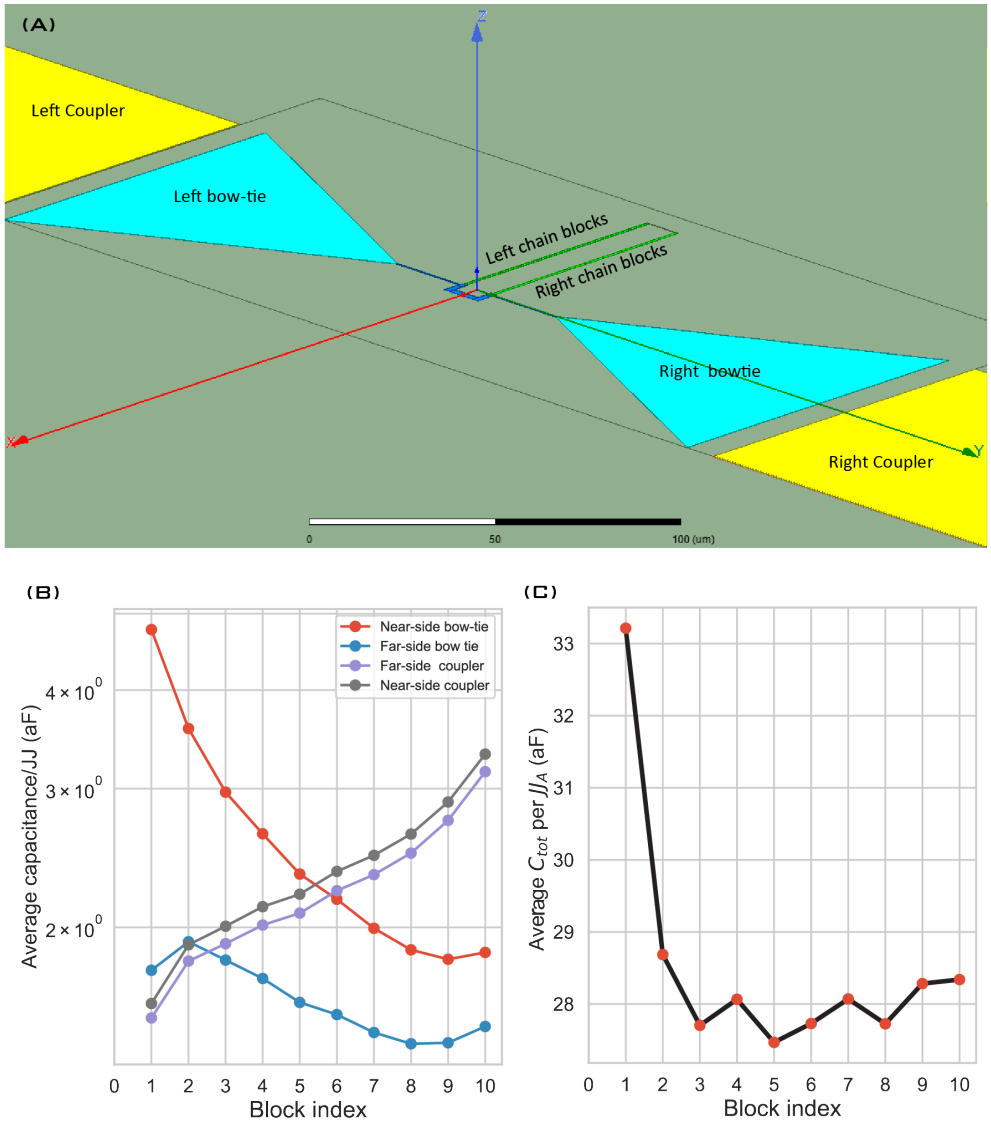

Figure 6.13: (A) An image of the finite element simulation which solves for an all to all capacitance matrix. The relevant circuit parameters are labeled. (B) The average capacitance of each JJ in the block index to the other metal structures in the circuit. (C) The average total capacitance of each JJ in each of the block indexes.

appears to agree quite nicely with the classical mode results which were based on the parameters extracted from the generic mode fit.

7
Fluxonia experiments

"When you have eliminated the impossible, whatever remains, however improbable, must be the truth."— Sir Arthur Conan Doyle, stated by Sherlock Holmes

7.1 Capacitively coupled fluxonia: overview

In the foremost part of the chapter, the effects of etching are quantified by extensively measuring capacitively coupled fluxonia with the energy scale combination #2: $E_J \approx E_C \ll E_L$.

Firstly, an unetched fluxonium is studied and ,then, the same exact sample is etched selectively around the JJ chain and coupling capacitors using SF_6. The selectively etched sample is measured once again in the same exact 3D cavity, in the same exact measurement line. Finally, an almost identical second sample is etched entirely off the silicon substrate using XeF_2 and is measured in the same exact measurement line. All three samples were made during the same deposition and measured in the same exact measurement line. Each circuits parameters are found by fitting the spectrum to the chain mode model where the E_J, E_C, E_L are all almost exactly the same only differing by about $\delta E_J \pm 0.5$ GHz, $\delta E_C \pm 0.1$ GHz, and $\delta E_L \pm 0.04$ GHz.

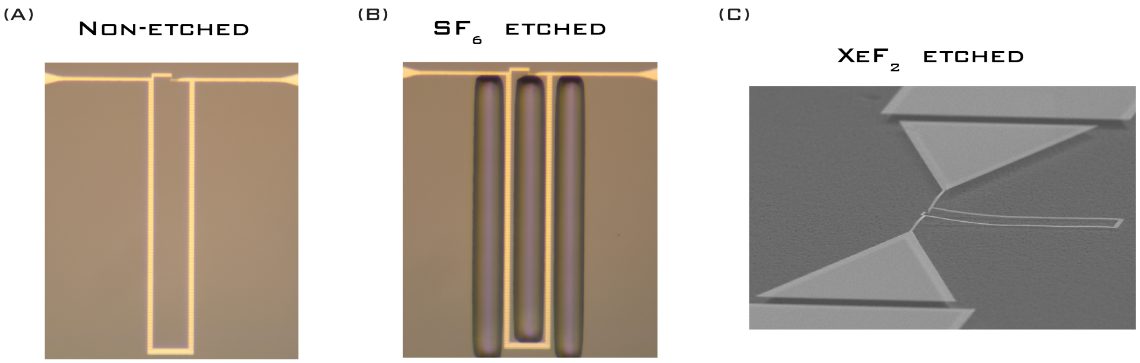

Figure 7.1: Device (A) and (B) are the same sample. (A) is unetched while (B) is selectively etched with SF_6 around the JJ chain. Device (C) is a different sample with slightly larger capacitor pads shunting the small junction. (C) is etched with XeF_2. Both devices were deposited at the same time.

The similarity in the device parameters and measurement lines allow for a fair comparison to reveal any effects which arise from etching our fluxonium circuits.

These qubit's lower energy transitions can be described by the phase slip Hamiltonian where the spectrum can be described by flux quanta tunneling in and out of the loop at all external flux bias points. This energy scale combination makes for high coherence values at both sweet spots alike; while T_1 remains large across all external flux bias values. The samples parameters are obtained by fitting the spectrum measured up to 12 GHz due to a low pass filtering of the input line. This experimental study will compare all three devices coherence times and will also help illustrate etching does not degrade coherence values. Likewise, each fluxonium has chain modes whose frequency and coupling are modified depending on the etching status.

7.2 Non-etched

The original non-etched sample, deposited on silicon, is made with a small capacitive "bow-tie" antenna on both sides of the small JJ which is shunted by a tightly-packed JJ array of nearly 300 junctions as shown in figure 7.2 (A). The small bow-tie antenna is capacitively coupled to large area aluminium stripes which ultimately couple the qubit to microwave signals entering and exiting through the cavity pins.

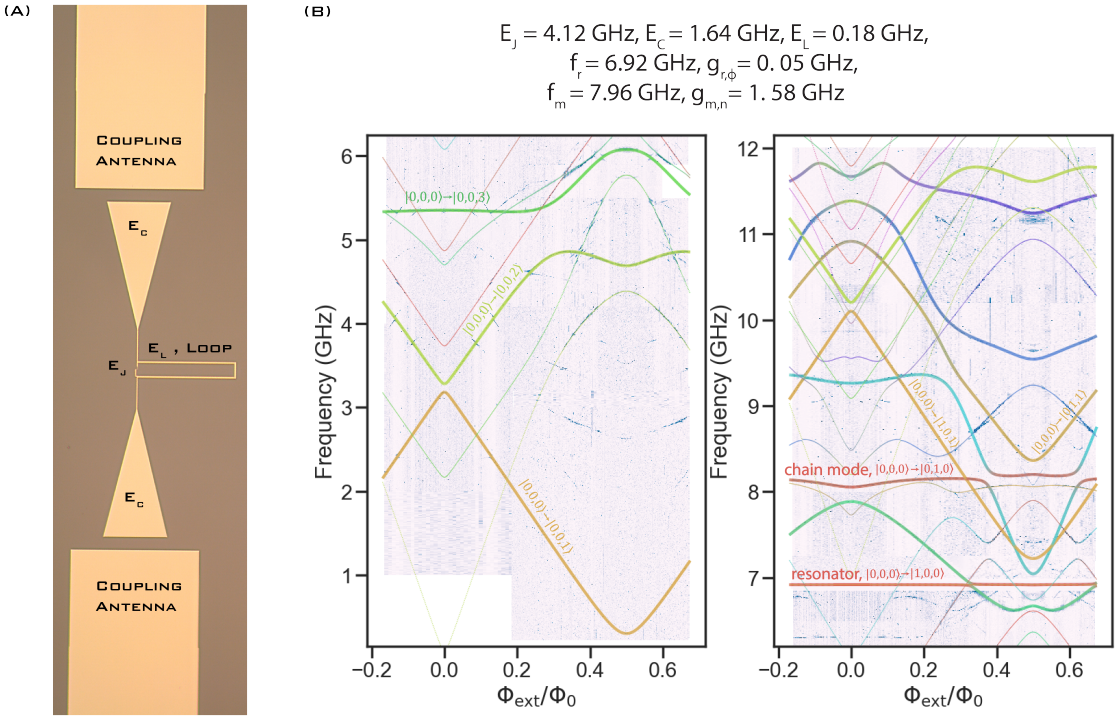

Figure 7.2: (A) An optical image of the non-etched device with the relevant circuit parameters labeling the actual physical circuit elements. (B) The device's spectrum and fit to the fluxonium coupled to a single chain mode and resonator. The single-photon transitions out of the ground state are the thick colored lines while the thin colored lines are single-photon transitions out of the first excited state.

Two-tone spectroscopy of the qubit is initially performed up to 12 GHz using the fundamental mode of the 3D copper cavity as read out. In this particular measurement, the read-out of the qubit state is a hangar style measurement where the cavity has both input and output pins; each with different values of κ where $\kappa_{\text{in}} < \kappa_{\text{out}}$. The read-out frequency is $f_0 = 6.92$ GHz while $Q_{\text{int}} \approx 25,000$ and $Q_{\text{ext}} \approx 1,000$. The experimentally measured qubit spectrum is fit to the fluxonium coupled to a single chain mode and resonator model. This fit gives fluxonium parameters $E_J = 4.12$ GHz, $E_C = 1.64$ GHz, and $E_L = 0.18$ GHz while the shunting inductance is found to host a mode at $f_m = 7.96$ GHz with a coupling strength $g_m^n = 1.58$ GHz. The qubit-cavity coupling strength is also found as $g = 0.051$ GHz. The total inductance of the device is $L_{\text{tot}} = 0.91\mu$H creating an impedance of the shunting inductance $Z_L = 2\pi f_m \times L_{\text{tot}} = 45$ kΩ.

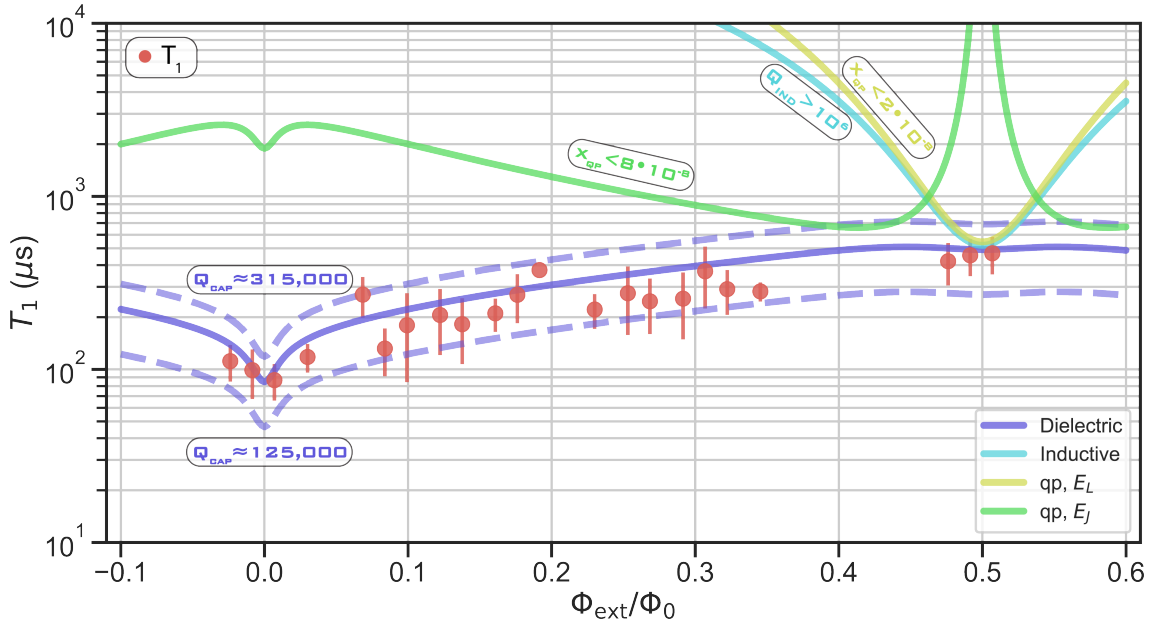

Figure 7.3: T_1 data as a function of the external flux bias superimposed with each relaxation method. The environmental variable limiting each individual relaxation source is shown. Dielectric loss appears to limit energy relaxation.

The fit spectrum highlights the single-photon transitions out of the $|000\rangle$ coupled basis state, while the light colored lines highlight the transitions out of the $|001\rangle$ coupled basis state. The other 1-photon transitions which are important to comment on are the resonator and the chain mode states which are represented as $|000\rangle \rightarrow |100\rangle$ and $|000\rangle \rightarrow |010\rangle$, respectively. Other transitions which are also labeled are of the qubit plus either the excited resonator or the excited chain mode; which are shown in the same color as the lower modes. The color change of the lines indicate how the pure fluxonium only transition energies are hybridized due to the resonator and chain modes alike.

Energy relaxation, T_1, data as a function of the external flux bias is measured many times over where the data plotted in figure 7.3 is the binned statistics of hundreds of data points making each value of T_1 displayed the collective average in that particular flux bias bin range. The error bars for each data point is the variance of T_1 within each bin. The T_1 versus flux is fit to each relaxation method individually to create a bound for the limiting noise source of each individual decay rate. The T_1 data as a function

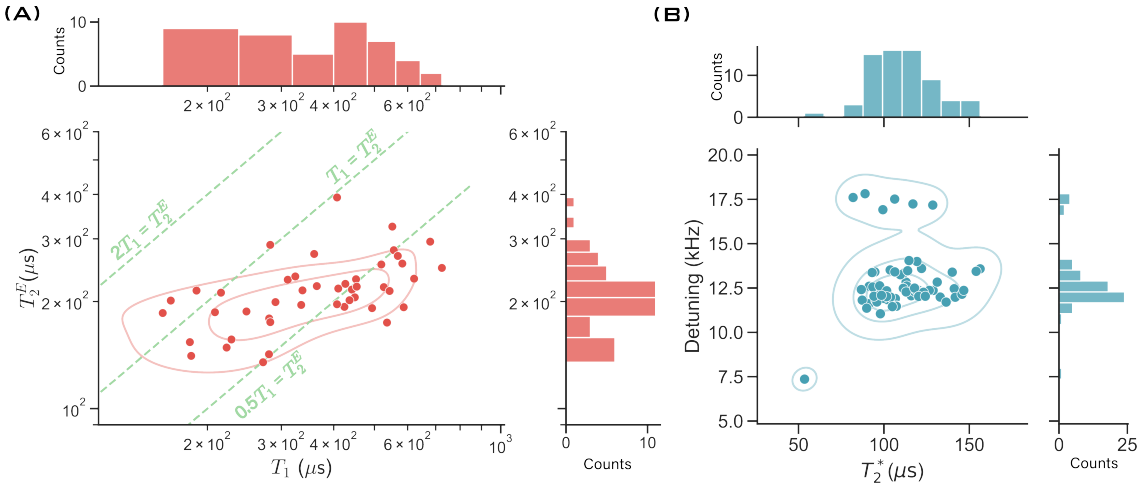

Figure 7.4: Indexed time domain measurements while biased at HFQ. (A) is the interleaved T_1, T_2^E measurements; each data point is obtained by a measurement which interleaves the T_1 pulse sequence and the T_2^E pulse sequence with a certain time delay; obtaining the traces for both simultaneously. While (B) is T_2^* which plots the decay time versus the qubit detuning frequency.

of flux indicates the major contribution to energy relaxation is dominated by dielectric loss. A upper and lower range for the dielectric quality factor can be set between $125,000 < Q_{\text{cap}} < 315,000$. The inductance originating from the JJ array has a high quality factor, $Q_{\text{cap}} > 10^6$ comparable to other experimental results in [94] and hosts a small density of $x_{\text{qp}} < 2 \times 10^{-8}$. The values obtained indicates a large shunting inductance does not significantly contribute to the relaxation processes for the measured times. There is also no evidence for quasiparticles tunneling across the small junction suggested by the lack of double exponetial behavior at all external flux bias points; however using the qp loss model puts a bound of $x_{\text{qp}} < 1 \times 10^{-7}$ similar to experimental results in [148].

This particular fluxonium has $T_1 > 80\ \mu$s at all external flux bias which is due to the small charge matrix elements. The wavefunctions and transition energy for 0-1 show, in fact, there are no plasmon like transitions. Instead the wavefunctions must tunnel into adjacent wells to execute a transition which is reflected by a zigzag shape versus external flux, characteristic for a fluxonium in the phase slip parameter regime.

Furthermore, indexed measurements at both sweet-spots were performed

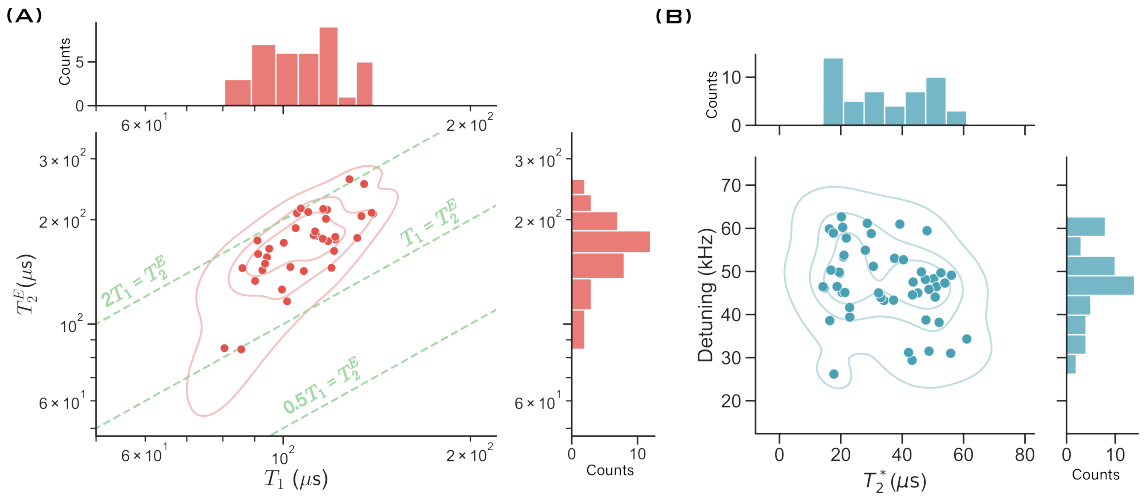

Figure 7.5: Indexed measurements while biased at IFQ. (A) is the interleaved T_1, T_2^E measurements while (B) is T_2^*.

for interleaved T_1, T_2^E and T_2^*. These measurements are performed to gain statistics for quantifying the consistency of the reported values. Interleaved time domain statistics at HFQ indicate: $\bar{T}_1 = 362 \pm 20$ μs, $\bar{T}_2^E = 212 \pm 6$ μs, and $\bar{T}_2^* = 110 \pm 30$ μs indicating $\bar{T}_1 > \bar{T}_2^E > \bar{T}_2^*$ such that T_2^E is not T_1 limited. The main source of decoherence is most probably associated with cavity photon shot noise. From the fit, $\chi_{01} \sim 2$ MHz at HFQ which enables to find the effective cavity temperature based on values from $\bar{T}_2^E$ corresponding to $T_{\text{eff}} \approx 55$ mK; right on par with the estimates due to thermalization from chapter 3 figure 4.2. At IFQ, this fluxonium has average interleaved values: $\bar{T}_1 = 109 \pm 2$ μs and $\bar{T}_2^E = 175 \pm 6$ μs. T_1 appears chiefly limited by dielectric loss while T_2^E is again limited by cavity photon shot noise; where the value of T_2^E and χ_{01} are roughly the same at IFQ as at HFQ. T_2^* is less than T_2^E with an average $\bar{T}_2^* = 38 \pm 2$ μs; indicating more low frequency noise at IFQ than at HFQ. This can be in-part due to the sharpness of the 0-1 transition at IFQ which is more susceptible to small offsets of external flux bias noise which then leads to a 1/f flux noise limitation when slightly detuned.

The frequency of the 0-1 transition at IFQ is $f_{01}^{\text{IFQ}} = 3.185$ GHz which is an order of magnitude larger than the transition at HFQ which is $f_{01}^{\text{HFQ}} = 0.303$ GHz. Furthermore, at IFQ, the 0-1 transition and the 0-2 transition are

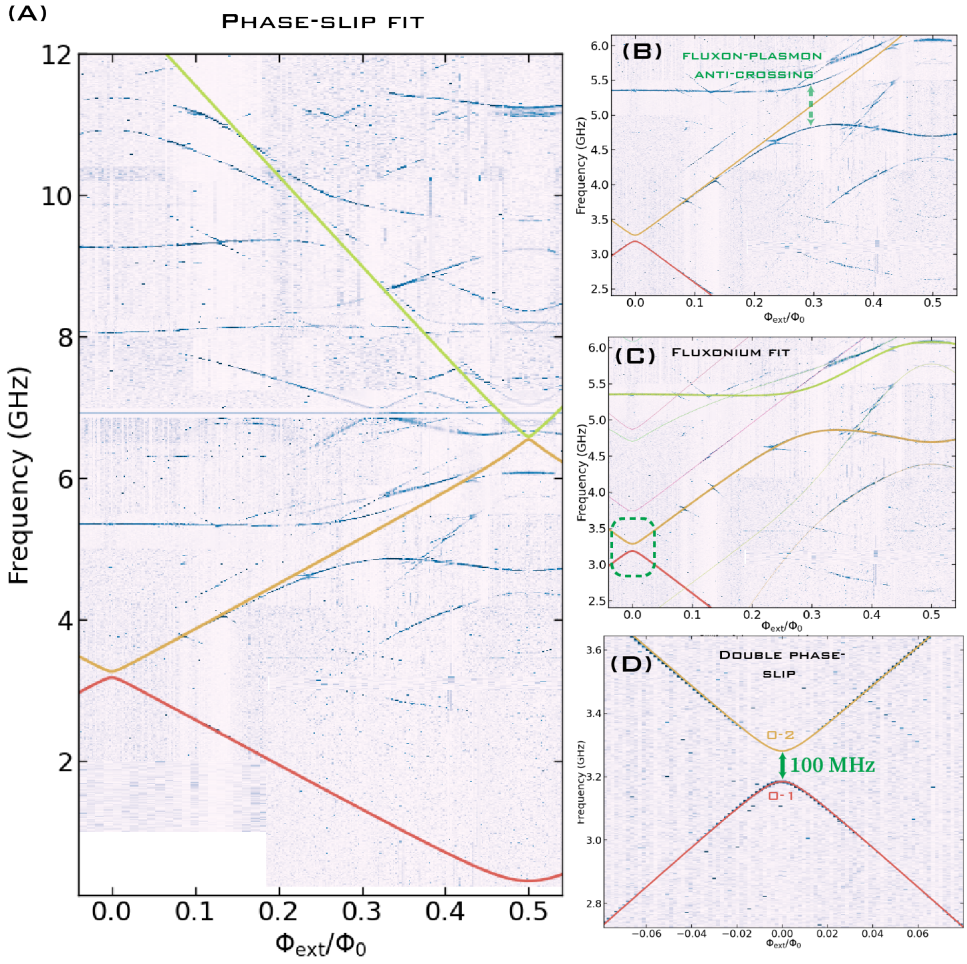

Figure 7.6: (A) The unetched fluxonium device spectrum is fit to a model which incorporates single and double phase-slips.(B) The phase-slip model fails at around 4.5 GHz when the plasmon frequency hybridizes with the fluxon state. (C,D) At IFQ, the 0-1, 0-2 transition is separated by approximately 100 MHz. The transition 1-2 is considered as a double phase slip transition.

only 97 MHz apart. This spectrum is fit to the quantum phase slip Hamiltonian, shown in figure 7.6, where the fit value of the single phase-slip energy is almost equivalent to f_{01}^{HFQ}, and is given as $\varepsilon_s = 0.308$ GHz and $E_L^{\mathrm{s}} = 0.162$ GHz; very similar to the fluxonium fit value. The 0-1 transition frequency at IFQ is then found by the expression: $f_{01}^{\mathrm{IFQ}} = 2\pi^2 E_L^{\mathrm{s}} = 3.198$ GHz.

The anti-crossing between the 0-1 and 0-2 transition can be interpreted as a double phase-slip in the small JJ changing the flux quanta occupation of the loop by two. This can also be thought of as a double tunneling fluxon event where the first eigenstate must tunnel across two Josephson well potentials to occupy the second excited state which in turn changes the reduced phase by two. When incorporating this into the model the double phase-slip energy is found to be: $\varepsilon_{s_2} = 0.074$ GHz; which is the approximate value of the anticrossing shown in figure 7.6 (D). The 0-2 transition begins being hybridized with the plasmon transition around $\Phi_{\mathrm{ext}} \approx 0.2\Phi_0$ and can be observed to anti-cross with the emerging plasmon transition. Furthermore, the slope of the 0-1 transition between the two sweet spots is approximately linear and is given by: $2\pi E_L = 1.02$ GHz/$(\Phi_0/2)$.

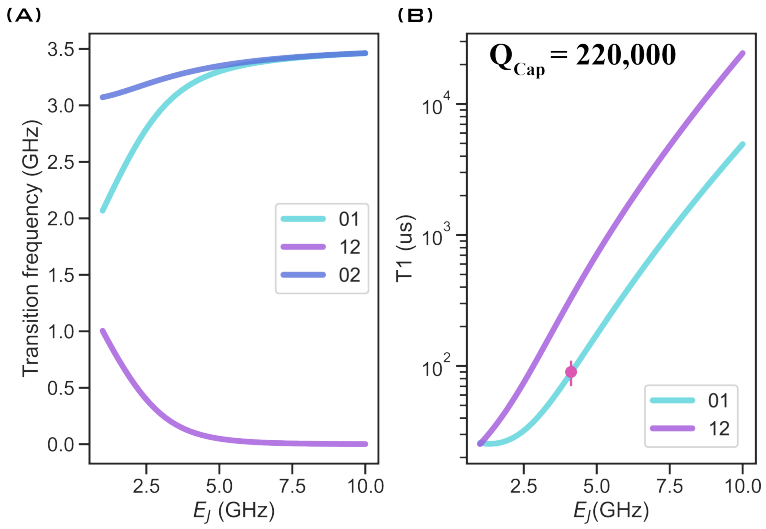

Figure 7.7: A simulation with the unetched samples E_C and E_L where the value of E_J is swept. (A) The transition frequency evolution incorporates the first three states. The 1-2 transition frequency becomes substantially suppressed when $E_J > E_C$. (B) The simulated time domain limit incorporates dielectric loss only. This shows increasing E_J can substantially decrease susceptibility to dielectric loss due to a decreasing charge matrix element.

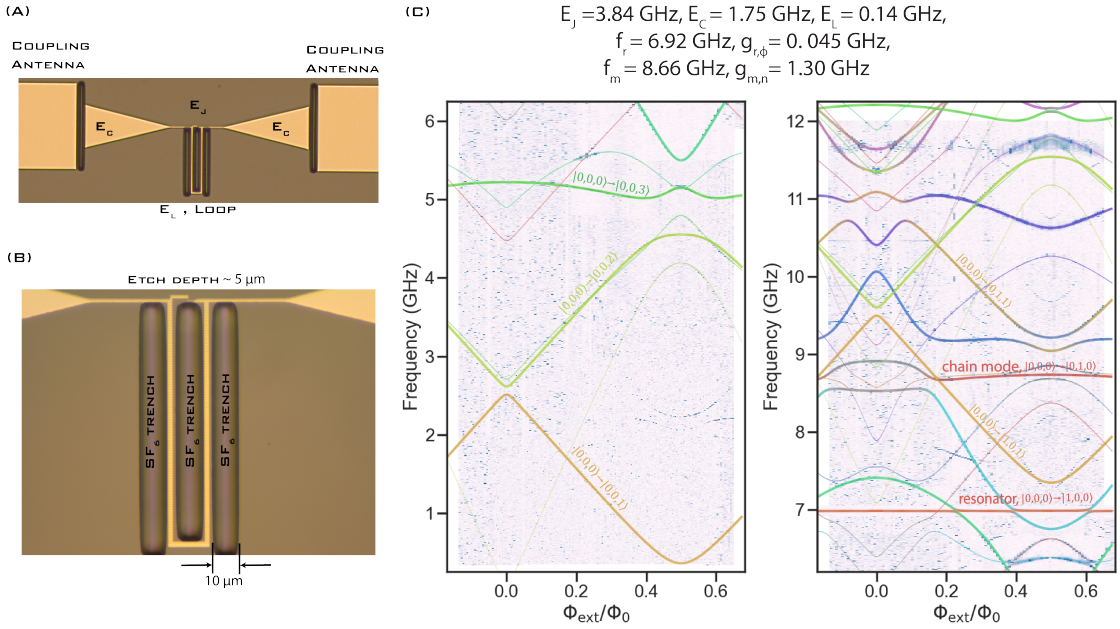

Figure 7.8: (A) An optical image of the SF_6 etched device with the relevant circuit parameters labeled. Notice the etching "trenches" in (B) between and to the sides of the JJ array and the etching between the couplers. (C) The device spectrum and fit.

The transition at IFQ appears as a good candidate for a qubit [77]. Due to the larger transition frequency, the 0-1 transition can be excited with a Gaussian pulse of width $\tau_\pi < 10$ ns. Which gives an approximate dephasing probability per gate: $p_\phi \approx \frac{\tau_\pi}{T_\phi} = 3 \times 10^{-5}$. Modifications of E_J of a similar device was simulated and indicates $T_1 \approx 1$ ms at IFQ for the limit of dielectric loss when $E_J = 7.5$ GHz where the qubit 0-1 and 0-2 splitting shrinks to values less than 10 MHz. There appears to be a great potential for using the three first transitions of fluxonium at IFQ as a qutrit. Effectively the first and second eigenstates are degenerate yet separated by two phase-slips instead of one like at HFQ. The low frequency of the 1-2 transition indicates an energy relaxation time always larger than the 0-1. Finally, IFQ is a sweet-spot after all meaning there is no first order effect from low-frequency flux noise which is detrimental to the dephasing time.

7.3 SF_6-etched

The non-etched sample, just measured, is now selectively etched with the SF_6 technique around the chain and between the coupling stripes and the bow-tie antenna. The etch creates trenches in the silicon substrate around 5-6 μm deep and 10 μm wide. Due to the protective covering, there was no under-etching of the device such that the small JJ and chain remain entirely attached to the substrate. The sample is measured in the same cavity with the same exact measurement configuration as before making any difference between the measurements presumably due to the selective etching of the sample.

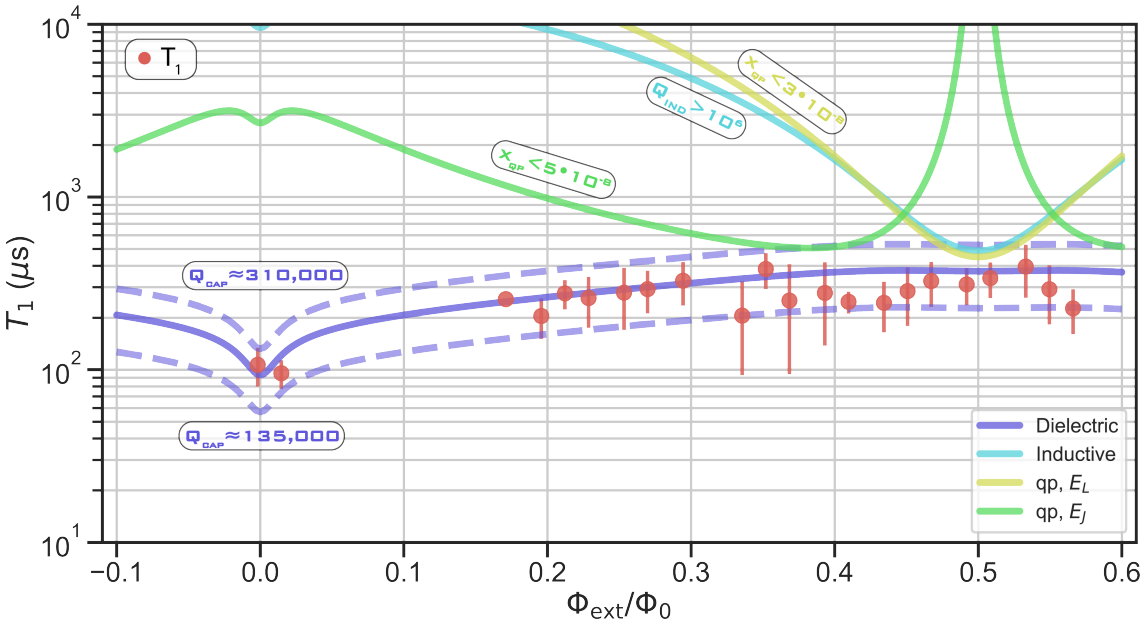

Figure 7.9: The T_1 data as a function of the external flux bias superimposed with each relaxation method. The environmental variable limiting each individual relaxation source is shown in the insets. Dielectric loss appears to limit energy relaxation and the Q_{cap} value remains basically unchanged compared to the non-etched version.

The two-tone spectroscopy reveals a slight modification of E_C, which is increased by 7% and is likely due to both the reduction in the chain's parasitic capacitance and the bow-tie capacitance to the coupling stripe antennas. While E_J and E_L are reduced only slightly which is expected with the normal aging of JJs. The coupling between the resonator and the qubit

is reduced by 5 MHz and can also be attributed to etching a silicon trench between the bow-tie and the coupling stripes.

Interestingly, the chain mode frequency increased by approximately 700 MHz while the chain mode-qubit coupling decreased slightly by 20 MHz. An estimation of the percentage of the total parasitic capacitance factor of $\Delta_{C_g} = \frac{\left(f_m^1\right)^2}{\left(f_m^0\right)^2} \cdot \frac{E_L^0}{E_L^1} = 1.52$. Likewise, the impedance modification of the chain can be approximated as $\Delta_Z = \sqrt{\Delta_{C_g} \frac{E_L^0}{E_L^1}} = 1.4$. The impedance of the shunt inductance is explicitly found as: $Z_L = 2\pi \cdot 8.66 \times 10^9 \cdot 1.17 \times 10^{-6} = 64$ kΩ. Taking the ratio with the previous device the impedance factor is the same as the estimate.

The qubit transition frequency at IFQ was reduced by nearly 700 MHz while the qubit transition's frequency at HFQ was increased by nearly 60 MHz making the reduction of the flux dispersion by approximately 760 MHz. This reduction from the unetched device is due to the modification of the fluxonium parameters which has the effect to produce larger φ_{zpf} or more delocalized ground state and first excited state wavefunctions.

Like the previous device, T_1 as a function of external flux bias was measured many times over and the data was binned and averaged where the error bars are the variance per bin. At certain external flux bias points, especially around IFQ, the qubit was difficult to measure due to the small dispersive shifts. The data indicates the major contribution to relaxation at all flux values is still dielectric loss with basically the same value of Q_{cap} with a lower and upper bound set at $135,000 < Q_{\text{cap}} < 310,000$ thus indicating no significant reduction or enhancement of the dielectric Q from this etching procedure. The dominating area the qubit's electric field occupies is mainly below the bow-tie antenna and extends into the unetched silicon substrate to approximately the depth of the separation between the leads. With that said, the results are not particularly surprising yet indicates no sever catastrophe associated with selectively etching. All other quantities did not significantly contribute to relaxation and the the limit of T_1 is more or less the same as the unetched version. Any small deviance to the previous sections measurement could be due to thermalization of the sample to the cavity or placement of

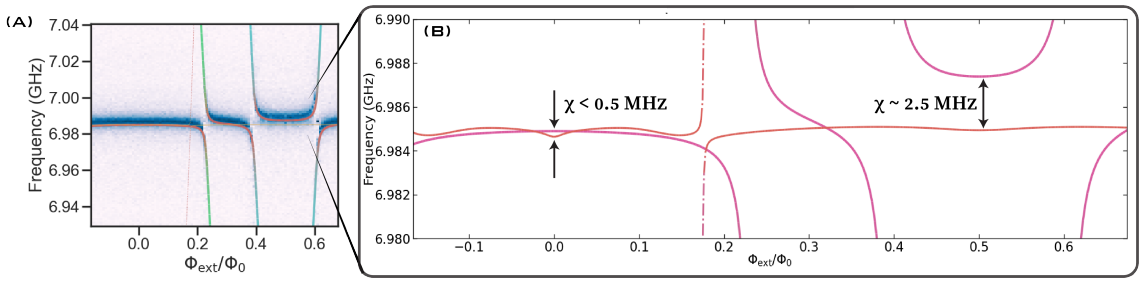

Figure 7.10: (A) A zoom in on the one-tone spectrum of the read-out cavity versus flux which includes the fit. (B) A further zoom in demonstrating the dispersive shift for external flux around IFQ is less than 500 kHz. The solid magenta line is the read-out only excited while the dot-dash is the qubit and read-out excited such that the difference is the dispersive shift.

the sample inside the cavity which could produce small effects which are not significant enough for quantitative results.

Indexed measurements at both the sweet spots were performed for interleaved T_1, T_2^E, and T_2^*. These measurements shows, at HFQ, $\bar{T}_1 = 330 \pm 20\ \mu$s, $\bar{T}_2^E = 270 \pm 30\ \mu$s, and $\bar{T}_2^* = 105 \pm 10\ \mu s$. In this device, $\bar{T}_1 \sim \bar{T}_2^E > \bar{T}_2^*$ where $\bar{T}_2^E$ is not $\bar{T}_1$ limited; further analysis of the decoherence times, once again, showed the selectively etched qubit was limited by cavity shot noise. The values of $T_2^E > T_2^*$ indicate low-frequency noise and while exploring this in more depth the indexed Ramsey measurements showed some spectacular sensitivity to the ambient magnetic field even with substantial shielding.

The indexed data for T_2^* took place for over a day and a half and reveals correlations between the qubit detuning frequency and the fridge's base plate temperature. The following observations took place while monitoring the data real time while also observing the fridge temperature. The measurement became even more interesting while being in the lab at the right times to note the usual coming and goings to further correlate the change of the qubit detuning frequency with the ambient lab conditions.

The sudden increase in base plate temperature of the fridge is due to the other measurement lines signal being attenuated such that the power dissipated by attenuators on the base plate temperature would increase the temperature from 8 mK to around 18 mK rather rapidly. The change in base plate temperature is observed to cause the qubit detuning frequency to

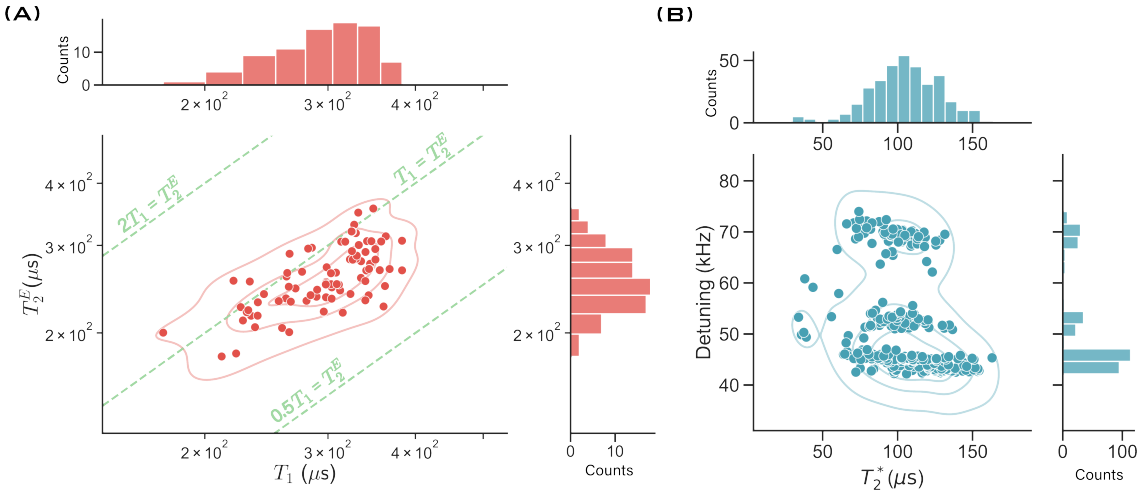

Figure 7.11: Indexed measurements while biased at HFQ. (A) shows interleaved T_1, T_2^E measurements while (B) shows T_2^* versus qubit detuning.

change by roughly 20 kHz at the same exact time the fridge temperature would spike. After the initial spike in temperature, the detuning frequency would stabilize at the modified detuning frequency only to return to the original detuning frequency once the temperature cooled to the original value again. The value of T_2^* would change as well but only momentarily while the temperature change was transient. This phenomenon was observed a total of three times during the same indexed Ramsey measurement with the detuning peaks and fridge temperature peaks lining up perfectly in time.

Another disturbance observed in the detuning frequency occurred when another dilution refrigerator, several meters away, was opened for maintenance. This normal lab work observed to shift the qubits detuning by roughly 10 kHz during the duration of the work. The detuning frequency was slowly displaced and was never truly stable while the adjacent fridge was opened. Once the work in the lab was wrapped up, the qubits detuning shifted back to the original detuning. An added bonus here is the temperature of the base plate was never modified during this occurrence.

The qubit's detuning frequencies extreme sensitivity to the temperature and the ambient magnetic field in the lab could be attributed to thermalization induced changes to the magnetic properties of surface defects and is proportional to the amount of trapped vortices in the system [163]. This

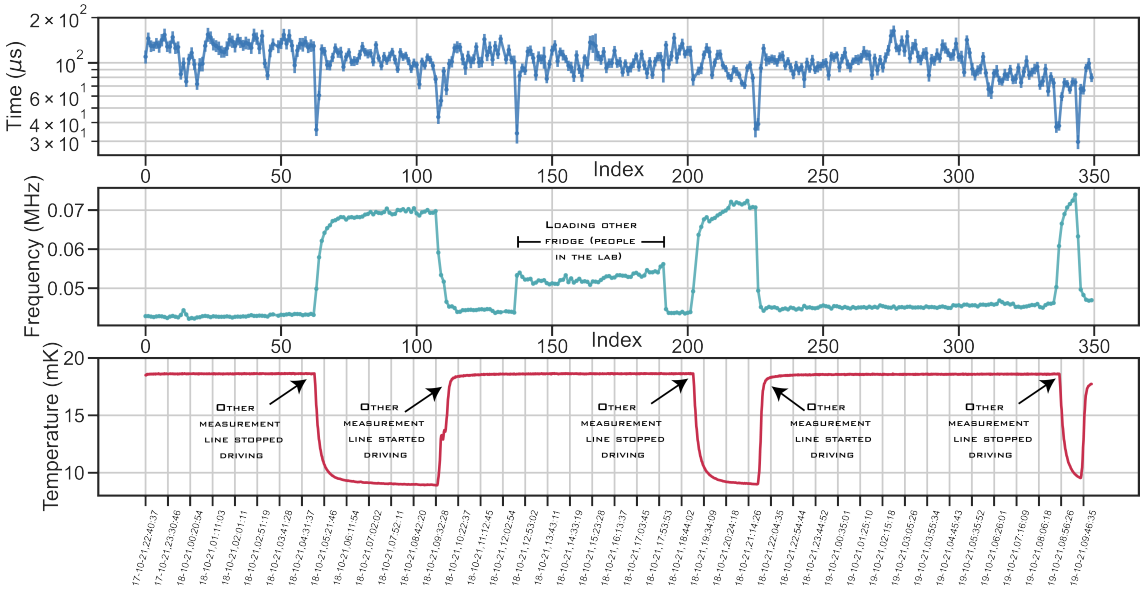

Figure 7.12: An indexed Ramsey measurement where the T_2^*, qubit-drive detuning, and base plate temperature are simultaneously monitored for over a day and a half. The change in temperature is correlated with the qubit's detuning frequency.

indexed Ramsey measurement indicates the potential extreme sensitivity of the qubit to temperature and the ambient magnetic field in the lab which is a testament to the wide range of applications for superconducting circuits; in this case the qubit can be used as a low-frequency magnetic field sensor to detect ultra-low noise signals [67]. This measurement is also a warning sign that cooling down in a large ambient magnetic field can induce a large susceptibility to small temperature changes (in this case 10 mK).

The T_2^* Ramsey as a function of flux around HFQ indicates a 1/f flux noise similar to other experiments [22, 135] $S_\Phi = 2 - 4\mu\Phi_0$. Due to the "softness" of the transition as a function of flux, measurements off HFQ by 2% were measurable with no signs of a Gaussian envelop decay [17]. In principle, with no other sources of decoherence, at HFQ, T_2^* diverges but in reality is limited by second order flux noise dephasing.

At IFQ, the interleaved data was difficult to measure due to the low dispersive shift, however with careful measurement parameter choices interleaved data reveals $T_2^E \approx 2T_1 \approx 200\mu$s meaning T_2^E is limited by T_1 which appears to be primarily limited by dielectric loss. The increase of T_2^E/T_1 and the decrease of the dispersive shift in this device at IFQ further provides

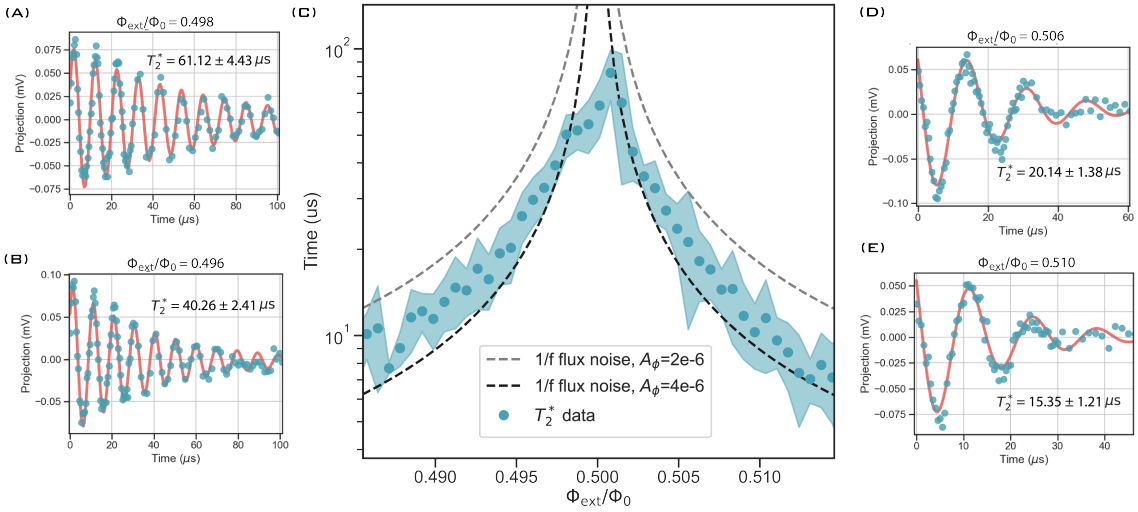

Figure 7.13: T_2^* as a function of external flux around the HFQ sweet spot. (A)(B)(D)(E) indicate no signs of a Gaussian decay envelope.

evidence the previous sample was limited by thermal photon shot noise. The measurements at this flux point were difficult and so time domain statistics were mainly taken for T_1 only. T_1 fluctuates slowly between 60 and 120 μs. T_2^* also has a very large spread in both characteristic time and detuning frequency.

At both sweet spots the time domain statistics reveal T_1 is on the same order as the unetched version yet there is a clear sign of a slowly fluctuating source of noise associated with flux and temperature for this particular device. Conclusions on this source of the low frequency noise are speculative yet only the T_2^* measurements were significantly affected.

7.4 XeF_2-etched

A sample, simultaneously fabricated as the previous, with a slightly larger area bow-tie antenna was etched completely utilizing the XeF_2 isotropic technique and systematically characterized. The sample's spectrum was initially measured during the same time as the SF_6 device and so this sample was placed into a different cavity whose read-out frequency was $f_0 = 7.27$ GHz. However, all time domain measurements were then performed in a separate cool-down and measured in the same measurement line as the other

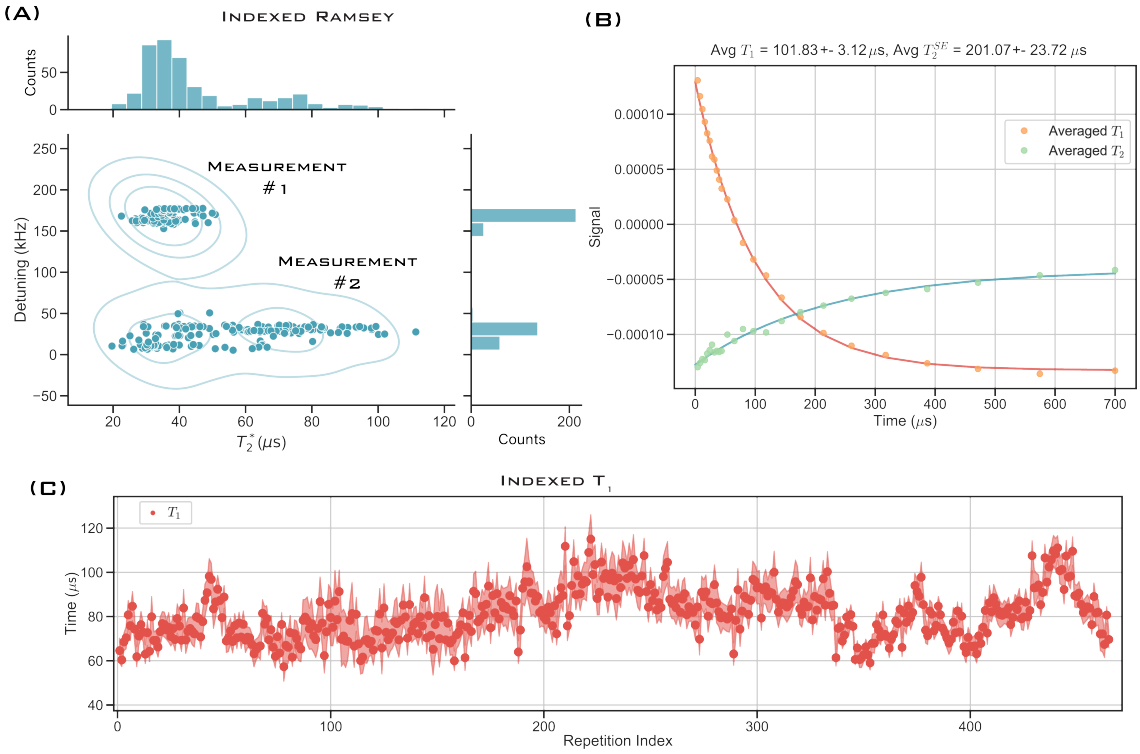

Figure 7.14: Indexed measurements while biased at IFQ. (A) T_2^* versus detuning for two seperate measurements. (B) An average trace of interleaved T_1 and T_2^E measurements. (C) Indexed T_1 measurements with an average value of these measurements: $\bar{T}_1 = 82 \pm 5\ \mu$s.

samples.

The two-tone spectroscopy reveals a modification of E_C, increasing the value from the predicted $E_C < 1.5$ GHz to $E_C = 1.83$ GHz. E_J and E_L are slightly different from the original non-etched device and this is attributed to the non-identical lithography of small JJ's between the two devices. The coupling between the resonator and the qubit is increased and is due to the larger dimensions of the bow-tie capacitively coupling the qubit to the antenna strip.

The most striking result of this device is the chain mode frequency increased by approximately 3.3 GHz despite having the same number of array junctions/array length/E_L as the original non etched version. The total parasitic capacitance change factor of $\Delta_{C\cdot g} = \frac{\left(f_m^2\right)^2}{\left(f_m^0\right)} \cdot \frac{E_L^0}{E_L^2} = 2.12$; a substantial enhancement from the SF_6 etching technique. Likewise, the chain mode-

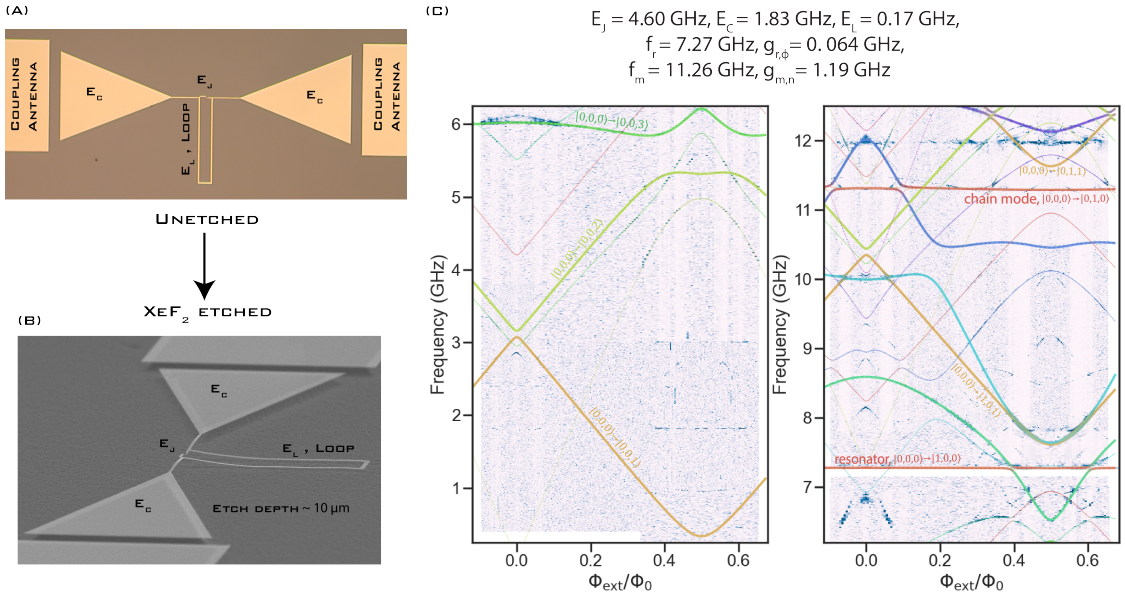

Figure 7.15: (A) The optical image of the pre-XeF_2 etched device with the relevant circuit parameters labeled. (B) An SEM image of the post-XeF_2 etched device with the relevant circuit parameters labeled. Notice the JJ array and leads to the small JJ are completely detached from the silicon substrate. (C) The devices spectrum and fit; highlighting the single-photon fit transitions from the ground state as thick colored lines while the thin colored lines are transitions from the first excited state.

qubit coupling decreased by 0.41 GHz. The total inductance of the XeF_2 device is $L_{\text{tot}} = 0.96\mu\text{H}$ creating an impedance of the shunting inductance $Z_L = 2\pi \cdot 11.26 \times 10^9 \cdot 0.96 \times 10^{-6} = 68\ \text{k}\Omega$.

Like the previous devices, T_1 as a function of external flux bias was measured many times over and the data was binned and averaged. The data, once again, indicates the major contribution to relaxation at all flux values is dielectric loss. A lower and upper bound can be set of $80,000 < Q_{\text{cap}} < 210,000$; which is less than the previous samples yet close enough indicating little to no reduction or enhancement of the dielectric Q from this etching procedure. The difference in Q_{cap} can be most likely contributed to using another silicon diced chip as the dielectric Q can vary with in the same wafer. All other quantities did not significantly contribute to relaxation and the variables setting the limit of T_1 is more or less the same as the non-etched version.

Indexed measurements at both the sweet spots were performed for in-

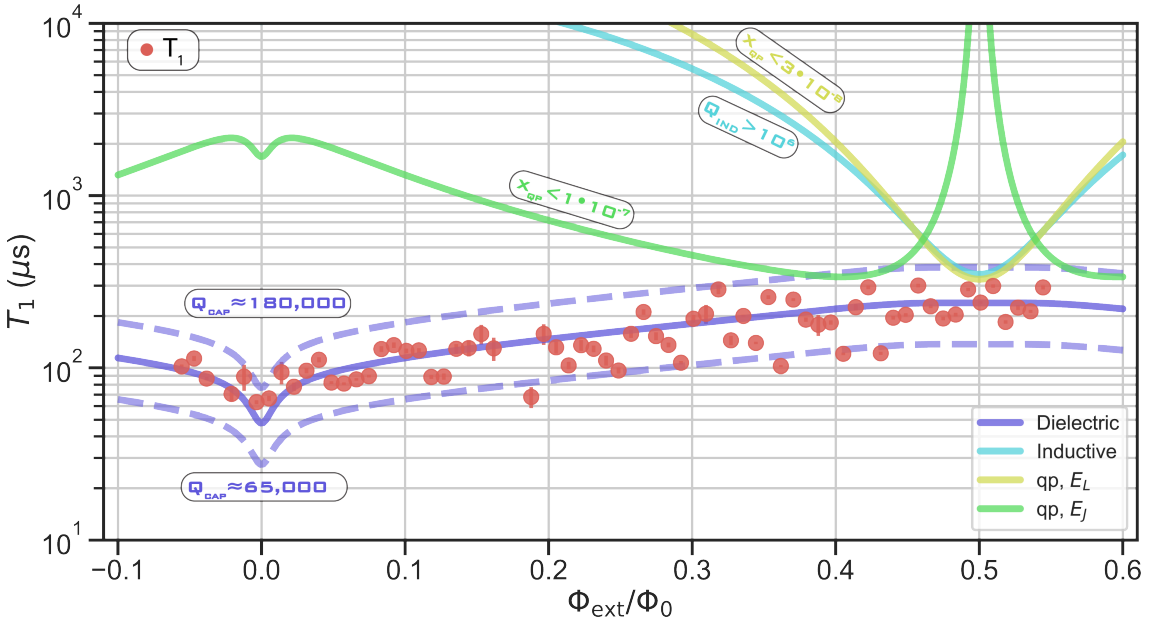

Figure 7.16: T_1 data as a function of the external flux bias superimposed with each relaxation method. The environmental variable limiting each individual relaxation source is shown. Dielectric loss appears to limit energy relaxation.

terleaved T_1, T_2^E and T_2^* to gain statistics. At HFQ $\bar{T}_1 = 263 \pm 6$ μs, $\bar{T}_2^E = 235 \pm 4$ μs, and $\bar{T}_2^* = 125 \pm 10$ μs such that $T_1 \approx T_2^E > T_2^*$. Nevertheless T_2^E is still not T_1 limited at HFQ and is due to cavity photon shot noise as was the case in all three samples. While at IFQ, interleaved $\bar{T}_1 = 54 \pm 3$ μs and $\bar{T}_2^E = 99 \pm 12\mu$s such that $T_2^E \approx 2T_1$. This means T_2^E is limited by T_1 again at IFQ such that the qubits coherence time at IFQ is limited by the energy relaxation processes associated with dielectric loss.

7.5 Comparison

In this section, a direct comparison is performed of the measured T_1 as a function of external flux for all three devices. The thermal photon shot noise from the cavity is also presumably the limiting source at HFQ for each sample and the specific conditions which produce this is considered. The energy scales and matrix elements of each of the devices are also compared to help quantitatively discuss the possibility of any modifications to the noise spectral densities or Q_{cap} of each qubit version due to the etching

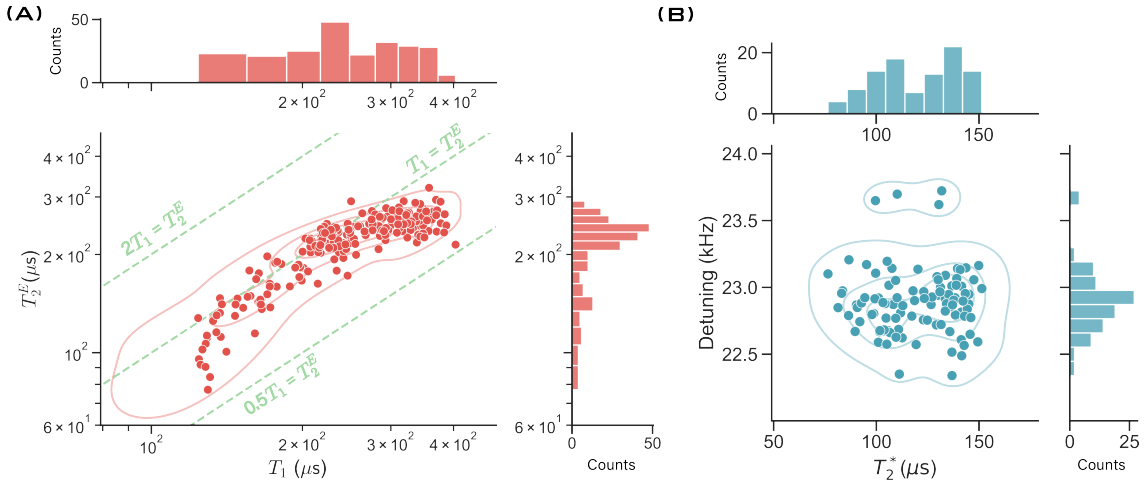

Figure 7.17: Indexed measurements while biased at HFQ. (A) is the interleaved T_1, T_2^E measurements while (B) is T_2^*.

procedure applied.

The two most notable things in this study are the likeliness of all three qubits to one another. The results show all three device's energy relaxation is limited by dielectric loss at all external flux points. The form of Fermi's Golden rule used for energy relaxation from dielectric loss is expressed equally using either the charge matrix elements or the phase matrix elements and can be expressed equivalent as:

$$\begin{aligned}\frac{1}{T_1} &= 32\pi E_C |\langle 0|n|1\rangle|^2 \tan\delta_C \\ &= \frac{\pi\omega^2}{2E_C} |\langle 0|\varphi|1\rangle|^2 \tan\delta_C \\ &= \frac{1}{4e^2} |\langle 0|\varphi|1\rangle|^2 S_{\text{diel}}(\omega)\ .\end{aligned} \tag{7.1}$$

Using both expressions we can gain different sources of insight into our system. In the first case, the dielectric quality factor Q_{cap} is quantified by solving the first expression proportional to loss tangent. While, secondly, the inverse noise spectral density scaling with frequency is found by multiplying $T_1 \times |\langle 0|\varphi|1\rangle|^2$.

Using the first expression, on average all devices have $Q_{\text{cap}} > 100,000$. The nonetched and SF_6 etched device have basically the same $Q_{\text{cap}} \approx 250,000$

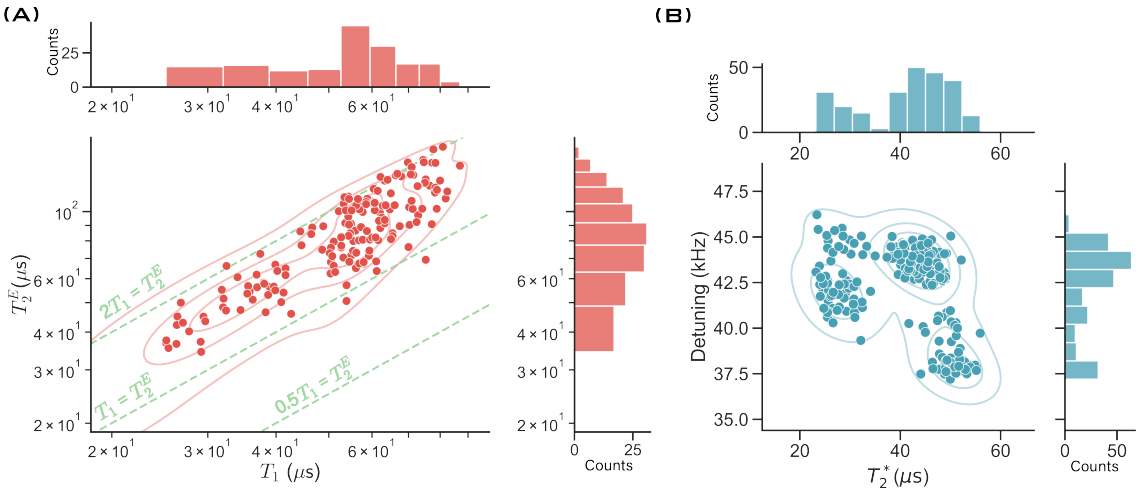

Figure 7.18: Indexed measurements while biased at IFQ. (A) The interleaved T_1, T_2^E measurements.(B) The indexed T_2^* versus qubit frequency detuning.

Etch	E_J (GHz)	E_C (GHz)	E_L (GHz)	f_r (GHz)	g_r^{φ} (MHz)	f_m (GHz)	g_m^n (GHz)
None	4.12	1.64	0.18	6.92	50	7.96	1.58
SF_6	3.84	1.75	0.14	6.92	45	8.66	1.30
XeF_2	4.60	1.83	0.17	7.27	64	11.26	1.19

Table 7.1: The table lists the energy scales of each of the qubits obtained from fitting the spectras.

while the XeF_2 device has the lowest $Q_{\text{cap}} \approx 150,000$. The SF_6 device has the largest variance which spans both typical values for the other two devices. This difference is not significant enough to draw the conclusion that etching with XeF_2 degrades the dielectric Q. Instead, the difference is most likely due to the difference in individual substrate Q's which vary across Si wafers. Also, the capacitive bow-tie antenna was modified to have a larger area, this modification can in turn change the participation ratio of lossy dielectric sources and in turn may account for the slight difference.

The variance of the dielectric Q from sample to sample fabricated from the same wafer is shown to vary by almost a factor of 4 in past experiments in our lab where the range for untreated silicon Q was: $200,000 < Q_{\text{cap}} < 800,000$ [135]. Measurements in this previous work only considered T_1 values measured at HFQ and not across the entire flux (frequency) range

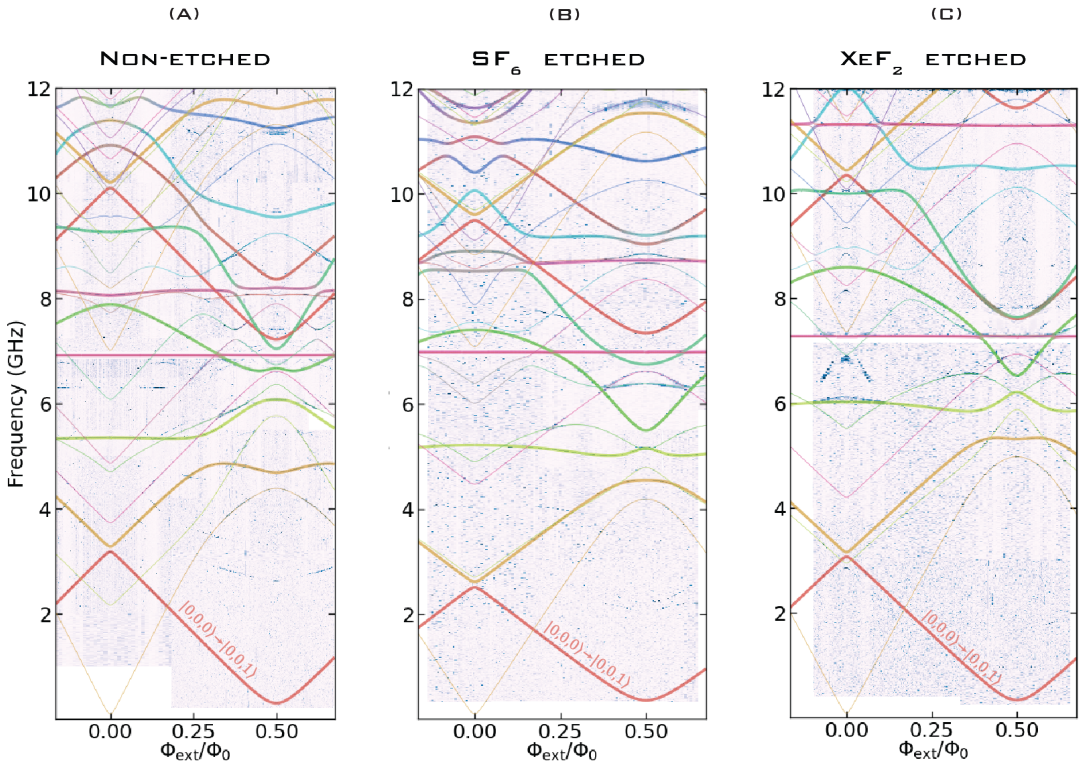

Figure 7.19: A direct side by side comparison of the measured spectrum and associated fits.

likewise the geometry of the antenna was drastically different yet shows the variance possible from qubit to qubit with the same geometry. Improvements to the capacitively coupled fluxonia in this section would come rather quickly with the optimal capacitance geometry.

The comparison of $T_1 \times |\langle 0|\varphi|1\rangle|^2 = \frac{1}{S(\omega)}$ illustrates the noise source limiting factor is inversly proportional to the qubit's transition frequency. We observe the scaled inverse spectral density is proportional to $\frac{1}{\omega^2}$; exactly the same way dielectric loss spectral density should scale. This furthermore illustrates the limiting source of each qubit must be dielectric loss producing the spectral densities displayed which all scale in the same manner.

An overwhelming positive when using etching is the chain modes show a significant increase in mode frequency while the coupling also drops. This is the major allure to utilizing etching techniques in ultra-high impedance SCQC especially when the samples are not affected negatively by both etch-

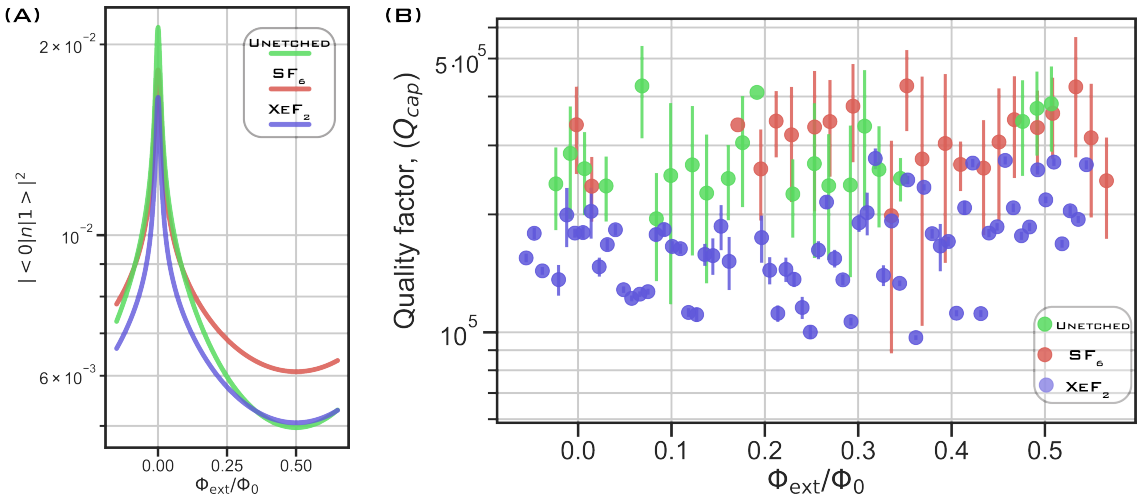

Figure 7.20: (A) the charge matrix element squared for all devices superimposed. The matrix elements squared change by approximately a factor of 4 across flux quantum. (B) The dielectric quality factor across flux quantum for all devices.

Etch	$\bar{T}_1^{\text{HFQ}}$ (μs)	$\bar{T}_2^{\text{HFQ}}$ (μs)	χ_{01}^r (MHz)	χ_{01}^m (MHz)	$\bar{T}_1^{\text{IFQ}}$ (μs)	$\bar{T}_2^{\text{IFQ}}$ (μs)
None	362	212	2	150	109	175
SF_6	330	270	2.5	60	101	201
XeF_2	263	235	5	9	54	99

Table 7.2: The table lists the average indexed time domain results along with the dispersive shifts of the 01 transition when biased at HFQ.

ing techniques. Therefore, using both etching techniques are found viable for creating fluxonium qubits with large energy relaxation characteristic times. To further compare these samples the $\bar{T}_2^E$ are compare at HFQ where the source of decoherence considered is photon shot noise at the cavity and the chain mode frequencies. The dispersive shifts used in the calculation are extracted from the detailed fluxonium coupled to a single chain mode and resonator fit. The temperature used in the simulation is $T_{\text{eff}} = 50$ mK. The total decay rate of thermal photon dephasing from the resonator and the chain mode are added in parallel. The analysis shows the non-etched and SF_6 sample is limited by the thermal photon shot noise from the chain modes which have large dispersive shifts. On the contrary, the XeF_2 etched sample has the thermal photon shot noise limited decoherence from the res-

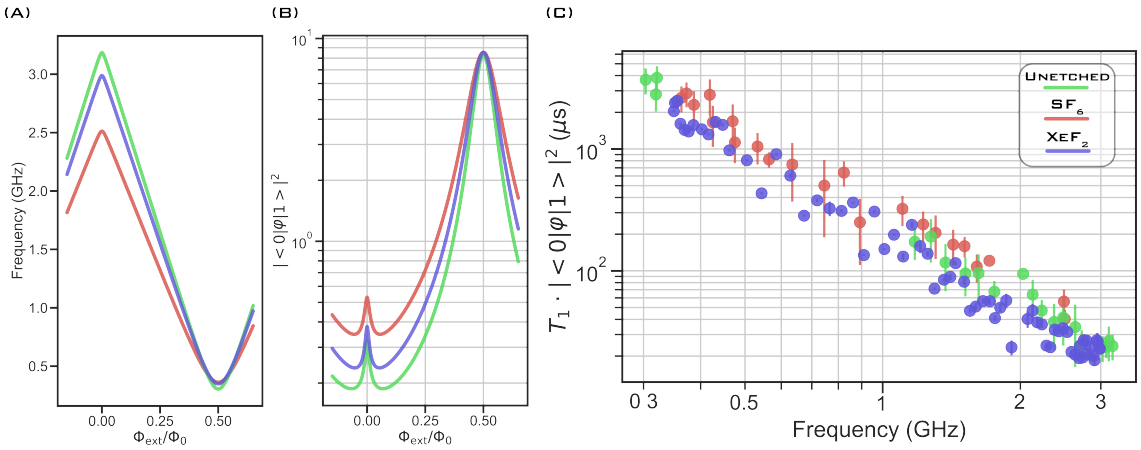

Figure 7.21: (A) The qubit frequencies superimposed for all three devices. (B) The phi matrix element squared for all devices superimposed. (C) The dielectric noise spectral densities as a function of transition frequencies for all devices.

onator. To optimize future devices, the coupling should be reduced such that the dispersive shift of the resonator is reduced. This result nevertheless provides result which support that increasing the chain mode frequency effectively mitigates the thermal photon dephasing induced by the chain mode. For large values of χ_{01}^{m} this effect saturates for values greater than 10 MHz.

7.6 Inductively coupled fluxonia: overview

The next fluxonia sample studied in depth consists of a qubit with energy scale combination # 2 with an on-chip 2D resonator as the readout mode. The on-chip resonator shares mutual JJs with the shunting inductance of the loop. The small JJ has large antenna pads used to set the E_C of the device such that it is comparable with the previous samples in this chapter and is shown labelled in figure 7.23.

7.6.1 Circuit parameters

The experimental spectrum reveals the parasitic chain mode and the 2D resonator frequency are situated only 300 MHz apart. The close vicinity of these object physically, on chip, and in frequency space produce a non-trivial hybridization between the two seen in the spectroscopy; most likely

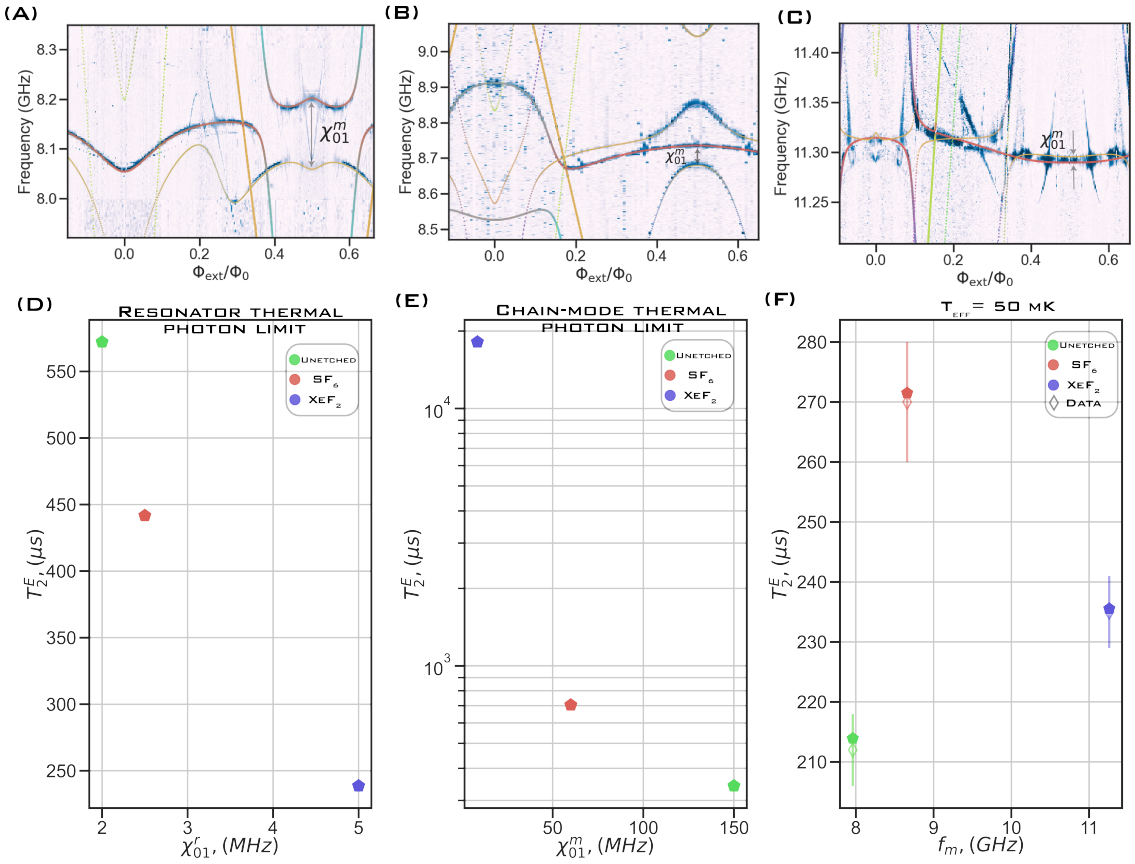

Figure 7.22: (A-C) The zoom in on the three samples spectra around the chain modes which includes the fit. (A) is the nonetched sample, (B) is the SF_6 sample, and (C) is the XeF_2 sample; where the dispersive shift is labeled at HFQ in each. (D) The simulated resonator thermal photon dephasing limit. (E) The simulated cavity thermal photon dephasing limit. (F) The combination of both superimposed with the averaged T_2^E data, simulated with an effective temperature of 50 mK.

caused by a non-negligible capactive coupling between the small JJ shunting capacitance and the resonator capacitance. This creates the necessity for a new term in the Hamiltonian which now must include coupling between the chain mode and the resonator. The new Hamiltonian used to fit this device includes this extra coupling term between the resonator and the chain taking

form:

$$\mathscr{H}_{frmj} = 4E_C\hat{n}^2 - E_J\cos(\hat{\varphi} - \varphi_{ext}) + \frac{1}{2}E_L\hat{\varphi}^2 + f_r r^\dagger r - ig_{rj}(r^\dagger - r)\hat{n} + f_m m^\dagger m - ig_{mj}(m^\dagger - m)\hat{n} + g_{mr}(r^\dagger - r)(m^\dagger - m) \tag{7.2}$$

Fitting the spectrum to this Hamiltonian the energy scales are extracted

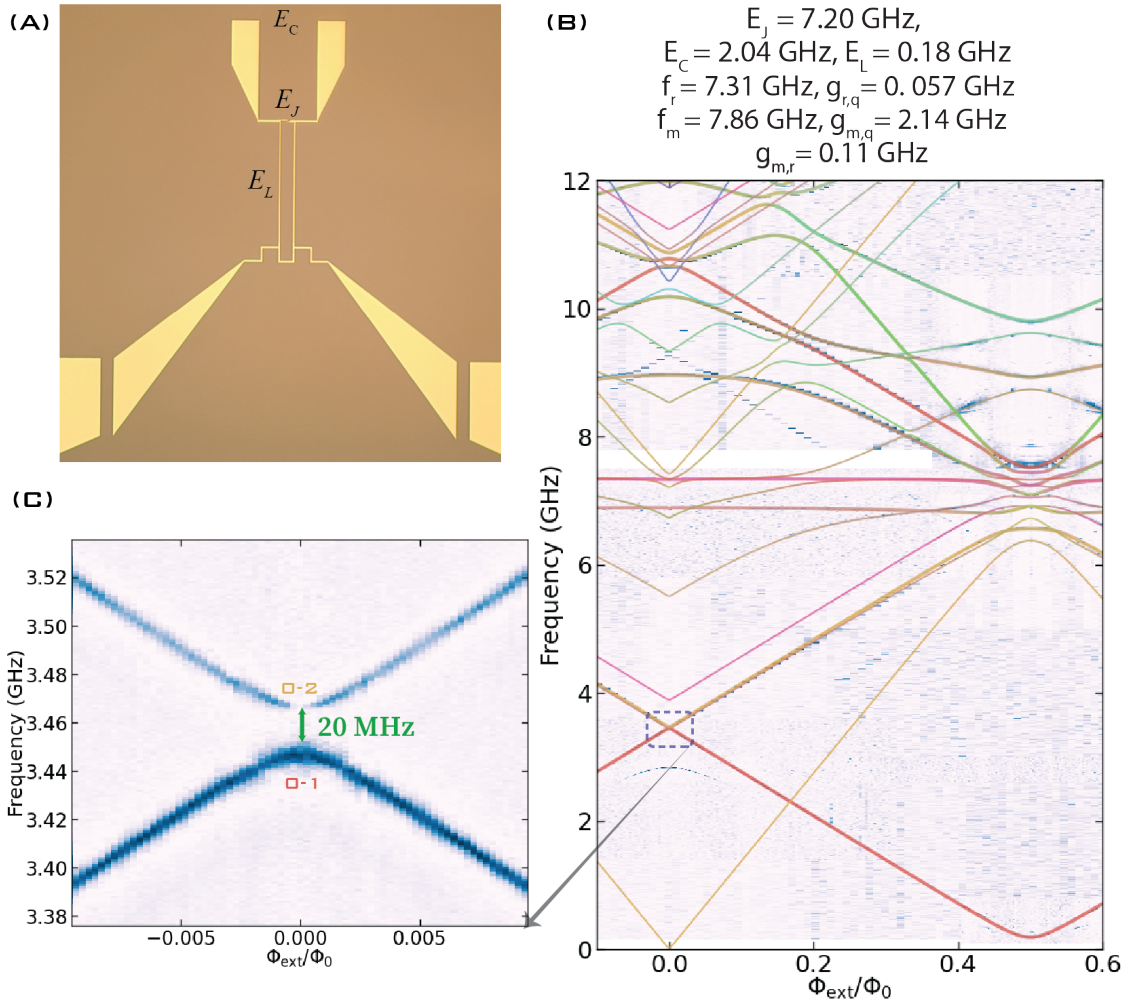

Figure 7.23: (A) An optical image of the inductively coupled device with the three main circuit parameters labeled. The leads at the bottom of the device are used to couple the resonator to the incoming microwave signals. (B) The spectrum and fit up to 12 GHz. (C) A zoom in of two-tone spectroscopy of the 0-1 and 0-2 transition at IFQ. These to transitions are separated by only 20 MHz.

where E_J of this device is slightly larger than the other samples studied

in this section. When considering all three coupling terms the designed qubit-resonator coupling $g_{r,q} = 0.057$ GHz is recovered with a qubit-chain mode coupling of $g_{m,q} = 2.14$ GHz and a resonator-chain mode coupling of $g_{m,r} = 0.11$ GHz. The new Hamiltonian fit reveals a non-trivial resonator-chain mode coupling which presumably arises due to the large shunting capacitors on either end of the junction. This creates a resonator and chain mode hybridized states making the distinction between the two in spectroscopy virtually impossible as we will later see. The chain mode is the differential mode and we expect to see no coupling from the common mode due to the (almost) perfect symmetry on either side of the small junction. It is true if there was asymmetric inductance or capacitance on either side of the small JJ a large coupling to the chain's common mode can occur. The qubit is considered to be in the second energy scale combination due to the ability to fit the first transition and the second transition using the phase-slip Hamiltonian while incorporating the double phase-slip term.

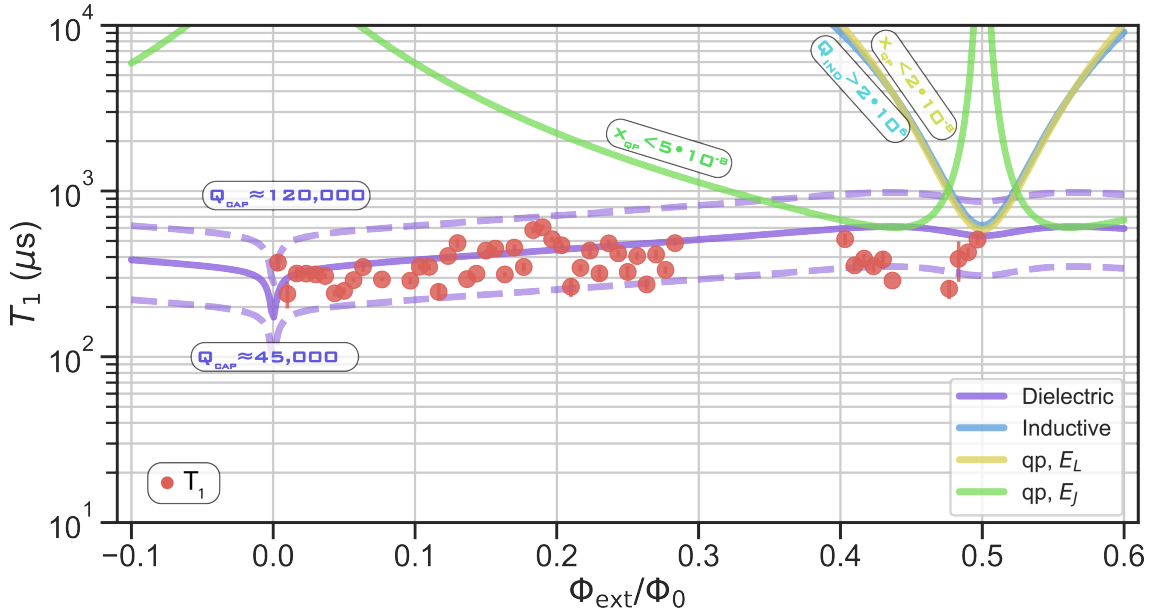

Figure 7.24: Energy relaxation across half of a flux quanta. The values for $T_1 > 200$ μs at every flux point. The main loss mechanism is from the lossy dielectric.

7.6.2 Time domain

The energy relaxation of the 0-1 transition is taken many times over and again statistically analyzed and fit to the various sources limiting this fluxonium qubit's lifetime. The dominant source of energy relaxation is the dielectric loss, where the bounds for Q_{cap} are less than the previous qubits with similar energy scales where $45,000 < Q_{\text{cap}} < 120,000$. This is due to the geometry of the shunting capacitance which is non-ideal in this qubit's geometry. However, this particular choice for the shape/direction of the shunting capacitance was made to reduce the stray coupling between itself and the resonator's bow-tie antenna.

The indexed measurements demonstrate at IFQ, $\bar{T}_1$ of the 0-1 transition is greater than 400 μs where values as large as $T_1 \sim 600$ μs were obtained for single measurements. The decoherence time measured at IFQ is $\bar{T}_2^E \approx 80$ μs on average which is photon shot limited by the resonator plus chain mode with the chain modes dispersive shift most likely being the main source. The Q-factors extracted from the 2D resonator at this flux bias are approximately $Q_{\text{int}} \sim 10^4$, $Q_{\text{ext}} \sim 10^3$ with a resonate frequency $f_0 = 7.31$ GHz with a linewidth of the read-out mode: $\frac{\kappa}{2\pi} = \frac{f_0}{Q_{\text{tot}}} = 9.5$MHz. To improve photon-shot noise Q_{ext} can be improved by moving the chip close to the edges of the 3D copper waveguide which effectively couples the sample less to the signal ports.

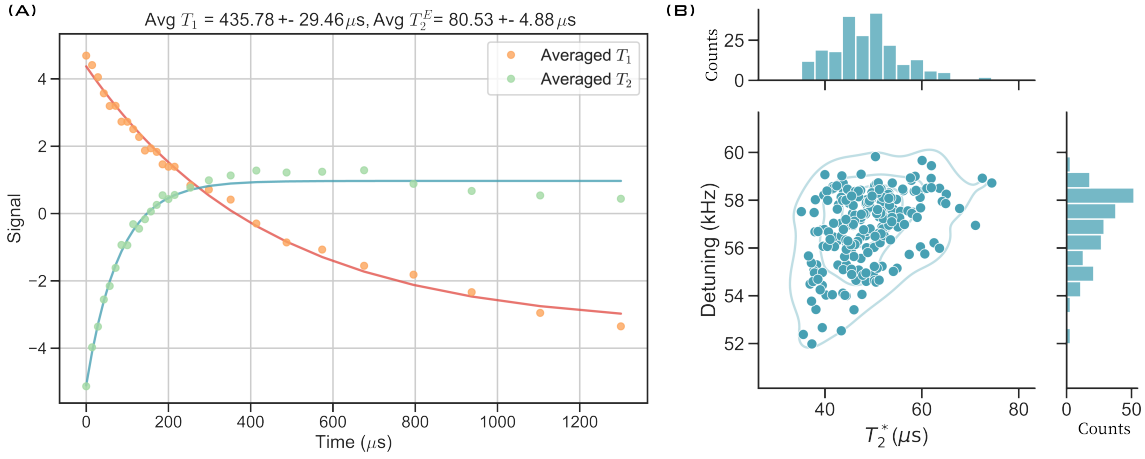

Figure 7.25: (A) An average trace of multiple T_1 and T_2^E traces taken one after another at IFQ. (B) An indexed T_2^* measurement.

While the qubit frequency at HFQ is situated at 178 MHz where T_1 is consistently greater than 500 μs with values as large as 800 μs being measured for a single trace. The $\bar{T}_2^*$ is around 100 μs which is severely limited by the photon-shot noise due to a large dispersive shift. At HFQ, the resonator and chain mode appears to be completely hybridized causing a lower Q_{int} than at IFQ where the resonator is further detuned from the chain mode. In fact, there are several resonator-like peaks that are resolvable in one-tone spectroscopy at HFQ. The resonator-chain mode hybridization at HFQ will be discussed in depth in the upcoming section where we utilize high-power single-shot readout.

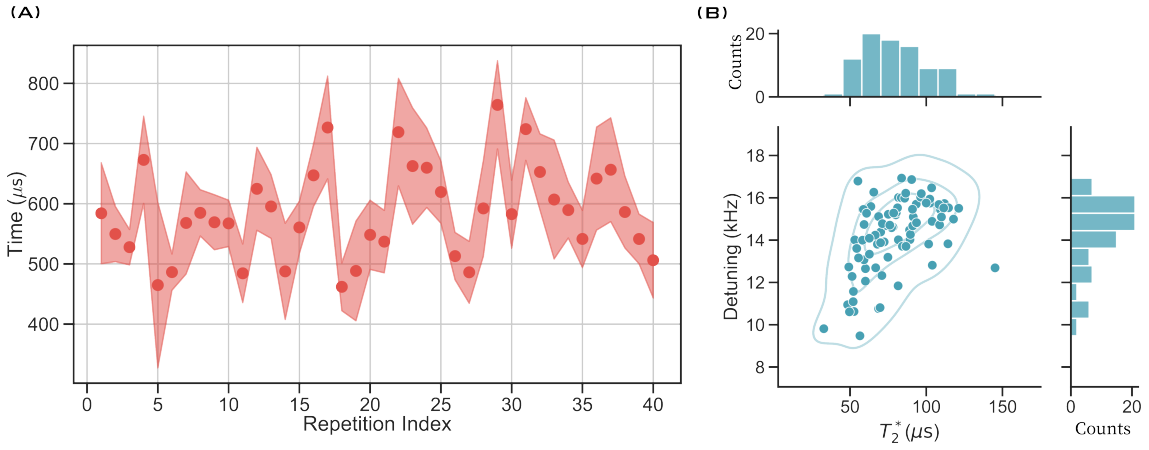

Figure 7.26: (A) Indexed T_1 measurements of the 0-1 transition at HFQ. (B) Indexed T_2^* measurements at HFQ.

Currently, the capacitance geometry appears to limit the T_1 supported by the decreased Q_{cap} found in the fit from other fluxonia in this chapter. The chain mode photon shot noise is the limiting source for T_2 and could be mitigated by etching the sample to mitigate the impact the chain mode has.

7.6.3 Single-shot read-out

We will first compare the fluxonium-only fit to the fluxonium coupled fit, using the Hamiltonian in equation 7.2, which should help disentangle the effects from the chain and resonator modes. The fluxonium fit is simulated with the three elementary circuit energy scales parameters extracted from the coupled fit and the obvious effects of the coupled modes emerge

by noticing the two flat transitions in figure 7.27 which appear at 6.9 GHz and 7.3 GHz. These modes mix the pure fluxonium transitions in a non-trivial way, especially around HFQ where many transitions become close in frequency. At HFQ, the experimental spectroscopy shows there are six transitions within a span of only 1.5 GHz. The purity of the coupled states is found by simplifying the chain-mode Hamiltonian (equation 7.2) into the superposition of several pure fluxonium states. This demonstrates the degree of mixing where the colored lines in the coupled fit displayed in figure 7.27 (B) is a visualization of this degree of mixing.

Away from HFQ, the read-out mode is the coupled state 0-4; at these external flux points the resonator has $Q_{\text{int}} \sim 10,000$. When the external flux bias is changed to HFQ state 0-4 becomes more of a qubit mode with the main contributing pure fluxonium transition being 0-2. While 0-5,0-6, and 0-7 all have reduced fluxonium purity and, therefore, must be a hybridization of states between the resonator, chain mode, and fluxonium modes alike.

At HFQ, the coupled states 0-4, 0-5, and 0-6 are all measurable by a single-tone measurement; which is typically not the case unless the transition is directly crossing the read-out mode. The 0-5 and 0-6 modes have their Q-factors extracted to show very similar values where $Q_{\text{int}} \sim 4,000$ decreased from the read-out mode used at IFQ; while the $Q_{\text{ext}} \sim 2,000$ is a slight increase. The optimal read-out point at HFQ was found neither at the 0-5 nor 0-6 transition but is a frequency situated between. At high resonator powers, a single shot read-out of the qubit state is possible when probing this optimal read-out frequency. The integration time initially used is for 7 μs to acquire a single record in the I-Q plane while 10k-30k records were usually taken for a histogram plot as seen in figure 7.30. Each record value is an individual point in the I-Q plane and these points are rotated to produce plots with meaningful information within a single quadrature. The data is rotated such that a straight line that passes through both "blob's" centers is either entirely on the real or imaginary axis. The data is then projected onto the parallel axis and binned into a histogram. The histogram is fit to a two

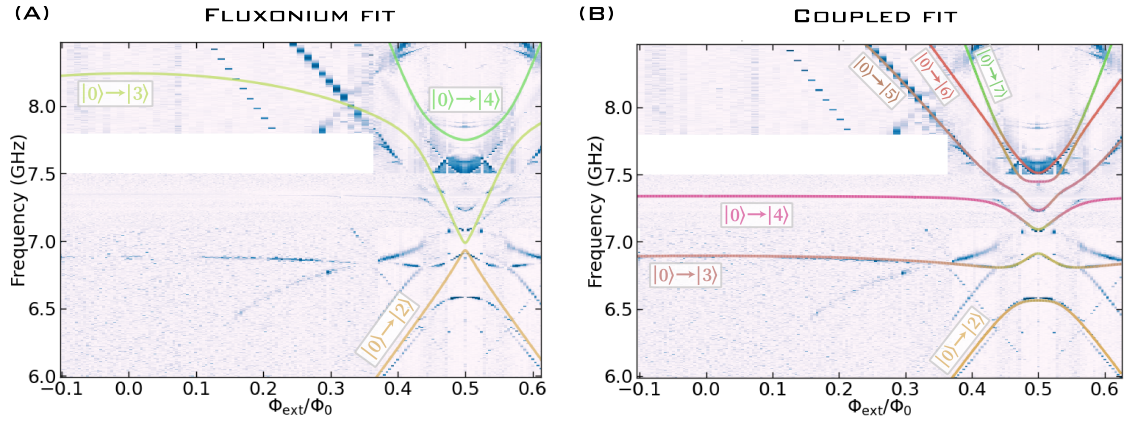

Figure 7.27: The fluxonium only fit compared to the fit including the resonator and chain mode shows the drastic hybridization between states. The two flat lines emerging in the spectrum are due to the two new modes introduced.

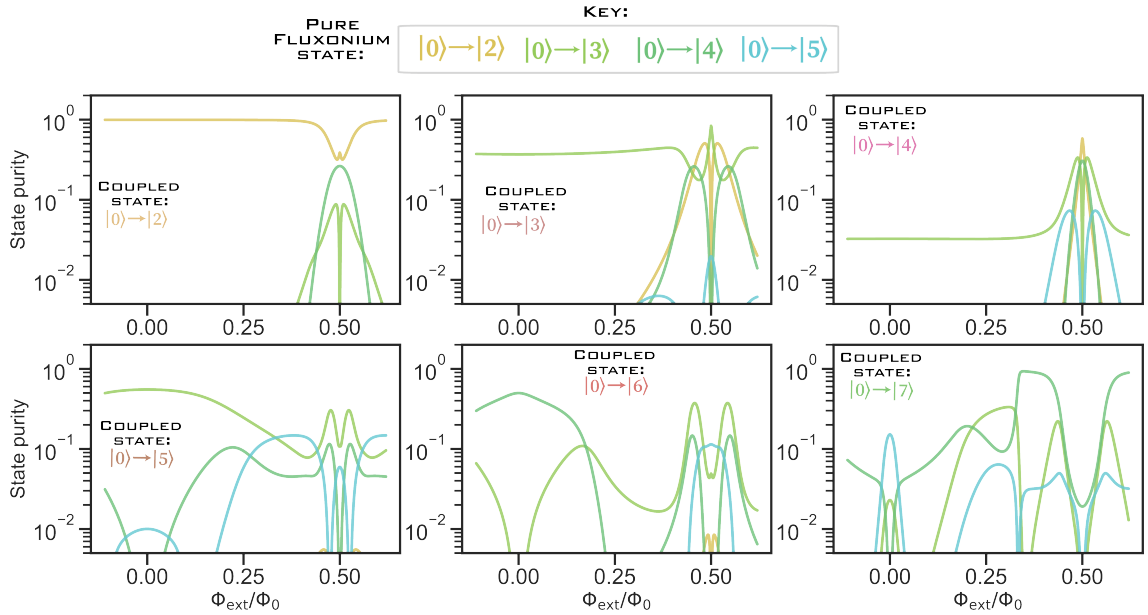

Figure 7.28: The new states from the coupled Hamiltonian 7.2 are comprised of the superposition of "pure" fluxonium-only states. The inner product of the new states with the pure fluxonium states is the "purity" of a specific transition. The purity is the amount the eigenvectors of the fluxonium only fit contributes to the new coupled states. The resonator and the chain mode coupling mix the pure fluxonium states, especially around HFQ where coupled states 0-4,0-5,0-6 all show up in one-tone spectroscopy.

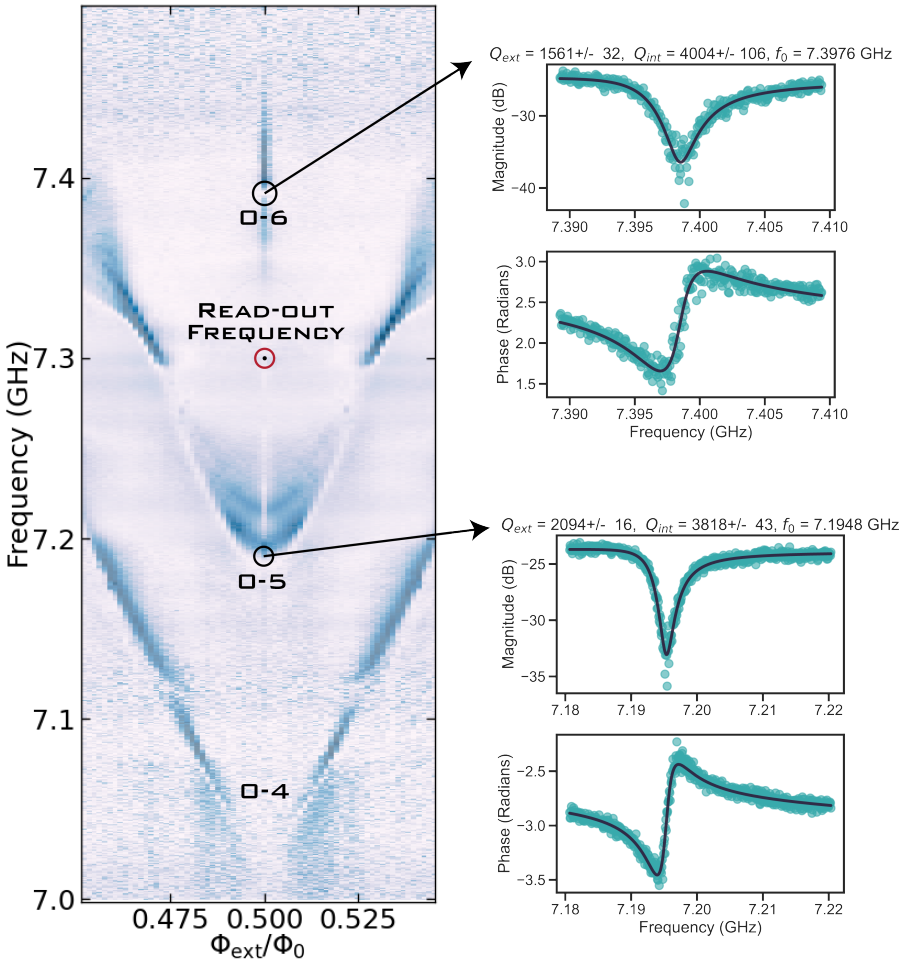

Figure 7.29: At HFQ the optimal readout frequency point is situated directly between the 0-5 and 0-6 transitions. Both modes have similar Q_{tot} which have smaller values than the value of the bare mode 0-4 at IFQ.

Gaussian function [171]:

$$f(x) = A_0 e^{-(x-x_0)^2/\sigma_0^2} + A_1 e^{-(x-x_1)^2/\sigma_1^2} \tag{7.3}$$

where $A_{0,1}$ are used to extract the populations of either the ground state or first excited by the relation:$p_{0,1} = \frac{A_{0,1}}{A_0+A_1}$. The populations can be used to extract the effective temperature of the qubit by the Boltzmann distribution:

$$\frac{p_1}{p_0} = e^{-hf_{01}/k_B T_{\text{eff}}} \tag{7.4}$$

Using these formulas and a single shot measurement without exciting the qubit state finds a qubit effective temperature of T_{eff} =10.5 mK. The extracted qubit temperature is comparable to the temperature of the base plate of the fridge which was consistently at 8 mK. To verify which I-Q blob rep-

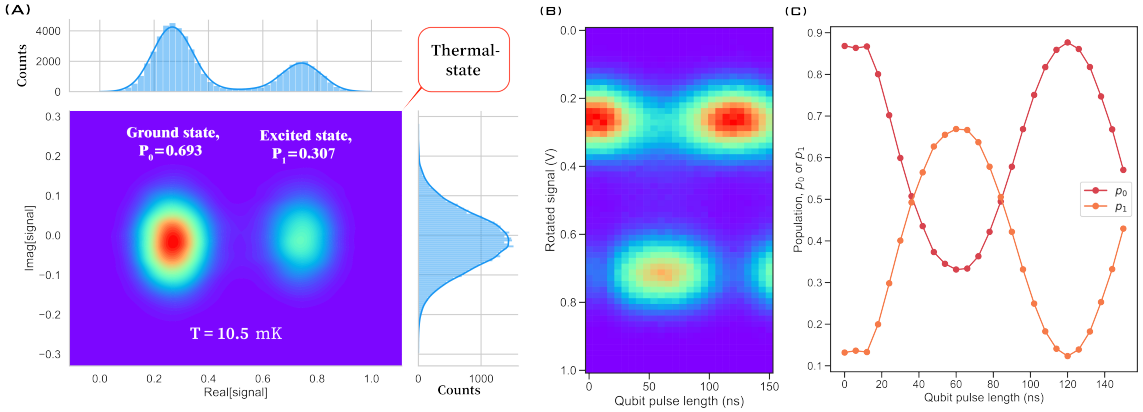

Figure 7.30: (A) Thermal state of the qubit at HFQ. The temperature of the qubit is found to be 10.5 mK. (B) Single shot histogram versus qubit pulse width shows two distinct blobs appearing in the I-Q plane. (C) The extracted populations of the single shot Rabi measurement.

resented the ground state of the qubit a Rabi pulse measurement with single shot readout was executed. For each pulse width a single shot measurement was taken and the results verified the more intense blob was indeed the ground state where the population values are observed to swap when sweeping the qubit pulse duration. The other two quantities are $x_{0,1}$ which is the center of each Gaussian fit, and $\sigma_{0,1}$ which is the variance of each Gaussian peak. These quantities can be used to find the signal-to-noise ratio

(SNR) given by the equation [68, 177]:

$$SNR = \frac{|x_1 - x_0|}{\sigma_0 + \sigma_1} \tag{7.5}$$

For initial measurements, SNR was 2.4 and observed to increase with in-

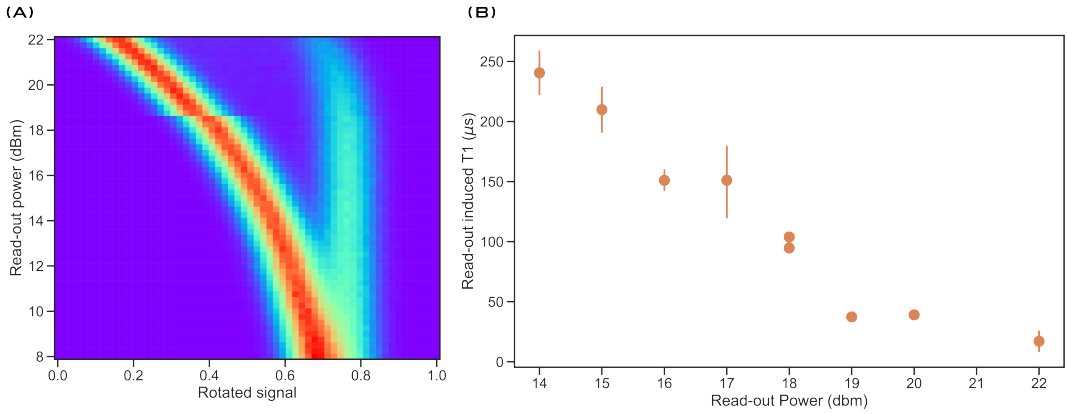

Figure 7.31: (A) The rotated single shot of the resonator at HFQ for varying resonator drive powers. Around 12 dBm two distinct resonator states become visible where the separation increases when increasing the power. (B) The resonator readout modifies the thermal state by enhancing the decay rate of p_1 into the ground state.

creasing readout power. However, the action of reading out by exciting the resonator induces the population to shift back into the ground state and the decay rate is further enhanced when increasing the power. The excited population characteristic decay time versus read-out length was fit at multiple read-out powers (as seen in 7.31 (B)) where the characteristic decay time at powers where two blobs become visible is less than the T_1 of the qubit when using measured at lower resonator power below 8 dBm. The read-out induced lifetime of the qubit for the single shot read-out power used was 120 μs for a power of 18 dBm.

Furthermore, the second excitation drive frequency was swept revealing the ability to resolve many different higher-level qubit transitions when using the single-shot method. The signature of the higher states was not the appearence of more blobs in the I-Q plane but instead was different population values between the ground and excited states.

The 0-2, 1-3, and 0-4 transitions were driven at different powers while

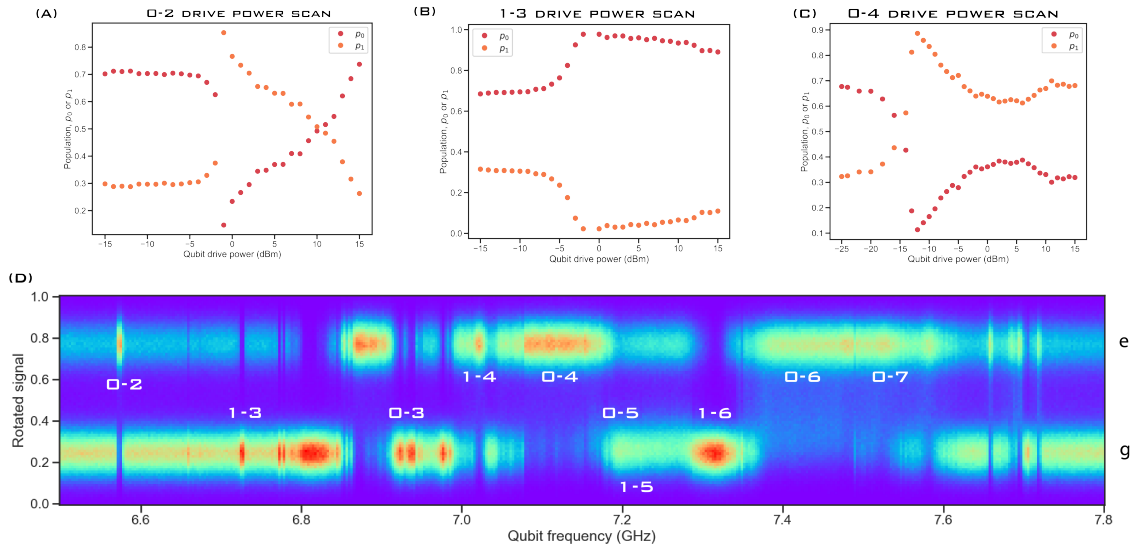

Figure 7.32: (A,C) Qubit populations versus the 0-2 (0-4) pump power. At -2 (-12) dBm the population is pumped into the first-excited state. (B) The 1-3 qubit transition is pumped at -1 dBm the population is pumped into the ground state. (D) The qubit pump tone is swept in the frequency range many transition's meet. When a tone is resonate with a qubit transition, either the ground or first excited state is populated. The bottom signal (centered around 0.25) represents the population in the g state while the top signal line (centered around 0.75) represents the population in the e state.

measuring single shot data with a 15 μs integration time and a total duty cycle greater than the cavity induced T_1. When pumped at certain powers the 0-2 and 0-4 transitions would transfer the populations into p_1. While when the 1-3 transition would transfer the population into p_0.

The transfer of population can be understood by parity rules with the φ matrix element inducing transitions. Since φ is an odd parity operator then the parity of the transition must be preserved. Therefore, if the 0-2 pump is moving the population into the 2 state then this can only decay to the 1 state and for the 3 state this can decay to 2 or 0. This effect has been studied in the previous experiment for a cavityless fluxonium [34].

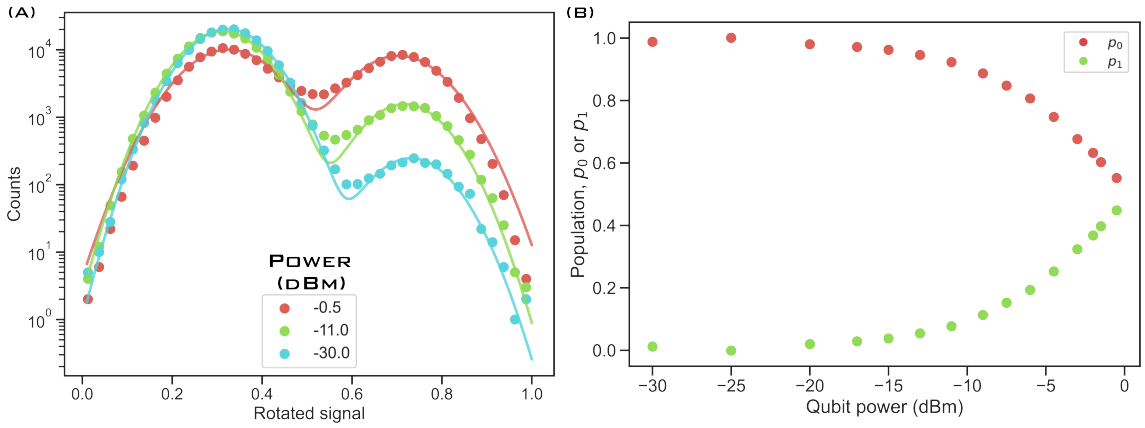

Figure 7.33: (A) The fitted histogram for various single-shot measurements at differing qubit drive powers. (B) The extracted populations coming from the fit in (A).

A low-power qubit excitation tone was continuously shined into the sample box while the qubit drive power was changed. Single-shot measurements were taken and the resulting populations were extracted. Increasing the qubit's power resulted in preparing a 50/50 state; known to happen when saturating the qubit with a long drive tone. Looking closely within a single record, quantum jumps were resolvable. A quantum jump is when the state of the qubit spontaneously becomes excited or de-excited through the emission of a photon [31]. The quantum jump scans were taken by piecewise demodulating an ongoing trace every 7 us. Doing so allows us to resolve when the qubit jumps into the first excited state or relaxes back to the ground state. Each "jump" above a certain voltage threshold value counts as a "click"; where the threshold is defined by the Gaussian blob fit of a single

record: $x_{\text{thr}} = x_0 + 2\sigma$ [195]. Quantum jump statistics have been studied in fluxonium qubits extensively in references [68, 94, 182]. The quantum jump

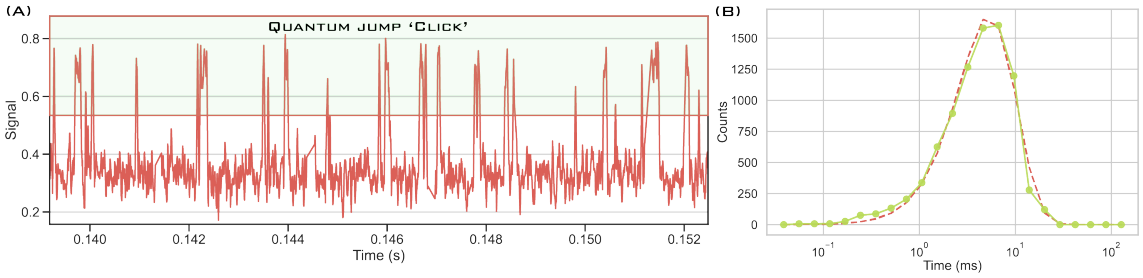

Figure 7.34: (A) A raw trace of an individual record. A quantum jump occurs in this trace when the signal is within the shaded region. (B) The Poisson distribution of an individual record. The trace has the time between clicks sorted into logarithmically spaced bins to create a histogram for the average time spent in the ground state. The trace shown is for the thermal equilibrium state with an average time $\bar{\tau} = 5.8$ms spent in the ground state before a quantum jump occurs.

traces were analyzed by finding the mean time between each quantum jump from the ground to the excited state. The method for analyzing the quantum jumps was performed and outlined in [182]. The time between jumps is sorted into logarithmically spaced bins where the histogram is multiplied by the bin spacing, defined as Δ. For a Poissonian process with the mean time between jumps τ, the distribution takes the form:

$$\tau \mathscr{P}(\tau) = \frac{\tau}{\bar{\tau}} e^{-\tau/\bar{\tau}} \,. \tag{7.6}$$

The distribution was further normalized by the total sum of measurements in the bin by multiplying the distribution by $\Sigma\Delta/\bar{\tau}$; where Σ was the sum of all histogram values. The binning was done on a logarithmic scale so an extra factor of $\ln(10)\tau$ was added to account for the bin sizes dependence on τ. The resulting distribution was used to fit the quantum jump data:

$$\tau \mathscr{P}(\tau) = \Sigma\Delta \ln(10) \frac{\tau^2}{\bar{\tau}^2} e^{-\tau/\bar{\tau}} \,. \tag{7.7}$$

The meaningful fit parameter is the meantime in the ground state, $\bar{\tau}$. For the qubit drive off, $\bar{\tau} = 5.8$ ms. The binned histograms are indeed described well by Possionian statistics indicating no quasiparticle disruption in the

fluxonium as can be seen from the deviation of the Poissonian fit [68, 182].

When the qubit power is increased the average time spent in the ground state decreases or, likewise the excitation rate $\Gamma_{\uparrow}$ increases with the microwave signal amplitude. This result has been shown to follow the following relation [58, 166]:

$$\Gamma_{\uparrow} = \frac{\Omega^2}{2(\gamma_2 + \Gamma_m/2)} \tag{7.8}$$

where Ω is the Rabi frequency proportional to the qubit drive amplitude, γ_2 is the average $1/T_2^* = 1/95\mu s^{-1}$ found in normal measurements, and Γ_m is the inverse measurement time. Fitting the data to this function shows the experimentally measured jump rate is dictated by the Zeno effect. The jump rate is due to the competition between the weak Rabi drive which flips the qubit population versus the readout of the qubit state which projects the qubit into an eigenstate of σ_z [58].

These results can be further used to explore the quantum Zeno effect in fluxonium qubits where the measurement and control effects on fluxonium states can be tested in further detail. Improvements can be made by decreasing the measurement times by utilizing TWPA amplifiers. This interesting effect also furthers the discussion about parasitic chain modes and their possible applications for modifying measurements performed on fluxoniums which now could be used as a possible source for high power single-shot measurements of the qubit state.

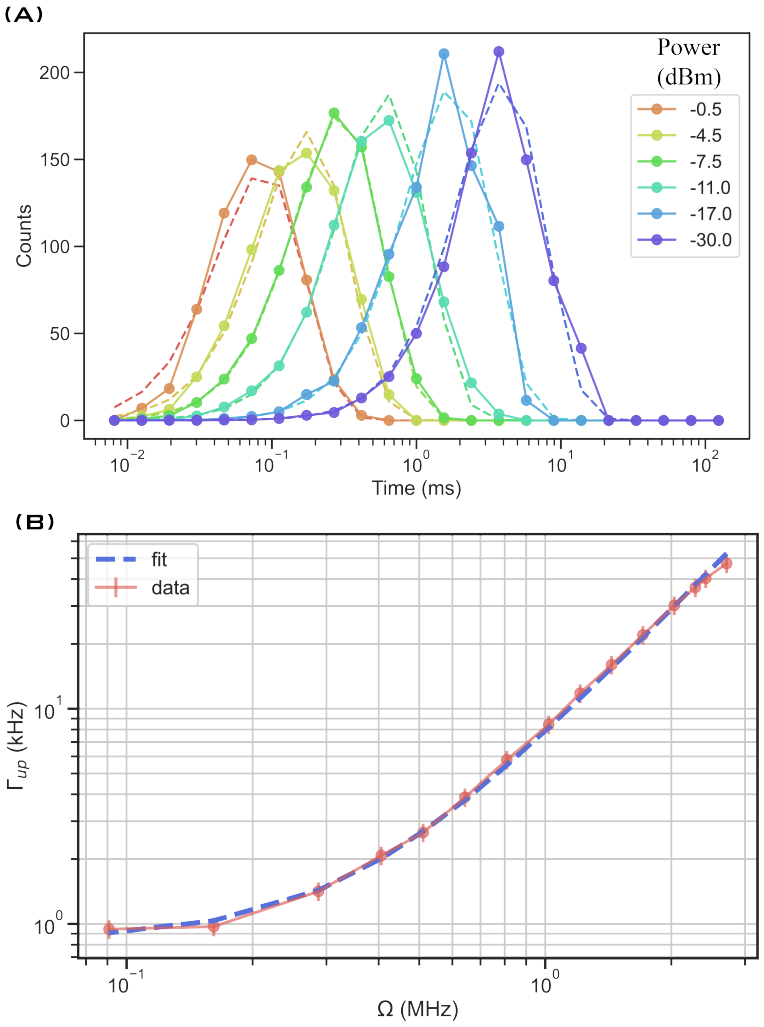

Figure 7.35: (A) The binned data fit to the Poissonian distribution for several qubit powers. (B) The excitation rate of the qubit versus microwave drive amplitude.

8
Blochnium

"And now I see with eye serene. The very pulse of the machine;" — William Wordsworth

8.1 Introduction

The blochnium [141] is experimentally created by shunting a weak junction with an exceptionally high-value inductance — simultaneously mitigating unwanted stray capacitance to the weak JJ while pushing the parasitic chain modes to a higher frequency. Both are accomplished experimentally by releasing the circuit from the silicon substrate using the XeF_2 etching technique. Releasing the circuit is the key technological innovation behind the realization of blochnium.

The main characterizing property of the etched circuits is the vanishing flux-sensitivity of the qubit transition between the ground and the first excited states which, nevertheless, rapidly recovers for transitions to higher energy states. The spectrum across devices agrees with a duality mapping of blochnium onto transmon, which replaces the external flux by the offset charge and introduces a new collective quasicharge variable in place of the

superconducting phase [93, 124].

Experimentally, in this chapter, the measured RF-excitation spectrum of an etched device, measured up to 20 GHz, is displayed and analyzed in detail. Secondly, an assortment of etched circuits are measured and characterized where the extracted parameters from spectrum and time domain data are discussed in depth. Our result unlocks the door to an unexplored regime of macroscopic quantum dynamics in ultrahigh-impedance circuits.

8.2 Generalized Bloch's theorem

Any solution of the Schrödinger equation describing a quantum particle subjected to a periodic potential gives rise to band structure [12]; where the particles energy can occupy bands of allowed states separated from other bands by a region of inaccessible energy states. This effect arises from an interference type phenomenon which is described by Bloch's theorem. A quantum particle traversing a periodic potential with period "a" has the eigenfunction solution to the Schrödinger equation:

$$\Psi_q(x) = u_q(x)e^{iqx} \tag{8.1}$$

where $u_q(x) = u_q(x+a)$. This solution is a function that encapsulates the periodic potential; making the solution a distance x+a away exactly equivalent to the wavefunction at x: $\Psi_q(x+a) = \Psi_q(x)e^{iqa}$. The quantity q has units inverse of x and is commonly called the quasimomentum. The energy eigenvalues depend on the continuous quantity q resulting from the bunched energy states that form a single band. Each band index is labeled as an integer "s".

In the reduced picture, the quasimomentum is defined within an interval of $\frac{-\pi}{a} \leq q \leq \frac{\pi}{a}$. This region is called the first Brillouin zone and each q differing by an integer multiple of the potential period $2\pi/a$ are equivalent:

$$q' = q + \frac{2\pi}{a}k\ . \tag{8.2}$$

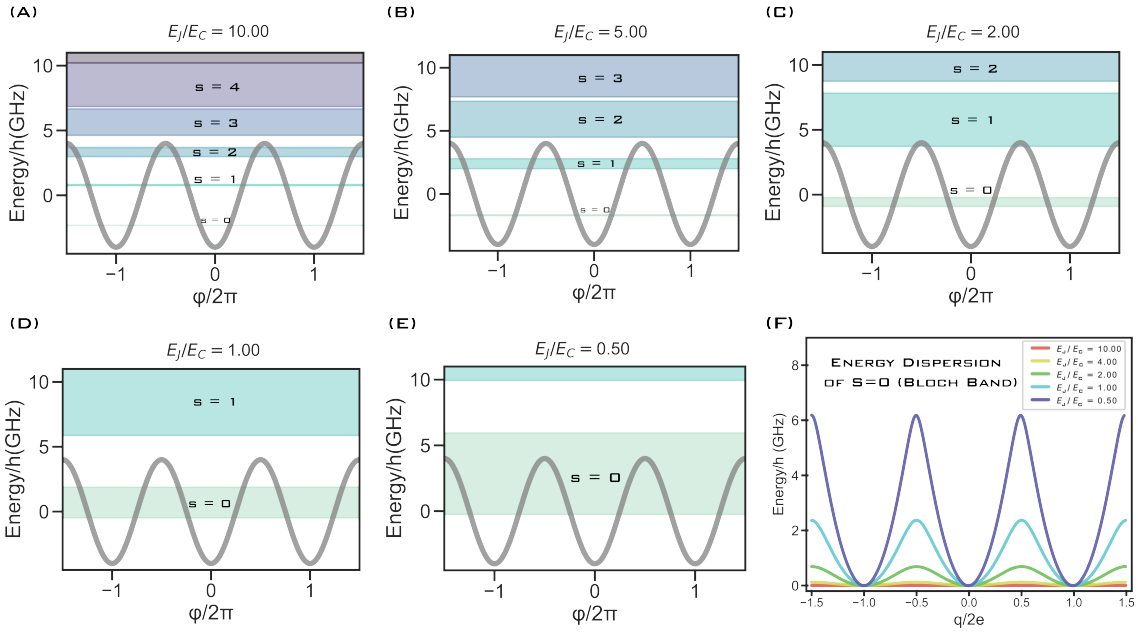

Figure 8.1: The JJ potential energy $E = -E_J \cos\varphi$, (E_J = 4GHz), creates a periodic potential for the fictitious JJ particle which has a kinetic energy E_C. The particle can tunnel into all wells which extend from $-\infty$ to ∞. The width of the resulting band depends on the ratio of the height of the potential E_J and the kinetic energy E_C. As the ratio decreases the width of the Bloch bands increases; as seen in (F).

8.3 Blochband description of a JJ

Josephson showed that a junction can be viewed as a non-linear inductance which carries flux $\varphi_0 \times \varphi$ with energy $E = -E_J \cos\varphi$. When quantum fluctuations of φ are small compared to 2π, the inductance can be linearized and the junction responds as a superconductor with a well defined phase difference φ. Yet, an opposite scenario was suggested in the case φ is free to extend beyond the 2π-interval [6]. In this scenario, when φ extends beyond a single Josephson well, it is essential to take into account the junction's intrinsic oxide capacitance across the Josephson element, C_J. The resulting circuit equations then mimic an electron in a crystal: the phase difference φ is the position, the capacitance is the mass, the charge on the capacitor is the momentum, while the Josephson energy corresponds to a periodic crystal potential. The dynamics of φ can therefore be described by extended Bloch waves and continuous Bloch bands [93].

The Schrödinger equation for an isolated JJ is:

$$\left\{4E_C\Big(-i\frac{\partial}{\partial\varphi}-q\Big)^2+E_J(1-\cos\varphi)\right\}\Psi_q = E_q\Psi_q \tag{8.3}$$

which takes the form of a Mathieu equation [33] that has periodic solutions, $\Psi_q(\varphi+2\pi) = \Psi_q(\varphi)$, in the form of Bloch waves: $\Psi_q(\varphi) = \psi_q(\varphi)e^{-iq\varphi/2e}$ where q is now the conjugate variable to the extended phase variable φ and is called the quasicharge, analogous to the quasimomentum.

This description of an isolated JJ demonstrates the extended scheme forms bands of energy which continuously depend on the quasicharge which arise from a quantum particle living in the Josephson potential. The energy bands are 2e-periodic in q and are equivalent when displacing the quasicharge by $2e \times k$ such that $E_B(q+2ek) = E_B(q)$ where k takes values of all real numbers. For simplicity, only the energy dispersion of the lowest (s = 0) Bloch band is considered and is denoted as $E_B(q)$; this is the energy dispersion of what is called the Bloch band (BB) of the JJ shown in figure 8.2 (A). Connecting the dynamics back to a crystal, a Cooper pair tunneling (q changing by 2e) is analogous to a Bragg reflection, where the quasicharge is physically the externally supplied charge to the junction. In

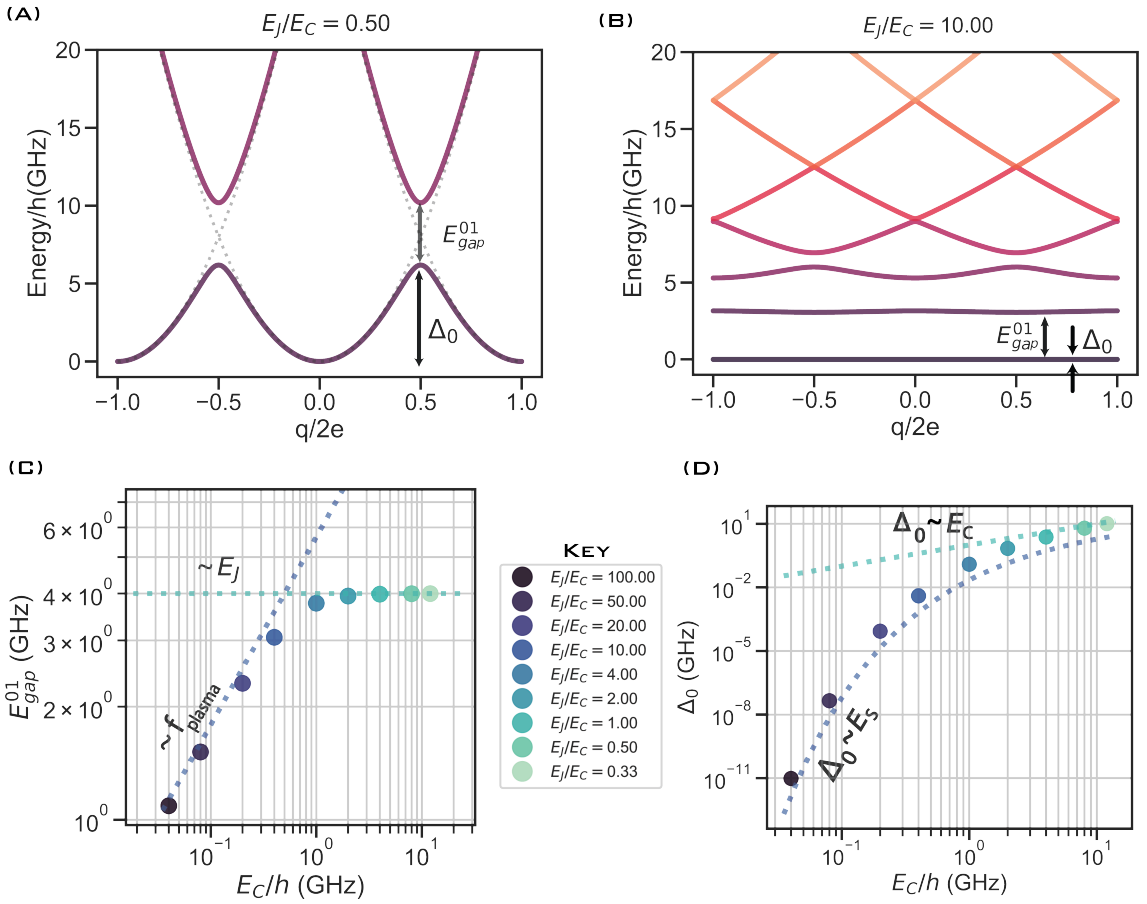

Figure 8.2: (A),(B) The s=0,1 Bloch bands (BB), with energy dispersion $E_B(q)$, are shown for two different ratios of E_J/E_C. The first two bands have a separation E^{01}_{gap} while the s=0 band has height Δ_0. When the ratio is low (<5) the gap is approximately E_J while when the states are localized the gap is approximately the plasma frequency $\sqrt{8E_JE_C}$. (C, D) The simulation of E^{01}_{gap} and Δ_0 for $E_J = 4$ GHz while sweeping the value of E_C.

other words, at low frequencies the junction stores charge q and is characterized by a $2e$-periodic charging energy $E_B(q)$. This transforms the junction into a non-linear "Bloch" capacitance (an equivalent of the effective mass). This idea is dual to the usual JJ behavior, where quantum fluctuations of φ are suppressed, but instead now when quantum fluctuations of q are suppressed the Bloch capacitance can be linearized and the junction responds as a capacitor.

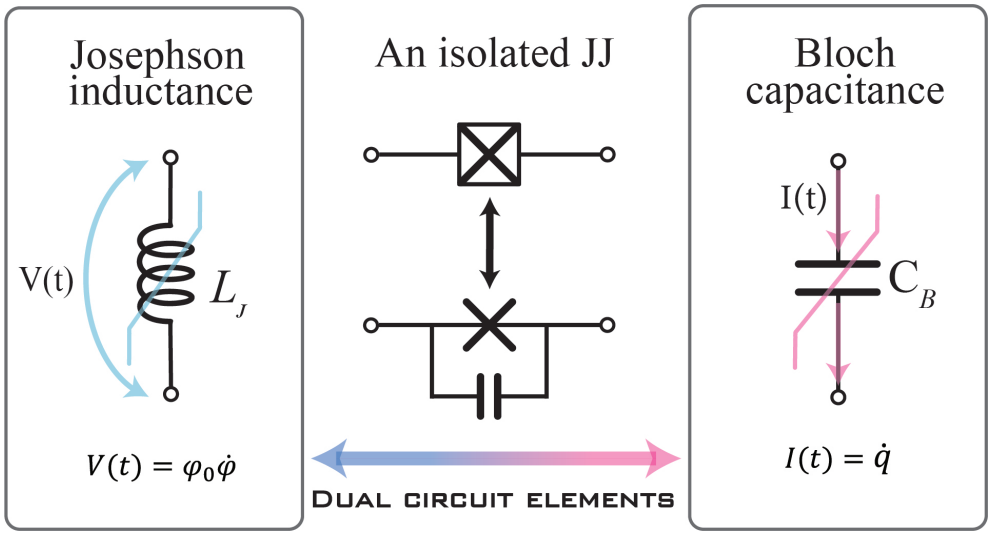

Figure 8.3: A JJ is approximately self-dual [128] and can behave as a nonlinear inductance or a nonlinear capacitance. On one hand, a single JJ creates a nonlinear current producing the Josephson inductance while on the other hand, the JJ has a periodic charging producing the Bloch capacitance.

The duality becomes more clear when asked: Is a Josephson tunnel junction between two superconductors a superconducting link or an insulating break? The answer is revealed when considering the impedance of the JJ embedding environment.

8.4 An inductively shunted JJ

In practice, measuring a perfectly isolated JJ is not feasible. There is always external leads which add extra capacitance to the innate junction capacitance, C_J, which in turn produces the localization of phase within the 2π interval. Therefore, the junction's external circuit, necessary for practical-

ity, plays a decisive role in choosing between the two antagonistic scenarios of phase localization or phase delocalization.

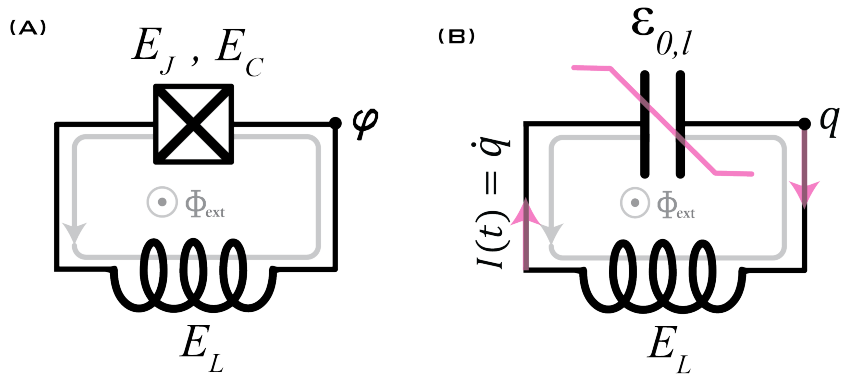

Figure 8.4: (A) The standard fluxonium qubit circuit diagram with the degree of freedom φ. (B) The Blochnium circuit diagram which consists of a non-linear capacitance shunted by a large inductance. The degree of freedom, in this case, is the quasicharge, q.

We circumvent this practical issue by shunting a weak JJ by a very large valued inductor ($L_{\text{tot}} > 2\mu\text{H}$), with minimal external capacitance. By doing so the phase is now defined across all space, $\varphi \in (-\infty, \infty)$ where the lower eigenstates are exposed to the periodic nature of the JJ potential corrugated by a slowly growing harmonic potential produced by the inductance. When $E_L \ll E_J < E_C$ the wavefunctions spread out into multiple Josephson wells at all flux values which enables a Bloch-band description of the energy spectrum – hence the name *Blochnium*. The resulting non-linear and non-dissipative electrical circuit is the first artificial atom to reach this regime.

To understand the nuances which arise from this description, we begin by starting with the fluxonium Hamiltonian with the external flux bias tunability in the inductive energy term:

$$\mathscr{H}_F = 4E_c(\hat{Q}/2e)^2 - E_J\cos(\hat{\varphi}) + \frac{E_L}{2}(\hat{\varphi} + \varphi_{\text{ext}})^2 \tag{8.4}$$

where the variable Q is conjugate to the phase difference φ. The wavefunctions in the Q picture can be found by a discrete Fourier transformation:

$$\Psi(Q/2e) = \sum_k \Psi(\varphi) \cdot e^{i\varphi Q_k/2e} \tag{8.5}$$

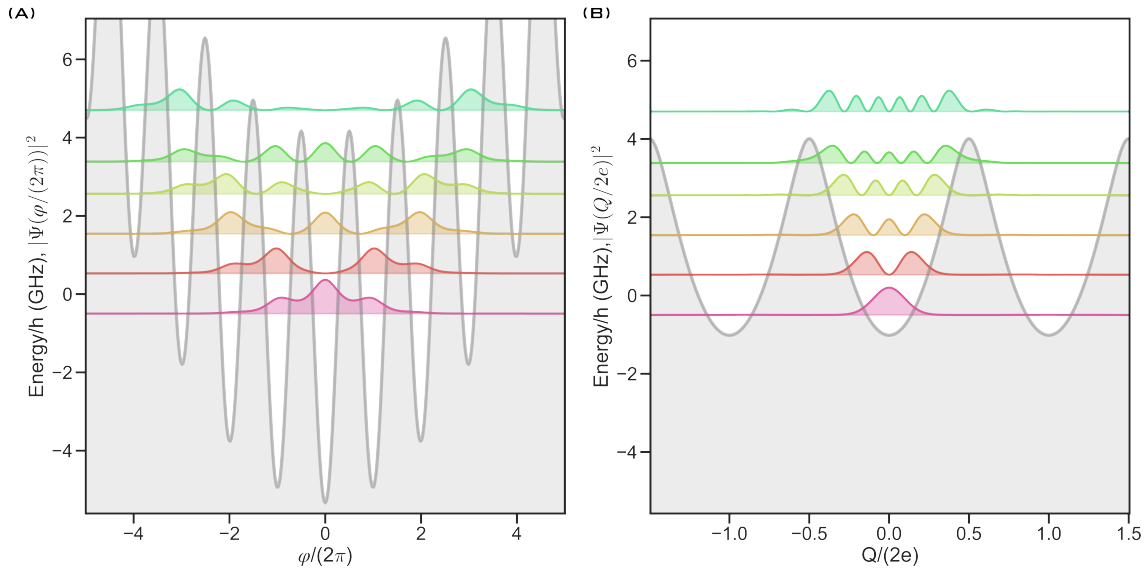

Figure 8.5: (A) Fluxonium wavefunctions in the φ picture for the circuit parameters: $E_J = 4$ GHz, $E_C = 7$ GHz, and $E_L = 0.02$ GHz at Φ_{ext}/Φ_0=0. The first five wavefunctions are spread into multiple Josephson wells. (B) Fluxonium wavefunctions in the Q picture where the states are localized within a single Bloch band potential.

The fluxonium picture results are completely correct yet only shows Q localization while the Bloch capacitance picture of an isolated JJ has not yet been mentioned. Since the wavefunctions are spread into multiple JJ wells at once, the quasicharge description becomes possible. The more spread the wavefunctions the more accurate the resulting Bloch capacitance picture becomes.

The origin of the Blochnium Hamiltonian arises when considering the charge dispersion energy of the weak JJ plus the inductive energy. Defining the Bloch band basis as: $\mathscr{H}_{BB}|s=0,q\rangle = E_B(q)|s=0,q\rangle$ and using this basis instead of the harmonic oscillator basis usually used in Fluxonium, the Hamiltonian takes the form [93]:

$$\mathscr{H}_{\mathscr{B}} = E_B(q) + \frac{1}{2}E_L(\hat{\varphi} + \varphi_{\text{ext}})^2 \,. \tag{8.6}$$

And furthermore we can represent $\mathscr{H}_{\mathscr{B}}$ solely in the quasicharge representation as:

$$\mathscr{H}_{\mathscr{B}} = \frac{E_L}{2}\left(i\frac{d}{dq} + \varphi_{\text{ext}}\right)^2 + E_B(q) \tag{8.7}$$

where now the potential energy is $E_B(q)$, and the kinetic energy is E_L. The Bloch band potential, $E_B(q)$, which is the charge dispersion of the lowest band of the small JJ can be described by a Fourier series approximation:

$$E_B(q) = \sum_{\ell=0}^{\infty} \varepsilon_{0,\ell} \cos\left(2\pi\ell q/2e\right) \tag{8.8}$$

where each ℓ is an integer index of the ℓth harmonic term contributing to the series. The first coefficient is just the average value of the BB amplitude

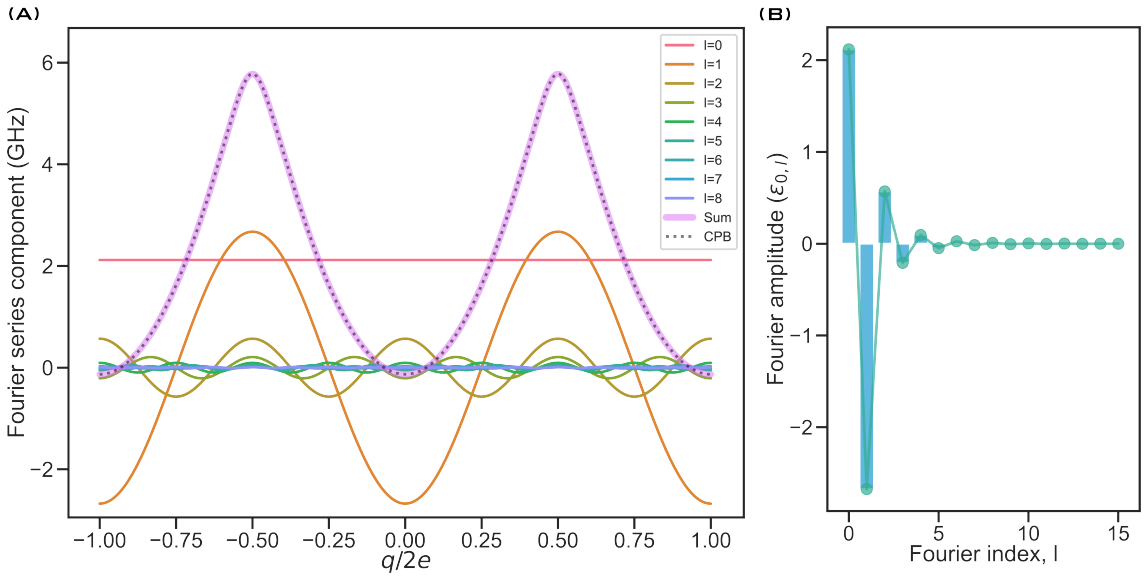

Figure 8.6: (A) The first eight Fourier series components are shown. The dashed line is the exact solution for the BB of an isolated junction which matches to a high degree the sum of all Fourier components up to ℓ=15. (B) The Fourier coefficients alternate sign and drop in amplitude for increasing index ℓ.

which can be thought of as an offset value given by $\varepsilon_{0,0} = \bar{E}_B$. The other amplitudes are found by taking the average value $\bar{E}_B$ modulated by the lth Fourier component over one period:

$$\varepsilon_{0,\ell>1} = \frac{1}{2e}\int_0^{q/2e} \bar{E}_B \cos\left(2\pi\ell q'/2e\right) dq' \ . \tag{8.9}$$

Inserting the Fourier series approximation for the charge dispersion into

the Blochnium Hamiltonian modifies the equation to:

$$\mathscr{H}_B = \frac{E_L}{2}\left(i\frac{d}{dq} + \varphi_{\text{ext}}\right)^2 + \sum_{\ell=0}^{\infty} \varepsilon_{0,\ell}\cos\left(2\pi\ell q/2e\right) . \tag{8.10}$$

This expression for the Blochnium Hamiltonian reveals a Mathieu equation for the energy states dual to the CPB Hamiltonian.

The quasicharge dynamics can be understood by oscillations of the small junction capacitance charging from -e to e and discharging by the tunneling of a Cooper-pair which is analogous to a Bragg reflection. These quasicharge oscillations are the essence to blochnium dynamics at low energies. The charging of the small junction's capacitance is nonlinear and periodic with 2e and forms the potential for the fictitious particle with kinetic energy E_L.

As shown, the Hamiltonian takes the form of the Mathieu equation with the quasicharge potential ($E_B(q)$) defined at all values of q and is periodic by 2e. These conditions allow for the conjugate variable, in this case, the flux in the loop, to be represented as integer values. The loop flux now takes the form of discrete values of the flux quantum indexed as m taking values of all real numbers. This treatment is exactly dual to the CPB where Cooper-pair number N is discrete and φ is continuous; however in this case the flux is discrete and the quasicharge is continuous. This leads to the discrete "fluxon-box" description as a superposition of different flux quanta states occupying the loop with a Hamiltonian:

$$\mathscr{H}_B = \sum_{m\in\mathbb{Z}} \left\{ 2\pi^2 E_L\left(m - \frac{\varphi_{\text{ext}}}{2\pi}\right)^2 |m\rangle\langle m| + \sum_{\ell=0}^{\infty} \frac{\varepsilon_{0,\ell}}{2}\left\{ |m\rangle\langle m+\ell| + |m+\ell\rangle\langle m| \right\} \right\} . \tag{8.11}$$

This Hamiltonian represents the discrete representation in the conjugate basis to quasicharge.

Now we can simulate the resulting spectrum and wavefunctions using both the quasicharge Hamiltonian (equation 8.10) and the discrete flux Hamiltonian (equation 8.11) with exactly the same parameters as the one introduced for the fluxonium picture in figure 8.5. The simulation results are shown in figure 8.7 where the eigenspectrum is the same for both basis. The

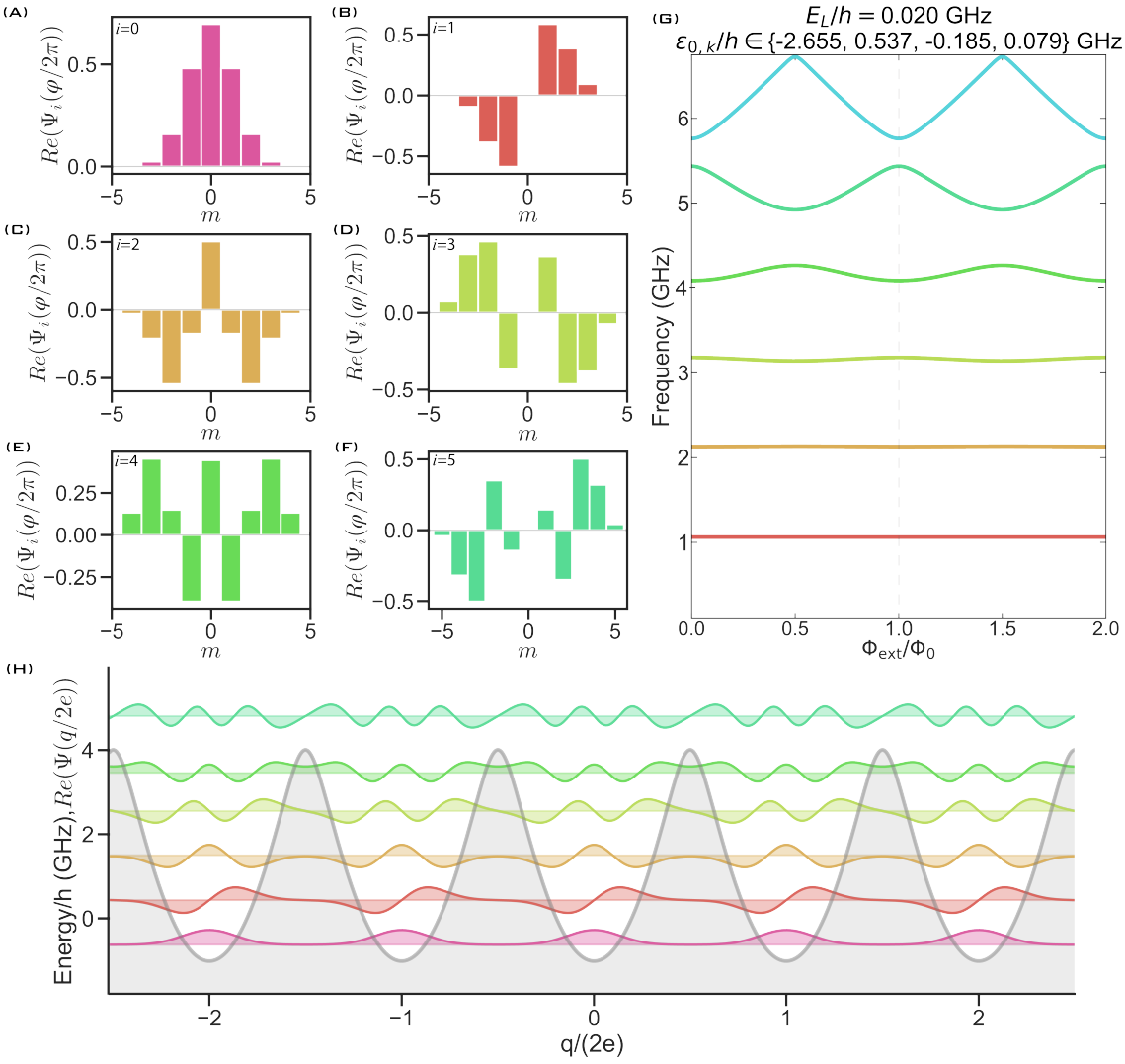

Figure 8.7: The quasicharge description of a circuit with the circuit parameters: $E_J = 4$ GHz, $E_C = 7$ GHz, and $E_L = 0.02$ GHz at Φ_{ext}/Φ_0=0. (A-F) The discrete flux-number wavefunctions show the superposition of flux quanta in the loop for the first six eigenstates. (G) The transition spectra where the first four Bloch-band Fourier coefficients are listed. (H) The wavefunctions in the quasicharge space extend to $\pm\infty$ and are periodic every $q = 2ek$. The first few eigenvalues are situated within the first Bloch band and the transitions can be thought of as quasicharge oscillations.

discrete flux wavefunctions display the superposition of multiple flux quanta occupying the loop simultaneously, where the flux-quanta in the loop can increase/decrease by any integer ℓ for a single tunneling event. The ability for the tunneling of multiple flux-quanta at once is encapsulated by the Fourier coefficient where the frequency of this tunneling is scaled by $|\varepsilon_{0,\ell}|$ which is seen to be sufficiently suppressed at $\ell > 3,4$. The quasicharge wavefunctions are localized within the BB potential and are periodic with q/2e. The transition from the ground to the first excited state can be thought of as a harmonic-like excitation of the quasicharge. Interestingly, this simulation looks almost identical to what one finds for a CPB except m is replaced by N and q/2e by $\varphi/2\pi$.

8.5 Duality with transmon

Blochnium can be thought of as the dual to the transmon. The transmon is a Josephson inductance shunted by a large-value linear capacitance where the large capacitance creates a low-impedance environment; effectively localizing the phase difference across the JJ to a well-defined value. Whilst the wavefunctions in the discrete charge basis, N, become a large superposition of integer charge values on the island. Creating a large superposition of charge states renders transmon much less sensitive to external charge offsets (δn_g) thus creating lower-level transitions that have virtually no sensitivity to offset the charge. While blochnium uses a high-impedance inductance that suppresses quantum fluctuations of q which becomes the well-defined variable, localized within the value of 2e seen as the quaicharge wavefunction is localized within a single well of the first Bloch band of the small JJ. Whilst the wavefunctions in the discrete flux basis become a large superposition of flux quanta occupying the loop. This superposition of flux quanta in the loop creates low-energy transitions that become less sensitive to external flux bias. The reduced sensitivity to external flux offsets ($\delta\varphi_{\text{ext}}$) is the main characteristic that is experimentally measurable by scanning the spectrum of such a device.

Due to the localization of the states within the respective continuous potentials, the low-energy excitations of blochnium are considered anharmonic

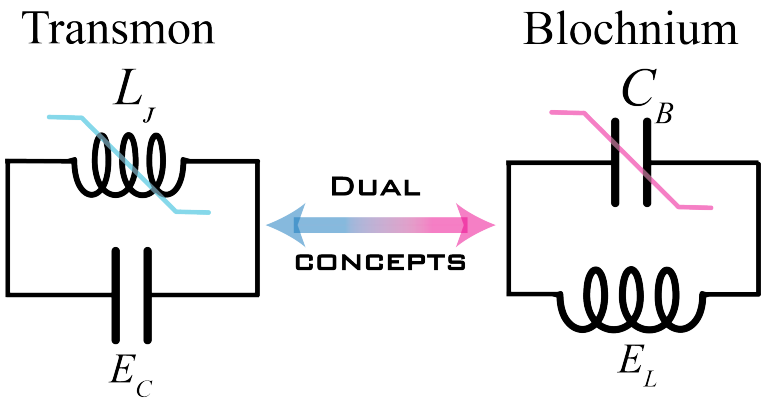

Figure 8.8: The transmon and blochnium are dual circuits. The transmon is a junction shunted by a large capacitance which responds as a non-linear inductance due to a well-defined phase difference across the junction. The blochnium is a junction shunted by a large inductance which responds as a non-linear capacitance due to the well-defined quasicharge on the junction's capacitance.

vibrations of quasicharge across the JJ while the low-energy excitations of transmon are considered anharmonic vibrations of the phase across the JJ. The transmon's transitions, from a first order approximation, is the plasma frequency $f_p = \sqrt{8E_J E_C}$ while the blochnium's is the quasicharge frequency $f_q = \sqrt{8E_L E_C^B}$. The charging energy E_C^B differs from the usual Coulomb energy and is found by using the Bloch capacitance C_B [47, 189, 200]:

$$C_B = 4e^2 \left\{ \frac{d^2 E_0(q)}{dq^2} \right\}^{-1} . \tag{8.12}$$

This equation shows mirrors the Josephson inductance, where the Bloch capacitance can take on negative values and is inversely proportional to the second-order derivative of the potential.

The transmon has protection against charge noise while the blochnium has protection against flux noise. The magnitude of the two noise sources are intrinstically different and so although the f_{01} frequency dispersion is smaller for transmon, the protection against the lesser magnitude flux noise compensates for the larger flux dispersion in the blochnium.

8.6 Experimental realization

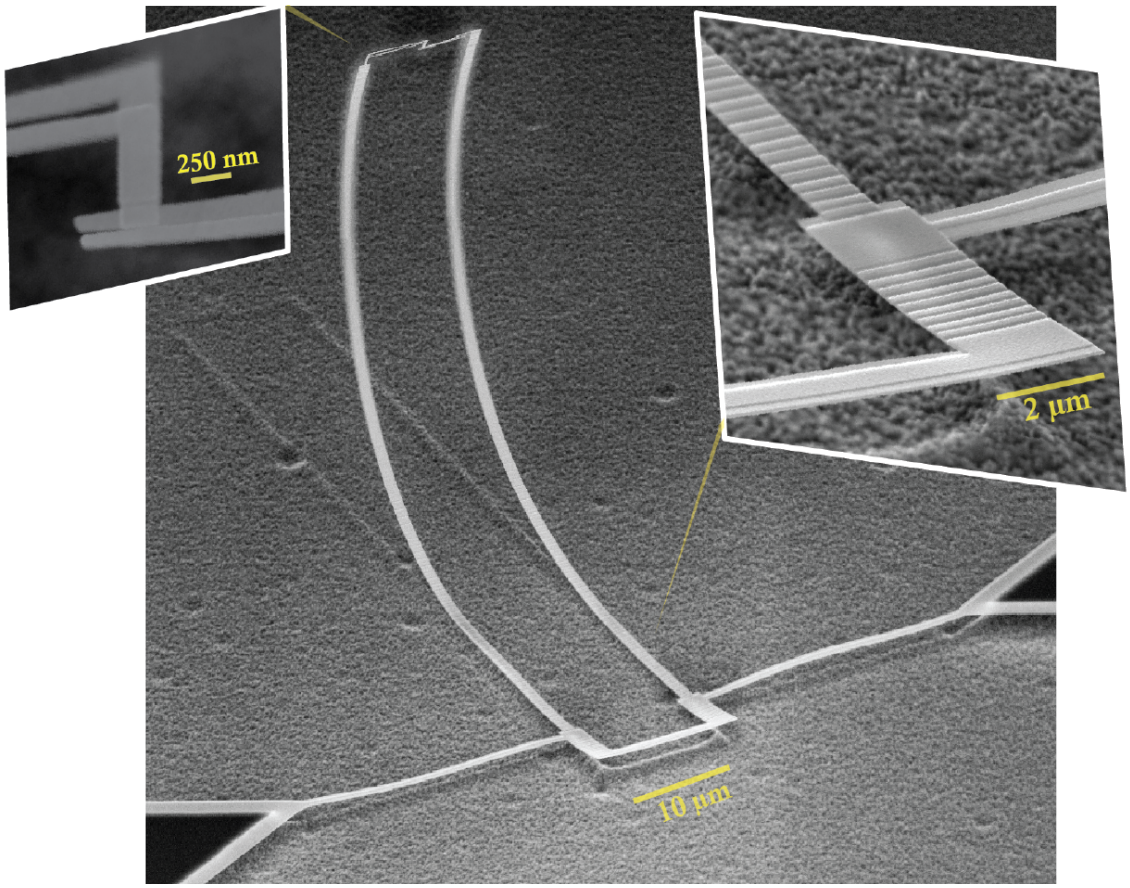

Figure 8.9: The etched blochnium device stands almost vertically in vacuum with the small JJ at the topmost position. The dielectric silicon substrate is effectively removed from between the adjacent chain leads ultimately reducing the parasitic capacitance (C_g) associated with parasitic chain modes. The device is inductively coupled to an on-chip 2D lumped element resonator used for readout. The resonator and qubit are coupled by sharing mutual junctions in the array and have a larger area to produce a more linear readout mode.

Building on fluxonium results, a small JJ is shunted by a compact inductance in the form of a Josephson junction chain. The key innovation here, setting this circuit apart from the conventional fluxonium, is the entire circuit is released from the substrate and suspended in vacuum. With optimally chosen junction parameters, the Josephson chain can obtain an exceptionally high inductance density of $L_J^A \approx 4.5$ nH/junction where the junction unit cell in the array is one junction every 350 nm with a width

of 1 μm. This means $L_\square \approx 12.5$ nH/μm or equivalently almost exactly $L_\square \approx 10^4 \mu_0/\mu$m ($\mu_0 = 4\pi$ pH/μm), where μ_0 is vacuum permeability. Further increasing the inductance density of the array would produce detrimental effects (quantum phase-slips) associated with the superconductor-insulator transition [103, 119]. Therefore, this value of inductance density is the largest practical value obtainable for a qubit with reasonable coherence.

Further consideration needs to take into account the fact that the chain modes should be sufficiently high ($f_m > 10$ GHz) to avoid any complications or distortions to the spectrum; this will also limit the total inductance value. This means the total value of inductance is also limited by the chain's self-capacitance, originating from the stray electrostatic coupling between the opposite-facing metal islands. Besides introducing parasitic chain modes, the self-capacitance contributes to C_{tot} and this effect prevents reducing E_L/E_C far below unity by further lengthening the chain to increase the total number of junctions. The stray capacitance, however, is found to be unnecessarily large in most superconducting circuits due to the high relative dielectric permittivity of the silicon ($\varepsilon \approx 12$) or sapphire ($\varepsilon \approx 10$) substrate, the two most common low-loss substrate materials. So by eliminating most of the substrate's contribution for hosting an enhanced electric field which in turn enhances the coupling of the two chain leads, the stray capacitance is reduced nearly tenfold by removing the substrate entirely. This fabrication feat provided the required leap in the practical inductance value obtainable and used in the device under study.

The substrate-free blochnium devices are created in a two-step fabrication process. First, a superconducting loop with up to 460 Al/AlOx/Al chain junctions and one small junction is fabricated using the standard Dolan bridge technique. Next, a gentle and fast dry isotropic silicon etch is applied using XeF_2 which has a high selectivity of silicon over Al and AlOx. Therefore, the oxidized Al film acts as a natural mask for our device. Because the silicon etching is isotropic (etches down and underneath equally) the skinnier leads at the small junction end of the chain detach from the substrate prior to the other parts and immediately curl upwards driven by the strain relaxation of the thin film. The curling effect is robust and reproducible.

This process is actually visible to the eye and uses already-established fabrication techniques. Moreover, it is possible to vary the amount of curling which is dependent on the length of the chain and the etch depth. Our main results focus on devices with a nearly vertically standing chain, where parasitic capacitance is minimal. The loop is inductively coupled to the on-chip readout circuitry following a previously developed method [94]. A small section of the loop is connected to a capacitive antenna which forms a readout resonator for coupling the device to the measurement apparatus. The device is loaded into a 3D copper waveguide and is measured at cryogenic temperatures.

The transition spectrum as a function of the external flux bias through the loop was measured using conventional two-tone RF-spectroscopy [161]. To identify transitions, the data was fit to the spectrum of a fluxonium. The simple fluxonium model accurately fits the lowest five transitions with energy scale fit parameters: $E_J = 4.70$ GHz, $E_C = 7.07$ GHz, and $E_L = 66.5$ MHz. These energy scales define a previously inaccessible spot on the circuit parameter map ($E_J/E_C = 0.66$, $E_L/E_C = 0.009$) and define the third energy scale combination discussed previously in depth. The capacitance $C \approx 2.7$ fF can be almost entirely accounted for by the small junction oxide capacitance. The inductance $L \approx 2.5\ \mu$H exceeds that of a typical fluxonium tenfold while showing no influence of parasitic modes within the entire frequency range up to 11 GHz.

Constructing blochnium experimentally amounts to choosing three energy scales properly: the Josephson energy E_J, the charging energy E_C, and the inductive energy E_L set the stage for which quantum variable is localized or delocalized. Our experimentally realized blochnium devices have $E_J/E_C \approx 1$ and $E_L/E_C \approx 1/100$. The first condition conveniently maximizes the width of the lowest Bloch band along with the gap to the next one. This condition creates the possibility for the quasicharge potential to host several energy eigenstates. Conventional fluxoniums have a Bloch band which is too narrow to host the eigenstates and usually only overlap at HFQ. As for the second condition, in the special case $E_L = 0$, what is left is just two isolated grains linked by the tunneling of a single Cooper pair, producing a charge qubit. In such a case, the quasicharge looses the continuous-valued

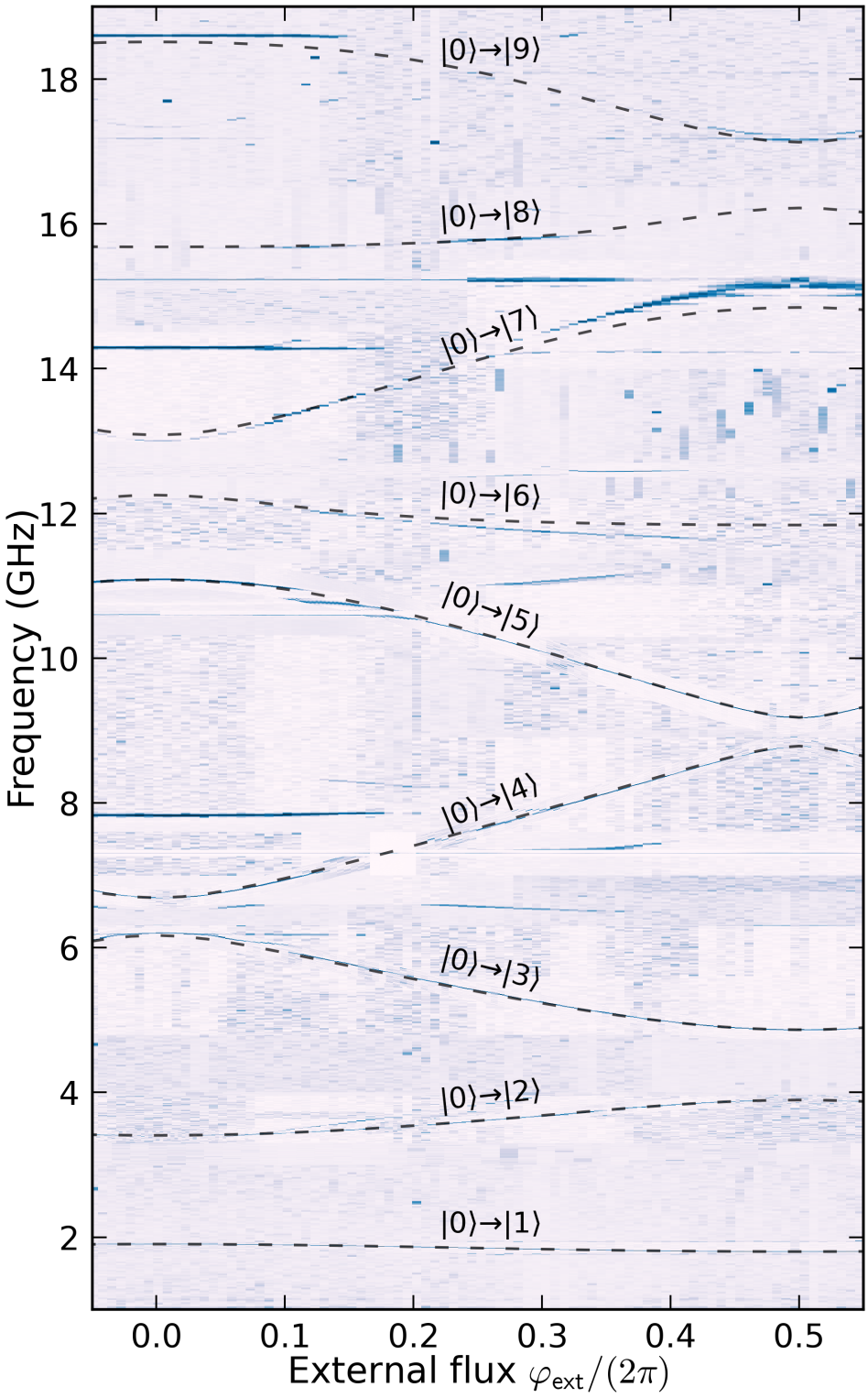

Figure 8.10: The spectrum of the device from 1 GHz up to 19 GHz. The fit transitions displayed are the fluxonium model fit results. The deviation from the fit occurs at around 11-12 GHz.

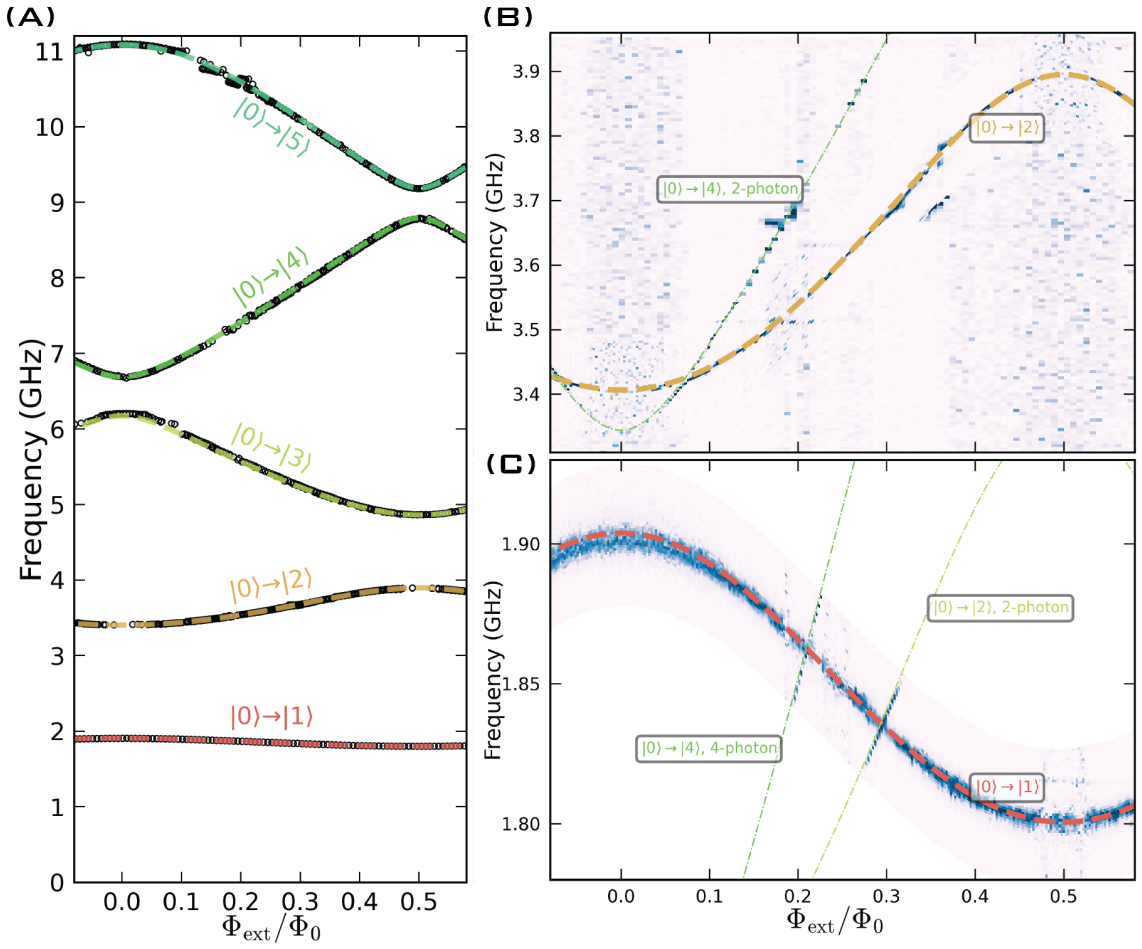

Figure 8.11: (A) Extracted transition peaks fit to the fluxonium model of the first five transitions out of the ground state. (B) A zoom-in on the 0-2 transition. (C) A zoom-in on the 0-1 transition where the transition dispersion with external flux bias is only 100 MHz.

dynamics and can now only be interpreted as a circuit with the availability for an external charge-offset. For $E_L/E_C \lesssim 1$, we get fluxonium [118, 134], a high-coherence implementation of a flux qubit, where a superconducting loop is disrupted by the tunneling of a single flux quantum. In a charge qubit, reducing E_C proliferates multiple Cooper pair tunneling [92], which establishes a well-defined phase-difference across the junction due to the Heisenberg uncertainty principle. This is how a charge qubit evolves into transmon for $E_J/E_C \sim 10-100$. Blochnium emerges from the dual evolution of a flux qubit/fluxonium on reducing E_L/E_C such that the probability to find the wavefunction outside a single Josephson well becomes significant for $E_L/E_C \lesssim 1/100$ across all external flux bias points. When these conditions are fulfilled, the lower-level transitions can be described by the quasicharge Hamiltonian.

Quasicharge description

The sample being discussed fulfills these requirements which enable us to use the measured spectrum to test the quasicharge Hamiltonian, suggesting the small JJ behaves as a non-linear capacitance. In this section, we fit the spectrum to the Blochnium Hamiltonian which uses either the quasicharge or the discrete flux picture. The experimental spectrum is fit using equation 8.11 where the Fourier coefficients are found by constraining the values to the first fifteen harmonics of a constrained fit to a $E_B(q)$ generated by sweeping the small junction E_J and E_C. Stepwise the fit procedure first generates the quasicharge dispersion (BB) of the small junction, finds the first fifteen harmonics ($\varepsilon_{0\ell}$) in the Fourier series (expression 8.8), and then uses equation 8.11 to generate the minimal distance fit to the spectrum points indicated.

The fit and the experimentally measured spectrum agree to a high level up to around 8.5 GHz. The fit only incorporated data points up to the second transition at around 4 GHz. The measured spectrum begins to deviate from the quasicharge description due to the eigenstates having energy greater than the width of the BB. Furthermore, the second BB comes into play at around 9 GHz, which is neglected in our fit. Considering interband transitions ($s > 0$) could indeed improve our higher frequency data fits. Incorporating interband transitions by modifying $\varphi = id/dq + \Omega$ [93, 199] can

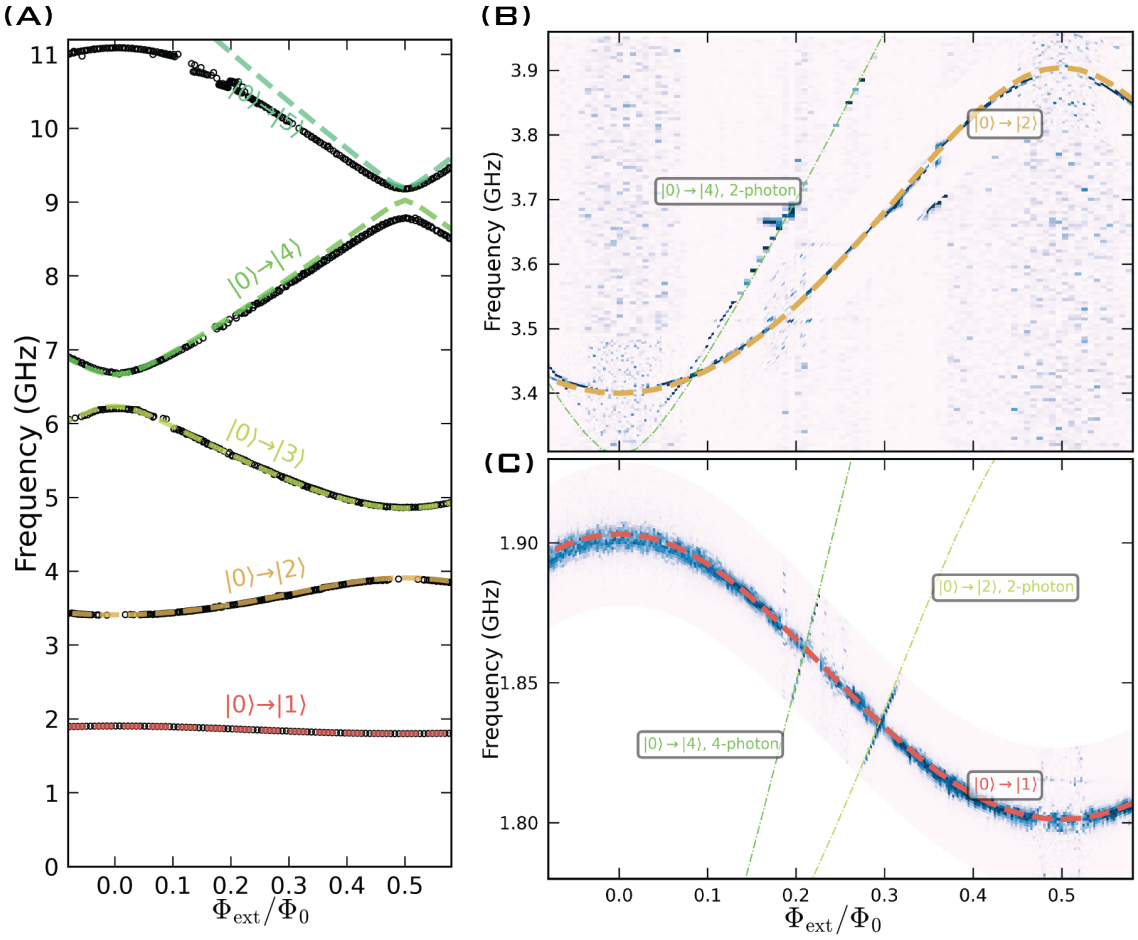

Figure 8.12: (A) The extracted transition frequencies are fit to the blochnium Hamiltonian 8.11. The fit begins to deviate from the data at around 8.5 GHz. (B,C) A zoom on the 0-2 (0-1) transition shows a high level of agreement between the measured data and the blochnium model.

remedy this discrepancy yet is unnecessary for fitting the lower-lying states situated within the first BB.

Considering the lowest BB only, the energy scale parameters extracted from the blochnium fit are $E_L = 0.062$ GHz and $\varepsilon_{0,\ell} = \{2.05, -2.66, 0.54, -0.19, 0.08, -0.04, 0.02\}$ GHz. This corresponds to a BB formed by a small junction with energy scales $E_J = 3.5$ GHz and $E_C = 7.4$ GHz. The blochnium energy scale parameters are close to the fluxonium fit parameters especially for E_L and E_C while E_J decreased by almost 25 %. The modification of E_J could be due to renormalization effects from the φ^A_{zpf} of the shunting array junctions [75, 106, 139]. The Fourier coefficients, $\varepsilon_{0,\ell}$, should not be interpreted as the phase-slip rates as is the case for single and double phase-slips which occur in the fluxoniums with the second energy scale combination. The delocalized nature of the lower eigenstates "smears" out the sharp jump of flux in the loop at all flux points. There is no connotation of plasmon or fluxon transitions; instead, these two types of transitions become completely hybridized in the fluxonium view forming what is called "metaplasmons" in the quasicharge description. [93, 199].

The blochnium fit eigenvalues are directly compared with the fluxonium fit eigenvalues in figure 8.13 (A). When the eigenstates are situated inside the first BB completely the two eigenenergies are basically equivalent. Deviations between the two models start becoming noticeable around the emergence of the second BB. Therefore supporting the first three eigenstates which are situated within the first BB can be described as quasicharge oscillations. The wavefunctions in figure 8.13 (B) and (C) compare both models' wavefunctions in the two conjugate basis. The wavefunctions amplitudes agree in the phase (discrete flux) picture while the fluxonium charge wavefunctions (Q) hardly exist outside $\pm e$ which coincides with the first period of the quasicharge wavefunctions within the Bloch band.

The transitions situated within the Bloch band potential can be thought of as quasicharge oscillations due to the localization of the expectation of the quasicharge accumulating on the junction capacitance to be within the $\pm e$ interval. The transition from the ground to the first excited state corresponds to the junction's capacitance accumulating quasicharge from initially $q = 0$ to a superposition of $q = \pm q_1$ where $q_1 < e$. The quasicharge value on

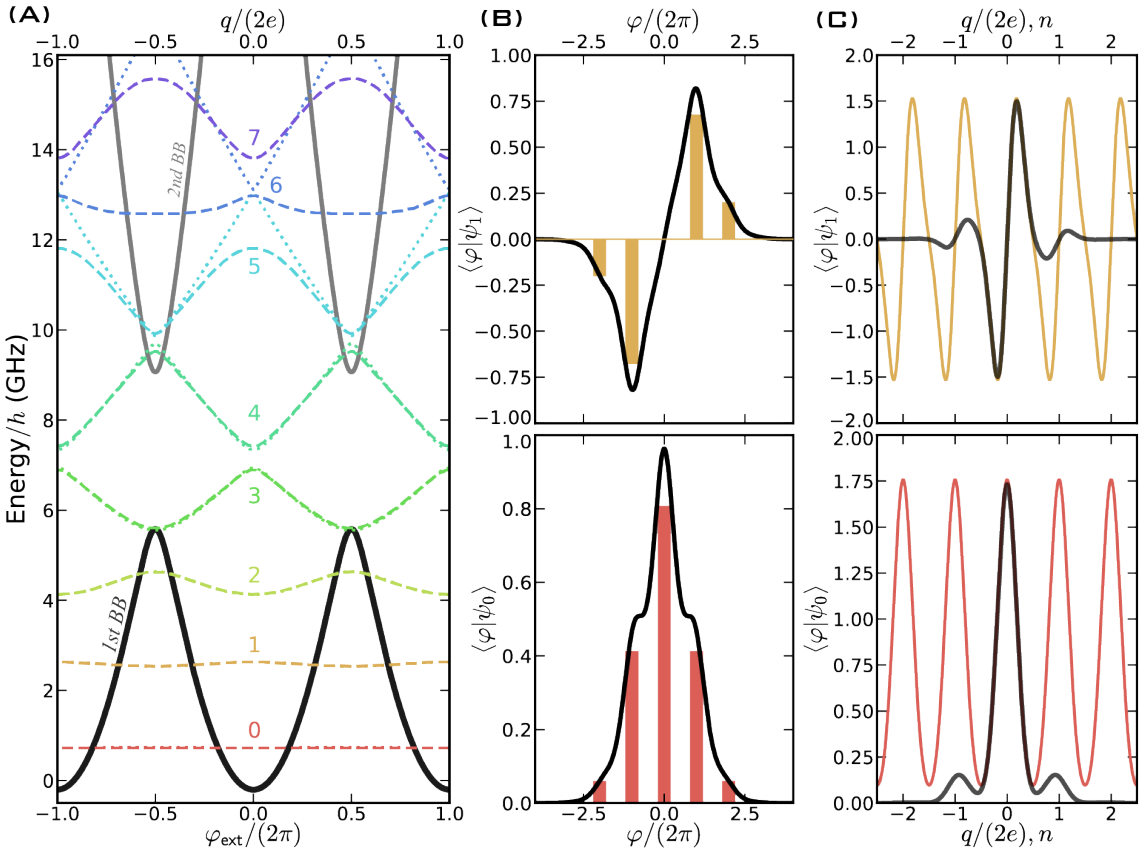

Figure 8.13: (A) The normalized eigenenergies of the fluxonium fit (dashed-line) and the blochnium fit (dotted-line) superimposed with the first BB (black line) and the second BB (grey line). (B) The fluxonium and blochnium wavefunctions in the continuous and discrete phase representations. (C) The wavefunctions in the charge and quasicharge representations. The color lines in (B,C) correspond to blochnium wavefunctions.

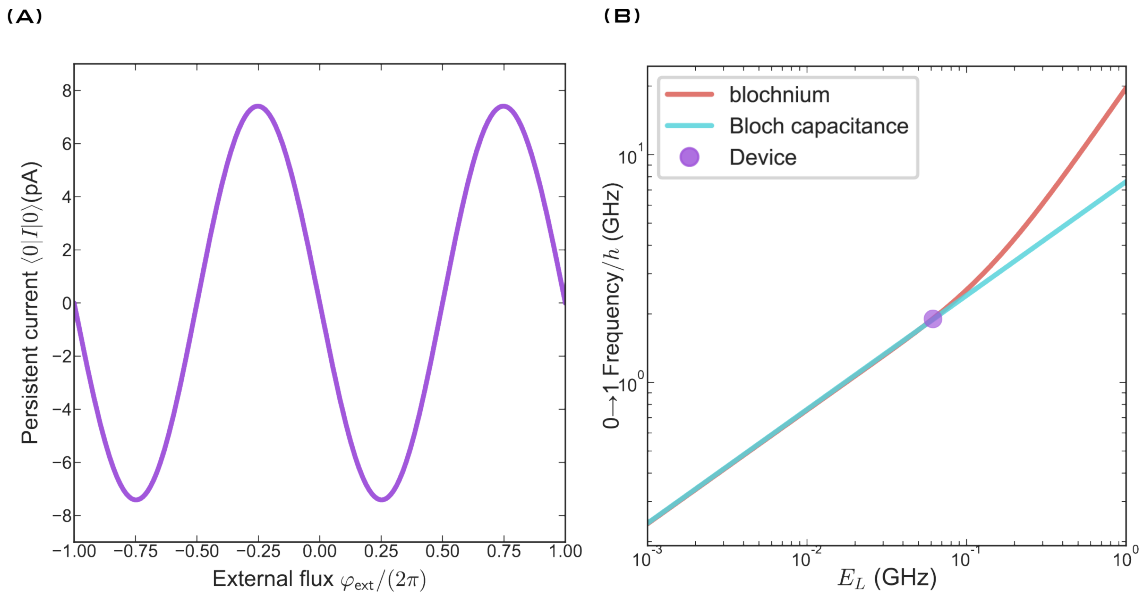

Figure 8.14: (A) The persistent current through the junction in the ground state. (B) A comparison of the 0-1 transition frequency with the blochnium model and with the quasicharge oscillator model which uses E_C^B.

the junctions capacitor oscillates back and forth charging and discharging through the large valued inductance connecting the two junction leads. In fact, the ground state has a vanishing persistent current value through the small JJ calculated by $I = I_0\langle 0|\sin(\varphi - \varphi_{\text{ext}})|0\rangle$ and is found to be oscillating between ± 7 pA; a current value three orders of magnitude less than the critical current value $I_0 = 9.5$ nA. Removing the tunneling component entirely and setting $E_J = 0$ the transition from the ground to the first excited state along with the φ matrix element are reproduced within a few percent accuracy [141]. To get an idea of what happens when the Josephson element is removed entirely, the simulation of the fluxonium for when $E_J = 4.7$ GHz is compared to when $E_J = 0$ in and is shown in figure 8.15. Furthermore, due to the lack of external parasitic capacitance seen by the small JJ, the capacitance in our results is almost entirely attributed to the innate junction oxide meaning the Bloch capacitance (equation 8.12) and the regular Coulomb capacitance is approximately equal, $C_B \approx C_J \approx C_\Sigma$. The charging energy associated with the Bloch capacitor can be found by using the

Fourier series representation:

$$E_C^B = \frac{1}{8}\frac{d^2E_B}{d(q/2e)^2}\bigg|_{q=0} = -\frac{\pi^2}{2}\sum_{\ell=1}\ell^2\varepsilon_{0,\ell}\ . \tag{8.13}$$

Using this approximation along with setting $E_J = 0$ forms the "quasicharge oscillator" whose transition frequency is defined as: $f_q = \sqrt{8E_L E_C^B}$; where the Bloch capacitance is linearized for the low-frequency transitions. The linearized Bloch capacitance is analogous to the linearized Josephson inductance; where the linearized Bloch capacitance becomes a better description for higher values of inductance as seen in figure 8.14 (B).

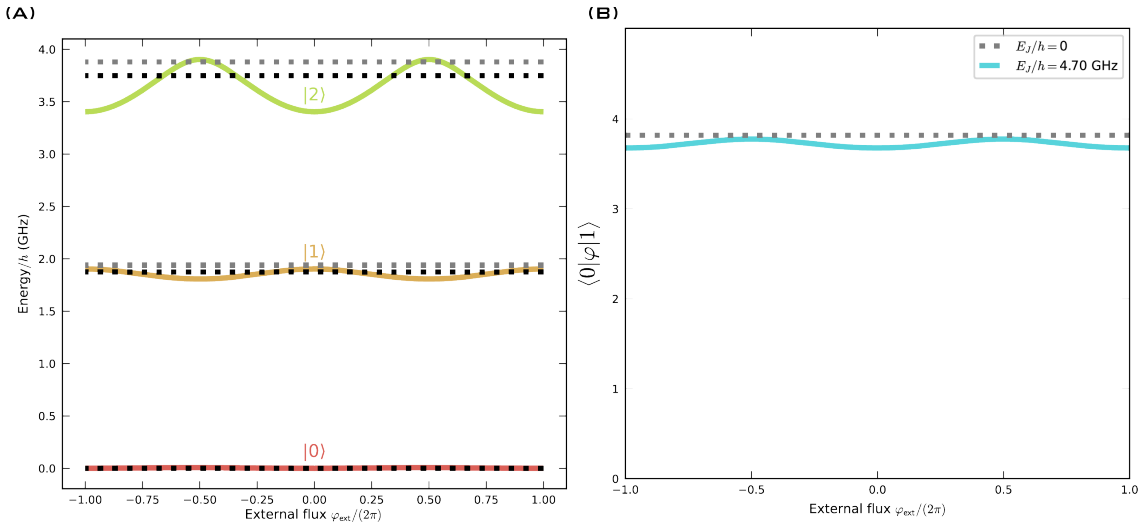

Figure 8.15: (A) State energy comparison between the fluxonium (solid), HO (grey-dashed), and the quasicharge oscillator (black-dashed). (B) Comparison of the φ matrix element for fluxonium and the HO.

This description is not suitable for the higher energy eigenstates which approach and exceed the BB potential maximum. These states begin recovering external flux tuneability; in our device, this is already seen for the second eigenstate where the flux dispersion is roughly half a GHz. This in turn eliminates any issues related to the anharmonicity of the eigenstates. Now returning back to the fluxonium picture, the higher states are observed to become localized in Josephson wells situated at $|\varphi/2\pi| > 2$. These states are considered as persistent-current states that depend on the external flux

and are hence flux tunable. Due to their external flux sensitivity, the higher level states could in fact be used for flux tunable interactions with external systems where the transition energy of the higher states can be tuned within the vicinity of the external system to enhance interactions while the lowest energy transitions remain more or less flux insensitive.

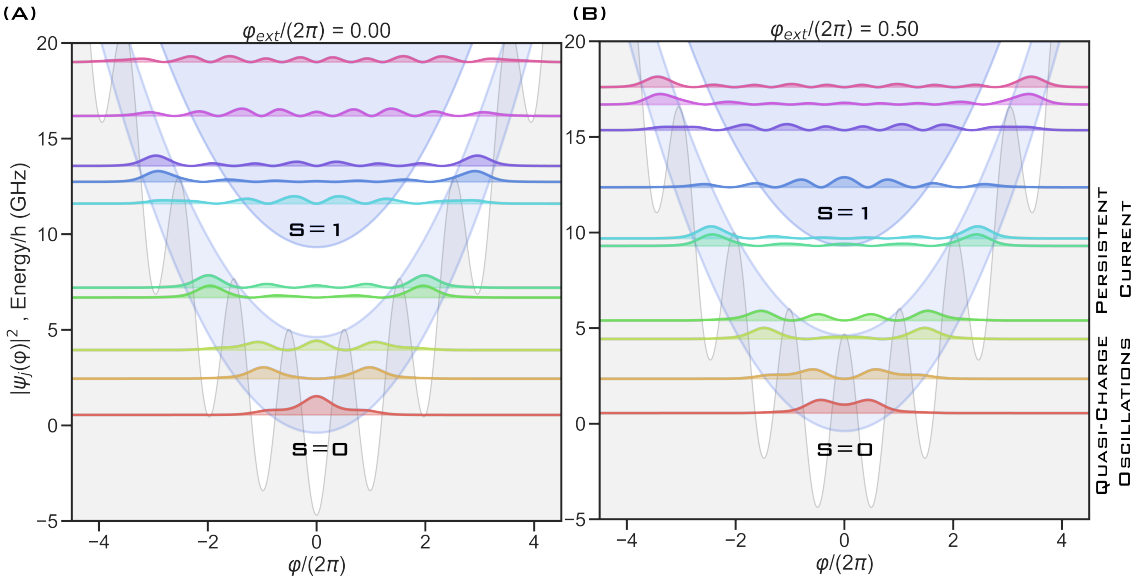

Figure 8.16: The wavefunctions within the first parabolically deformed BB are categorized as either quasicharge oscillations or persistent current states. The first three eigenstates are quasicharge oscillations while state 4,5 are persistent current like at IFQ and states 5,6 are persistent current like at HFQ.

The persistent current states commonly overlap with the first and second BBs causing interband coupling. To illustrate this the BBs are deformed by the inductive energy term and superimposed with the fluxonium wavefunction picture in figure 8.16. The wavefunctions which overlap with both the s=0 and s=1 parabolically deformed bands clearly can not be accurately described with the single BB model. The fifth eigenstate (light blue wf) and all higher eigenstates overlap with the two bands at all external flux bias points.

8.7 Blochnium as a protected qubit

Due to the significantly reduced 01 transition flux dispersion, blochnium becomes protected against 1/f flux noise dephasing at all external flux bias points, where the dephasing rate is proportional to [70]:

$$\Gamma_\phi \propto \left| \frac{\partial \omega_{01}}{\partial \Phi_{\text{ext}}} \right|^2 S_{1/f}(\omega \to 0) \ . \tag{8.14}$$

Another way to view the insensitivity of blochnium's 01 transition is as the

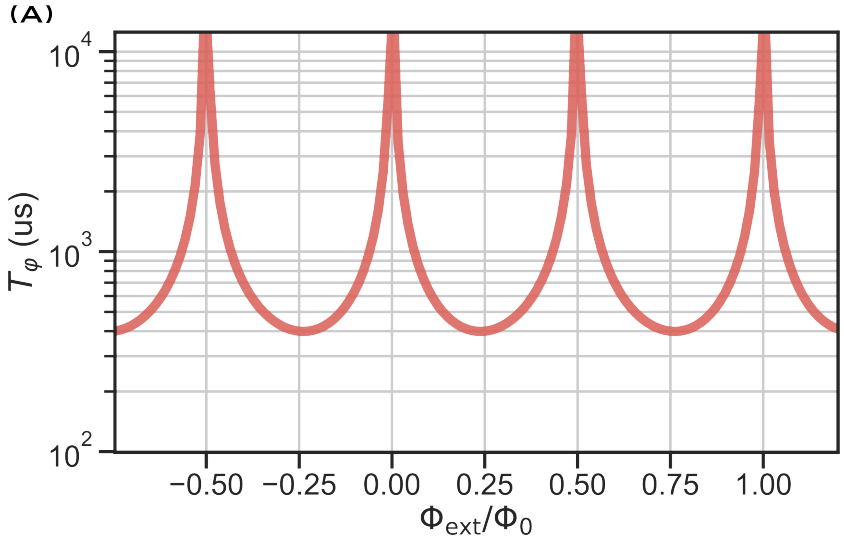

Figure 8.17: The simulated T_ϕ for the blochnium sample with the noise spectral density 2 $\mu\Phi_0$. The simulation demonstrates the flux insensitivity is sufficient enough to elevate the expected $T_\phi > 300$ μs at all external flux values.

difference of the φ expectation value for each state involved in the transition [76]:

$$\mathscr{M}^2 = |\langle 1|\hat{\varphi}|1\rangle - \langle 0|\hat{\varphi}|0\rangle|^2 \ . \tag{8.15}$$

This value will tend to zero at both sweet spots, however, between $\mathscr{M}^2$ is significantly reduced compared to conventional flux qubits due to the wavefunction overlap. In other words, the states are delocalized into multiple Josephson wells such that a small change in the external flux field hardly affects the number of flux quanta in the loop and therefore has little effect on the transition frequency.

The dephasing rate (Γ_ϕ) is found to be exponentially suppressed scaling as: $\exp\{-4\sqrt{|\varepsilon_{0,0}|/E_L}/\pi\}$ [93] which becomes $\exp\{-4\sqrt{E_C/E_L}/\pi\}$ [76] when the small JJ has $E_J/E_C \leq 1$. Intuitively, the flux dispersion $\Delta_{01} = f_{01}(\varphi_{\text{ext}} = 0) - f_{01}(\varphi_{\text{ext}} = 0.5)$ also follows the same scaling behavior dependent on the ratio of E_L/E_C as seen in figure 8.18 (A).

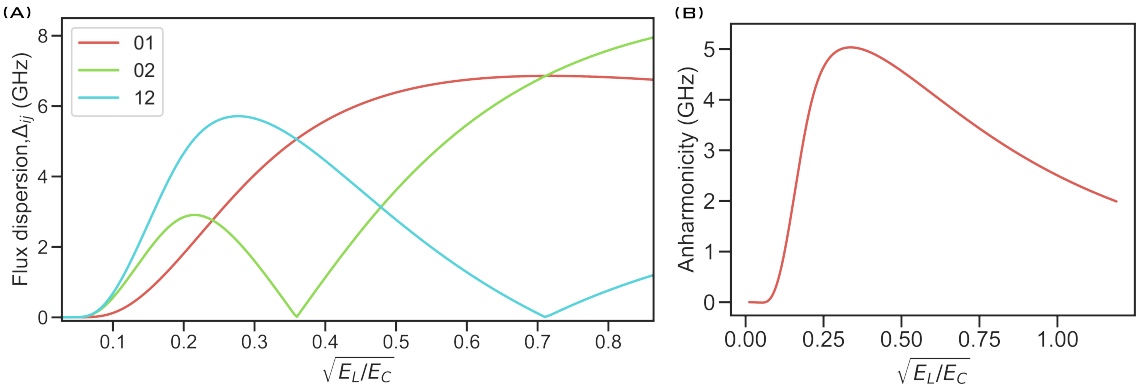

Figure 8.18: (A) The flux dispersion ($\Delta_i j$) for the transitions involving the first three eigenstates as a function of $\sqrt{E_L/E_C}$. (B) Anharmonicity (α) as a function of $\sqrt{E_L/E_C}$.

Interestingly, the qubit's anharmonicity scales slower than the 01 flux dispersion scaling. The anharmonicity defined as $\alpha = f_{21}(\varphi_{\text{ext}}) - f_{01}(\varphi_{\text{ext}})$ [92], is key to have fast gate times which is often lacking from other T_ϕ protected qubits. The importance of anharmonicity is shown by the probability of state leakage into the f state when driving e-g is approximately given by: $p_l \approx \frac{\hbar\Omega_R}{\alpha}$. For the blochnium sample under extensive discussion, the anharmonicity at HFQ is around 0.4 GHz.

The device reported on extensively had an average $\bar{T}_1 = 9.65\ \mu$s and $\bar{T}_2^E = 12.79\ \mu$s. These values were consistent at all external flux bias points. Energy relaxation appears to be the limiting factor that is primarily limited by the consistently large value of the φ matrix element coupling to various noise sources where energy relaxation is: $1/T_1 \propto |\langle 0|\hat{\varphi}|1\rangle|^2 S(\omega = \omega_{01})$. The large overlap of the delocalized blochnium wavefunctions illustrates why 1/f protection against flux is gained yet this protection against flux noise comes at the price of a large φ matrix element. This is the first conception of a blochnium qubit and will only be further improved from here by optimizing the circuit and the environment which will of course take time. The

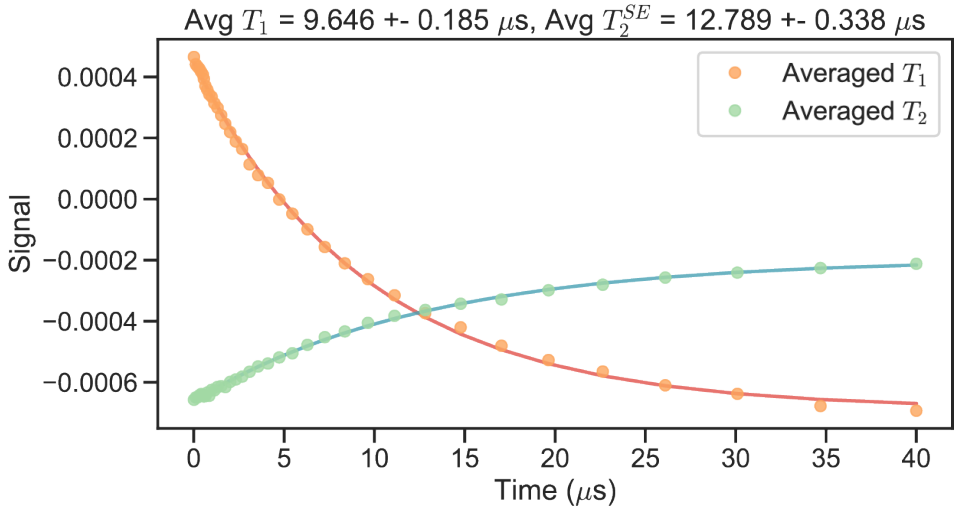

Figure 8.19: Average interleaved T_1 and T_2^E data.

energy relaxation times are more or less comparable to the first conceptions of transmon whose T_1 has risen by two orders of magnitude in about two decades. Furthermore, the scalability of blochnium will also take time to develop; this first version is a proof of concept not state of the art, ingenuity will push the design to conform with the necessary constraints presented to the application.

8.8 All quasicharge sample summary

Many blochnium samples were measured to study the consistency of the etching process while also probing time domain characteristics. The samples extensively studied are listed in the table below.

	E_J	E_C	E_L	δf_{01}	f_{01}^{HFQ}	$\lvert\langle 0\rvert\hat{\varphi}\lvert 1\rangle\rvert^2$	$\lvert\langle 0\rvert\hat{n}\lvert 1\rangle\rvert^2$	$\bar{T}_1$ (μs)	$\bar{T}_2{}^E$ (μs)
A	7.29	5.63	0.163	1.6	1.58	9.45	0.012	5.46	8.17
B	6.43	5.59	0.173	1.33	1.29	9.30	0.014	–	–
C	5.30	5.19	0.106	0.70	1.53	10.31	0.014	14.48	14.96
D**	4.52	9.44	0.129	0.21	2.88	12.54	0.018	6.32	11.21
E	4.11	8.01	0.066	0.06	1.99	15.23	0.015	4.27	1.12
F*	4.95	7.29	0.072	0.18	1.63	13.93	0.015	4.10	1.03
G	3.12	8.34	0.080	0.055	2.21	14.54	0.016	2.51	4.09
H	4.69	7.07	0.067	0.10	1.80	14.46	0.014	9.65	12.79

* indicates unetched device, ** indicates device measured in “high-coherence” set up.

In summary, the table shows a noticeably large $\lvert\langle 0\rvert\hat{\varphi}\lvert 1\rangle\rvert^2$ matrix ele-

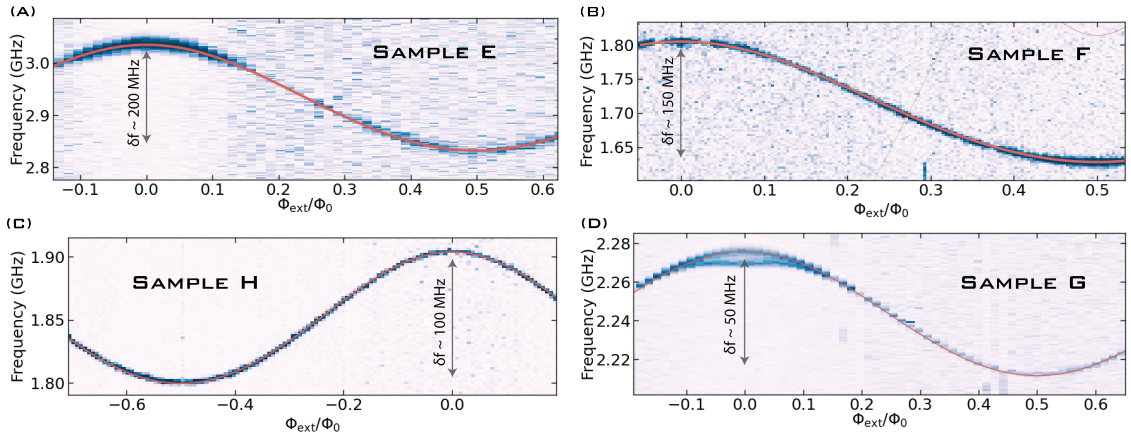

Figure 8.20: Experimental two-tone spectroscopy superimposed with the fit of the 0-1 qubit transitions. The flux dispersion ranges between 50 MHz $< \delta f_{01} <$ 150 MHz.

ment which is greater than 10 in most samples; while the flux dispersion $\delta f_{01} < 250$ MHz in the samples with $E_C > 7$ GHz. Both properties indicate delocalization of $\Psi(\varphi)$ for groundstate wavefunctions. The average T_1, T_2 is below 10 μs. However, with a very large $|\langle 0|\varphi|1\rangle|^2$ and a relatively large transition frequency at HFQ ($f_{01} > 1.5$ GHz) this value for energy relaxation is somewhat predictable. In fact, probing the exact mechanism causing losses in blochnium has proved a challenge because of the flatness of the matrix elements and of the transition frequencies rendering the same loss values at all external flux bias points. This behavior is different than figuring out the fluxonium losses, say with the second energy scale combination, where the matrix elements and transition frequencies scale more dramatically with external flux. When debugging the sources of loss the flux sensitivity certainly makes the investigation simpler.

The samples whose $E_J \approx 4.5$ GHz are shown to follow the simulated flux dispersion of 0-1, 0-2, and 1-2 for various values of E_L/E_C. Sample G had the lowest flux dispersion of $\sim$ 50 MHz and the lowest ratio of $E_L/E_C \sim 0.08$. Large E_C is necessary for low flux dispersion yet creates a larger than optimal 0-1 frequency.

The samples with $T_2 < T_1$ were most likely limited by phase slips in the array junctions which was later addressed by nearly doubling the area of the array junctions. Other than that, the focus of these measurements was to

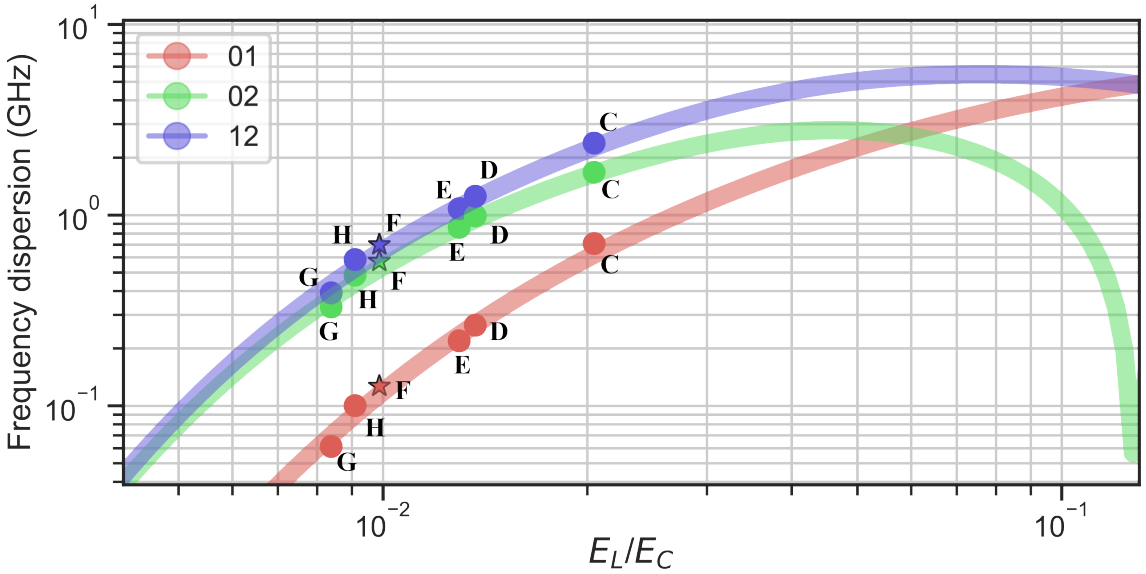

Figure 8.21: The samples whose $E_J \approx 4.5$ GHz are shown to follow the simulated flux dispersion as a function of E_L/E_C. The star point is the only unetched sample whose energy scale values were obtained through a coupled fluxonium-chain mode fit.The rest of the energy scale parameters were obtained with the standard fluxonium fit.

study the energy relaxation properties first since a large T_2 should naturally follow.

The best time domain data was measured for device C whose E_C and frequency were the lowest of the bunch while the flux dispersion is second largest at around 1.3 GHz. At HFQ, T_1 and T_2 were around 50 μs on average. Due to the larger than several hundred MHz flux dispersion the matrix element had some tunability. Although not as flux insensitive as we would like, this sample was an etched version of "blochnium" with a max $T_1 > 80$ μs which is a promising lead for future experiments.

Probably one of the most promising blochnium results is from sample D, whose $E_C \sim 9.45$ GHz, the largest value out of the bunch, yet with an $E_L \sim 0.13$ GHz which can easily be further pushed to lower values. Nevertheless, the promising result is referring to the average $\bar{T}_1 \approx 6\mu$s while $\bar{T}_2 \approx 2\bar{T}_1$. The actual value of energy relaxation is not state of the art in the field but noteworthy due to the large value of $|\langle 0|\varphi|1\rangle|^2 \times T_1$ compared to the typical expected values as shown in figure 8.24.

To fairly compare samples T_1 values across different energy scale combi-

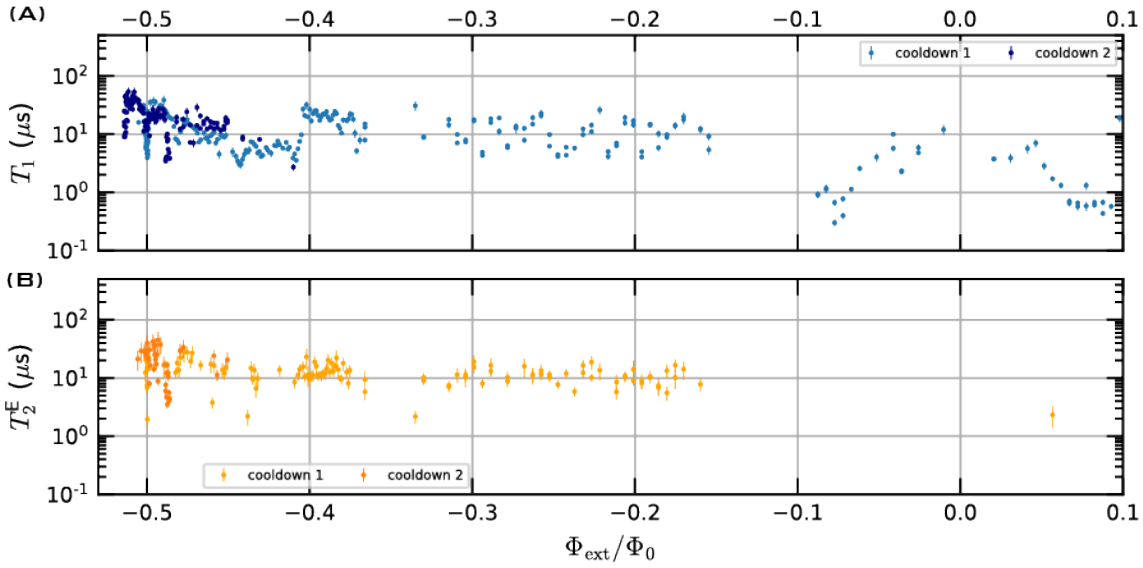

Figure 8.22: Time domain statistics for device C for two separate cooldowns.

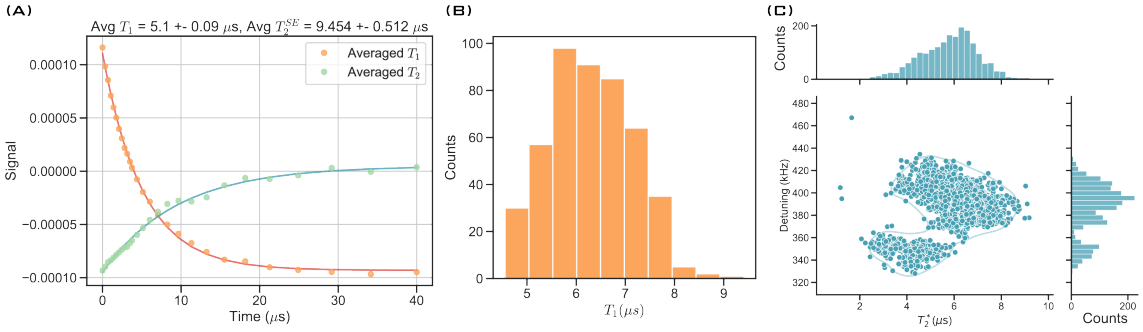

Figure 8.23: Device D time domain statistics while biased at IFQ.

nations the quanitity of $|\langle 0|\varphi|1\rangle|^2 \times T_1$ is used and is essentially the inverse of the frequency-dependent spectral density. The blochnium samples in the table are compared with the results from fluxonias in chapter 7 as well as other results from our lab reported in [135]. The blochnium data points are not flux dependent like the results from fluxonia in chapter 7 however the devices follow the same trend and are even sometimes higher in value.

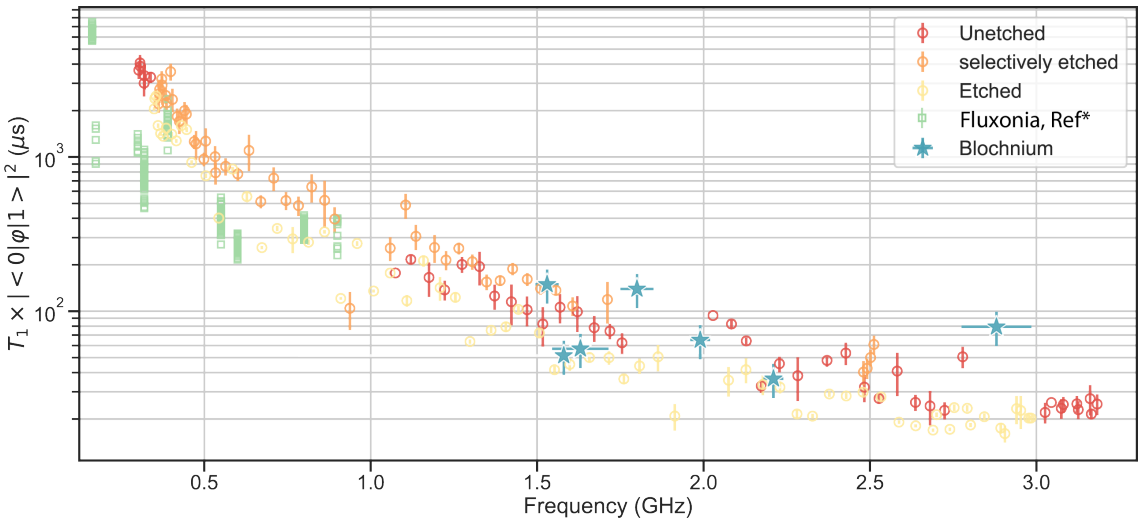

Figure 8.24: A comparison of $T_1 \times |\langle 0|\varphi|1\rangle|^2$ with other fluxonia from [135] as well as chapter 7.

The data comparison to fluxonias across flux to the data in blochnium is fair due to the established mechanism remaining consistently as dielectric loss for the frequency-dependent samples. The dielectric Q-factor for these values of T_1 for blochnium give $40,000 < Q_{\text{cap}} < 140,000$ which is on par with the other *etched* fluxonia. The only major difference is the detached nature of the circuit for blochnium. A participation ratio for the various lossy interfaces should be considered in the future. With this correlation established one can determine the operating frequency necessary to produce a blochnium sample with large $|\langle 0|\hat{\varphi}|1\rangle|^2$ matrix element necessary to produce a sample with $T_1 > 100$ and operating frequency at $f_{01} \approx 0.5$ GHz is required.

8.9 Outlook

Blochnium is enabled by a new circuit element to sometimes referred to as "hyperinductance" [141] which was created in our demonstration of blochnium whose lossless linear inductance $L \approx 2.5\ \mu$H that operates beyond the frequency $\omega/2\pi \approx 11$ GHz, such that $Z \sim \omega L > 180\ \text{k}\Omega$. This impedance value is a factor of 30 greater than the resistance quantum for Cooper pairs and is likely the highest characteristic impedance an electromagnetic structure has attained so far. Among other applications, hyperinductance has long been sought after for realizing fault-tolerant logical operations on superconducting qubits [8, 19, 46] and for implementing the quantum current standard via Bloch oscillations [40].

In reference [144] further exploration of ultra-high impedance superconducting qubits using geometrical superinductances was reported. A fluxonium qubit with reduced external flux sensitivity ($f_{01} \sim 1$ GHz) was reported with $Z >> R_Q$. This sample's reduced flux sensitivity appears due to the extremely small value of E_J (1.99 GHz) where the wavefunctions are primarily localized within the φ^2 potential and are not spread into multiple Josephson wells simultaneously. This energy scale combination offers another route for creating flux-insensitive transitions and may offer an easier route.

Another direction demonstrated in reference [168] to reduce the flux sensitivity of f_{01} of a flux qubit is to create a protected form using a new element (called the KITE) which reduces the Josephson cosine potential periodicity. This essentially enhances the delocalization of the resulting wavefunction into double the amount of Josephson wells which is shown to significantly reduce the external flux dispersion to values < 200 MHz. This clever trick reproduces the blochnium spectrum by utilizing the KITE circuit element biased at a particular flux. To describe this circuit with quasicharge, the conjugate Bloch band potential would then get double as wide. This means the wavefunctions in the quasicharge space would become localized to the scale of pairs of Cooper-pairs or 4e.

9
Bloch Oscillations

"Creativity is a wild mind & a disciplined eye." — Dorothy Parker

The response of a single Josephson junction which emerges from the extension of phase fluctuations beyond the 2π-interval [6, 20, 157, 160] has profound effects when applying a DC current, an oscillating voltage appears which is proportional to the amount of applied current. Evidence for such an effect was found in an out-of-equilibrium dc-transport through junctions connected to high-impedance leads [32, 35, 99, 143, 186], although a full consensus is absent to date [25, 52, 131].

This chapter discusses the preliminary results of experiments on applications of a Bloch capacitance embedded in an ultra-high impedance JJ transmission line which has a DC current bias applied. This measurement has the capability to contribute to the field of quantum metrology [142].

9.1 Fundamentals

The elusive Bloch oscillations occur at a frequency $f_B = \langle I \rangle / 2e$ which are expected in response to a DC-current $I = \dot{q}$ driven through a Joseph-

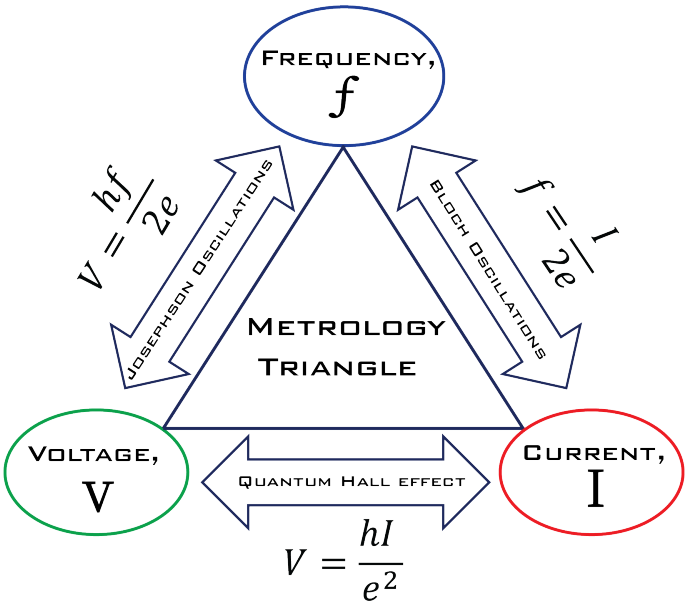

Figure 9.1: The metrology triangle of electrical standards offers a way to connect voltage, current, and frequency by only fundamental constants of nature.

son junction behaving as a Bloch capacitance by an infinite-impedance current source [6]. By contrast, Josephson oscillations occur at a frequency $f_J = 2e\langle V\rangle/\hbar$ and are induced as a response to a DC-voltage $V = (\hbar/2e)\dot{\varphi}$ across the junction applied by a zero-impedance voltage source. Josephson oscillations occur when the phase difference is a well-defined semi-classical variable while Bloch oscillations occur when the quasicharge is a well-defined semi-classical variable. The duality can be observed by simply interchanging the variables [128]:

$$\begin{aligned} E_J(\varphi) &\leftrightarrow E_B(q) \\ \frac{2e}{\hbar}\frac{d\varphi}{dt} &\leftrightarrow \frac{2\pi}{2e}\frac{dq}{dt}\,. \end{aligned} \tag{9.1}$$

The cosinusodial Josephson potential, periodic in the phase difference, φ, is replaced by the Bloch band potential, periodic in the quasicharge, q, and represented by the Fourier sum:

$$E_B(q) = \sum_{\ell=0}^{\infty} \varepsilon_{0,l} \cos\left(2\pi\ell q/2e\right) \tag{9.2}$$

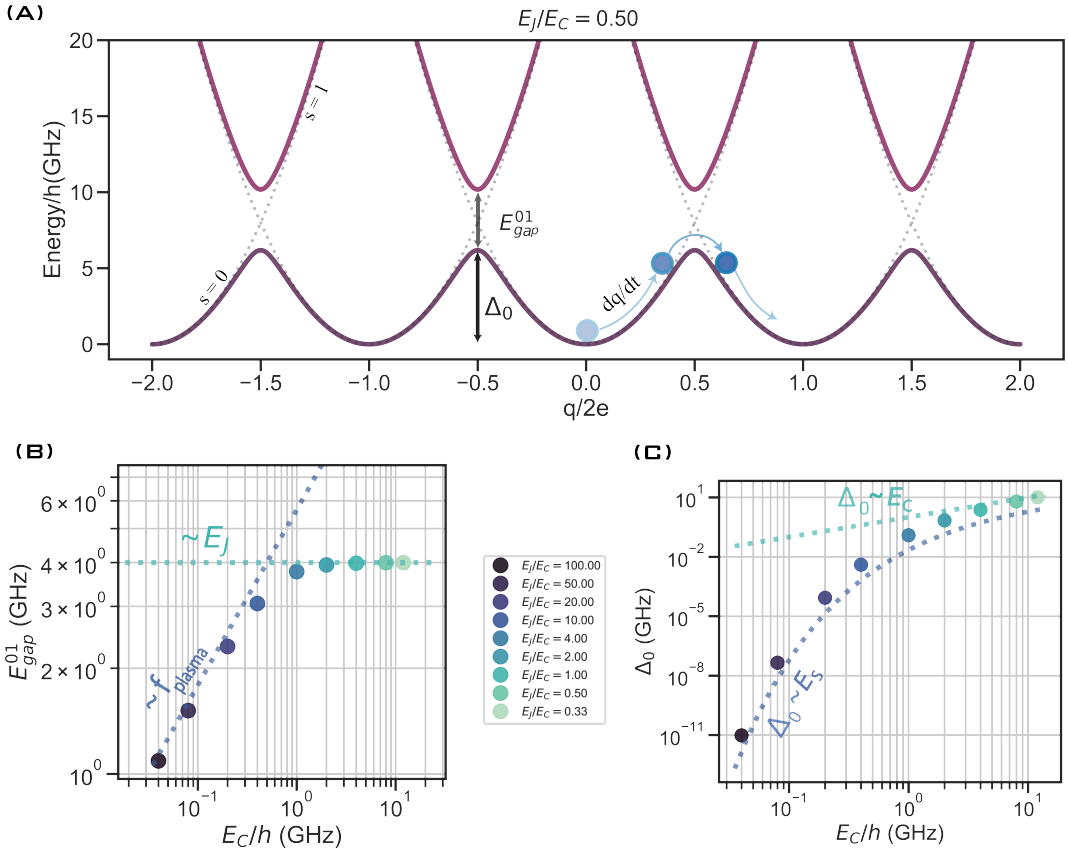

Figure 9.2: The Bloch band potential for $E_J/E_C = 0.5$. The first band height is given by E_C when $E_C \gg E_J$ while the gap between the two first bands at q=e is given by E_J. A fictitious particle moves along the potential with a "velocity" given by the voltage which will oscillate in time.

where each ℓ is the integer harmonic term contributing to the series. The velocity of the fictitious particle is analogous to the voltage $V(q) = dE_B(q)/dq$ and the external force applied to the particle is the applied current such that $dq/dt = I(t)$. Integrating this equation, while assuming the external bias current is constant gives $q(t) = tI_{\text{bias}} + q_0$ which is then substituted into the expression for voltage:

$$V(q) = -\frac{\pi}{e}\sum_{\ell=0}^{\infty} \ell\varepsilon_{0,\ell}\sin\left(2\pi\ell q/2e\right) = -\frac{\pi}{e}\sum_{\ell=0}^{\infty} \ell\varepsilon_{0,\ell}\sin\left\{\frac{2\pi\ell}{2e}\times I_{\text{bias}}t\right\}. \tag{9.3}$$

This equation shows the junction's voltage will oscillate at a frequency proportional to the average constant biasing current, $f_B = \langle I_{\text{bias}}\rangle/2e$. This strik-

ing result is the fundamental idea behind Bloch oscillations in the absence of dissipation.

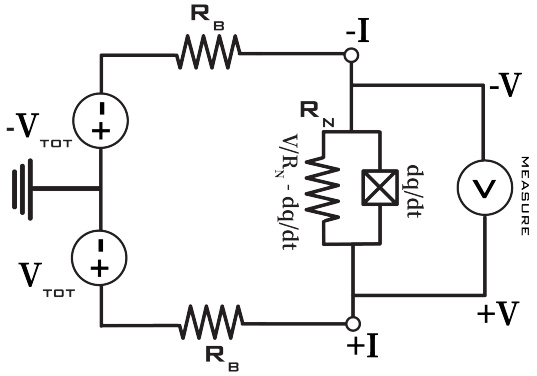

Figure 9.3: The circuit diagram for measuring Bloch oscillations shiunted by a resistance.

When considering dissipation due to the normal resistance of the current biased Josephson junction, R_N must be taken into account for the energy loss due to the presence of quasiparticle tunneling. As long as $R_N \geq R_Q$ such that fluctuations due to the normal current are not too high, the quasicharge dynamics can be described according to the Langevin equation [6, 82, 109]:

$$\frac{dq}{dt} = I_{\text{bias}} - \frac{V}{R_N} \,. \tag{9.4}$$

For the case $E_C \gg E_J$, the Bloch band height is given by E_C such that the voltage is given by $V(q) = q/C_J$; where the charging time constant for the capacitance is introduced as $\tau = R_N C_J$. Explicitly integrating the Langevin expression a time-dependent expression for quasicharge is found [82]:

$$q(t) = \tau \left\{ I_{\text{bias}} - e^{-t/\tau} \left(I_{\text{bias}} - \frac{q(0)}{\tau} \right) \right\} \,. \tag{9.5}$$

Letting $q(0) = -e$ then the time to accumulate $q(t_B) = +e$ on the capacitance is defined as:

$$t_B = \tau \ln \left\{ \frac{I_{\text{bias}} + e/\tau}{I_{\text{bias}} - e/\tau} \right\} \,. \tag{9.6}$$

This time is required for the capacitance to charge from -e to +e which amounts to traversing a single Bloch band period. Finally, the time-averaged

voltage takes the form:

$$V = \frac{1}{t_B C_J}\int_0^{t_B} q(t)dt = R_N\left\{I_{\text{bias}} - H(I_{\text{bias}} - I_t)\times\frac{2e}{t_B}\right\} \tag{9.7}$$

where H is the Heaviside step function which is zero if $I_{\text{bias}} < I_t$ or one if $I_{\text{bias}} > I_t$. Further defining I_t as the "threshold" current given by $I_t = e/\tau$. When the bias current is below the threshold value current will only flow through the resistive part such that $V = I_{\text{bias}}R_N$. Playing on the analogy, if the force (current) supplied is less than required by the particle to submit the potential well then it becomes stuck within a single Bloch band where current will only flow through the normal resistor. However, when the bias current is above the threshold value then the capacitance can fully charge and discharge to $q = \pm e$ such that the voltage is now periodic with respect to 2e:

$$V = R_N\left\{I_{\text{bias}} - \frac{2e}{t_B}\right\} = R_N\left\{I_{\text{bias}} - \frac{1}{R_N}\frac{dE_B(q)}{dq}\right\}. \tag{9.8}$$

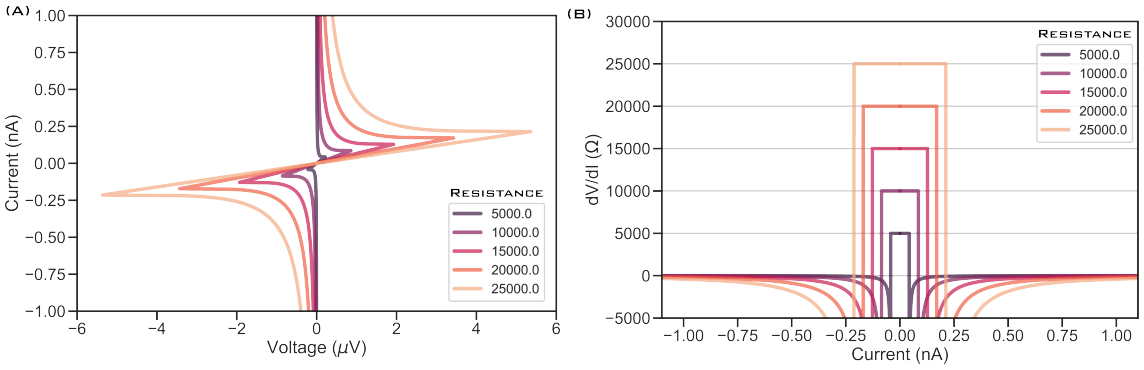

Figure 9.4: The simulated IV and dV/dI characteristics for different values of normal resistance. Larger resistance increases the Coulomb blockade region.

A region of "negative" resistance appears in the I-V characteristics once surpassing the threshold current. This feature indicates the system is absorbing power to charge and discharge the Bloch capacitance at a growing rate proportional to the bias current. The dV/dI curve shows once surpassing the threshold voltage the differential resistance is negative indicating a power radiating-like behavior. The value of t_B can be re-expressed in terms

of the threshold current which is a more experimental variable:

$$2e/t_B = 2I_t \left[\ln \left\{ \frac{I_{\text{bias}} + I_t}{I_{\text{bias}} - I_t} \right\} \right]^{-1} . \tag{9.9}$$

Combining this equation as well as solving equation 9.7 for $1/t_B$ demonstrates the Bloch oscillation frequency in the presence of an Ohmic shunt is the frequency of voltage oscillations occurring at:

$$f_B = \frac{1}{2e} \left\{ I_{\text{bias}} - \frac{V}{R_N} \right\} = \frac{1}{e} I_t \left[\ln \left\{ \frac{I_{\text{bias}} + I_t}{I_{\text{bias}} - I_t} \right\} \right]^{-1} . \tag{9.10}$$

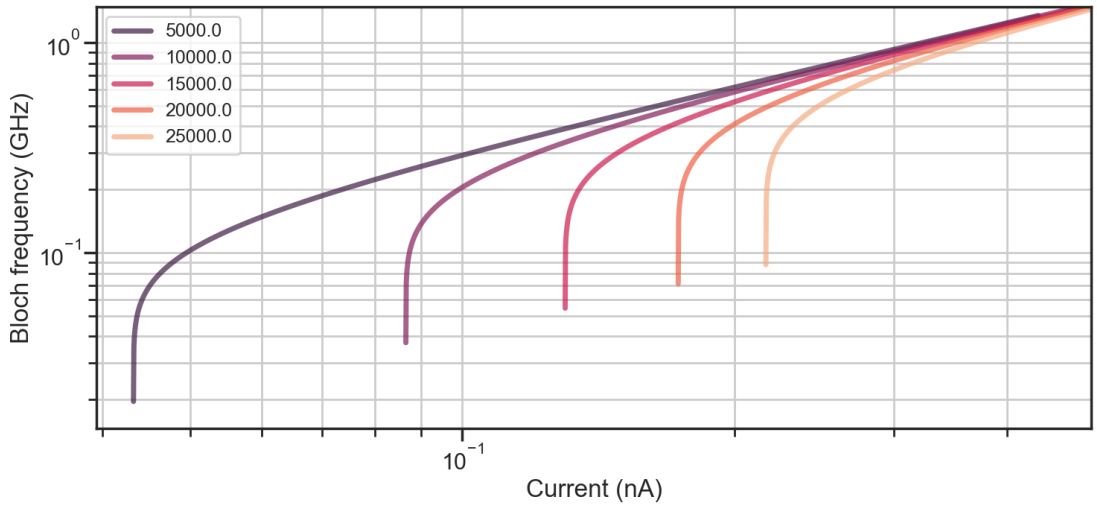

Figure 9.5: The frequency which Bloch oscillations will take place as a function of normal resistance R_N. Increasing R_N increases the Coulomb blockade width which effectively increases the lowest frequency at which the Bloch capacitance can oscillate. The frequency just after the threshold current is exceeded is extremely sensitive to the bias current, this effect may produce a wider decay of the Coulomb blockade region.

This equation illustrates the threshold current ($I_t = e/\tau$) sets the lowest frequency at which the system can undergo Bloch oscillations while also demonstrating near the threshold current that the frequency of oscillation is extremely sensitive to current fluctuations.

An external microwave source can be utilized to further probe Bloch os-

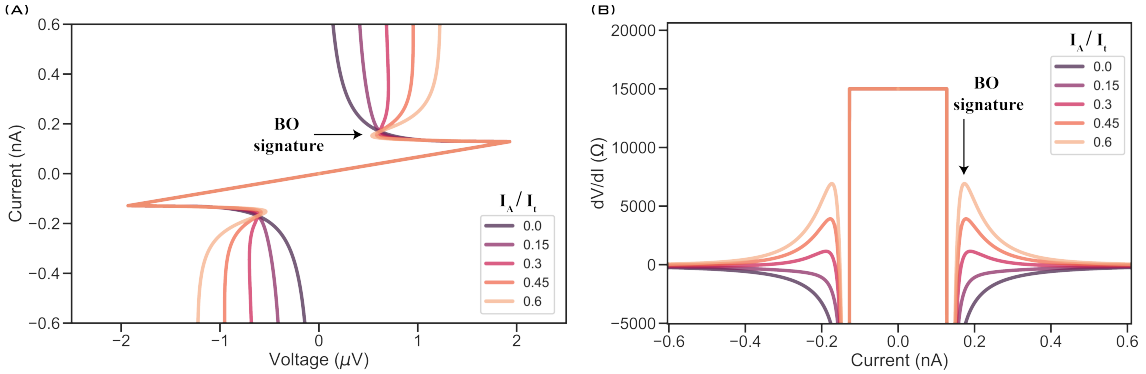

Figure 9.6: The simulated IV and dV/dI characteristics when the junction has a harmonic current added. In this simulation $f = 200$ MHz. The amplitude of the current is increased which shows the increase signal strength for larger I_A.

cillation dynamics. Irradiating the system at frequency ω which will induce a current of amplitude I_A. This signal will in turn have an effect on the voltage, modifying the static bias current to a time-varying one. The Langevin equation becomes modified:

$$\frac{dq}{dt} = I_{\text{bias}} + I_A \cos(\omega t) - \frac{q}{\tau} \,. \tag{9.11}$$

Which can be integrated as before to find the time dependence of the quasicharge. Furthermore the averaged voltage becomes [82]:

$$V = \frac{1}{t_B C_J} \int_0^{t_B} q(t) dt = R_N \left\{ I_{\text{bias}} - H(I_{\text{bias}} - I_t) \times \left(\frac{2e}{t_B} - I_A \frac{\sin(\omega t_B)}{\omega t_B} \right) \right\} \tag{9.12}$$

The addition of the external microwave source modifies the current-voltage characteristics with the emergence of a positive differential resistance peak when $2e/t_B < I_{\text{bias}} + I_A \frac{\sin(\omega t_B)}{\omega t_B}$.

Once the bias current exceeds a certain value called the "Zener Current" the fictitious particle now has enough force to be kicked into the higher Bloch band. The probability to pass from the lowest BB to the next should

be minimized and is given by [188]:

$$P_Z = \exp\left\{\frac{-\pi}{4}\frac{E_{\text{gap}}^2}{E_C f_{\text{app}}}\right\} = \exp\left\{\frac{-I_Z}{I_{\text{bias}}}\right\}. \tag{9.13}$$

where I_Z is the Zener tunneling current which is the current necessary to push the particle out of the first BB. The Zener tunneling current is further estimated as $I_Z = \frac{\pi I_0}{4}\sqrt{2R_Q/R_N}$ [73]. When incorporated into the Langevin equation a separate resistance R_Z should be used. This has the effect of

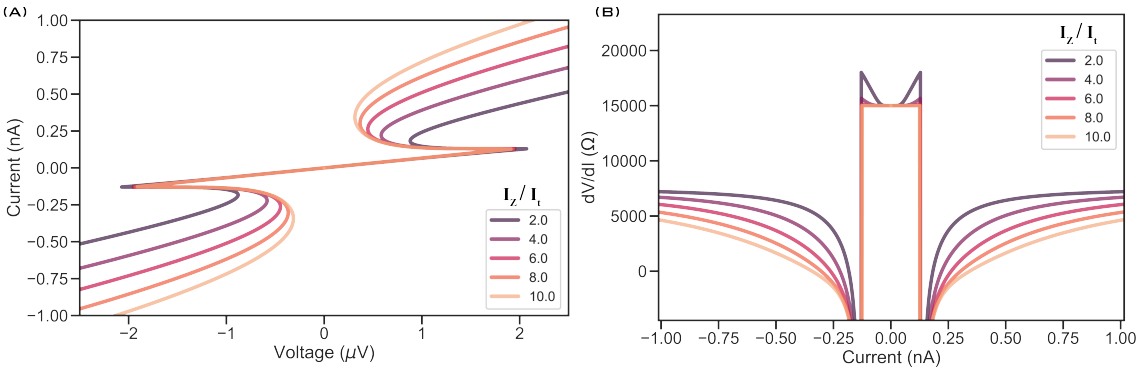

Figure 9.7: The simulated IV and dV/dI characteristics when incorporating different values for the Zener current. The effect is to make the resistance positive.

bending the IV characteristics to positive slope values when I_{bias} approaches I_Z. The separation of the two lowest bands when $q = e$ and $E_C \gg E_J$ is E_J which in itself is low valued due to the necessary charging effect regime. Therefore, the external bias current must be changed adiabatically to avoid this detrimental effect. Furthermore, Zener transitions could be induced due to thermal effects which are not considered in this basic introduction analysis.

9.2 Preliminary experiment

The strategy in this work is to current bias a small JJ, with a tunable E_J, shunted by an ultra-high impedance environment in the form of an etched JJ transmission line. The transmission line modifies the impedance seen by the small junction which now no longer has just an Ohmic shunt but a frequency-dependent impedance. The current-voltage characteristics of

small junctions in the presence of environmental modes has been extensively considered in past investigations by: [39, 84]. Conclusively, the electromagnetic environmental modes modify the junction's I-V characteristics where current peaks are shown as the result of the environmental impedance's resonant modes.

In the simplest consideration, the total impedance seen by the tunneling electrons through the junction becomes $Z_t(\omega) = \frac{1}{i\omega C_J + Z^{-1}(\omega)}$; where $Z(\omega)$ is the frequency-dependent impedance of the JJ transmission line. The effect of the environmental modes will be to cause a perturbation to the superconducting current/voltage [79, 83]. Therefore when exciting the environmental modes, these should in turn "phase-lock" [109] to the current-voltage dynamics associated with the Bloch oscillations of the small junction which was utilized in the experimental results [100].

9.2.1 Superconducting Quantum Interference Device

A squid is a Superconducting Quantum Interference Device where a loop consists of two JJ in parallel. The advantage of using squids is the ability

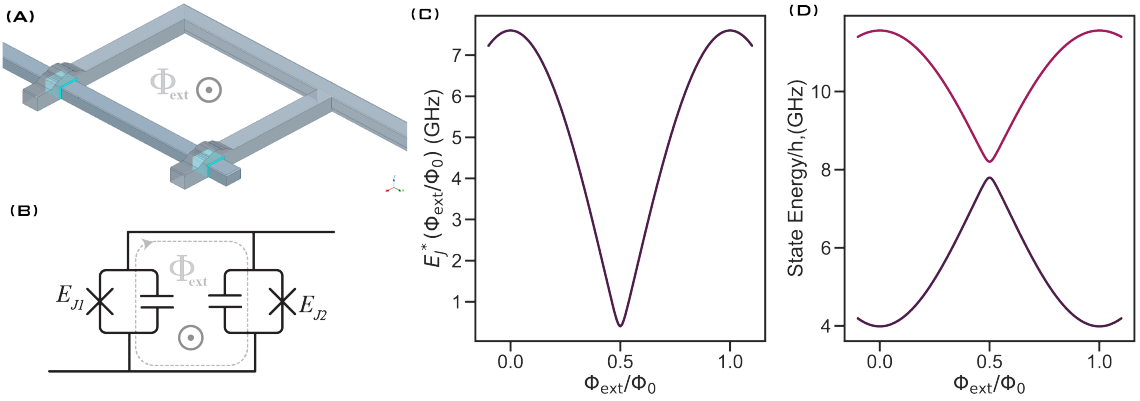

Figure 9.8: (A) An illustration showing the geometry of the squid used in our experiments. (B) The circuit representation of a squid. (C) The Josephson energy as a function of flux threading through the squid loop is modulated with a minimum value occurring at HFQ. (D) The energy of the first two BBs when $q = 0$.

to tune the Josephson energy with an external flux bias. Where an effective

Josephson energy ($E_J^*(\Phi_{\text{ext}})$) is defined as:

$$E_J^*(\Phi_{\text{ext}}) = E_{J_\Sigma}\sqrt{\cos^2(\pi\phi_{\text{ext}}) + \gamma\sin^2(\pi\phi_{\text{ext}})} \tag{9.14}$$

where $E_{J_\Sigma} = E_{J1} + E_{J2}$ and $\gamma = \frac{E_{J1}/E_{J2}-1}{E_{J1}/E_{J2}+1}$ is the sum of the two JJ energies and γ is the asymmetry of the two junctions in parallel; usually about 5%. The capacitive energy is the addition of two small junction capacitances in parallel. Squids are used in our experiment due to the tunability of the BB gap and height by adjusting the external flux bias.

9.2.2 Device and preliminary results

The experimental device is a JJ transmission line that is selectively etched using SF_6 and shorted at one end with a squid loop of small JJs in parallel. We have the capability to probe both DC and RF and use the same hybrid setup described in chapter 4.

The transmission line is first characterized and the extracted dispersion of the chain modes is fit. The parameters of the transmission line found are: $Z_\infty = 33\text{k}\Omega$ with $L_J^A = 3.55$ nH and $C_g = 7.04$ aF. The total shunting inductance is calculated to be 35.5 μH in total. This transmission line has the highest characteristic impedance reported in this thesis with a plasma frequency of 20.56 GHz.

The next measurement was to perform dV/dI as a function of external flux shown in figure 9.10 (A). There is a clear trend that the dV/dI curve "opens" up when the external flux is biased at IFQ where effective E_J^* is at a maximum meaning the largest E_J/E_C and therefore the flattest BB. The closer the device is biased to HFQ the smaller the dV/dI gap gets until a resistive peak around zero bias current appears. The resistive peak is the largest at HFQ where effective E_J^* is at a minimum due to the smallest E_J/E_C. The peak around zero current bias is considered as the Coulomb blockade [30] where charging effects dominate the tunneling of charge carriers. The differential resistance measured at zero-bias current is the value of R_N which we use where the extracted values are shown in figure 9.10 (B).

The IV characteristics were measured at different flux points where the traces exhibit a "Bloch nose" or the region where there is negative resis-

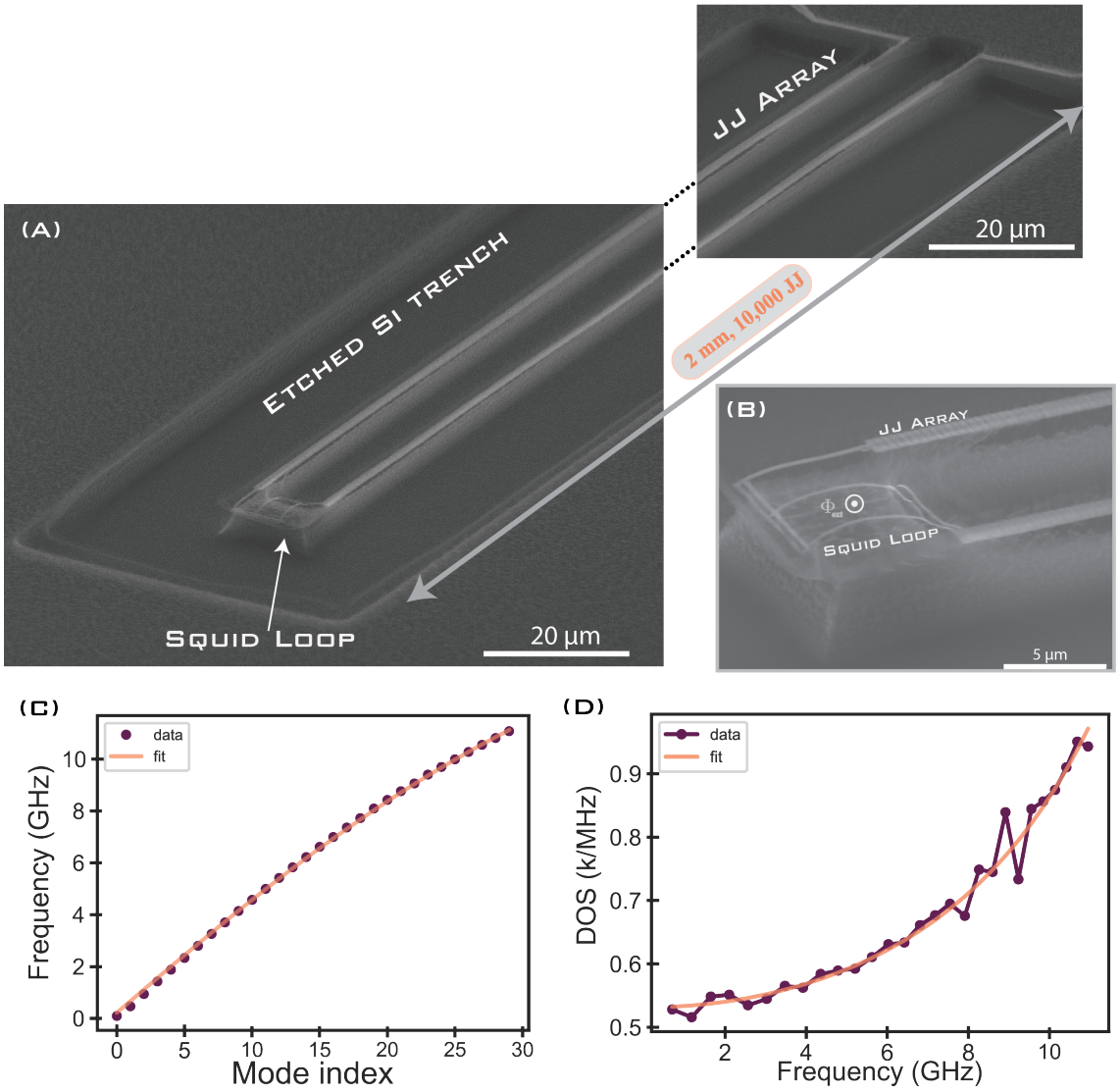

Figure 9.9: (A,B) The device is a small squid loop embedded in an ultra-high impedance JJ transmission line. (C,D) The dispersion and density of states for the standing wave modes of the transmission line. These measurements were used to characterize the transmission line.

tance. The critical voltage decreased the further away from HFQ indicating the BB amplitude was also shrinking. Interestingly the region exhibiting negative differential resistance appears to grow when sweeping flux away from HFQ. This is most likely due to the probability of Zener transitions shrinking meaning the lowest two BBs have a larger gap between them at $q = \pm e$. This particular device had negative differential resistance for only very small values of bias current $2\ \text{pA} < I_{\text{bias}} < 10\ \text{pA}$. It's important to note no RF source was irradiating the sample during these measurements.

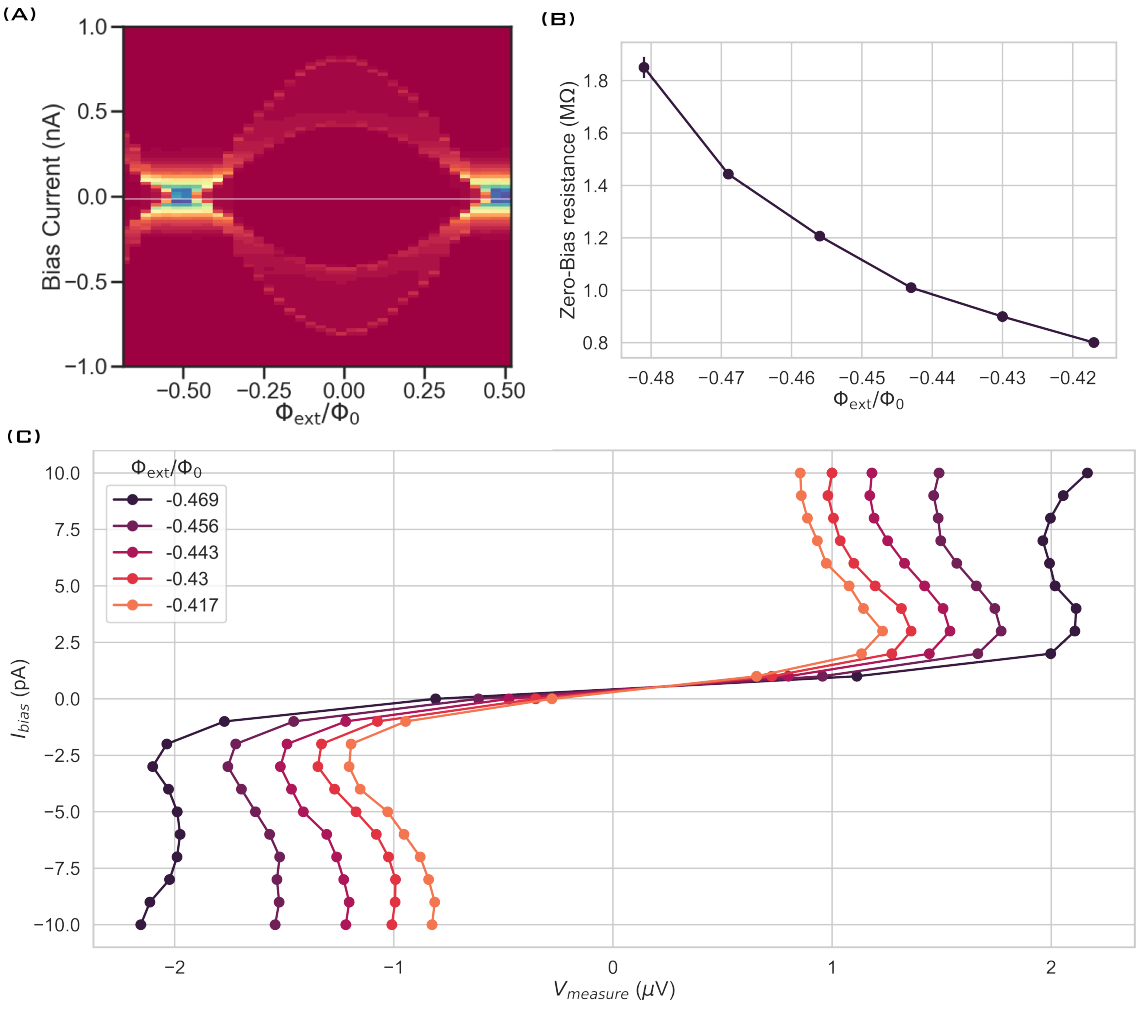

Figure 9.10: (A) The differential resistance as a function of the external flux. This is a rough sweep to find the dependence on external flux. (B) The extracted R_N at zero-current bias for the curves displayed in (C). The IV characteristics of the device biased at different flux points. The traces exhibit a "Bloch nose" which exhibits negative resistance.

A measured dV/dI curve at IFQ, where E_J/E_C is the largest, is shown in figure 9.11. At this flux bias point, the small junction still has a Coulomb blockade feature appearing as a peak centered at zero bias current. The value of resistance is reduced by almost two orders of magnitude compared to the data around HFQ and has the value $R_N \sim 10k\Omega$. By analyzing the features of the measurement a threshold current $I_t = 24.5$ pA is estimated. When the bias current exceeds I_t the resistance drops to non-negative values and is then followed by two small peaks at $I_{\text{bias}} = 49, 70$ pA. Following these peaks, the resistance increases slightly most likely due to Zener tunneling before stabilizing at around 2 kΩ. The peaks are an intriguing feature since one would first conclude these are signatures of Bloch oscillations yet the system is not irradiated by any microwave source. However, the shunting chain has standing modes that can phase lock to the Bloch oscillations yet no negative differential resistance is conclusively observed. This feature could be the modifications of the IV characteristics due to the external modes of the transmission line environment. This is an ongoing experiment presently, however, we hope these results are a positive indication that phase-locking the Bloch oscillations in the small JJ to the standing modes of the JJ transmission line is possible.

Currently, Bloch oscillations in an array of JJs were measured by [35] in a voltage-biased measurement which included phase locking a resonator driven at high power to the oscillations of the array junction. This is a promising result that offers evidence for such a phenomenon yet measured in another configuration. Finally, full on quantized current steps were measured by [164] using a constricted NbN thin film as a phase-slip element which was shunted by on-chip inductors and resistors. The on-chip circuitry appears to be the way to go where the current bias and voltage sense had their own on-chip resistors each of value $R \sim 23.5$ kΩ which lead to inductances of $L \sim 4.4$ μH and ultimately to the phase-slip center. This design allowed for Bloch oscillations occurring between $\sim 15 - 31$ GHz. This state-of-the-art experiment could possibly be replicated using JJ yet with Bloch frequencies less than the plasma frequency. Nevertheless, this is an interesting experiment still ripening in the field of superconducting circuits yet theorized about in the 1980s.

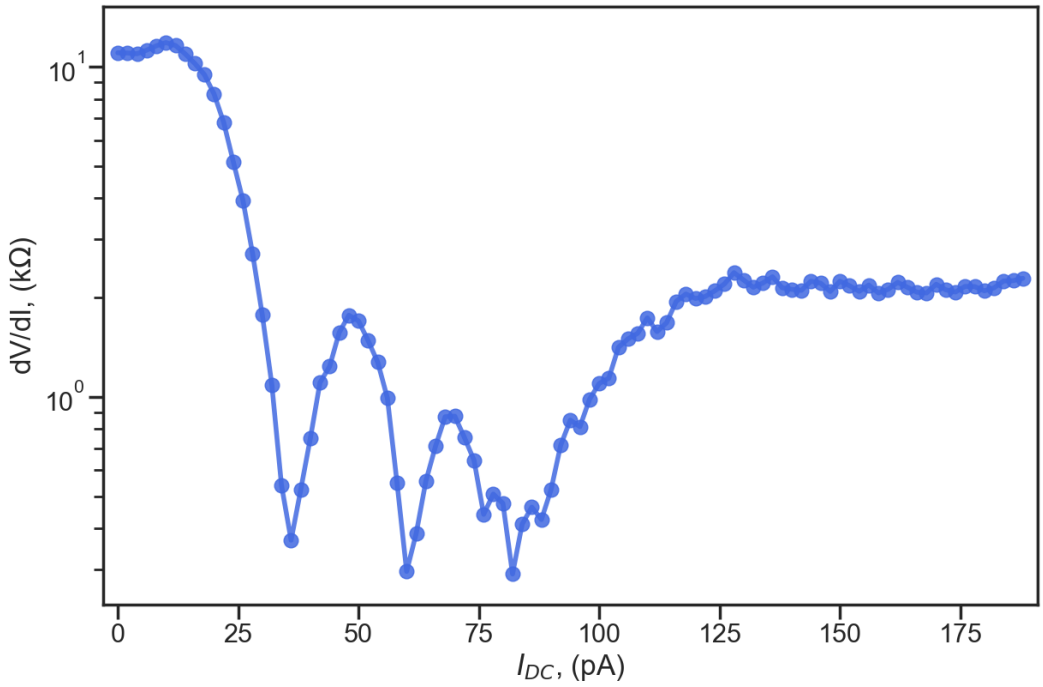

Figure 9.11: (A) A differential resistance (dV/dI) measurement taken at IFQ and averaged over several traces. No external RF source was irradiating our sample during these traces.

10
Conclusions

"There is nothing like a dream to create the future."
— Victor Hugo

Ultra-high impedance SCQC are completely realizable using standard industry fabrication techniques and is demonstrated to show promise for exploring new parameter regimes in superconducting circuits. The dry etching techniques presented in this thesis is more proof-of-concept rather than a state-of-the-art demonstration and can be refined further, undoubtedly.

Using these etching techniques we have established the ability to produce ultra-high impedance JJ transmission lines with wave impedance greater than $Z_\infty > 32$ kΩ while still maintaining high-quality factors. Next, we explored high-inductance fluxona; where the parasitic chain mode, arising from the stray capacitance of the elongated chain, was shown to ultra-strongly couple to the qubit causing effective circuit parameters when just fitting to the fluxonium-only Hamiltonian. A generic model was introduced which reproduced experimental results from 100 MHz to 16 GHz that incorporated four parasitic modes. The fluxonium qubit was then used to demonstrate the energy relaxation, T_1, usually limited by lossy capacitance, is not negatively affected by either etching procedure. Simultaneously, we

explored a new energy scale combination that produced $T_1 > 400\mu$s at all flux values. These results demonstrate the richness and possibilities the fluxonium energy scale combination parameter map has to offer.

Pushing the fluxonium into the ultra-high impedance regime by completely releasing the chain from the substrate, the blochnium emerged with inductance $L_{\text{tot}} > 2\mu$H and no apparent chain mode below 11 GHz. This is a newly realized qubit, first of the quasicharge kind, whose low-energy transitions are describable with a Hamiltonian in the quasicharge basis. The blochnium offers a 0-1 transition which is nearly flux insensitive thus creating a qubit protected from 1/f flux noise.

Finally, the preliminary results of our experiment on probing Bloch oscillations which combines the ultra-high impedance JJ transmission lines with a Bloch capacitance was introduced. The preliminary measurements foster future hopes of systematically demonstrating Bloch oscillations of a single JJ embedded in high-Z circuitry.

10.1 Future perspectives

Improving the blochnium's T_1 in order to access the T_2 protection the circuit has to offer will most likely come in the form of lowering the 0-1 transition frequency. The blochnium's main attraction is a low-frequency dispersion with the external flux bias control which comes at a cost of having large E_C – meaning a high transition frequency. There exists an energy combination that combines low flux dispersion and low operating frequency, this parameter regime comes in the form of lowering $E_J < 2$ GHz such that E_C can be lowered as well while maintaining an $E_J/E_C < 1$. Lowering E_J to this value may take a new fabrication technique that makes the junction barrier more opaque than normal rather than reducing the size of the small JJ to an area below approximately 50 nm by 50 nm. Furthermore, reducing E_C allows for the ability to design a low-loss antenna which could increase the effective Q_{cap} of the circuit. With these improvements, a $f_{01} <1$ GHz is conceivable with $T_1 > 100\mu$s at all flux points while the higher transitions still retain flux sensitivity allowing for multi-qubit architecture which has flux tuneable interactions despite f_{01} is more or less flux insensitive. This

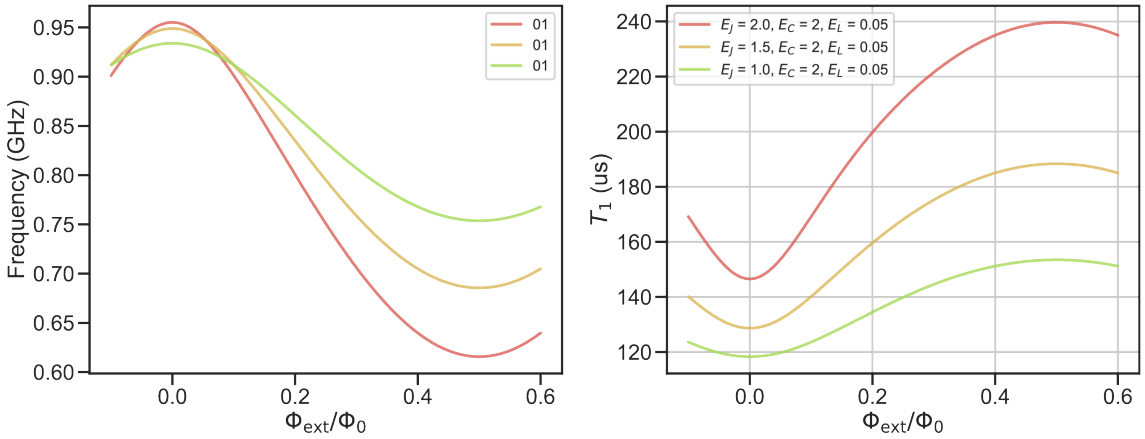

Figure 10.1: The 0-1 transition frequencies and expected T_1 due to dielectric loss of blochnium for lower than normal E_J with $E_C = 2$ GHz. The Q_{cap} in this simulation is 400,000.

would open the door for exploring blochnium as a viable option for multi-qubit processing.

A proposal for a two-qubit blochnium gate is a c-phase gate that uses fast-flux pulses on just one qubit to modify interactions between the two qubits. The design of this gate is similar to the Strauch-gate [174] and would be implemented similarly to the work done in [42]. Essentially the computational state of $|00\rangle \rightarrow |11\rangle$ anticrosses with the non-computational state $|00\rangle \rightarrow |02\rangle$ which when tuned to the region of anticrossing will cause the qubits to accumulate phase amounting to the time parked at the interacting point. This gate has the advantage that, when blochnium acquires the larger T_1, will have a T_2 which is not severely limited by 1/f flux noise.

Furthermore, the fluxonium in the second energy scale combination should be explored in further depth at IFQ. The double-phase slip feature makes T_1 very large at higher than normal frequency (for a fluxonium) which means faster control pulses. The energy landscape at this flux bias point would also make studying a qutrit at IFQ a very interesting experiment where the 12 transition is a mere several ten of MHz. Another asset worth exploring is using the parasitic chain modes as a way to read out the qubit.

Finally, the blochnium should be made such that it is completely suspended in vacuum with no substrate around it. This is the absolute bottom limit for reducing the parasitic capacitance and is completely doable with a

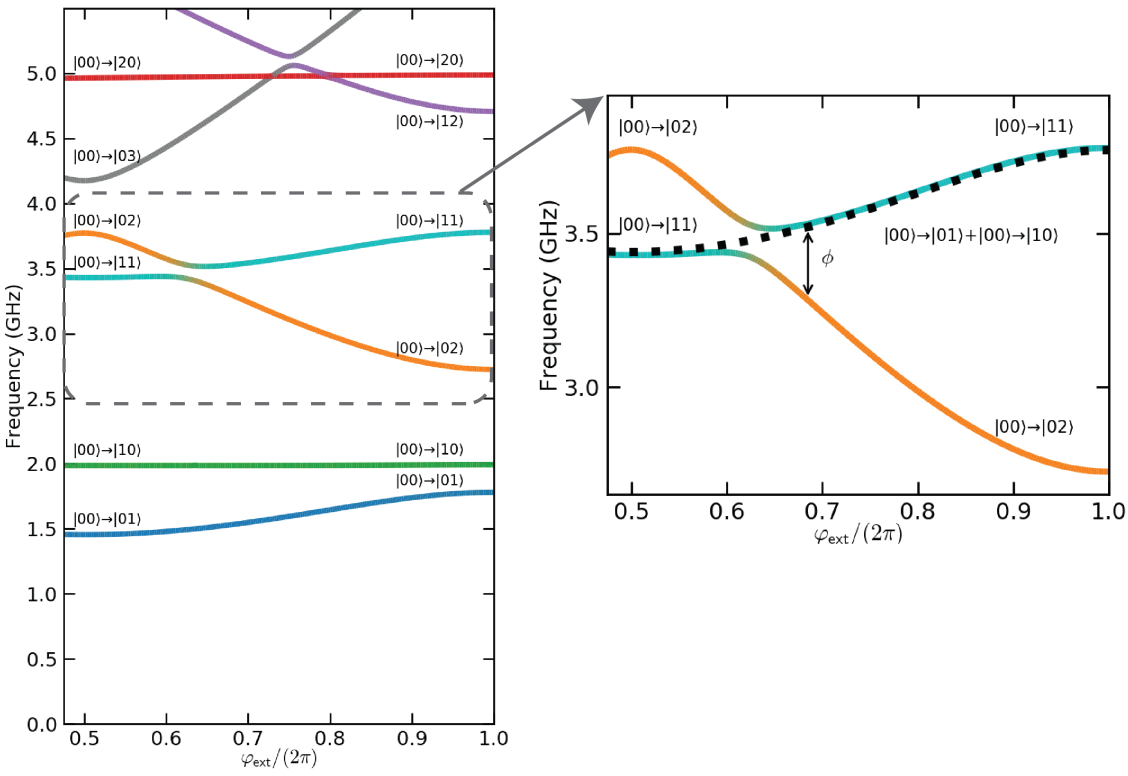

Figure 10.2: The spectrum of two coupled blochnium qubits where only one has external flux tuneability.

proper fabrication facility.

Appendix A: Reactive evaporation of Titanium Nitride

In this work, we discuss the process of growing highly disorder TiN thin flims by reactive e-beam deposition. These thin films exhibit high kinetic inductance which is demonstrated to be tunable based on the partial pressure of N_2 gas during deposition and on the films thickness. Furthermore, the film's RF properties are investigated by lumped-element and distributed resonators.

Journal of Applied Physics ARTICLE scitation.org/journal/jap

Superconducting titanium nitride films grown by directional reactive evaporation

Cite as: J. Appl. Phys. **130**, 225109 (2021); doi: 10.1063/5.0048819
Submitted: 26 February 2021 · Accepted: 15 November 2021 ·
Published Online: 13 December 2021

Raymond Mencia,[1] Yen-Hsiang Lin,[1,2,a)] and Vladimir Manucharyan[1]

AFFILIATIONS

[1]Physics Department, Joint Quantum Institute, and Quantum Materials Center, University of Maryland, College Park, Maryland 20742, USA
[2]Physics Department, National Tsing Hua University, Hsinchu 30013, Taiwan

[a)]**Author to whom correspondence should be addressed:** yhlin@phys.nthu.edu.tw

ABSTRACT

We report a novel method of growing strongly disordered superconducting titanium nitride (TiN) thin films by reactive electron-beam deposition. The normal state sheet resistance and superconducting critical temperature (T_c) can be tuned by controlling the deposition pressure in the range of 1.1×10^{-6}–3.1×10^{-5} mbar. For 10 nm thick films, the sheet resistance ($R_\square$) reaches 1361Ω/□ and $T_c = 0.77$ K, which translates into an estimate for the sheet inductance as large as $L_\square = 2.4$ nH/□. Benefiting from the directionality of reactive evaporation, we fabricated RF test devices with micrometer-sized dimensions using a resist mask and a lift-off process, which would be difficult with sputtering or atomic layer deposition methods. The spectroscopic measurements result in consistent sheet inductance values in two different device geometries, and the quality factors ranged from Q = 300 to 2200. The loss is possibly due to the presence of titanium oxynitride (TiN_xO_y) in the morphological composition of our films. The flexibility of the lift-off process suggests applications of reactively evaporated TiN for making supporting structures around quantum circuits, such as readout resonators or compact on-chip filters.

I. INTRODUCTION

High kinetic inductance of disordered superconducting films is a useful asset for device applications, including detectors, amplifiers, resonators, and qubits.[1–7] Due to self-capacitance, the characteristic impedance of typical geometric inductance is limited at the order of vacuum impedance, $Z_{vac} = 377\,\Omega$. The high geometric inductance can typically have a low unwanted self-resonance mode frequency to couple to the functioning circuit parts. Therefore, the high kinetic inductance is required for the application of high-impedance circuit applications. The high kinetic inductance by highly disordered superconducting films usually are compound materials, such as titanium nitride (TiN), niobium nitride (NbN), or niobium titanium nitride (NbTiN). The two standard processes for creating highly disordered superconducting thin films are sputtering[8,9] and atomic layer deposition (ALD).[10,11] However, these methods are generally incompatible with depositing through a resist mask, which would be useful for fabricating devices, especially in a situation where the wafer already contains structures from the previous fabrication step. Here, we explore a novel approach that utilizes reactive electron-beam (e-beam) evaporation to fabricate TiN thin films. Such a process generates a directional TiN flux for deposition, while the substrate is maintained at room temperature. This allows for the patterning of a device with standard e-beam lithography resist masks without additional postdeposition fabrication and processing. Our growth technique produces highly disordered films whose superconducting critical temperature T_c is in the range from 0.77 to 3.17 K, which is lower than the $T_c = 5.4$ K of a single crystal TiN film.[12] The resistivity is in the range of 520–6000 μΩ cm, which is two to three orders of magnitude larger than 5–18 μΩ cm of single crystal TiN films.[12,13] The sheet inductance values are as high as $L_\square = 2.4$ nH/□, which is larger than any reported TiN films grown by other growth methods with a similar film thickness.[11,14–16] From morphology and composition analysis, we find that the strong disorder of e-beam deposited TiN films may originate from mostly amorphous-phased titanium oxynitride (TiN_xO_y) with nano-crystalline TiN embedded sparsely throughout. This fabrication process may provide an alternative way to produce devices with high kinetic inductance.

II. TITANIUM NITRIDE FABRICATION

Our TiN thin films are deposited by reactive e-beam evaporation on silicon-(100) oriented substrates. The substrates were prepared by sonication in acetone and isopropanol and then blown dry with nitrogen. The devices fabricated for DC transport properties were patterned with a Hall bar geometry created by a physical shadow mask. The devices fabricated for RF measurements were patterned by electron-beam lithography using a MMA-EL13 resist mask.

The substrates were then loaded into a Plassys MEB550S e-beam evaporation system where the main deposition scheme is shown in Fig. 1. The main deposition chamber is pumped down to a pressure below 5.0×10^{-7} mbar before beginning the deposition. We first utilize an *in situ* argon ion gun to perform a 20 s argon ion milling to clean the surface. The deposition procedure started with heating a titanium (with purity 99.995%) source with the e-beam. Once the titanium evaporation rate is stabilized, we performed a deposition of pure titanium on the shutter at least 5 min with a deposition rate of 0.10 nm/s. The purpose of this deposition is not only for cleaning the titanium target but also use the evaporate titanium material as getter pumping. After deposition of titanium, a controlled flow of ultrahigh pure nitrogen gas (with purity 99.999%) was introduced into the deposition chamber. Due to the high energy of the e-beam and the high temperature of the titanium source, the nitrogen gas reacts with the titanium flux to form TiN.

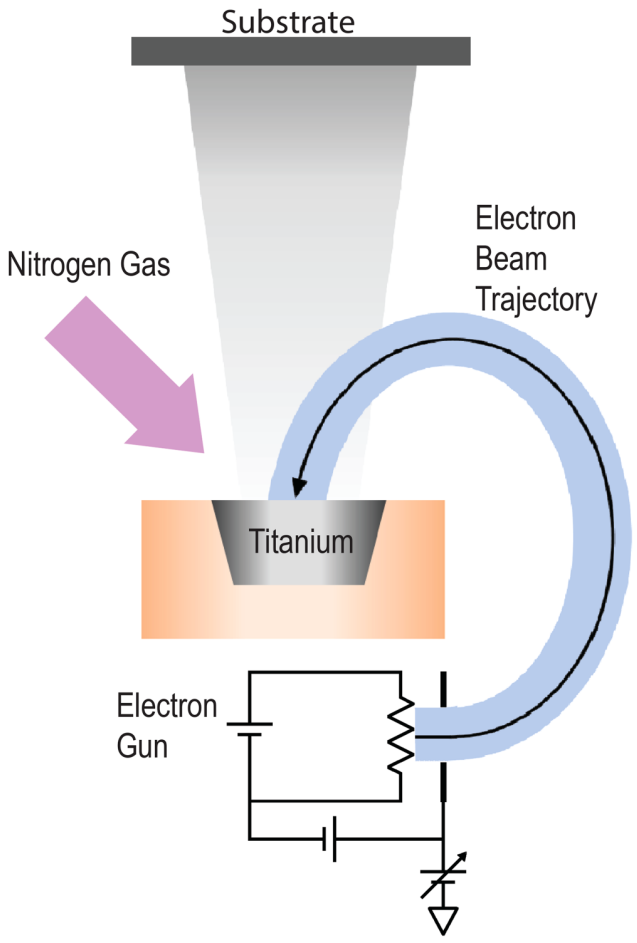

FIG. 1. A schematic diagram of the nitrogen reactive electron-beam evaporation. An ultrahigh nitrogen gas flow is introduced into a deposition chamber, while a 10 keV e-beam evaporator performs titanium deposition. The precision of gas flow control is down to 0.1 standard cubic centimeters per minute (SCCM).

During deposition, the chamber deposition pressure is determined by a titanium deposition rate and a nitrogen gas flow rate. Clearly, the higher the nitrogen gas flow rate, the higher the chamber pressure. However, the evaporated titanium material can both simultaneously generate titanium flux (raising the chamber pressure) and serve as a titanium sublimation pump (reducing the chamber pressure). To control the chamber pressure and the reaction condition, a feedback circuit loop of the e-beam current maintains a constant titanium deposition rate at 0.15 nm/s for all TiN films in this study. The chamber pressure is then tuned by a nitrogen flow rate, which is controlled in the range of 0–20 standard cubic centimeters per minute (SCCM) and has a precision of 0.1 SCCM. The actual TiN deposition only started once both the deposition rate and chamber pressures have reached stable values. Unlike ALD growth, the substrate is always maintained at room temperature during the whole deposition process. Also, the evaporated material flux is directional—the same as the normal e-beam evaporation process. Thus, this film growth process is suitable for both photo- and e-beam resist mask fabrication techniques. The only required postdeposition step of fabricating RF devices is the standard lift-off procedure of the e-beam mask by a heated acetone bath for approximately 1 h. It is worth mentioning that the same substrate, substrate cleaning, and lift-off process have been used to fabricate high coherence fluxonium superconducting qubits, where loss tangent is lower than 4.0×10^{-6}.[17]

III. DC TRANSPORT MEASUREMENTS

We utilize a physical properties measurement system (PPMS) to characterize DC transport properties of TiN films. All the samples for DC transport are performed by standard four terminal measurements and summarized in Table I. We found that deposition pressure P_{dep} and film thickness d significantly affect the properties of the grown TiN films.

In Fig. 2(a), we compare sheet resistance ($R_{\square}$) vs temperature of seven 100 nm thick films (A–G) grown at deposition pressures, P_{dep}, in a range from 1.1×10^{-6} to 3.1×10^{-5} mbar. The normal $R_{\square}$ at 10 K increases more than one order of magnitude from 52 to 600Ω/□ (corresponding to resistivity from 520 to 6000 μΩ cm, respectively). On the other hand, the T_c first increases but then decreases with increasing P_{dep}. The highest T_c peaked at 3.03 K with the $P_{dep} = 5.5 \times 10^{-6}$ mbar. The non-monotonic behavior of T_c with P_{dep} suggests that there is a competition between nitrogen incorporation[15,18] and suppression of T_c due to disorder.[10,19] According to the Ambegaokar–Baratoff relation and BCS theory,

TABLE I. Summary of TiN film growth conditions and DC transport measurements. All films are grown with the same growth rate of 0.15 nm/s. The sheet kinetic inductance $L_\square$ is estimated by the Ambegaokar–Baratoff relation and the BCS theory. Normal sheet resistance and normal resistivity are measured at 10 K.

	d (nm)	P_{dep} (mbar)	$R_\square$ ($\Omega/\square$)	ρ ($\mu\Omega$ cm)	T_c (K)	$L_\square$ (pH/$\square$)
A	100	1.1×10^{-6}	52	520	1.85	27
B	100	2.6×10^{-6}	157	1570	2.95	73
C	100	5.5×10^{-6}	250	2500	3.03	114
D	100	6.1×10^{-6}	316	3160	2.95	148
E	100	7.3×10^{-6}	451	4510	2.7	231
F	100	1.2×10^{-5}	534	5340	2.58	286
G	100	3.1×10^{-5}	600	6000	2.35	353
H	300	1.2×10^{-5}	85	2550	3.17	37
I	200	1.2×10^{-5}	135	2700	3.02	62
J	30	1.2×10^{-5}	855	2565	2.4	492
K	20	1.2×10^{-5}	961	1922	1.91	674
L	10	1.2×10^{-5}	1361	1361	0.77	2442

the sheet kinetic inductance can be estimated as $L_\square = \hbar R_\square / 1.76\pi k_B T_c$.[20] Accordingly, we obtained a wide range of $L_\square$ for samples A–G ranging from 27 to 353 pH/$\square$.

The TiN film properties are also tunable by changing the film thickness d. Figure 2(b) shows $R_\square$ vs temperature of six films (samples F and H to L), all grown at the same $P_{dep} = 1.2\times10^{-5}$ mbar, with the thicknesses ranging from 10 to 300 nm thick. The normal $R_\square$ increases with decreasing film thickness. Interestingly, the critical temperature of TiN films decreases with decreasing film thickness. The 10 nm film shows a critical temperature of 0.77 K, while it has the highest normal $R_\square = 1361\,\Omega/\square$ at 10 K. Such behaviors have been observed with strongly disordered superconducting films near thickness tuned superconductor–insulator (SI) transitions.[10,19] With such tunability, the $L_\square$ of a 10 nm TiN film reaches up to 2.4 nH/$\square$, which is nearly one order of magnitude larger than $L_\square$ of TiN films grown by sputter and ALD.[11,14,15] Interestingly, in sample F and H to L, the resistivity is non-monotonically changing with decreasing thickness. This may be related to the evolution of different morphologies as a function of film thickness or diffusion of elements so that the stoichiometry may vary with thickness.

Additionally, the superconductivity of these TiN films can tolerate large perpendicular magnetic fields. Figure 2(c) shows the $R_\square$ of samples H, F, J vs perpendicular magnetic fields at 1.8 K. The critical magnetic field for samples H, F, and J are 5.3, 2.9, and 0.4 T, respectively. The critical field is also one to two orders of magnitude larger than the typical aluminum based Josephson junction array devices. This demonstrates that disordered TiN films can still serve as a high-impedance device in a high magnetic field environment.

IV. RF DEVICE AND MEASUREMENTS

To probe the RF properties of TiN films, we patterned two different types of devices: (1) resonators [shown in Fig. 3(a)] and (2) high-impedance transmission lines [shown in Fig. 3(c)]. The measurement utilized the same setup of Kuzmin *et al.*[21] The devices are capacitively coupled to a single-port 3D copper waveguide, which is then mounted to a dilution refrigerator, and the microwave reflection response is probed with a vector network analyzer (VNA).

The resonator device was deposited at $P_{dep} = 6.3\times10^{-6}$ mbar with a 100 nm thick TiN film. There were a total of six resonators with a separation of at least 2 mm to the nearest neighboring resonator such that the coupling between resonators is weak. The capacitance value is dominated by the two $175\times175\,\mu m^2$ square pads. The capacitance of the antenna was determined by HFSS simulations to be 39 fF. The geometric sheet inductance of the thin wire is calculated to be 1 pH, which is two orders of magnitude lower than the kinetic inductance. Therefore, the inductance value is dominated by the kinetic inductance of the 100 μm long thin wire connecting the two pads. The width of the wires is chosen to be 1.575, 2, 2.25, 2.5, 3, and 3.55 μm for these six different resonators.

The magnitude of the reflected signal, $S11$, is shown in Fig. 3(b). There are six dips at 8.6, 9.5, 10.1, 10.7, 11.7, and 12.5 GHz, which correspond to the resonance frequencies of the six resonators. The total inductance of each resonator can be extrapolated from the measured resonance frequencies and a simulated capacitance value. Assuming that the inductance values here are all provided by the kinetic inductance of the disordered TiN film, we find the sheet inductance value of each resonator to be 139, 146, 145, 142, 145, and 146 pH. The maximum difference between individual resonator's sheet inductance is about 4%, which reveals the non-uniformity of the TiN film within a single deposition. Moreover, the thickness and deposition pressure of this device are controlled to be the same as film D in the DC measurement experiment, but each sample was deposited in two different depositions. The DC measurement analysis of film D revealed a sheet inductance of 148 pH, which has only a 3% difference to the average sheet inductance value of the six resonators in the RF measurement. The systematic difference from deposition to deposition is comparable to sputtering TiN and Josephson junction chains.[15,18,22] To extrapolate the intrinsic quality factor (Q_{int}), we used the common expression to fit the reflection coefficient as a function of frequency,[21,23]

$$S_{11}(f) = \frac{2i(f-f_0)/f_0 - Q_{ext}^{-1} + Q_{int}^{-1}}{2i(f-f_0)/f_0 + Q_{ext}^{-1} + Q_{int}^{-1}}. \quad (1)$$

We obtained Q_{int} values in the range of 1500–2200 for the six resonance peaks.

The transmission line device is designed with two parallel 10 mm long, 3 μm wide TiN wires shown in Fig. 3(c). The TiN waveguide was deposited 30 nm thick with $P_{dep} = 7.0\times10^{-6}$ mbar. One end of the wire is short circuited and the other end is connected to an antenna, which capacitively couples to a 3D copper waveguide.[21] The magnitude of a single-tone reflection signal, S11, as a function of probe frequency is shown in Fig. 3(d). S11 reveals resonance dips with equal frequency spacing $f_{n+1} - f_n = 200$ MHz. The wave-number difference of adjacent modes is defined as $k_{n+1} - k_n = \pi/l$, where $l = 10$ mm is the length of the line. In the measured frequency range, we observed a linear dispersion relation, which gives a slow wave velocity $v = 4.0\times10^6$ m/s. The value of

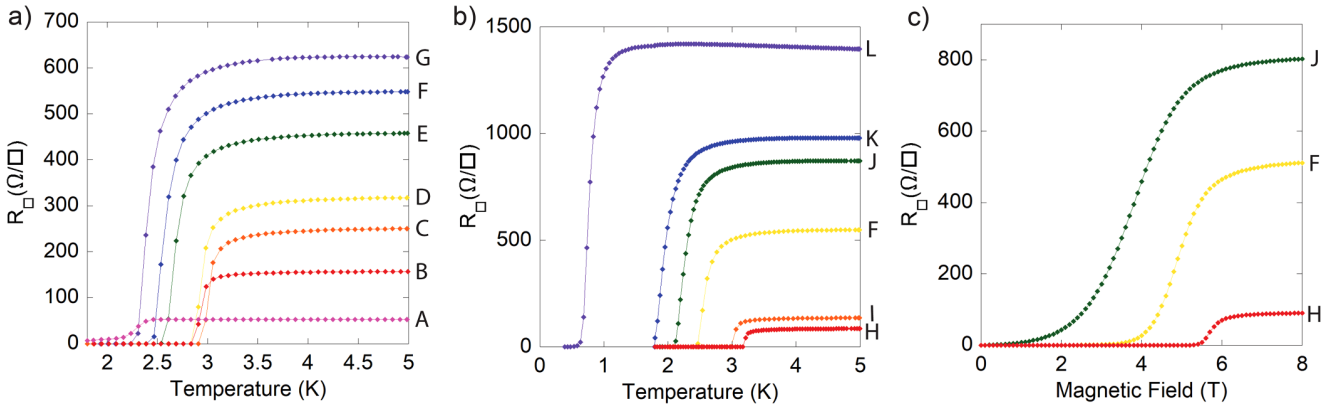

FIG. 2. DC transport measurements of sheet resistance $R_\square$ as a function of temperature for sets of (a) samples (A–G) grown in different deposition pressures P_{dep} and (b) samples (F and H to L) of different film thickness d. (c) $R_\square$ as a function of perpendicular magnetic field of samples H, F, and J. The growth condition of all samples is listed in Table I.

capacitance per micrometer is 42 aF/μm, which is calculated with a common formula for two coplanar strip lines on top of a silicon substrate.[24] Thus, we can obtain the sheet inductance value of TiN for this particular device as 465 pH/□. The sheet inductance value is smaller than the value of sample K found via DC measurements. Presumably, this is due to a slightly lower TiN deposition pressure of the transmission line device. We also obtained the Q_{int} for each mode with Eq. (1). The value of Q_{int} is between 300 and 700 with an average of 470. Note that the values of Q_{int} for both types of resonators are all lower than all the other reported literature.[11,15,25] This result may be due to the morphology and composition, which will be discussed in Sec. V.

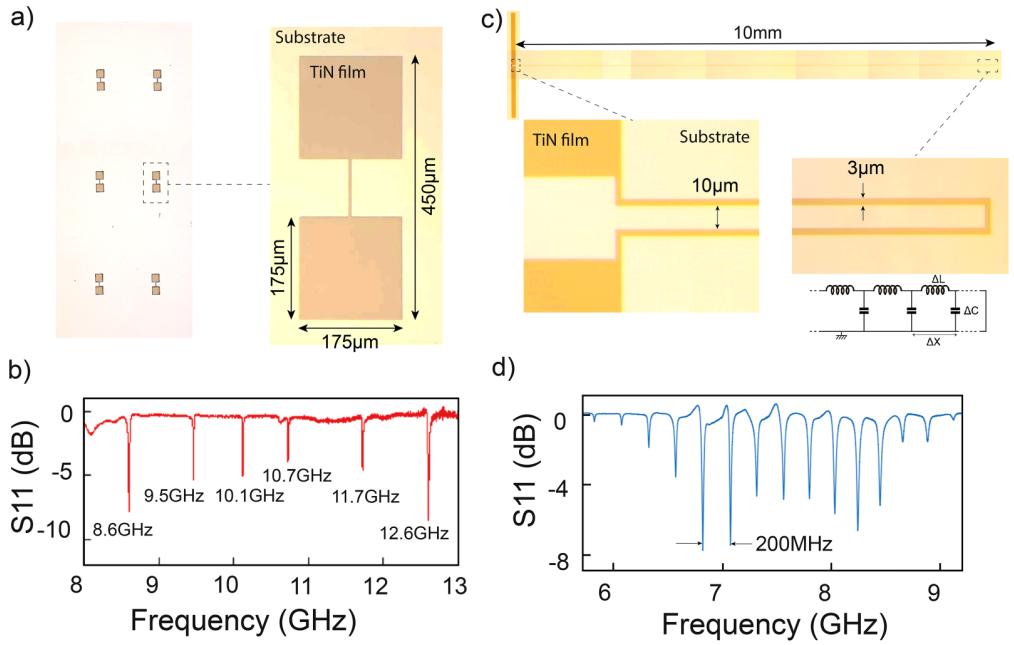

FIG. 3. The optical microscope image of (a) six RF resonators and (c) a transmission line RF device with an effective circuit model shown at the bottom. In the resonator device, the two square electrode pads provide capacitance of the resonator and couple to a 3D waveguide for measurements. The transmission line device consists of 10 mm long TiN wires. One end of the transmission line is shorted, while the other end links to an antenna. The reflection response S11, measured by a VNA, is shown in (b) and (d).

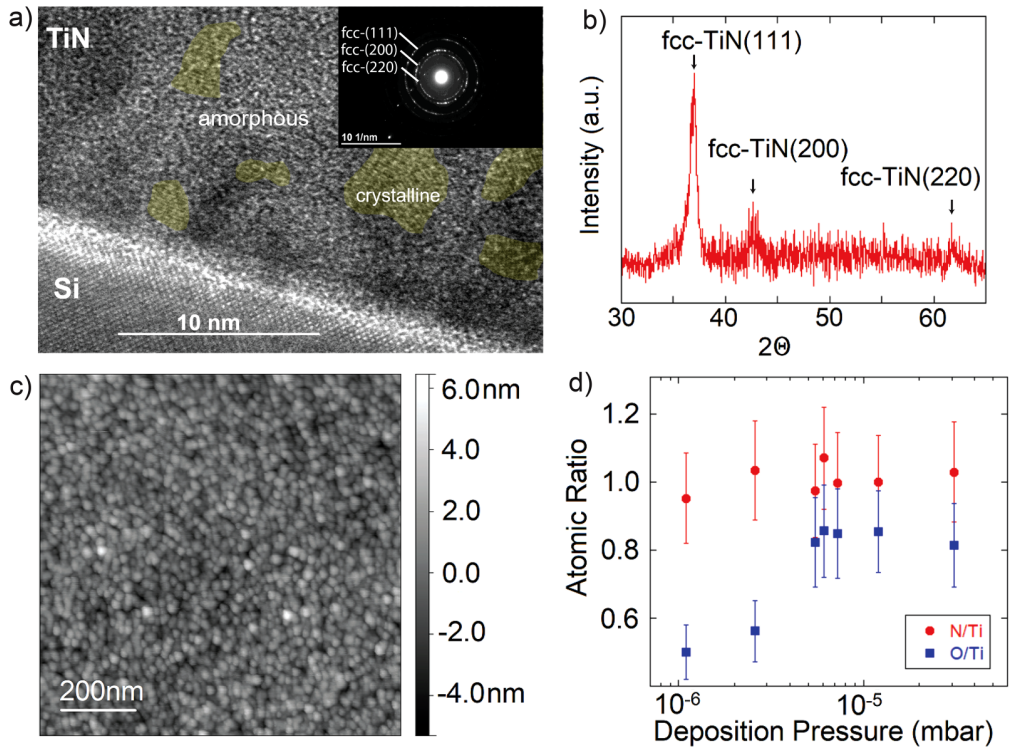

FIG. 4. The morphology analysis of grown TiN films. (a) Transmission electron microscopy (TEM) of a TiN sample grown in conditions similar to sample F. The false color area labels the crystalline features, while the other area is mainly amorphous. The inset shows the selected area diffraction (SAD) pattern, which reveals the crystalline orientations of TiN. (b) X-ray diffraction (XRD) of theta-2 theta analysis. (c) Atomic force microscope (AFM) scan of the surface structure. (d) Atomic ratios of nitrogen to titanium and oxygen to titanium measured by energy-dispersive X-ray spectroscopy (EDX). These results reveal that the atomic composition of grown films is, in fact, titanium oxynitride TiN_xO_y.

V. MORPHOLOGY AND ATOMIC COMPOSITION CHARACTERIZATION

To further understand the origin of the disorder and the morphology in the TiN films, we performed various morphology analyses to the films grown with the same conditions of sample F in Table I.

First, we used transmission electron microscopy (TEM) to analyze local crystalline morphology of the TiN films. The most striking feature is that most areas are amorphous with only sporadic poly-crystalline embedded within, as shown in Fig. 4(a). The false color area labeled "crystalline area" shows the formation of nano-crystals, which typically have a size less than 5 nm. The fact that the majority of the film morphology is amorphous confirms that these TiN films are strongly disordered. The different crystalline orientations seen in TEM are determined with the selected area diffraction (SAD) pattern, as shown in the inset of Fig. 4(a). The locations of the ring like features indicate that the different crystalline orientations are fcc-TiN (111), fcc-TiN (200), and fcc-TiN (220).[26] Furthermore, we performed x-ray diffraction (XRD) theta-2 theta analysis to confirm crystalline orientations, as shown in Fig. 4(b). The peaks found at 36.5°, 42.5°, and 42° correspond to fcc-TiN (111), fcc-TiN (200), and fcc-TiN (220), respectively, and are consistent with SAD's results. Despite the different growth method, the same crystalline orientations have also been found in ALD and sputtered TiN thin films.[11,15,18,25,27]

We then utilize atomic force microscopy (AFM) to study the surface morphology of the TiN films. Figure 4(c) shows an example of a $1 \times 1\,\mu m^2$ AFM scan performed on a 100 nm thick TiN film grown at the deposition pressure of sample E. The surface of TiN consists of grains with a diameter around 20 nm. The root mean square surface roughness is 1.2 nm, while the maximum thickness variation is less than 12 nm. Therefore, films thinner than 10 nm may result in physically disconnected structures. To avoid weak links or an unwanted vortex structure, the thickness of TiN films should be thicker than 30 nm while fabricating RF devices.

The atomic composition of the TiN films was analyzed by energy-dispersive x-ray spectroscopy (EDX) with a 5 keV accelerating voltage variable pressure Hitachi scanning electron microscope. Contrary to the expected composition of just titanium and nitrogen, a large amount of oxygen was present in all TiN films. Figure 4(d) shows a summary of the EDX atomic ratio of nitrogen to titanium (N/Ti) and oxygen to titanium (O/Ti) as a function of

deposition pressure. The nitrogen to titanium ratio is nearly 1:1 within the measurement error, which indicates that the nitrogen atom indeed incorporates in the form of titanium nitride. Interestingly, the oxygen to titanium atomic ratio increases from 0.5 to 0.8 with an increase in the deposition pressure. An oxidation process under ambient conditions and the large amounts of oxygen in the chemical composition have also been reported in TiN thin films grown by ALD and sputtering.[11,15] Since SAD and XRD both confirmed that crystalline regimes are formed by TiN, we conclude that the oxygen is diffused into the amorphous regions and forms TiN_xO_y. The large portion of amorphous TiN_xO_y reveals that the origin of the strongly disordered, highly resistive properties may come from amorphous oxides. One possible conjecture is that oxygen is much easier to diffuse into our film and form oxides once the film is exposed to the ambient condition. It is worth noting that we observed the color of our films changed once we vent the deposition chamber to air, which may be due to oxidation of films after exposure to air. Typically, amorphous oxides have a higher loss tangent value and may explain the low quality factors than other studies.

VI. CONCLUSION

In conclusion, the values of the sheet kinetic inductance of TiN films prepared by nitrogen assisted reactive e-beam deposition can be tuned by two orders of magnitude from 27 pH/□ to 2.4 nH/□. The tuning knobs are deposition pressure and film thickness. The variations of kinetic inductance within the same deposition and between different depositions are within about 5%. Although the quality factors of our lift-off devices are short of the values accessible with more traditional sputtering or ALD film growth methods, our process can be useful in creating compact high-impedance resonators and filters that survive in relatively high magnetic fields.

ACKNOWLEDGMENTS

The method for directional reactive TiN deposition was suggested by the late Patrick Smuteck, to whom this article is dedicated. The authors thank Dr. Sz-Chian Liou from the Advanced Imaging and Microscopy Lab in the University of Maryland for his assistance in TEM imaging and analysis and Dr. Joshua Higgins for assistance with XRD analysis and PPMS measurements. This work was supported by the National Science Foundation (NSF) Career Grant (No. DMR 1455261) and by the Army Research Office (ARO)-LPS program "New and Emerging Qubit Science and Technology" (No. W911NF1810115).

AUTHOR DECLARATIONS

Conflict of Interest

The authors have no conflicts to disclose.

DATA AVAILABILITY

The data that support the findings of this study are available from the corresponding author upon reasonable request.

REFERENCES

[1]B. H. Eom, P. K. Day, H. G. LeDuc, and J. Zmuidzinas, "A wideband, low-noise superconducting amplifier with high dynamic range," Nat. Phys. **8**, 623–627 (2012).
[2]P. K. Day, H. G. LeDuc, B. A. Mazin, A. Vayonakis, and J. Zmuidzinas, "A broadband superconducting detector suitable for use in large arrays," Nature **425**, 817–821 (2003).
[3]J. T. Peltonen, O. V. Astafiev, Y. P. Korneeva, B. M. Voronov, A. A. Korneev, I. M. Charaev, A. V. Semenov, G. N. Golt'sman, L. B. Ioffe, T. M. Klapwijk, and J. S. Tsai, "Coherent flux tunneling through NbN nanowires," Phys. Rev. B **88**, 220506 (2013).
[4]H. G. Leduc, B. Bumble, P. K. Day, B. H. Eom, J. Gao, S. Golwala, B. A. Mazin, S. McHugh, A. Merrill, D. C. Moore, O. Noroozian, A. D. Turner, and J. Zmuidzinas, "Titanium nitride films for ultrasensitive microresonator detectors," Appl. Phys. Lett. **97**, 102509 (2010).
[5]N. Samkharadze, A. Bruno, P. Scarlino, G. Zheng, D. P. DiVincenzo, L. DiCarlo, and L. M. K. Vandersypen, "High-kinetic-inductance superconducting nanowire resonators for circuit QED in a magnetic field," Phys. Rev. Appl. **5**, 044004 (2016).
[6]J. B. Chang, M. R. Vissers, A. D. Córcoles, M. Sandberg, J. Gao, D. W. Abraham, J. M. Chow, J. M. Gambetta, M. Beth Rothwell, G. A. Keefe, M. Steffen, and D. P. Pappas, "Improved superconducting qubit coherence using titanium nitride," Appl. Phys. Lett. **103**, 012602 (2013).
[7]T. M. Hazard, A. Gyenis, A. Di Paolo, A. T. Asfaw, S. A. Lyon, A. Blais, and A. A. Houck, "Nanowire superinductance fluxonium qubit," Phys. Rev. Lett. **122**, 010504 (2019).
[8]E. F. C. Driessen, P. C. J. J. Coumou, R. R. Tromp, P. J. de Visser, and T. M. Klapwijk, "Strongly disordered TiN and NbTiN *s*-wave superconductors probed by microwave electrodynamics," Phys. Rev. Lett. **109**, 107003 (2012).
[9]D. Niepce, J. Burnett, and J. Bylander, "High kinetic inductance NbN nanowire superinductors," Phys. Rev. Appl. **11**, 044014 (2019).
[10]T. I. Baturina, A. Y. Mironov, V. M. Vinokur, M. R. Baklanov, and C. Strunk, "Localized superconductivity in the quantum-critical region of the disorder-driven superconductor-insulator transition in TiN thin films," Phys. Rev. Lett. **99**, 257003 (2007).
[11]A. Shearrow, G. Koolstra, S. J. Whiteley, N. Earnest, P. S. Barry, F. J. Heremans, D. D. Awschalom, E. Shirokoff, and D. I. Schuster, "Atomic layer deposition of titanium nitride for quantum circuits," Appl. Phys. Lett. **113**, 212601 (2018).
[12]A. Torgovkin, S. Chaudhuri, A. Ruhtinas, M. Lahtinen, T. Sajavaara, and I. Maasilta, "High-quality superconducting titanium nitride thin film growth using infra-red pulsed laser deposition," Superconductor Sci. Technol. **31**, 055017 (2018).
[13]B. O. Johansson, J.-E. Sundgren, J. E. Greene, A. Rockett, and S. A. Barnett, "Growth and properties of single crystal TiN films deposited by reactive magnetron sputtering," J. Vac. Sci. Technol. A **3**, 303 (1985).
[14]P. C. J. J. Coumou, M. R. Zuiddam, E. F. C. Driessen, P. J. de Visser, J. J. A. Baselmans, and T. M. Klapwijk, "Microwave properties of superconducting atomic-layer deposited TiN films," IEEE Trans. Appl. Supercond. **23**, 7500404 (2013).
[15]S. Ohya, B. Chiaro, A. Megrant, C. Neill, R. Barends, Y. Chen, J. Kelly, D. Low, J. Mutus, P. J. J. O'Malley, P. Roushan, D. Sank, A. Vainsencher, J. Wenner, T. C. White, Y. Yin, B. D. Schultz, C. J. Palmstrøm, B. A. Mazin, A. N. Cleland, and J. M. Martinis, "Room temperature deposition of sputtered TiN films for superconducting coplanar waveguide resonators," Superconductor Sci. Technol. **27**, 015009 (2013).
[16]A. Torgovkin, S. Chaudhuri, J. Malm, T. Sajavaara, and I. J. Maasilta, "Normal-metal–superconductor tunnel junction with atomic-layer-deposited titanium nitride as superconductor," IEEE Trans. Appl. Supercond. **25**, 1101604 (2015).
[17]L. B. Nguyen, Y.-H. Lin, A. Somoroff, R. Mencia, N. Grabon, and V. E. Manucharyan, "High-coherence fluxonium qubit," Phys. Rev. X **9**, 041041 (2019).
[18]M. R. Vissers, J. Gao, J. S. Kline, M. Sandberg, M. P. Weides, D. S. Wisbey, and D. P. Pappas, "Characterization and *in situ* monitoring of sub-stoichiometric

adjustable superconducting critical temperature titanium nitride growth," Thin Solid Films **548**, 485–488 (2013).
[19]D. B. Haviland, Y. Liu, and A. M. Goldman, "Onset of superconductivity in the two-dimensional limit," Phys. Rev. Lett. **62**, 2180–2183 (1989).
[20]M. Tinkham, *Introduction to Superconductivity*, 2nd ed. (Dover Publications, 2004).
[21]R. Kuzmin, R. Mencia, N. Grabon, N. Mehta, Y.-H. Lin, and V. E. Manucharyan, "Quantum electrodynamics of a superconductor–insulator phase transition," Nat. Phys. **15**, 930–934 (2019).
[22]N. A. Masluk, I. M. Pop, A. Kamal, Z. K. Minev, and M. H. Devoret, "Microwave characterization of josephson junction arrays: Implementing a low loss superinductance," Phys. Rev. Lett. **109**, 137002 (2012).
[23]Z. Frait and C. E. Patton, "Simple analytic method for microwave cavity Q determination," Rev. Sci. Instrum. **51**, 1092 (1980).
[24]V. H. Fouad, "Finite boundary corrections to coplanar stripline analysis," Electron. Lett. **16**, 604 (1980).
[25]M. Sandberg, M. R. Vissers, J. S. Kline, M. Weides, J. Gao, D. S. Wisbey, and D. P. Pappas, "Etch induced microwave losses in titanium nitride superconducting resonators," Appl. Phys. Lett. **100**, 262605 (2012).
[26]H. Ju, N. Ding, J. Xu, L. Yu, Y. Geng, F. Ahmed, B. Zuo, and L. Shao, "The influence of crystal structure and the enhancement of mechanical and frictional properties of titanium nitride film by addition of ruthenium," Appl. Surf. Sci. **489**, 247–254 (2019).
[27]F. Vaz, P. Machado, L. Rebouta, J. Mendes, S. Lanceros-Méndez, L. Cunha, S. Nascimento, P. Goudeau, J. Riviére, E. Alves, and A. Sidor, "Physical and morphological characterization of reactively magnetron sputtered TiN films," Thin Solid Films **420–421**, 421–428 (2002).

Appendix B: All qubit parameters

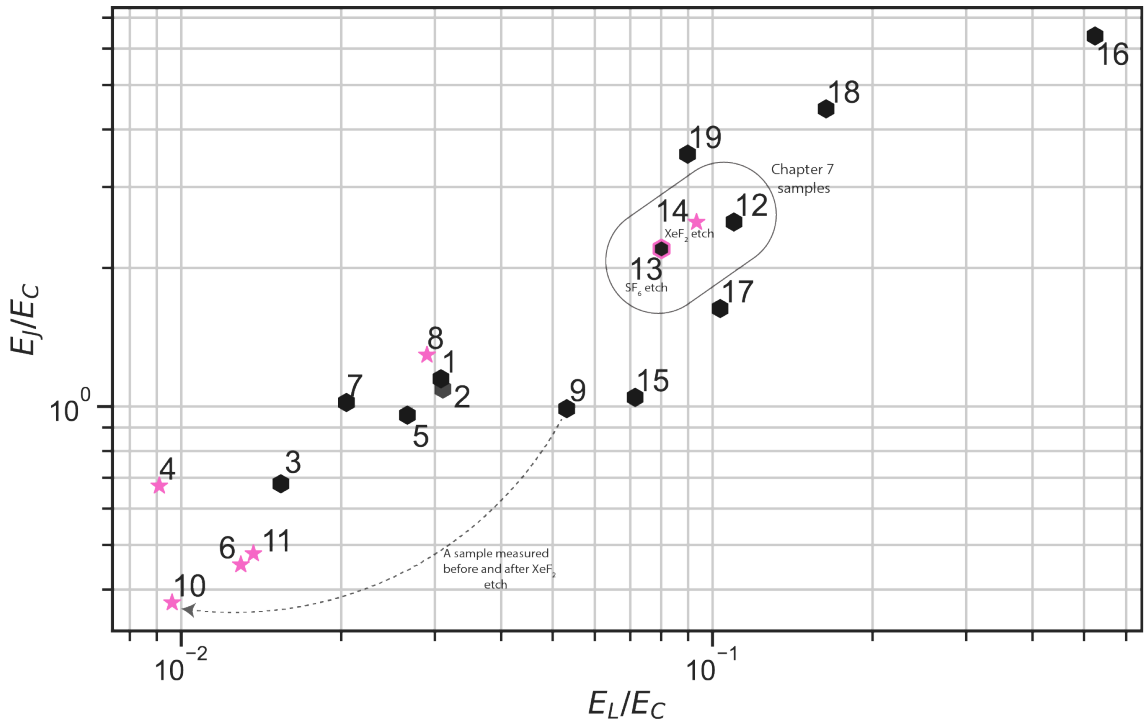

Figure B.1: All qubit samples measured extracted parameters. The black hexagon data points indicate no etch performed while the magenta stars indicate the sample was etched using XeF_2.

Appendix C: Chain mode energy constants

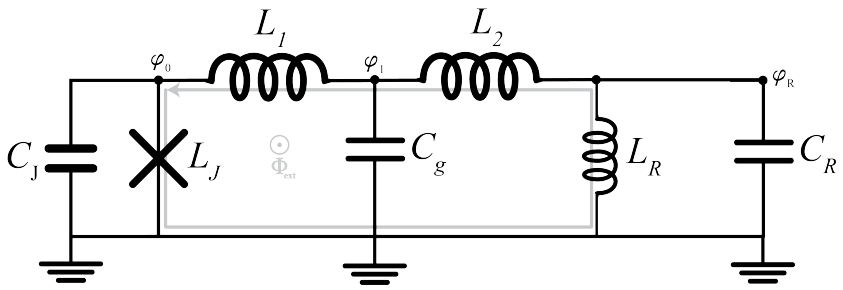

Figure C.1: The circuit for analysis of a chain mode fluxonia with an inductively coupled resonator.

C.1 flux-coupled

$$E_L^m = \varphi_0^2 \left(\frac{1}{L_1} + \frac{1}{L_2} \right) \tag{C.1}$$

$$E_L^r = \varphi_0^2 \left(\frac{1}{L_2} + \frac{1}{L_r} \right) \tag{C.2}$$

$$E_L^j = \left(\frac{\varphi_0^2}{L_1} \right) \tag{C.3}$$

$$g_{rj} = 0 \tag{C.4}$$

$$g_{mj} = \frac{-\varphi_0^2}{hL_1} \left(\frac{2E_C^m}{E_L^m} \right)^{1/4} \tag{C.5}$$

$$g_{mr} = \frac{-\varphi_0^2}{hL_2}\left(\frac{4E_C^m E_C^r}{E_L^m E_L^r}\right)^{1/4} \tag{C.6}$$

C.2 charge-coupled

$$E_L^m = \varphi_0^2\left(\frac{1}{L_1}+\frac{1}{L_2}\right) \tag{C.7}$$

$$E_C^m = \frac{e^2}{2}\left\{\frac{1}{C_m}+\frac{1}{C_r}\left(\frac{L_1}{L_1+L_2}\right)^2+\frac{1}{C_j}\left(\frac{L_2}{L_1+L_2}\right)^2\right\} \tag{C.8}$$

$$E_L^r = \varphi_0^2\left(\frac{1}{L_1+L_2}+\frac{1}{L_r}\right) \tag{C.9}$$

$$E_C^r = \frac{e^2}{2}\left\{\frac{1}{C_r}+\frac{1}{C_j}\left(\frac{L_r}{L_1+L_2+L_r}\right)^2\right\} \tag{C.10}$$

$$E_L^j = \left(\frac{\varphi_0^2}{L_1}\right) \tag{C.11}$$

$$g_{rj} = \frac{4E_C}{h}\left(\frac{L_r}{L_1+L_2+L_r}\right)\left(\frac{E_L^r}{2E_C^r}\right)^{1/4} \tag{C.12}$$

$$g_{mj} = \frac{4E_C}{h}\left(\frac{L_2}{L_1+L_2}\right)\left(\frac{E_L^m}{2E_C^m}\right)^{1/4} \tag{C.13}$$

$$g_{mr} = \frac{e^2}{2}\left(\frac{1}{C_r}\frac{L_1}{L_1+L_2}-\frac{1}{C_j}\frac{L_2}{L_1+L_2}\frac{L_r}{L_1+L_2+L_r}\right)\left(\frac{E_L^m E_L^r}{4E_C^m E_C^r}\right)^{1/4} \tag{C.14}$$

Appendix D: Classical mode analysis matrix

$$\mathrm{C} = \begin{pmatrix} C_c + C_J^A + C_g & -C_J^A & 0 & \cdots & 0 & 0 & 0 & -C_g \\ -C_J^A & 2C_J^A + C_g & -C_J^A & 0 & \cdots & 0 & -C_g & 0 \\ 0 & -C_J^A & 2C_J^A + C_g & -C_J^A & 0 & \cdots & 0 & 0 \\ 0 & 0 & -C_J^A & 2C_J^A + C_g & -C_J^A & \cdots & 0 & 0 \\ \vdots & \vdots & \vdots & \ddots & \ddots & \ddots & \vdots & \vdots \\ 0 & 0 & -C_g & \cdots & -C_J^A & 2C_J^A + C_g & -C_J^A & 0 \\ 0 & -C_g & 0 & \cdots & 0 & -C_J^A & 2C_J^A + C_g & -C_J^A \\ -C_g & 0 & 0 & \cdots & 0 & 0 & -C_J^A & C_c + C_J^A + C_g \end{pmatrix}$$

$$L^{-1} = \frac{1}{L_J^A} \begin{pmatrix} 1 & -1 & 0 & \cdots & 0 & 0 & 0 & 0 \\ -1 & 2 & -1 & 0 & \cdots & 0 & 0 & 0 \\ 0 & -1 & 2 & -1 & 0 & \cdots & 0 & 0 \\ 0 & 0 & -1 & 2 & -1 & 0 & \cdots & 0 \\ \vdots & \vdots & \vdots & \ddots & \ddots & \ddots & \vdots & \vdots \\ 0 & 0 & 0 & \cdots & -1 & 2 & -1 & 0 \\ 0 & 0 & 0 & \cdots & 0 & -1 & 2 & -1 \\ 0 & 0 & 0 & \cdots & 0 & 0 & -1 & 1 \end{pmatrix}$$

Appendix E: Fitting spectra

The way to extract the circuits parameters is to measure the spectrum of the device and fit it to the corresponding model which is most suitable.

The fit is performed by choosing 'anchor points' of transitions and minimizing the distance between the experimental point and some theoretical value for the transition energy which tweeks the energy scales. This is performed via python while minimizing the rms fit error defined as:

$$\sigma_{fit} = \sqrt{\frac{1}{M}\sum_{i=1}^{M}\left\{\frac{f_i^{exp} - f_i^{thy}}{f_i^{exp}}\right\}^2} \tag{E.1}$$

Bibliography

[1] A. Abragam. *The Principles of Nuclear Magnetism*. The international series of monographs on physics. Clarendon Press, 1970.

[2] Anthony J Annunziata, Daniel F Santavicca, Luigi Frunzio, Gianluigi Catelani, Michael J Rooks, Aviad Frydman, and Daniel E Prober. Tunable superconducting nanoinductors. *Nanotechnology*, 21(44):445202, 2010.

[3] Leonel R Arana, Nuria de Mas, Raymond Schmidt, Aleksander J Franz, Martin A Schmidt, and Klavs F Jensen. Isotropic etching of silicon in fluorine gas for mems micromachining. *Journal of Micromechanics and Microengineering*, 17(2):384, 2007.

[4] George B Arfken and Hans J Weber. Mathematical methods for physicists, 1999.

[5] O. V. Astafiev, L. B. Ioffe, S. Kafanov, Yu. A. Pashkin, K. Yu. Arutyunov, D. Shahar, O. Cohen, and J. S. Tsai. Coherent quantum phase slip. *Nature*, 484(7394):355, 2012.

[6] D. V. Averin, A. B. Zorin, and K. K. Likharev. Bloch oscillations in small Josephson junctions. *Sov. Phys. JETP*, 61(2):407–413, 1985.

[7] Feng Bao, Hao Deng, Dawei Ding, Ran Gao, Xun Gao, Cupjin Huang, Xun Jiang, Hsiang-Sheng Ku, Zhisheng Li, Xizheng Ma, et al. Fluxonium: an alternative qubit platform for high-fidelity operations. *Physical Review Letters*, 129(1):010502, 2022.

[8] M. T. Bell, I. A. Sadovskyy, L. B. Ioffe, A. Yu. Kitaev, and M. E. Gershenson. Quantum superinductor with tunable nonlinearity. *Phys. Rev. Lett.*, 109(13):137003, 2012.

[9] Kevin Bladh, Tim Duty, David Gunnarsson, and Per Delsing. The single cooper-pair box as a charge qubit. *New Journal of Physics*, 7(1):180, 2005.

[10] Alexandre Blais, Jay Gambetta, Andreas Wallraff, David I Schuster, Steven M Girvin, Michel H Devoret, and Robert J Schoelkopf. Quantum-information processing with circuit quantum electrodynamics. *Physical Review A*, 75(3):032329, 2007.

[11] Alexandre Blais, Arne L Grimsmo, Steven M Girvin, and Andreas Wallraff. Circuit quantum electrodynamics. *Reviews of Modern Physics*, 93(2):025005, 2021.

[12] Felix Bloch. Quantum mechanics of electrons in crystal lattices. *Z. Phys*, 52:555–600, 1928.

[13] Maxime Boissonneault, Jay M Gambetta, and Alexandre Blais. Dispersive regime of circuit qed: Photon-dependent qubit dephasing and relaxation rates. *Physical Review A*, 79(1):013819, 2009.

[14] Vincent Bouchiat. *Quantum fluctuations of the charge in single electron and single Cooper pair devices*.

[15] Vincent Bouchiat, D. Vion, P. Joyez, D. Esteve, and M. H. Devoret. Quantum coherence with a single Cooper pair. *Physica Scripta*, 1998(T76):165, 1998.

[16] J Bourassa, F Beaudoin, Jay M Gambetta, and A Blais. Josephson-junction-embedded transmission-line resonators: From kerr medium to in-line transmon. *Physical Review A*, 86(1):013814, 2012.

[17] Jochen Braumüller, Leon Ding, Antti P Vepsäläinen, Youngkyu Sung, Morten Kjaergaard, Tim Menke, Roni Winik, David Kim, Bethany M Niedzielski, Alexander Melville, et al. Characterizing and optimizing qubit coherence based on squid geometry. *Physical Review Applied*, 13(5):054079, 2020.

[18] Nicholas T Bronn, Yanbing Liu, Jared B Hertzberg, Antonio D Córcoles, Andrew A Houck, Jay M Gambetta, and Jerry M Chow. Broadband filters for abatement of spontaneous emission in circuit quantum electrodynamics. *Applied Physics Letters*, 107(17):172601, 2015.

[19] Peter Brooks, Alexei Kitaev, and John Preskill. Protected gates for superconducting qubits. *Phys. Rev. A*, 87(5):052306, 2013.

[20] S. A. Bulgadaev. Phase diagram of a dissipative quantum system. *JETP Lett.*, 39(6):264–267, 1984.

[21] M. Büttiker. Zero-current persistent potential drop across small-capacitance Josephson junctions. *Phys. Rev. B*, 36(7):3548, 1987.

[22] Jonas Bylander, Simon Gustavsson, Fei Yan, Fumiki Yoshihara, Khalil Harrabi, George Fitch, David G Cory, Yasunobu Nakamura, Jaw-Shen Tsai, and William D Oliver. Noise spectroscopy through dynamical decoupling with a superconducting flux qubit. *Nature Physics*, 7(7):565–570, 2011.

[23] G. Catelani, J. Koch, L. Frunzio, R. J. Schoelkopf, M. H. Devoret, and L. I. Glazman. Quasiparticle relaxation of superconducting qubits in the presence of flux. *Phys. Rev. Lett.*, 106:077002, Feb 2011.

[24] Gianluigi Catelani, Robert J Schoelkopf, Michel H Devoret, and Leonid I Glazman. Relaxation and frequency shifts induced by quasiparticles in superconducting qubits. *Physical Review B*, 84(6):064517, 2011.

[25] Karin Cedergren, Roger Ackroyd, Sergey Kafanov, Nicolas Vogt, Alexander Shnirman, and Timothy Duty. Insulating Josephson junction chains as pinned luttinger liquids. *Phys. Rev. Lett.*, 119(16):167701, 2017.

[26] Floy I Chang, Richard Yeh, Gisela Lin, Patrick B Chu, Eric G Hoffman, Ezekiel J Kruglick, Kristofer SJ Pister, and Michael H Hecht. Gas-phase silicon micromachining with xenon difluoride. In *Microelectronic structures and microelectromechanical devices for optical processing and multimedia applications*, volume 2641, pages 117–128. SPIE, 1995.

[27] Irinel Chiorescu, Y Nakamura, CJP Ma Harmans, and JE Mooij. Coherent quantum dynamics of a superconducting flux qubit. *Science*, 299(5614):1869–1871, 2003.

[28] John Clarke, Andrew Cleland, Michel H. Devoret, Daniel Esteve, and John Martinis. Quantum mechanics of a macroscopic variable: The phase difference of a Josephson junction. *Science*, 239(4843):992–997, 1988.

[29] John Clarke and Frank K. Wilhelm. Superconducting quantum bits. *Nature*, 453(7198):1031–1042, 2008.

[30] Andrew Nicholas Cleland. *Macroscopic quantum tunneling in Josephson tunnel junctions and Coulomb blockade in single small tunnel junctions*. University of California, Berkeley, 1991.

[31] Richard J Cook. What are quantum jumps? *Physica Scripta*, 1988(T21):49, 1988.

[32] Silvia Corlevi, Wiebke Guichard, Frank W. J. Hekking, and David B. Haviland. Phase-charge duality of a Josephson junction in a fluctuating electromagnetic environment. *Phys. Rev. Lett.*, 97(9):096802, 2006.

[33] Audrey Cottet. *Implementation of a quantum bit in a superconducting circuit*. PhD thesis, PhD Thesis, Université Paris 6, 2002.

[34] Nathanaël Cottet, Haonan Xiong, Long B Nguyen, Yen-Hsiang Lin, and Vladimir E Manucharyan. Electron shelving of a superconducting artificial atom. *Nature communications*, 12(1):1–6, 2021.

[35] Nicolò Crescini, Samuel Cailleaux, Wiebke Guichard, Cécile Naud, Olivier Buisson, Kater Murch, and Nicolas Roch. Evidence of dual shapiro steps in a josephson junctions array. *arXiv preprint arXiv:2207.09381*, 2022.

[36] M. H. Devoret. Quantum fluctuations in electrical circuits. *Les Houches Lectures, Session LXIII*, 1995.

[37] M.H. Devoret, Steven Girvin, and Robert Schoelkopf. Circuit-qed: How strong can the coupling between a Josephson junction atom and a transmission line resonator be? *Ann. Phys.*, 16(10-11):767–779, 2007.

[38] Michel H Devoret. Does brian josephson's gauge-invariant phase difference live on a line or a circle? *Journal of Superconductivity and Novel Magnetism*, 34(6):1633–1642, 2021.

[39] Michel H Devoret, Daniel Esteve, Hermann Grabert, G-L Ingold, Hugues Pothier, and Cristian Urbina. Effect of the electromagnetic environment on the coulomb blockade in ultrasmall tunnel junctions. *Physical review letters*, 64(15):1824, 1990.

[40] Angelo Di Marco, Frank W. J. Hekking, and Gianluca Rastelli. Quantum phase-slip junction under microwave irradiation. *Phys. Rev. B*, 91(18):184512, 2015.

[41] Agustin Di Paolo, Thomas E Baker, Alexandre Foley, David Sénéchal, and Alexandre Blais. Efficient modeling of superconducting quantum circuits with tensor networks. *npj Quantum Information*, 7(1):1–11, 2021.

[42] L. DiCarlo, J. M. Chow, J. M. Gambetta, Lev S. Bishop, B. R. Johnson, D. I. Schuster, J. Majer, A. Blais, L. Frunzio, S. M. Girvin, et al. Demonstration of two-qubit algorithms with a superconducting quantum processor. *Nature*, 460(7252):240, 2009.

[43] A Yu Dmitriev and OV Astafiev. A perspective on superconducting flux qubits. *Applied Physics Letters*, 119(8):080501, 2021.

[44] Ebru Dogan, Dario Rosenstock, Loïck Le Guevel, Haonan Xiong, Raymond A Mencia, Aaron Somoroff, Konstantin N Nesterov, Maxim G Vavilov, Vladimir E Manucharyan, and Chen Wang. Demonstration of the two-fluxonium cross-resonance gate. *arXiv preprint arXiv:2204.11829*, 2022.

[45] G. J. Dolan. Offset masks for lift-off photoprocessing. *Appl. Phys. Lett.*, 31(5):337–339, 1977.

[46] B. Douçot and L. B. Ioffe. Physical implementation of protected qubits. *Reports on Progress in Physics*, 75(7):072001, 2012.

[47] Tim Duty, Goeran Johansson, Kevin Bladh, David Gunnarsson, Chris Wilson, and Per Delsing. Observation of quantum capacitance in the cooper-pair transistor. *Physical review letters*, 95(20):206807, 2005.

[48] Riccardo d'Agostino and Daniel L Flamm. Plasma etching of si and sio2 in sf6–o2 mixtures. *Journal of Applied Physics*, 52(1):162–167, 1981.

[49] Nathan Earnest, Srivatsan Chakram, Yao Lu, Nicholas Irons, Ravi K Naik, Nelson Leung, Leo Ocola, David A Czaplewski, Brian Baker, Jay Lawrence, et al. Realization of a λ system with metastable states of a capacitively shunted fluxonium. *Physical review letters*, 120(15):150504, 2018.

[50] Clayton Easter and Chad O'Neal. Xef2 etching of silicon for the release of microcantilever based sensors. In *ASME International Mechanical Engineering Congress and Exposition*, volume 48746, pages 697–701, 2008.

[51] Jack Ekin. *Experimental techniques for low-temperature measurements: cryostat design, material properties and superconductor critical-current testing*. Oxford university press, 2006.

[52] Adem Ergül, Jack Lidmar, Jan Johansson, Yağız Azizoğlu, David Schaeffer, and David B. Haviland. Localizing quantum phase slips in one-dimensional Josephson junction chains. *New J. Phys.*, 15(9):095014, 2013.

[53] David G Ferguson, Andrew A Houck, and Jens Koch. Symmetries and collective excitations in large superconducting circuits. *Physical Review X*, 3(1):011003, 2013.

[54] Richard P. Feynman, Robert B. Leighton, and Matthew Sands. *Feynman lectures on physics. Volume 2: Mainly electromagnetism and matter*. Addison-Wesley, 1964.

[55] Quentin Ficheux. *Quantum trajectories with incompatible decoherence channels*. PhD thesis, École normale supérieure-ENS PARIS, 2018.

[56] Quentin Ficheux, Long B Nguyen, Aaron Somoroff, Haonan Xiong, Konstantin N Nesterov, Maxim G Vavilov, and Vladimir E Manucharyan. Fast logic with slow qubits: microwave-activated controlled-z gate on low-frequency fluxoniums. *Physical Review X*, 11(2):021026, 2021.

[57] Luigi Frunzio, Andreas Wallraff, David Schuster, Johannes Majer, and Robert Schoelkopf. Fabrication and characterization of superconducting circuit qed devices for quantum computation. *IEEE transactions on applied superconductivity*, 15(2):860–863, 2005.

[58] Jay Gambetta, Alexandre Blais, Maxime Boissonneault, Andrew A Houck, DI Schuster, and Steven M Girvin. Quantum trajectory approach to circuit qed: Quantum jumps and the zeno effect. *Physical Review A*, 77(1):012112, 2008.

[59] Jiansong Gao. *The physics of superconducting microwave resonators*. California Institute of Technology, 2008.

[60] K Geerlings, S Shankar, E Edwards, L Frunzio, RJ Schoelkopf, and MH Devoret. Improving the quality factor of microwave compact resonators by optimizing their geometrical parameters. *Applied Physics Letters*, 100(19):192601, 2012.

[61] Steven M Girvin. Circuit qed: superconducting qubits coupled to microwave photons. *Quantum machines: measurement and control of engineered quantum systems*, pages 113–256, 2014.

[62] Martin Göppl, A Fragner, M Baur, R Bianchetti, Stefan Filipp, Johannes M Fink, Peter J Leek, G Puebla, L Steffen, and Andreas Wallraff. Coplanar waveguide resonators for circuit quantum electrodynamics. *Journal of Applied Physics*, 104(11):113904, 2008.

[63] Nicholas Christopher Grabon. *Interacting Photons in Circuit Quantum Electrodynamics: Decay of the Collective Phase Mode in One-Dimensional Josephson Junction Arrays Due to Quantum Phase-Slip Fluctuations*. PhD thesis, University of Maryland, College Park, 2020.

[64] Lukas Grünhaupt, Martin Spiecker, Daria Gusenkova, Nataliya Maleeva, Sebastian T Skacel, Ivan Takmakov, Francesco Valenti, Patrick Winkel, Hannes Rotzinger, Wolfgang Wernsdorfer, et al. Granular aluminium as a superconducting material for high-impedance quantum circuits. *Nature Materials*, 18(8):816–819, 2019.

[65] David Gunnarsson, Tim Duty, Kevin Bladh, and Per Delsing. Tunability of a 2 e periodic single cooper pair box. *Physical Review B*, 70(22):224523, 2004.

[66] David Gunnarsson, Juha-Matti Pirkkalainen, Jian Li, Gheorghe Sorin Paraoanu, Pertti Hakonen, Mika Sillanpää, and Mika Prunnila. Dielectric losses in multi-layer josephson junction qubits. *Superconductor Science and Technology*, 26(8):085010, 2013.

[67] Simon Günzler, Patrick Winkel, Dennis Rieger, Kiril Borisov, Martin Spiecker, Alexey V Ustinov, Ioan M Pop, and Wolfgang Wernsdorfer. Superconducting microwave magnetometer for absolute flux detection. *arXiv preprint arXiv:2107.05929*, 2021.

[68] Daria Gusenkova, Martin Spiecker, Richard Gebauer, Madita Willsch, Dennis Willsch, Francesco Valenti, Nick Karcher, Lukas Grünhaupt, Ivan Takmakov, Patrick Winkel, et al. Quantum nondemolition dispersive readout of a superconducting artificial atom using large photon numbers. *Physical Review Applied*, 15(6):064030, 2021.

[69] Simon Gustavsson, Fei Yan, Gianluigi Catelani, Jonas Bylander, Archana Kamal, Jeffrey Birenbaum, David Hover, Danna Rosenberg, Gabriel Samach, Adam P. Sears, Steven J. Weber, Jonilyn L. Yoder, John Clarke, Andrew J. Kerman, Fumiki Yoshihara, Yasunobu Nakamura, Terry P. Orlando, and William D. Oliver. Suppressing relaxation in superconducting qubits by quasiparticle pumping. *Science*, 354(6319):1573–1577, 2016.

[70] András Gyenis, Agustin Di Paolo, Jens Koch, Alexandre Blais, Andrew A Houck, and David I Schuster. Moving beyond the transmon: Noise-protected superconducting quantum circuits. *PRX Quantum*, 2(3):030101, 2021.

[71] Serge Haroche and Jean-Michel Raimond. *Exploring the quantum: atoms, cavities, and photons*. Oxford university press, 2006.

[72] Farid Hassani, Matilda Peruzzo, Lucky N. Kapoor, Andrea Trioni, Martin Zemlicka, and Johannes M. Fink. A superconducting qubit with noise-insensitive plasmon levels and decay-protected fluxon states. 2 2022.

[73] DB Haviland, LS Kuzmin, P Delsing, KK Likharev, and T Claeson. Experimental evidence for the coulomb blockade of cooper pair tunneling and bloch oscillations in single josephson junctions. *Zeitschrift für Physik B Condensed Matter*, 85(3):339–347, 1991.

[74] TM Hazard, ADPA Gyenis, Agustin Di Paolo, AT Asfaw, SA Lyon, AAHA Blais, and AA Houck. Nanowire superinductance fluxonium qubit. *Physical review letters*, 122(1):010504, 2019.

[75] FWJ Hekking and LI Glazman. Quantum fluctuations in the equilibrium state of a thin superconducting loop. *Physical Review B*, 55(10):6551, 1997.

[76] David A Herrera-Martí, Ahsan Nazir, and Sean D Barrett. Tradeoff between leakage and dephasing errors in the fluxonium qubit. *Physical Review B*, 88(9):094512, 2013.

[77] María Hita-Pérez, Pedro Orellana, Juan José García-Ripoll, and Manuel Pino. Bound states in the continuum in a heavy fluxonium qutrit. *arXiv preprint arXiv:2205.07757*, 2022.

[78] María Hita-Pérez, Pedro Orellana, Juan José García-Ripoll, and Manuel Pino. Bound states in the continuum in a fluxonium qutrit, 2022.

[79] T Holst, D Esteve, C Urbina, and MH Devoret. Effect of a transmission line resonator on a small capacitance tunnel junction. *Physical review letters*, 73(25):3455, 1994.

[80] A. A. Houck, J. A. Schreier, B. R. Johnson, J. M. Chow, Jens Koch, J. M. Gambetta, D. I. Schuster, L. Frunzio, M. H. Devoret, S. M. Girvin, et al. Controlling the spontaneous emission of a superconducting transmon qubit. *Phys. Rev. Lett.*, 101(8):080502, 2008.

[81] M Houzet, K Serniak, G Catelani, MH Devoret, and LI Glazman. Photon-assisted charge-parity jumps in a superconducting qubit. *Physical review letters*, 123(10):107704, 2019.

[82] GY Hu and RF O'Connell. Bloch oscillations in small-capacitance josephson junctions. *Physical Review B*, 47(14):8823, 1993.

[83] Gert-Ludwig Ingold, Hermann Grabert, and Udo Eberhardt. Cooper-pair current through ultrasmall josephson junctions. *Physical Review B*, 50(1):395, 1994.

[84] Gert-Ludwig Ingold and Yu V Nazarov. Charge tunneling rates in ultrasmall junctions. In *Single charge tunneling*, pages 21–107. Springer, 1992.

[85] G. Ithier, E. Collin, P. Joyez, P. J. Meeson, D. Vion, D. Esteve, F. Chiarello, A. Shnirman, Y. Makhlin, J. Schriefl, and G. Schön. Decoherence in a superconducting quantum bit circuit. *Phys. Rev. B*, 72:134519, Oct 2005.

[86] G Ithier, E Collin, P Joyez, PJ Meeson, Denis Vion, Daniel Esteve, F Chiarello, A Shnirman, Yu Makhlin, Josef Schriefl, et al. Decoherence in a superconducting quantum bit circuit. *Physical Review B*, 72(13):134519, 2005.

[87] John David Jackson. Classical electrodynamics, 1999.

[88] J Robert Johansson, Paul D Nation, and Franco Nori. Qutip: An open-source python framework for the dynamics of open quantum systems. *Computer Physics Communications*, 183(8):1760–1772, 2012.

[89] Brian David Josephson. Possible new effects in superconductive tunnelling. *Physics Letters*, 1(7):251–253, 1962.

[90] Alan M. Kadin and Herbert Kroemer. *Introduction to superconducting circuits*. 1999.

[91] Phillip Kaye, Raymond Laflamme, and Michele Mosca. *An introduction to quantum computing*. OUP Oxford, 2006.

[92] J. Koch, T. M. Yu, J. Gambetta, A. A. Houck, D. I. Schuster, J. Majer, A. Blais, M. H. Devoret, S. M. Girvin, and R. J. Schoelkopf. Charge-insensitive qubit design derived from the Cooper pair box. *Phys. Rev. A*, 76(4):042319, 2007.

[93] Jens Koch, V. Manucharyan, M. H. Devoret, and L. I. Glazman. Charging effects in the inductively shunted Josephson junction. *Phys. Rev. Lett.*, 103(21):217004, 2009.

[94] A. Kou, W. C. Smith, U. Vool, I. M. Pop, K. M. Sliwa, M. Hatridge, L Frunzio, and M. H. Devoret. Simultaneous monitoring of fluxonium qubits in a waveguide. *Phys. Rev. Appl.*, 9(6):064022, 2018.

[95] A Kou, WC Smith, U Vool, RT Brierley, H Meier, L Frunzio, SM Girvin, LI Glazman, and MH Devoret. Fluxonium-based artificial molecule with a tunable magnetic moment. *Physical Review X*, 7(3):031037, 2017.

[96] Philip Krantz, Morten Kjaergaard, Fei Yan, Terry P Orlando, Simon Gustavsson, and William D Oliver. A quantum engineer's guide to superconducting qubits. *Applied Physics Reviews*, 6(2):021318, 2019.

[97] Sebastian Krinner, Simon Storz, Philipp Kurpiers, Paul Magnard, Johannes Heinsoo, Raphael Keller, Janis Luetolf, Christopher Eichler, and Andreas Wallraff. Engineering cryogenic setups for 100-qubit scale superconducting circuit systems. *EPJ Quantum Technology*, 6(1):2, 2019.

[98] Yu Krupko, VD Nguyen, Thomas Weißl, É Dumur, J Puertas, R Dassonneville, C Naud, FWJ Hekking, DM Basko, O Buisson, et al. Kerr nonlinearity in a superconducting josephson metamaterial. *Physical Review B*, 98(9):094516, 2018.

[99] L. S. Kuzmin and D. B. Haviland. Observation of the Bloch oscillations in an ultrasmall Josephson junction. *Phys. Rev. Lett.*, 67(20):2890, 1991.

[100] LS Kuzmin, Yu V Nazarov, DB Haviland, P Delsing, and T Claeson. Coulomb blockade and incoherent tunneling of cooper pairs in ultrasmall junctions affected by strong quantum fluctuations. *Physical review letters*, 67(9):1161, 1991.

[101] Roman Kuzmin, Nitish Mehta, Nicholas Grabon, and Vladimir E Manucharyan. Tuning the inductance of josephson junction arrays without squids. *arXiv preprint arXiv:2210.12119*, 2022.

[102] Roman Kuzmin, Nitish Mehta, Nicholas Grabon, Raymond Mencia, and Vladimir E Manucharyan. Superstrong coupling in circuit quantum electrodynamics. *npj Quantum Information*, 5(1):1–6, 2019.

[103] Roman Kuzmin, Raymond Mencia, Nicholas Grabon, Nitish Mehta, Yen-Hsiang Lin, and Vladimir E. Manucharyan. Quantum electrodynamics of a superconductor-insulator phase transition. *Nature Physics*, 2019.

[104] Sangil Kwon, Akiyoshi Tomonaga, Gopika Lakshmi Bhai, Simon J Devitt, and Jaw-Shen Tsai. Gate-based superconducting quantum computing. *Journal of Applied Physics*, 129(4):041102, 2021.

[105] Nathan K Langford. Circuit qed-lecture notes. *arXiv preprint arXiv:1310.1897*, 2013.

[106] Sébastien Léger, Javier Puertas-Martínez, Karthik Bharadwaj, Rémy Dassonneville, Jovian Delaforce, Farshad Foroughi, Vladimir Milchakov, Luca Planat, Olivier Buisson, Cécile Naud, et al. Observation of quantum many-body effects due to zero point fluctuations in superconducting circuits. *Nature communications*, 10(1):1–8, 2019.

[107] Anthony J Leggett. Macroscopic quantum systems and the quantum theory of measurement. *Progress of Theoretical Physics Supplement*, 69:80–100, 1980.

[108] Peng Li and Xinxin Li. A single-sided micromachined piezoresistive sio2 cantilever sensor for ultra-sensitive detection of gaseous chemicals. *Journal of Micromechanics and Microengineering*, 16(12):2539, 2006.

[109] Konstantin K Likharev. *Dynamics of Josephson junctions and circuits*. Routledge, 2022.

[110] Yen-Hsiang Lin, J Nelson, and AM Goldman. Superconductivity of very thin films: The superconductor–insulator transition. *Physica C: Superconductivity and its Applications*, 514:130–141, 2015.

[111] Yen-Hsiang Lin, Long B Nguyen, Nicholas Grabon, Jonathan San Miguel, Natalia Pankratova, and Vladimir E Manucharyan. Demonstration of protection of a superconducting qubit from energy decay. *Physical review letters*, 120(15):150503, 2018.

[112] Rodney Loudon. *The quantum theory of light*. OUP Oxford, 2000.

[113] H Mabuchi and AC Doherty. Cavity quantum electrodynamics: coherence in context. *Science*, 298(5597):1372–1377, 2002.

[114] Vladimir E. Manucharyan. Superinductance. *Thesis*, 2012.

[115] Vladimir E Manucharyan, Alexandre Baksic, and Cristiano Ciuti. Resilience of the quantum rabi model in circuit qed. *Journal of Physics A: Mathematical and Theoretical*, 50(29):294001, 2017.

[116] Vladimir E Manucharyan, Jens Koch, Markus Brink, Leonid I Glazman, and Michel H Devoret. Coherent oscillations between classically separable quantum states of a superconducting loop. *arXiv preprint arXiv:0910.3039*, 2009.

[117] Vladimir E Manucharyan, Jens Koch, Leonid I Glazman, and Michel H Devoret. Fluxonium: Single cooper-pair circuit free of charge offsets. *Science*, 326(5949):113–116, 2009.

[118] Vladimir E. Manucharyan, Jens Koch, Leonid I. Glazman, and Michel H. Devoret. Fluxonium: Single Cooper-pair circuit free of charge offsets. *Science*, 326(5949):113–116, 2009.

[119] Vladimir E. Manucharyan, Nicholas A. Masluk, Archana Kamal, Jens Koch, Leonid I. Glazman, and Michel H. Devoret. Evidence for coherent quantum phase slips across a Josephson junction array. *Phys. Rev. B*, 85(2):024521, 2012.

[120] John M Martinis, Michel H Devoret, and John Clarke. Quantum josephson junction circuits and the dawn of artificial atoms. *Nature Physics*, 16(3):234–237, 2020.

[121] John M. Martinis, S. Nam, J. Aumentado, and C. Urbina. Rabi oscillations in a large Josephson-junction qubit. *Phys. Rev. Lett.*, 89(11):117901, 2002.

[122] Nicholas A. Masluk. Reducing the losses of the fluxonium artificial atom. *Thesis*, 2012.

[123] Nicholas A Masluk, Ioan M Pop, Archana Kamal, Zlatko K Minev, and Michel H Devoret. Microwave characterization of josephson junction arrays: Implementing a low loss superinductance. *Physical review letters*, 109(13):137002, 2012.

[124] K. A. Matveev, A. I. Larkin, and L. I. Glazman. Persistent current in superconducting nanorings. *Phys. Rev. Lett.*, 89(9):96802, 2002.

[125] Corey Rae Harrington McRae, Haozhi Wang, Jiansong Gao, Michael R Vissers, Teresa Brecht, Andrew Dunsworth, David P Pappas, and Josh Mutus. Materials loss measurements using superconducting microwave resonators. *Review of Scientific Instruments*, 91(9):091101, 2020.

[126] Nitish Jitendrakumar Mehta. *Quantum impurity regime of circuit quantum electrodynamics*. PhD thesis, 2022.

[127] Raymond Mencia, Yen-Hsiang Lin, and Vladimir Manucharyan. Superconducting titanium nitride films grown by directional reactive evaporation. *Journal of Applied Physics*, 130(22):225109, 2021.

[128] J. E. Mooij and Yu. V. Nazarov. Superconducting nanowires as quantum phase-slip junctions. *Nature Physics*, 2(3):169, 2006.

[129] JE Mooij and CJPM Harmans. Phase-slip flux qubits. *New Journal of Physics*, 7(1):219, 2005.

[130] Paul Müller, Alexey V Ustinov, and VV Schmidt. The physics of superconductors. introduction to fundamentals and applications. 1997.

[131] Anil Murani, Nicolas Bourlet, Hélène le Sueur, Fabien Portier, Carles Altimiras, Daniel Esteve, Hermann Grabert, Jürgen Stockburger, and Philippe Joyez. Absence of a dissipative quantum phase transition in Josephson junctions. *arXiv preprint arXiv:1905.01161*, 2019.

[132] Conal E Murray. Material matters in superconducting qubits. *Materials Science and Engineering: R: Reports*, 146:100646, 2021.

[133] Y. Nakamura, Y. A. Pashkin, and J. S. Tsai. Coherent control of macroscopic quantum states in a single-Cooper-pair box. *Nature*, 398(6730):786–788, 1999.

[134] Long B. Nguyen, Yen-Hsiang Lin, Aaron Somoroff, Raymond Mencia, Nicholas Grabon, and Vladimir E. Manucharyan. The high-coherence fluxonium qubit. *arXiv preprint arXiv:1810.11006*, 2018.

[135] Long B Nguyen, Yen-Hsiang Lin, Aaron Somoroff, Raymond Mencia, Nicholas Grabon, and Vladimir E Manucharyan. High-coherence fluxonium qubit. *Physical Review X*, 9(4):041041, 2019.

[136] Long Bao Nguyen. *Toward the Fluxonium Quantum Processor*. PhD thesis, University of Maryland, College Park, 2020.

[137] Michael A Nielsen and Isaac Chuang. Quantum computation and quantum information, 2002.

[138] P Pai, FK Chowdhury, Carlos H Mastrangelo, and M Tabib-Azar. Mems-based hemispherical resonator gyroscopes. In *SENSORS, 2012 IEEE*, pages 1–4. IEEE, 2012.

[139] SV Panyukov and AD Zaikin. Quantum fluctuations and the current-phase relation in josephson junctions and squids. *Physica B: Condensed Matter*, 152(1-2):162–164, 1988.

[140] David P. Pappas, Michael R. Vissers, David S. Wisbey, Jeffrey S. Kline, and Jiansong Gao. Two level system loss in superconducting microwave resonators. *IEEE Transactions on Applied Superconductivity*, 21(3):871–874, 2011.

[141] Ivan V Pechenezhskiy, Raymond A Mencia, Long B Nguyen, Yen-Hsiang Lin, and Vladimir E Manucharyan. The superconducting quasicharge qubit. *Nature*, 585(7825):368–371, 2020.

[142] Jukka P Pekola, Olli-Pentti Saira, Ville F Maisi, Antti Kemppinen, Mikko Möttönen, Yuri A Pashkin, and Dmitri V Averin. Single-electron current sources: Toward a refined definition of the ampere. *Reviews of Modern Physics*, 85(4):1421, 2013.

[143] J. S. Penttilä, Ü. Parts, Pertti J. Hakonen, M. A. Paalanen, and E. B. Sonin. "superconductor-insulator transition" in a single Josephson junction. *Phys. Rev. Lett.*, 82(5):1004, 1999.

[144] Matilda Peruzzo, Farid Hassani, Gregory Szep, Andrea Trioni, Elena Redchenko, Martin Žemlička, and Johannes M Fink. Geometric superinductance qubits: Controlling phase delocalization across a single josephson junction. *PRX Quantum*, 2(4):040341, 2021.

[145] Matilda Peruzzo, Andrea Trioni, Farid Hassani, Martin Zemlicka, and Johannes M Fink. Surpassing the resistance quantum with a geometric superinductor. *Physical Review Applied*, 14(4):044055, 2020.

[146] Alexander PM Place, Lila VH Rodgers, Pranav Mundada, Basil M Smitham, Mattias Fitzpatrick, Zhaoqi Leng, Anjali Premkumar, Jacob Bryon, Andrei Vrajitoarea, Sara Sussman, et al. New material platform for superconducting transmon qubits with coherence times exceeding 0.3 milliseconds. *Nature communications*, 12(1):1–6, 2021.

[147] C.P. Poole, H.A. Farach, R.J. Creswick, and R. Prozorov. *Superconductivity*. Elsevier Science, 2010.

[148] Ioan M. Pop, Kurtis Geerlings, Gianluigi Catelani, Robert J. Schoelkopf, Leonid I. Glazman, and Michel H. Devoret. Coherent suppression of electromagnetic dissipation due to superconducting quasiparticles. *Nature*, 508(7496):369–372, 2014.

[149] Ioan Mihai Pop, Benoît Douçot, L Ioffe, I Protopopov, Florent Lecocq, Iulian Matei, Olivier Buisson, and Wiebke Guichard. Experimental demonstration of aharonov-casher interference in a josephson junction circuit. *Physical Review B*, 85(9):094503, 2012.

[150] Ioan Mihai Pop, I Protopopov, Florent Lecocq, Zhihui Peng, Bernard Pannetier, Olivier Buisson, and Wiebke Guichard. Measurement of the effect of quantum phase slips in a josephson junction chain. *Nature Physics*, 6(8):589–592, 2010.

[151] David M Pozar. *Microwave engineering; 3rd ed.* Wiley, Hoboken, NJ, 2005.

[152] Javier Puertas Martínez, Sébastien Léger, Nicolas Gheeraert, Rémy Dassonneville, Luca Planat, Farshad Foroughi, Yuriy Krupko, Olivier Buisson, Cécile Naud, Wiebke Hasch-Guichard, et al. A tunable josephson platform to explore many-body quantum optics in circuit-qed. *npj Quantum Information*, 5(1):1–8, 2019.

[153] Edward M Purcell, Henry Cutler Torrey, and Robert V Pound. Resonance absorption by nuclear magnetic moments in a solid. *Physical review*, 69(1-2):37, 1946.

[154] Ivaylo W Rangelow and Hans Löschner. Reactive ion etching for microelectrical mechanical system fabrication. *Journal of Vacuum Science & Technology B: Microelectronics and Nanometer Structures Processing, Measurement, and Phenomena*, 13(6):2394–2399, 1995.

[155] Gianluca Rastelli, Ioan M. Pop, and Frank W. J. Hekking. Quantum phase slips in Josephson junction rings. *Phys. Rev. B*, 87(17):174513, 2013.

[156] Jun John Sakurai. *Advanced quantum mechanics*. Pearson Education India, 2006.

[157] Albert Schmid. Diffusion and localization in a dissipative quantum system. *Phys. Rev. Lett.*, 51(17):1506, 1983.

[158] R. J. Schoelkopf, A. A. Clerk, S. M. Girvin, K. W. Lehnert, and M. H. Devoret. *Qubits as Spectrometers of Quantum Noise*, pages 175–203. Springer Netherlands, Dordrecht, 2003.

[159] RJ Schoelkopf, AA Clerk, SM Girvin, KW Lehnert, and MH Devoret. Qubits as spectrometers of quantum noise. In *Quantum noise in mesoscopic physics*, pages 175–203. Springer, 2003.

[160] Gerd Schön and Andrej Dmitievič Zaikin. Quantum coherent effects, phase transitions, and the dissipative dynamics of ultra small tunnel junctions. *Physics Reports*, 198(5-6):237–412, 1990.

[161] D. I. Schuster, Andreas Wallraff, Alexandre Blais, L Frunzio, R-S Huang, J Majer, S. M Girvin, Schoelkopf, and R. J. ac stark shift and dephasing of a superconducting qubit strongly coupled to a cavity field. *Phys. Rev. Lett.*, 94(12):123602, 2005.

[162] David Isaac Schuster. *Circuit quantum electrodynamics*. Yale University, 2007.

[163] S Sendelbach, D Hover, A Kittel, M Mück, John M Martinis, and R McDermott. Magnetism in squids at millikelvin temperatures. *Physical review letters*, 100(22):227006, 2008.

[164] Rais S Shaikhaidarov, Kyung Ho Kim, Jacob W Dunstan, Ilya V Antonov, Sven Linzen, Mario Ziegler, Dmitry S Golubev, Vladimir N Antonov, Evgeni V Il'ichev, and Oleg V Astafiev. Quantized current steps due to the ac coherent quantum phase-slip effect. *Nature*, 608(7921):45–49, 2022.

[165] Irfan Siddiqi. Engineering high-coherence superconducting qubits. *Nature Reviews Materials*, 6(10):875–891, 2021.

[166] DH Slichter, Clemens Müller, R Vijay, SJ Weber, Alexandre Blais, and Irfan Siddiqi. Quantum zeno effect in the strong measurement regime of circuit quantum electrodynamics. *New Journal of Physics*, 18(5):053031, 2016.

[167] WC Smith, A Kou, U Vool, IM Pop, L Frunzio, RJ Schoelkopf, and MH Devoret. Quantization of inductively shunted superconducting circuits. *Physical Review B*, 94(14):144507, 2016.

[168] William C Smith, Marius Villiers, Antoine Marquet, Jose Palomo, MR Delbecq, Takis Kontos, Philippe Campagne-Ibarcq, Benoît Douçot, and Zaki Leghtas. Magnifying quantum phase fluctuations with cooper-pair pairing. *Physical Review X*, 12(2):021002, 2022.

[169] William Clarke Smith. *Design of protected superconducting qubits*. PhD thesis, Yale University, 2019.

[170] Aaron Somoroff. *Quantum Computing with Fluxonium: Digital and Analog Directions*. PhD thesis, 2022.

[171] Aaron Somoroff, Quentin Ficheux, Raymond A Mencia, Haonan Xiong, Roman V Kuzmin, and Vladimir E Manucharyan. Millisecond coherence in a superconducting qubit. *arXiv preprint arXiv:2103.08578*, 2021.

[172] Jeremy Stevens. *Effect of the Environment on Fluxonium Qubits and Thermodynamics of Quantum Measurement*. PhD thesis, Lyon, 2021.

[173] Anna Stockklauser, Pasquale Scarlino, Jonne V. Koski, Simone Gasparinetti, Christian Kraglund Andersen, Christian Reichl, Werner Wegscheider, Thomas Ihn, Klaus Ensslin, and Andreas Wallraff. Strong coupling cavity qed with gate-defined double quantum dots enabled by a high impedance resonator. *Phys. Rev. X*, 7(1):011030, 2017.

[174] Frederick W Strauch, Philip R Johnson, Alex J Dragt, CJ Lobb, JR Anderson, and FC Wellstood. Quantum logic gates for coupled superconducting phase qubits. *Physical review letters*, 91(16):167005, 2003.

[175] Michael Tinkham. *Introduction to Superconductivity*. Dover Publications, 2 edition, 2004.

[176] C Veyres and V Fouad Hanna. Extension of the application of conformal mapping techniques to coplanar lines with finite dimensions. *International Journal of Electronics Theoretical and Experimental*, 48(1):47–56, 1980.

[177] R Vijay, DH Slichter, and I Siddiqi. Observation of quantum jumps in a superconducting artificial atom. *Physical review letters*, 106(11):110502, 2011.

[178] Giovanni Viola and Gianluigi Catelani. Collective modes in the fluxonium qubit. *Phys. Rev. B*, 92(22):224511, 2015.

[179] D. Vion, A. Aassime, A. Cottet, P. Joyez, H. Pothier, C. Urbina, D. Esteve, and M. H. Devoret. Manipulating the quantum state of an electrical circuit. *Science*, 296(5569):886–889, 2002.

[180] Denis Vion. Josephson quantum bits based on a cooper pair box. *Quantum entanglement and information processing, session LXXIX (Proceedings of the Les Houches Summer School)*, 2003.

[181] Denis Vion, A. Aassime, Audrey Cottet, P. Joyez, H. Pothier, C. Urbina, Daniel Esteve, and Michel H. Devoret. Manipulating the quantum state of an electrical circuit. *Science*, 296(5569):886–889, 2002.

[182] Uri Vool, Ioan M. Pop, Katrina Sliwa, Baleegh Abdo, Chen Wang, Teresa Brecht, Yvonne Y. Gao, Shyam Shankar, Michael Hatridge, Gianluigi Catelani, et al. Non-poissonian quantum jumps of a fluxonium qubit due to quasiparticle excitations. *Phys. Rev. Lett.*, 113(24):247001, 2014.

[183] Andreas Wallraff, David I. Schuster, Alexandre Blais, L. Frunzio, R.-S. Huang, J. Majer, S. Kumar, Steven M. Girvin, and Robert J. Schoelkopf. Strong coupling of a single photon to a superconducting qubit using circuit quantum electrodynamics. *Nature*, 431(7005):162–167, 2004.

[184] Chen Wang, Christopher Axline, Yvonne Y. Gao, Teresa Brecht, Y. Chu, L. Frunzio, M. H. Devoret, and R. J. Schoelkopf. Surface participation and dielectric loss in superconducting qubits. *Appl. Phys. Lett.*, 107(16):162601, 2015.

[185] Chenlu Wang, Xuegang Li, Huikai Xu, Zhiyuan Li, Junhua Wang, Zhen Yang, Zhenyu Mi, Xuehui Liang, Tang Su, Chuhong Yang, et al. Towards practical quantum computers: transmon qubit with a lifetime approaching 0.5 milliseconds. *npj Quantum Information*, 8(1):1–6, 2022.

[186] Michio Watanabe and David B. Haviland. Coulomb blockade and coherent single-Cooper-pair tunneling in single Josephson junctions. *Phys. Rev. Lett.*, 86(22):5120, 2001.

[187] Thomas Weißl, Bruno Küng, Étienne Dumur, Alexey K Feofanov, Iulian Matei, Cécile Naud, Olivier Buisson, Frank WJ Hekking, and Wiebke Guichard. Kerr coefficients of plasma resonances in josephson junction chains. *Physical Review B*, 92(10):104508, 2015.

[188] Thomas Weißl, Gianluca Rastelli, Iuliana Matei, Ioan M Pop, Olivier Buisson, Frank WJ Hekking, and Wiebke Guichard. Bloch band dynamics of a josephson junction in an inductive environment. *Physical Review B*, 91(1):014507, 2015.

[189] A Widom, G Megaloudis, TD Clark, JE Mutton, RJ Prance, and H Prance. The josephson pendulum as a nonlinear capacitor. *Journal of low temperature physics*, 57(5):651–658, 1984.

[190] HF Winters and JW Coburn. The etching of silicon with xef2 vapor. *Applied Physics Letters*, 34(1):70–73, 1979.

[191] Howard M Wiseman and Gerard J Milburn. *Quantum measurement and control*. Cambridge university press, 2009.

[192] Haonan Xiong, Quentin Ficheux, Aaron Somoroff, Long B Nguyen, Ebru Dogan, Dario Rosenstock, Chen Wang, Konstantin N Nesterov, Maxim G Vavilov, and Vladimir E Manucharyan. Arbitrary controlled-phase gate on fluxonium qubits using differential ac stark shifts. *Physical Review Research*, 4(2):023040, 2022.

[193] Fei Yan, Simon Gustavsson, Archana Kamal, Jeffrey Birenbaum, Adam P Sears, David Hover, Ted J Gudmundsen, Danna Rosenberg, Gabriel Samach, Steven Weber, et al. The flux qubit revisited to enhance coherence and reproducibility. *Nature communications*, 7(1):1–9, 2016.

[194] Fumiki Yoshihara, Tomoko Fuse, Sahel Ashhab, Kosuke Kakuyanagi, Shiro Saito, and Kouichi Semba. Superconducting qubit–oscillator circuit beyond the ultrastrong-coupling regime. *Nature Physics*, 13(1):44–47, 2017.

[195] Y Yuzhelevski, M Yuzhelevski, and G Jung. Random telegraph noise analysis in time domain. *Review of Scientific Instruments*, 71(4):1681–1688, 2000.

[196] Gengyan Zhang, Yanbing Liu, James J Raftery, and Andrew A Houck. Suppression of photon shot noise dephasing in a tunable coupling superconducting qubit. *npj Quantum Information*, 3(1):1–4, 2017.

[197] Helin Zhang, Srivatsan Chakram, Tanay Roy, Nathan Earnest, Yao Lu, Ziwen Huang, D. K. Weiss, Jens Koch, and David I. Schuster. Universal fast-flux control of a coherent, low-frequency qubit. *Phys. Rev. X*, 11:011010, Jan 2021.

[198] Guanyu Zhu, David G. Ferguson, Vladimir E. Manucharyan, and Jens Koch. Circuit qed with fluxonium qubits: Theory of the dispersive regime. *Phys. Rev. B*, 87(2):024510, 2013.

[199] Guanyu Zhu and Jens Koch. Asymptotic expressions for charge-matrix elements of the fluxonium circuit. *Physical Review B*, 87(14):144518, 2013.

[200] AB Zorin. Bloch inductance in small-capacitance josephson junctions. *Physical review letters*, 96(16):167001, 2006.